



HAL
open science

Study of Photovoltaic System Integration in Microgrids through Real-Time Modeling and Emulation of its Components Using HiLeS

Alonso Gutiérrez Galeano

► **To cite this version:**

Alonso Gutiérrez Galeano. Study of Photovoltaic System Integration in Microgrids through Real-Time Modeling and Emulation of its Components Using HiLeS. Micro and nanotechnologies/Microelectronics. Université Paul Sabatier - Toulouse III, 2017. English. NNT : 2017TOU30178 . tel-01978781v2

HAL Id: tel-01978781

<https://laas.hal.science/tel-01978781v2>

Submitted on 6 Nov 2017

HAL is a multi-disciplinary open access archive for the deposit and dissemination of scientific research documents, whether they are published or not. The documents may come from teaching and research institutions in France or abroad, or from public or private research centers.

L'archive ouverte pluridisciplinaire **HAL**, est destinée au dépôt et à la diffusion de documents scientifiques de niveau recherche, publiés ou non, émanant des établissements d'enseignement et de recherche français ou étrangers, des laboratoires publics ou privés.

Université Fédérale



Toulouse Midi-Pyrénées



Universidad de
los Andes

THÈSE

En vue de l'obtention du

**DOCTORAT DE L'UNIVERSITÉ FÉDÉRALE
TOULOUSE MIDI-PYRÉNÉES**

**DOCTORADO UNIVERSIDAD DE LOS ANDES
BOGOTA-COLOMBIA**

Délivré par :

l'Université Toulouse 3 Paul Sabatier (UT3 Paul Sabatier)

Cotutelle Universidad de los Andes - Colombia

Présentée et soutenue le *06/09/2017* par :

ALONSO GUTIÉRREZ GALEANO

**Study of Photovoltaic System Integration in Microgrids
through Real-Time Modeling and Emulation of its
Components Using HiLeS**

JURY

GERMAIN GARCIA	Professeur d'Université	Président du Jury
RUBBY CASALLAS G.	Professeur d'Université	Membre du Jury
JUAN JOSÉ RODRIGUEZ A.	Professeur d'Université	Membre du Jury
OSWALDO LOPEZ SANTOS	Professeur d'Université	Membre du Jury
CARLOS CARREJO	Chargé de Recherche	Membre du Jury

École doctorale et spécialité :

GEET : Composants et Systèmes de Gestion de l'Énergie

Unité de Recherche :

Laboratoire d'Analyse et d'Architecture des Systèmes, LAAS-CNRS

Directeur(s) de Thèse :

Corinne ALONSO (UT3) et José Fernando JIMÉNEZ VARGAS (UniAndes)

Co-encadrant Michael BRESSAN

Rapporteurs :

Rubby CASALLAS GUTIERREZ et Juan José RODRIGUEZ ANDINA

**Study of Photovoltaic System Integration in Microgrids
through Real-Time Modeling and Emulation of its
Components Using HiLeS**

**Étude de l'Intégration des Systèmes Photovoltaïques aux
Microgrids par la Modélisation et Emulation Temps Réel de
ses Composants en Utilisant HiLeS**

Alonso GUTIÉRREZ GALEANO

Université de Toulouse III, Paul Sabatier - Universidad de los Andes
Advisors: Corinne ALONSO and José Fernando JIMÉNEZ VARGAS
Co-Advisor : Michael BRESSAN

October 2017

Acknowledgements

I would like to express my sincere gratitude to my advisors Pr. Fernando Jiménez, Pr. Corinne Alonso and Dr. Michael Bressan for their continuous support of my PhD study and related research.

My sincere thanks also goes to the Universidad de los Andes who funding my PhD research through the program *Crédito Condonable para Doctorado* and the Conv. 727-2015 of Colciencias. I wish to express my gratefulness to the Université Paul Sabatier, the doctoral school GEET and the Laboratory of Analysis and Architecture of Systems (LAAS-CNRS). Without their support it would not be possible to conduct this research.

Last but not the least, I would like to give a special acknowledgment to my wife Mara Calderón and my parents for encouraging me throughout this thesis and my life in general.

Abstract

Nowadays, the integration of photovoltaic systems into electrical grids is encouraging the expansion of microgrids. However, this integration has also increased the power system complexity leading to new research challenges. Some of these research challenges require the development of innovative modeling approaches able to deal with this increasing complexity. Therefore, this thesis is intended to contribute with an innovative methodology component-based for modeling and emulating in real-time photovoltaic systems integrated to microgrids.

The proposed modeling approach uses the Systems Modeling Language (SysML) to describe the structure and behavior of integrated photovoltaic systems. In addition, this study presents the High Level Specification of Embedded Systems (HiLeS) to transform automatically the developed SysML models in embedded code and Petri nets. These characteristics of automatic code generation and design based on Petri nets allow taking advantage of FPGAs for application of real-time emulation of photovoltaic systems.

This dissertation is focused on partially shaded photovoltaic systems and flexible power electronics architectures because of their relevant influence on current microgrids. Furthermore, this research perspective is intended to evaluate control and supervision strategies in normal and fault conditions. This work represents the first step to develop an innovative real-time approach to model and emulate complex photovoltaic systems considering properties of modularity, high degree of scalability, and non-uniform working conditions. Finally, experimental and analytical results validate the proposed methodology.

Résumé

L'intégration actuelle des systèmes photovoltaïques dans les systèmes d'alimentation conventionnels a montré une croissance importante, ce qui a favorisé l'expansion rapide des micro-réseaux du terme anglais microgrid. Cette intégration a cependant augmenté la complexité du système d'alimentation qui a conduit à de nouveaux défis de recherche. Certains de ces défis de recherche encouragent le développement d'approches de modélisation innovantes en temps réel capables de faire face à cette complexité croissante. Dans ce contexte, une méthodologie innovante est proposée et basée sur les composants pour la modélisation et l'émulation de systèmes photovoltaïques en temps réel intégrés aux microgrids. L'approche de modélisation proposée peut utiliser le langage de modélisation des systèmes (SysML) pour décrire la structure et le comportement des systèmes photovoltaïques intégrés en tenant compte de leurs caractéristiques multidisciplinaires. De plus, cette étude présente le cadre de spécification de haut niveau des systèmes embarqués (HiLeS) pour transformer les modèles SysML développés en code source destinés à configurer le matériel intégré. Cette caractéristique de la génération automatique de code permet de profiter de dispositifs avec un haut degré d'adaptabilité et de performances de traitement.

Cette méthodologie basée sur HiLeS et SysML est axée sur l'étude des systèmes photovoltaïques partiellement ombragés ainsi que des architectures flexibles en électronique de puissance en raison de leur influence sur les microgrids actuels. En outre, cette perspective de recherche est utilisée pour évaluer les stratégies de contrôle et de supervision dans les conditions normales et de défauts. Ce travail représente la première étape pour développer une approche innovante en temps réel pour modéliser et émuler des systèmes photovoltaïques complexes en tenant compte des propriétés de modularité, de haut degré d'évolutivité et des conditions de travail non uniformes. Les résultats expérimentaux et analytiques valident la méthodologie proposée.

0.1 Introduction

Dans le nouveau contexte de l'industrie électrique, l'un des défis mondiaux les plus importants est la conversion traditionnelle de la distribution du réseau électrique en microgrid afin de maximiser la qualité de l'énergie, de prédire et gérer l'utilisation de l'énergie électrique, pour éviter l'instabilité du réseau. Les systèmes photovoltaïques (PV) sont une solution attrayante pour répondre à cette contrainte de la connexion microgrid en utilisant des convertisseurs d'électronique de puissance spécifiques. Développement de plusieurs outils permettant de gérer l'intermittence PV et de répondre au problème d'approvisionnement et d'utilisation de l'énergie produite.

L'utilisation étendue de convertisseurs d'électronique de puissance et de générateurs photovoltaïques en microgrids a augmenté la complexité du système d'alimentation [1][2]. De nouvelles stratégies de modélisation sont nécessaires pour représenter et comprendre le mieux possible le comportement des systèmes photovoltaïques connectés à un microgrid dans des conditions normales de fonctionnement et de défaillance. Les simulations en temps réel et la conception de systèmes de contrôle dans l'électronique de puissance proposent des dispositifs de fréquence de commutation élevée augmentant les exigences de vitesse de traitement [3][4]. Des appareils de hautes performances sont nécessaires pour répondre aux exigences de ces fonctionnalités de traitement.

Les technologies photovoltaïques augmentent de façon continue autour de la demande mondiale d'électricité. L'intérêt croissant pour les systèmes PV avec un grand nombre des panneaux PV ont développé un besoin important de plateformes pour concevoir et tester ces systèmes [5]. L'émulation de la cellule aux champs PV en passant par le panneau est l'une de ces possibilités pour représenter l'association photovoltaïque avec les systèmes et les dispositifs associés à eux [6]. Cependant, plusieurs paramètres doivent être pris en compte pour développer ces émulateurs PV, tels que les conditions environnementales et les charges non-linéaires [7][8]. Toutes ces raisons encouragent la croissance des travaux de recherche dans la modélisation des cellules PV aux réseaux photovoltaïques, des convertisseurs électroniques de puissance et de leur implémentation matérielle en émulations en temps réel [9].

Cette étude se concentre sur les systèmes photovoltaïques dans des conditions d'ombrages partielles en raison de la présence inévitable d'ombres dans les installations photovoltaïques causant un impact important sur la production d'énergie. Une nouvelle stratégie de modélisation est appliquée à des architectures de l'électronique de puis-

sance afin de faciliter l'adaptation du modèle aux changements continus imposés par l'interaction inhérente entre les composants du microgrid. Les résultats des modèles PV en condition normal et d'ombrage partiel ainsi que les structures d'électroniques de puissance sont analysés et intégrés pour évaluer les stratégies temps réel d'innovations de contrôle et de supervision avec un haut niveau de précision.

0.2 Systèmes photovoltaïques en microgrids

Ce chapitre présente les concepts fondamentaux des systèmes photovoltaïques et de leur intégration dans les microgrids. Les concepts principaux des systèmes photovoltaïques connectés dans un microgrid sont présentés tels que la génération d'énergie, la description de l'architecture du système photovoltaïque, l'interconnexion avec les convertisseurs de puissance et les défauts communs d'un système photovoltaïque. La nécessité d'une émulation en temps réel est décrite avec les méthodes utilisées pour les systèmes photovoltaïques. Enfin, ce chapitre montre les défis actuels de recherche en matière de modélisation et d'émulation pour étudier l'intégration du système photovoltaïque en microgrid.

Les ressources d'information permettent de prédire la tendance de la croissance des systèmes PV installés dans le monde. Une réduction remarquable des prix des modules photovoltaïques confirme la loi de Swanson pour une réduction progressive des prix, ce qui motive encore plus l'insertion du générateur photovoltaïque sur le marché électrique. Cependant, les systèmes photovoltaïques sont également vulnérables aux conditions internes et externes et des mesures préventives devraient être prises afin de réduire leur impact sur la fiabilité du système et la production d'énergie.

Un microgrid est un groupe de charges inter-connectés avec des ressources énergétiques distribuées et définies qui agissent comme une entité contrôlable par rapport au réseau. L'intégration de ces systèmes de génération photovoltaïque dans un microgrid nécessite des équipements électroniques de puissance appropriés pour adapter les caractéristiques du système. Ces équipements connus sous le nom de convertisseurs de puissance permettent le contrôle de l'alimentation électrique. Ces convertisseurs sont en mesure de définir le point de fonctionnement de puissance maximal d'un générateur PV afin d'obtenir efficacement la puissance maximale disponible. Ces équipements électroniques de puissance permettent une interconnexion fiable des systèmes photo-

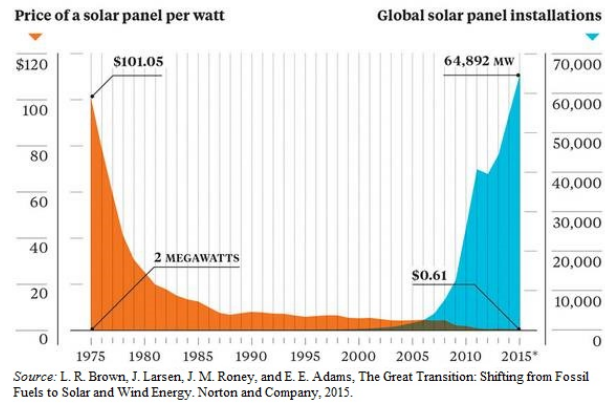


Fig. 1 La croissance des installations de systèmes photovoltaïques dans le monde entier

voltaïques à courant continu avec des systèmes d'alimentation alternatifs.

Les convertisseurs de puissance ont été présentés comme éléments d'interface fondamentaux entre l'énergie fournie par les générateurs photovoltaïques et les exigences du réseau électrique. Les architectures d'électronique de puissance ont montré des caractéristiques appropriées en fonction des conditions d'intégration de sécurité. La plupart des préoccupations concernant l'interaction des systèmes photovoltaïques et des microgrid dépendent de ces appareils électriques. Par conséquent, des méthodes de modélisation et de conception appropriées sont étudiées afin d'assurer leur fiabilité et leur fonctionnement normal. Cette étude s'est concentrée sur le micro-onduleur basé sur la topologie Boost Inverter pour l'intégration de systèmes photovoltaïques dans un microgrid (Fig. 2).

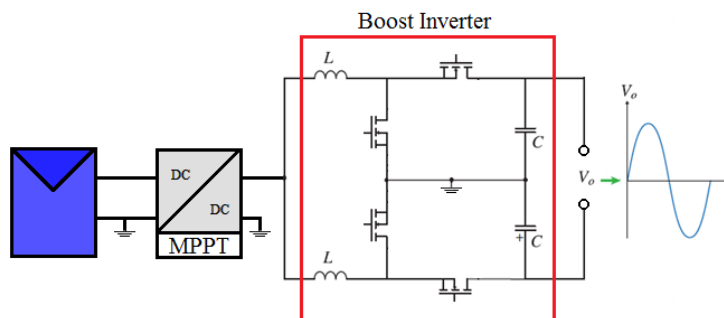


Fig. 2 Micro-onduleur basé sur la topologie Boost Inverter

Les méthodes de simulation et d'émulation ont été analysées pour identifier leurs principaux défis et ainsi fournir une approche utile dans l'étude de connexion des

systèmes photovoltaïques dans les microgrids. L'utilisation de FPGA a été identifiée comme le dispositif de traitement le plus approprié pour traiter le degré complexe et élevé d'émulation en temps réel des systèmes photovoltaïques. Une méthodologie appropriée est nécessaire pour développer des modèles de systèmes photovoltaïques en profitant de puissantes caractéristiques de traitement des FPGA.

Fig. 3 montre la feuille de route pour concevoir le prototypage virtuel de systèmes photovoltaïques intégrés aux microgrids. Grâce à ce travail, la feuille de route présentée à la Fig. 3 sera suivie. La première étape de ce travail consiste à développer des modèles de générateurs photovoltaïques et de convertisseurs de puissance. Ensuite, ces modèles sont validés grâce à la comparaison avec des mesures expérimentales. Pour finir, l'émulation en temps réel de ce modèle est implémentée dans FPGA pour valider la partie expérimentale.

0.3 Modélisation du système photovoltaïque dans conditions d'ombre

Ce chapitre présente la modélisation et l'étude des micro-onduleurs basés sur la topologie de l'onduleur Boost. La première partie présente les concepts fondamentaux des topologies de micro-onduleurs et présente la méthodologie de modélisation des composants proposés. Ensuite, la méthodologie proposée est appliquée à la modélisation du convertisseur Boost unidirectionnel et bidirectionnel. L'onduleur Boost est modélisé à partir de l'interaction du modèle conventionnel Boost bidirectionnel, et les résultats expérimentaux sont présentés pour valider la méthodologie de modélisation proposée. Enfin, une étude du convertisseur Boost est présentée. En la dernière section, le modèle d'intégration du micro-onduleur connecté au réseau est développé.

Le chapitre précédent a montré l'importance de modéliser avec précision le comportement électrique du système photovoltaïque en conditions d'ombrages. L'intégration actuelle des systèmes photovoltaïques dans les réseaux électriques peut être affectée par des facteurs internes et externes. Les facteurs externes tels que l'ombrage ont une incidence plus fréquente. L'ombrage peut être caractérisé sous différentes formes telle que la salisurre ou une ombre liée aux environnements proches. Les ombres diminuent l'énergie fournie [10] par le système photovoltaïque et augmentent le risque de pannes

Roadmap of Virtual Prototyping

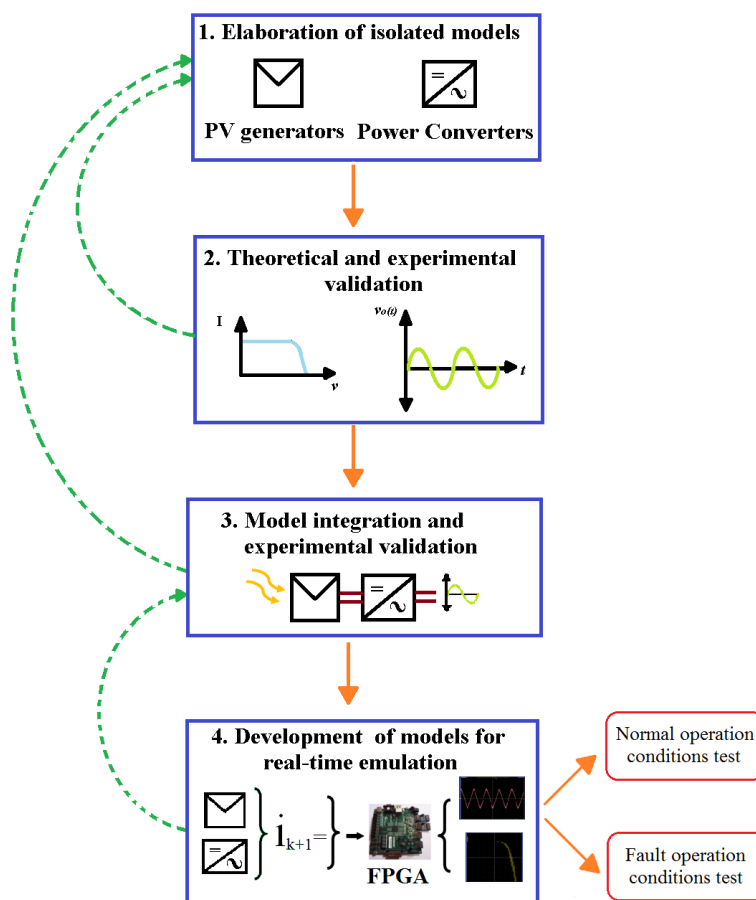


Fig. 3 Feuille de route du prototypage virtuel dans ce document

structurelles en augmentant la température des cellules ombragées [11] [12].

Une situation typiquement ombragée a été testée expérimentalement comme le montre la Fig.4 et Fig. 4b. Les résultats expérimentaux de la Fig. 4b montrent une partie réduite de la cellule ombrée sur le module PV de la Fig. 4a qui a un impact important sur les caractéristiques courant tension (I.V).L'étude de Bressan [11] montre que l'ombrage non uniforme a un impact important sur les performances PV malgré l'activation des diodes bypass, comme le montre la Fig. 5. Dans la Fig. 3.2, de [11], une thermographie I-R permet d'identifier la présence d'une zone de point chaud sur une cellule PV ombrée augmentant la température de la cellule.

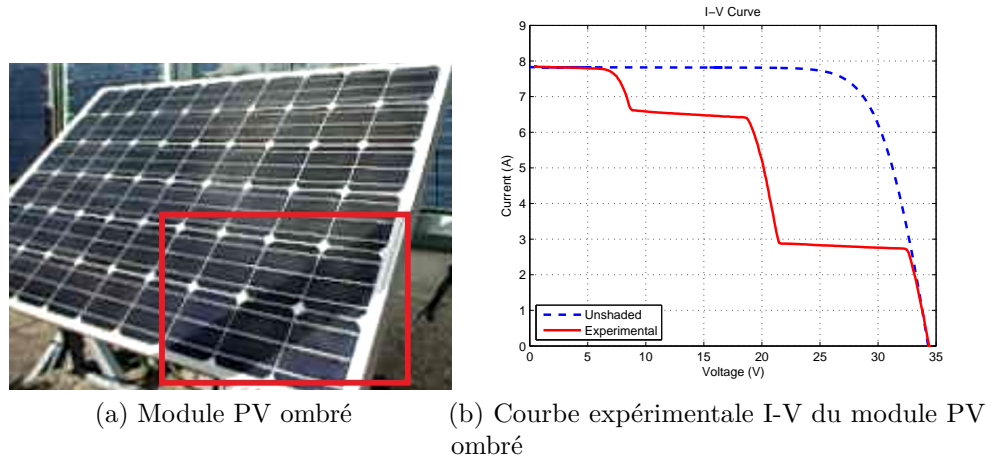


Fig. 4 Test du module PV sous condition ombragée

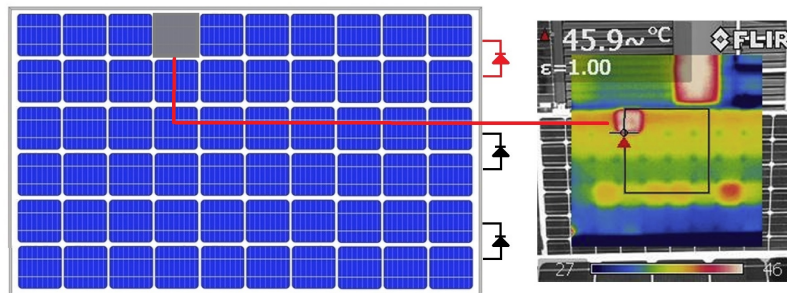


Fig. 5 Impact thermique de la cellule ombragée

Des méthodes de modélisation bien connues pour décrire le comportement du système photovoltaïque dans des conditions normales de fonctionnement sont largement étudiées dans la littérature [13]. D'autres auteurs ont montré que la modélisation des systèmes photovoltaïques partiellement ombragés est une réelle préoccupation pour les systèmes photovoltaïques intégrés au réseau [14]. Peu de méthodologies en temps réel existent pour le test de système de diagnostic en tenant compte des différents types de caractéristiques des ombres et de leur impact sur le comportement électrique du système photovoltaïque.

Les systèmes photovoltaïques interagissent également avec des convertisseurs de puissance à fréquence de commutation élevée [15], des systèmes de contrôle [16] et des méthodes de détection de défauts [17]. L'étude des interactions entre les systèmes photovoltaïques partiellement ombragés et les systèmes de traitement à grande vitesse [6][18] est un nouveau défi important de recherche. Selon les auteurs dans [19], les

approches en temps réel sont fondamentales pour la conception et la vérification des algorithmes de contrôle, des stratégies de supervision et des interfaces électroniques de puissance en PV Systèmes. Les modèles précis des systèmes photovoltaïques ombragés partiellement sont difficiles à développer pour ces applications en raison de la charge de calcul et de la complexité du modèle [20].

Pour répondre à cette problématique, l'étude proposée est une méthodologie appropriée qui implique des caractéristiques géométriques et optiques des ombres et leur relation avec les paramètres électriques PV. Cette approche fournit un coefficient d'ombrage qui permet d'augmenter la précision du modèle sans augmenter la complexité de calcul pour les émulations temps réel. Le modèle proposé est évalué et validé avec des mesures expérimentales sur site effectuées sur des systèmes photovoltaïques ombrés.

Premièrement le modèle proposé est décrit pour des conditions ombragées partiellement. La procédure expérimentale est expliquée pour valider le modèle. La validation du modèle et les résultats expérimentaux sont discutés. Cette étude est étendue aux structures de génération PV centralisées et décentralisées afin de comparer les performances des deux topologies.

La méthodologie présentée montre la précision et la portée des approches de modélisation conventionnelles des systèmes photovoltaïques. La principale contribution de cette approche est de définir une relation simplifiée qui dénote le coefficient d'ombrage δ pour décrire le comportement complexe des modules photovoltaïques dans des conditions ombragées partiellement (Fig. 6).

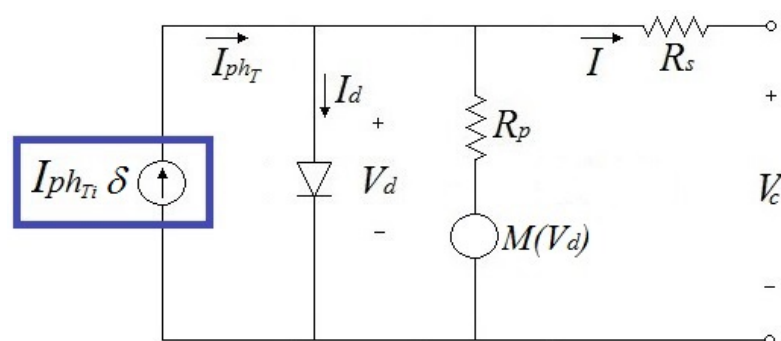


Fig. 6 Circuit équivalent électrique de cellule photovoltaïque modifié

Le test pour valider le modèle proposé est illustré à la Fig. 7. Des modules PV avec des ombres intentionnelles sont utilisés pour valider le modèle proposé. Fig. 7 décrit l'installation expérimentale. Dans cette configuration, un traceur de courbe I-V mesure les signaux de tension de courant. Un appareil photo numérique enregistre simultanément le patron de l'ombre pour un traitement ultérieur de l'image. Un modèle de pyromètre détecte l'éclairement solaire et une caméra thermographique est utilisée pour surveiller périodiquement la température du module PV.

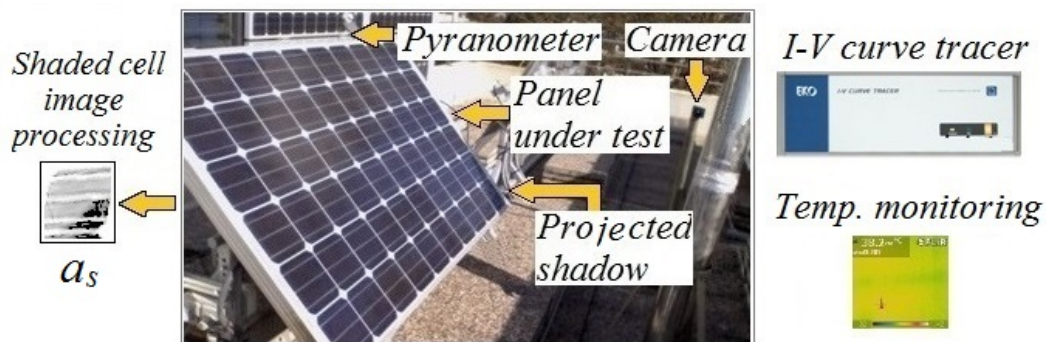


Fig. 7 Montage expérimental

Le test expérimental est expliqué comme suit. Tout d'abord, l'installation expérimentale stocke les mesures des courbes I-V, de l'irradiance solaire, de la température du module PV et de l'ombre. Les dernières informations enregistrées à la première étape sont comparées avec un patron de l'ombre spécifique. Ensuite, le coefficient d'ombre est calculé. Le facteur d'ombrage est par la suite calculé. Pour finir, les coefficients d'ombrages sont calculés pour chaque cellule photovoltaïque ombrée compte tenu de leur zone d'ombrage et du même facteur d'ombrage pour toutes les cellules ombrées. Fig. 8 montre les résultats.

L'analyse des résultats permet des interactions identifiées entre l'ombre et les changements de tension de courant dans des conditions partiellement ombragées. Les résultats ont montré que les approches conventionnelles qui peuvent ignorer les caractéristiques de l'ombre telles que la zone ombragée ou le facteur d'ombrage peuvent conduire à des résultats inexacts lorsque les modèles sont comparés avec des systèmes photovoltaïques sous des ombres partielles réelles.

Ce chapitre décrit le comportement du générateur PV dans des conditions ombrées et sans ombre. La méthodologie de modélisation a été étendue aux architectures PV

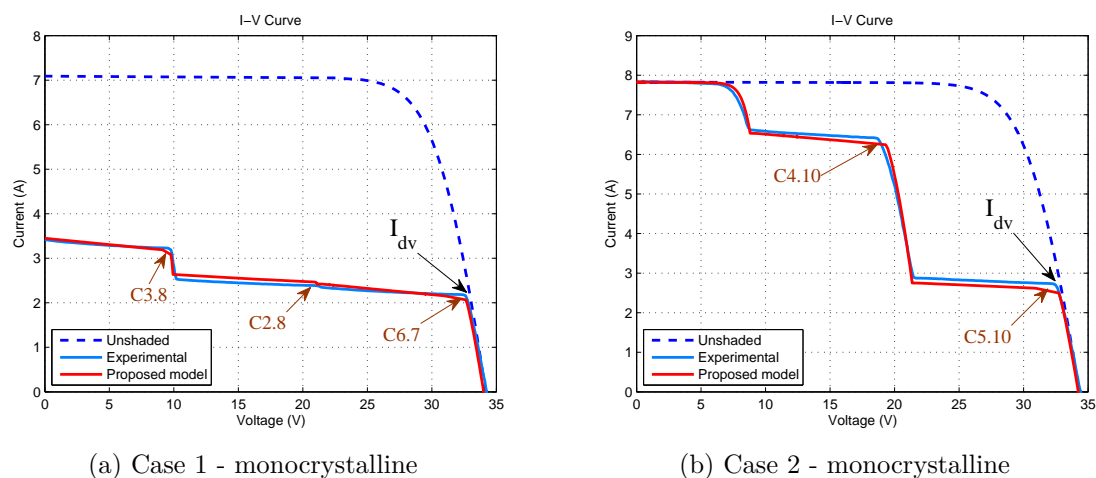


Fig. 8 I-V curves for test of monocrystalline PV module

centralisées et décentralisées. Les résultats et les études sur les architectures centralisées et décentralisées ont montré que la meilleure performance est obtenue grâce au cas décentralisé. Le chapitre suivant abordera la modélisation et l'étude d'une topologie de convertisseur de puissance pour les architectures décentralisées connues sous le nom d'onduleur Boost et son intégration aux systèmes de production photovoltaïque.

0.4 Développement du modèle Boost Inverter pour les applications photovoltaïques en microgrids

La discussion du *chapitre 0.2* a soutenu que la génération de photovoltaïque est une ressource énergétique alternative prometteuse capable d'être intégrée dans les réseaux électriques actuels. Cependant, dans le *chapitre 0.3*, on a montré que les systèmes photovoltaïques peuvent être fortement affectés par des facteurs externes tels que des ombres partielles. Les résultats du *chapitre 0.3* font également remarquer que les petites ombres relatives peuvent affecter toute la chaîne de production d'énergie dans les structures photovoltaïques centralisées car les modules photovoltaïques sont interconnectés en série et les défauts se propagent à travers la chaîne de production d'énergie [21].

En outre, la comparaison des topologies de génération PV centralisées et décentralisées dans le *chapitre 0.3*, les performances des cas décentralisés sont supérieures

aux configurations centralisées [22][23]. Cependant, l'étape de l'électronique de puissance dans les architectures décentralisées peut augmenter la complexité du système d'alimentation et diminuer l'efficacité globale car le taux d'élévation plus élevé [22]. Dans ce contexte, les défis de recherche actuels se posent pour étudier et modéliser des topologies novatrices capables de surmonter les inconvénients des topologies décentralisées et de tirer parti de leurs caractéristiques. Par conséquent, des architectures conventionnelles de micro-onduleurs basées sur des topologies à deux étapes, des convertisseurs Boost-Buck DC-DC / DC-AC ont été étudiés et généralisés dans la littérature [24][25]. Cependant, d'autres architectures de micro-onduleurs avec une efficacité et une fiabilité supérieures basées sur les topologies de l'onduleur Boost sont moins rapportées dans la littérature [26].

Les micro-onduleurs basés sur la topologie de l'onduleur Boost montrent des caractéristiques plus adaptables [27], une fiabilité plus élevée [28], des propriétés d'évolutivité [23] et des fonctions connectées au réseau à un seul étage en utilisant moins d'appareils électroniques de puissance [29][30]. Par conséquent, en tenant compte des avantages des architectures décentralisées et des perspectives prometteuses de l'onduleur Boost dans les systèmes d'énergie photovoltaïque [23], ce chapitre présentera l'étude et la modélisation de ce convertisseur afin de contribuer à la connaissance de son intégration dans les systèmes photovoltaïques (Voir la Fig. 9).

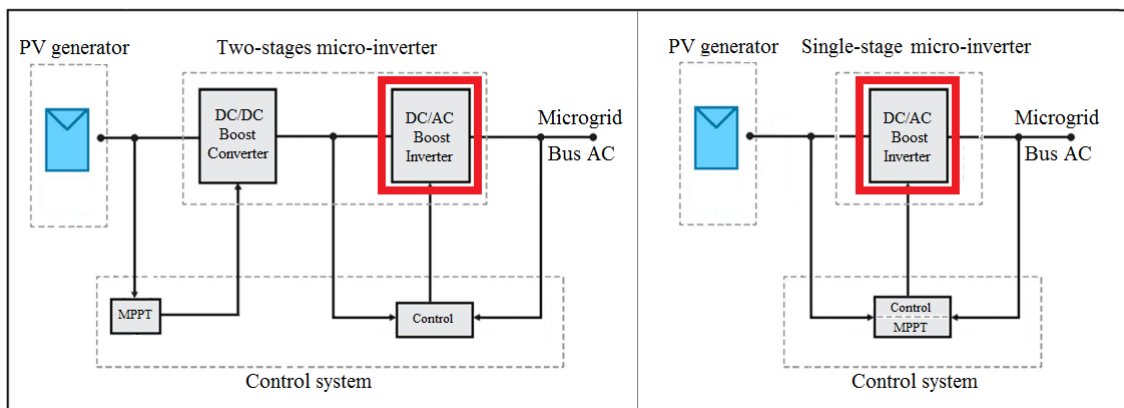


Fig. 9 Micro-onduleurs à deux étages et à un seul étage basés sur l'onduleur Boost pour l'intégration des systèmes photovoltaïques.

Cette étude développe une méthodologie basée sur les composants pour modéliser les convertisseurs de puissance appliqué au convertisseur Boost et aux topologies de

l'onduleur Boost. La méthodologie de modélisation basée sur les composants proposée est destinée à modéliser le convertisseur de puissance en tant que bloc de construction qui interagit avec son environnement par étapes de couplage. Cette approche permet aux convertisseurs de puissance de modélisation avec un haut degré de détail ignorant l'influence des changements dans la source d'alimentation et les modèles de charge. Par conséquent, ces modèles générés du convertisseur Boost et du convertisseur Boost peuvent être intégrés à d'autres modèles pour générer des structures plus complexes adaptées à la modélisation du système d'alimentation en microgrids qui sont composées de plusieurs types de sources d'énergie, de convertisseurs de puissance et de charges.

Cette méthodologie de modélisation proposée est destinée à des émulations en temps réel dans le matériel intégré, car les avantages inhérents à l'émulation en temps réel en cours d'étude de l'intégration des systèmes d'alimentation en microgrids [31][32]. Les émulations en temps réel permettent d'évaluer les performances des convertisseurs de puissance plus proches des conditions de fonctionnement réelles [33]. En effet, les émulations en temps réel des systèmes photovoltaïques en microgrids sont en mesure d'étudier l'interaction des convertisseurs de puissance et des générateurs photovoltaïques dans des conditions normales et de défaut [33]. Ces études et tests peuvent être développés dans un environnement sécurisé sans dommage sur les équipements et les utilisateurs [4]. Dans d'autres chapitres, cette méthodologie de modélisation proposée sera utilisée en émulations temps réel d'onduleurs Boost dans les systèmes photovoltaïques.

L'onduleur Boost est un convertisseur d'électronique de puissance qui fait partie d'une famille d'onduleurs formé par deux convertisseurs CC / CC couplés à une tension de sortie différentielle, comme le montre la Fig. 10. L'onduleur Boost est un convertisseur de puissance sans transformateur qui fournit une tension de sortie CA d'augmentation de deux convertisseurs bidirectionnels DC-DC Boost [34]. Fig. 10 montre le principe de fonctionnement de cet onduleur. Lorsque les convertisseurs Boost bidirectionnels produisent des signaux de sortie sinusoïdale polarisés à courant alternatif de 180° , la sortie différentielle est une tension de sortie CA.

Cette section développe une méthodologie basée sur les composants pour modéliser les convertisseurs de puissance appliqués aux topologies du convertisseur Boost unidirectionnel et bidirectionnel. La méthodologie de modélisation basée sur les composants proposée est destinée à modéliser les convertisseurs Boost en tant que blocs de construction qui interagissent avec leur environnement par des étapes de couplage, comme

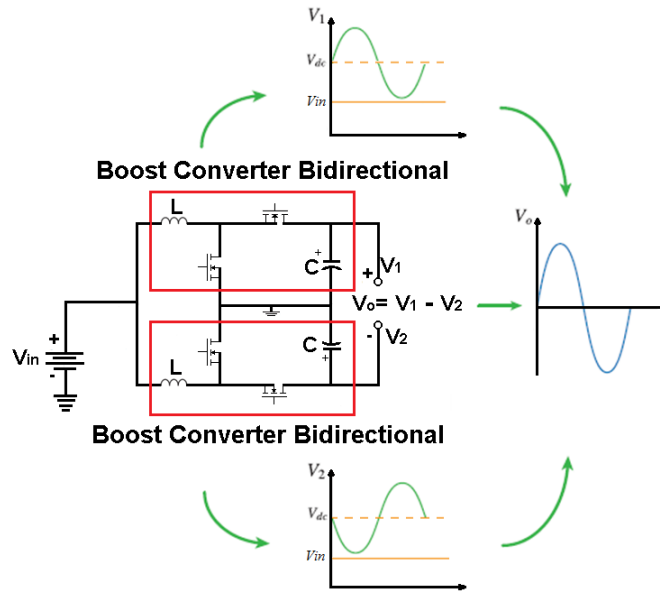


Fig. 10 Principe de fonctionnement de l'ondulateur Boost.

le montre la Fig. 11. Fig. 12 résume les étapes de la méthodologie de modélisation.

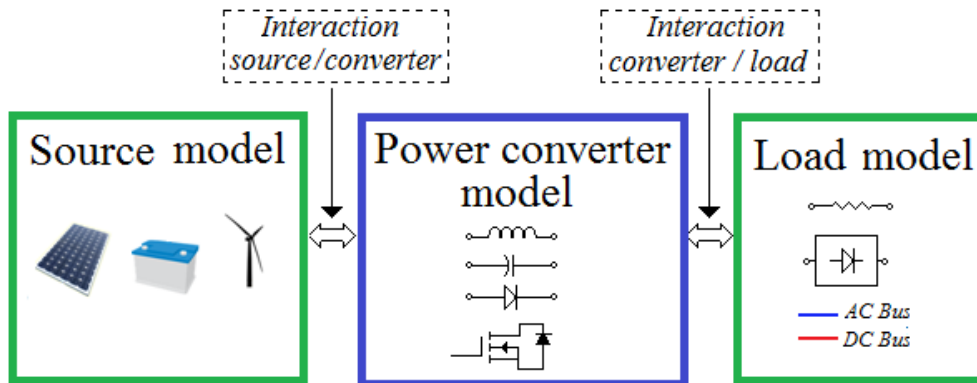


Fig. 11 Méthode de modélisation basée sur les composants.

L'onduleur Boost peut être considéré comme un système où quatre composants interagissent comme le montre la Fig. 13. Les quatre composants sont la source d'alimentation, la charge et les deux bidirectionnels Boost. Le modèle basé sur les composants suivant pour l'onduleur Boost est formulé à partir de l'analyse développée dans la section précédente. Le modèle proposé est illustré et mis en œuvre dans Simulink® dans la Fig. 14.

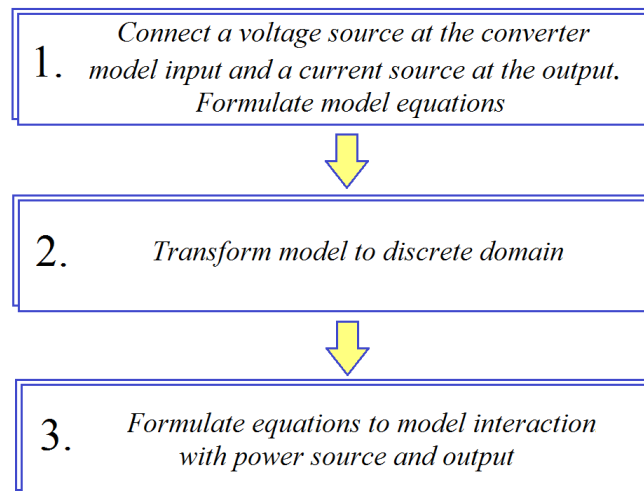


Fig. 12 Étapes pour la méthode de modélisation proposée.

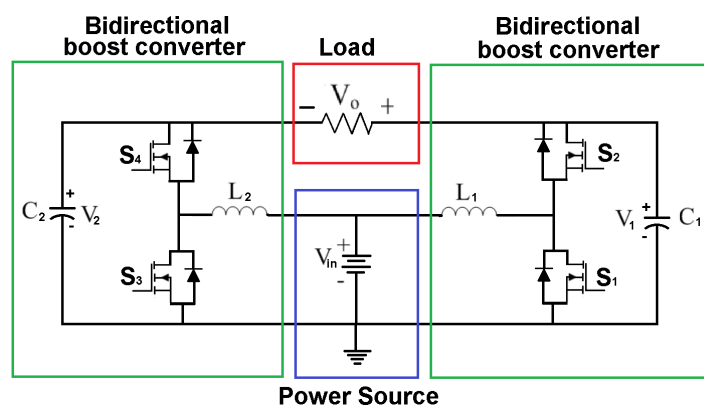


Fig. 13 Onduleur Boost en tant que système basé sur les composants

La discussion de ce chapitre a proposé une méthodologie basée sur les composants pour modéliser les systèmes photovoltaïques. Cette approche a été utilisée pour modéliser les topologies du convertisseur Boost. Cette méthodologie a permis de modéliser les convertisseurs de puissance indépendamment des modifications du type de source ou de la charge. Les modèles résultants peuvent être intégrés à d'autres modèles pour générer des systèmes plus complexes. Cette caractéristique est pertinente dans l'évolution actuelle des convertisseurs de puissance où les changements continus sur leurs limites électriques devraient être évalués.

Les résultats expérimentaux et théoriques ont validé les modèles de convertisseurs Boost présentés. L'intégration de ces modèles développés avec des sources non linéaires et des charges non linéaires a montré des résultats appropriés. Ces résultats ont

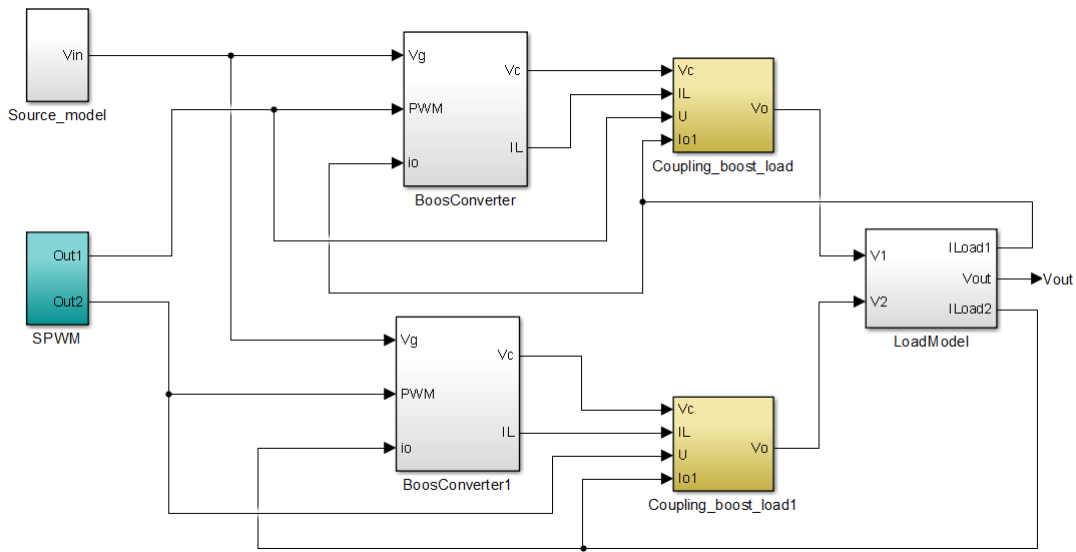


Fig. 14 Modèle de l'onduleur Boost basé sur les composants

permis de reproduire dans les simulations le comportement dynamique des composants modélisés par rapport au comportement des éléments physiques. En conséquence, les résultats réussis ont permis de vérifier la précision, l'adaptabilité et l'évolutivité de l'approche proposée. En outre, les résultats confirment le potentiel de l'approche proposée pour imiter des systèmes complexes tels que les systèmes photovoltaïques intégrés aux microgrids. Ce chapitre présente également une approche de niveau hiérarchique multiple destinée à intégrer les modèles développés des composants microgrids.

0.5 Développement d'un modèle de système photovoltaïque pour l'émulation en temps réel à l'aide de HiLeS

À ce stade, le présent chapitre vise à récupérer les travaux précédents des chapitres 0.3 et 0.4 pour générer des modèles d'émulation en temps réel. Le but de ces modèles d'émulation en temps réel est d'apporter des outils utiles pour l'étude et le développement de systèmes complexes tels que les systèmes d'énergie photovoltaïque en microgrids. Ensuite, ces modèles proposés en temps réel cherchent à tirer parti de la précision des modèles développés et de l'adaptabilité des émulations en temps réel[35][36].Cependant, ce double objectif nécessite une méthodologie de conception de

structure qui représente un défi de recherche en raison du compromis entre adaptabilité et précision [37].

Dans ce contexte, ce chapitre présente l'outil de licence gratuit HiLeS pour développer les systèmes d'émulation en temps réel des systèmes photovoltaïques. Le framework HiLeS repose sur une méthodologie descendante capable d'aider au processus de conception des systèmes d'émulation en temps réel. La fonctionnalité pertinente de HiLeS est la génération automatique de code à partir des spécifications SysML. En outre, HiLeS apporte un soutien aux concepteurs à partir de l'étape de description des besoins jusqu'au processus final de vérification. Ces avantages découlent du fait que le framework HiLeS est pris en charge par deux fondamentaux bien structurés, SysML et les réseaux de Petri. Fig. 15 montre la chaîne de transformation de modèles en HiLeS.

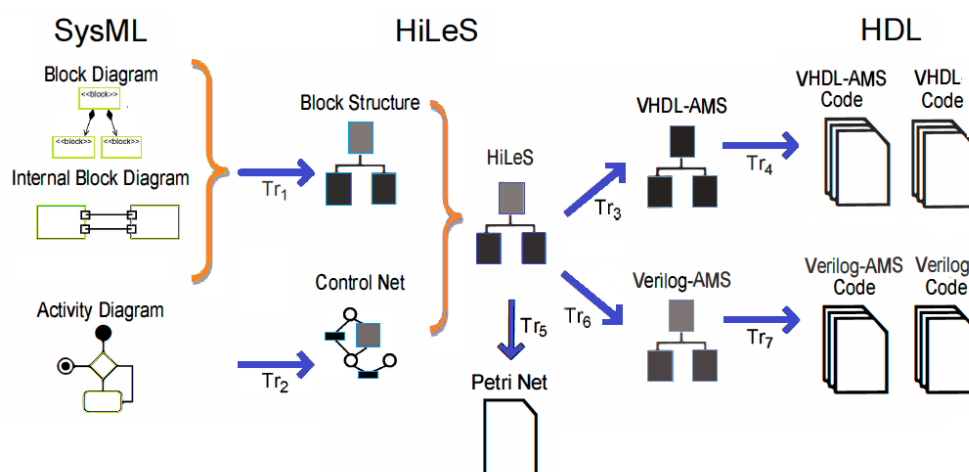


Fig. 15 Chaîne de transformation modèle HiLeS

Les dispositifs de traitement sont nécessaires pour accomplir les contraintes de haute performance dans l'émulation en temps réel des systèmes d'alimentation. Par conséquent, pour cette tâche exigeante, les FPGA sont sélectionnés comme un dispositif de traitement compte tenu de leurs caractéristiques pertinentes du traitement à grande vitesse, de l'adaptabilité et de l'évolutivité [33].

Ces fonctionnalités sont adaptées aux émulations en temps réel et correspondent parfaitement à l'approche de modélisation basée sur les composants présentée au *chapitre 0.4*. En outre, le framework HiLeS permet de profiter des fonctionnalités

FPGA et de la modélisation basée sur les composants. En effet, ce cadre peut s'étendre à l'approche de niveau hiérarchique multiple présentée dans la section précédente pour développer des systèmes intégrés complexes à partir de composants structurels bien définis, comme le montre la Fig. 16.

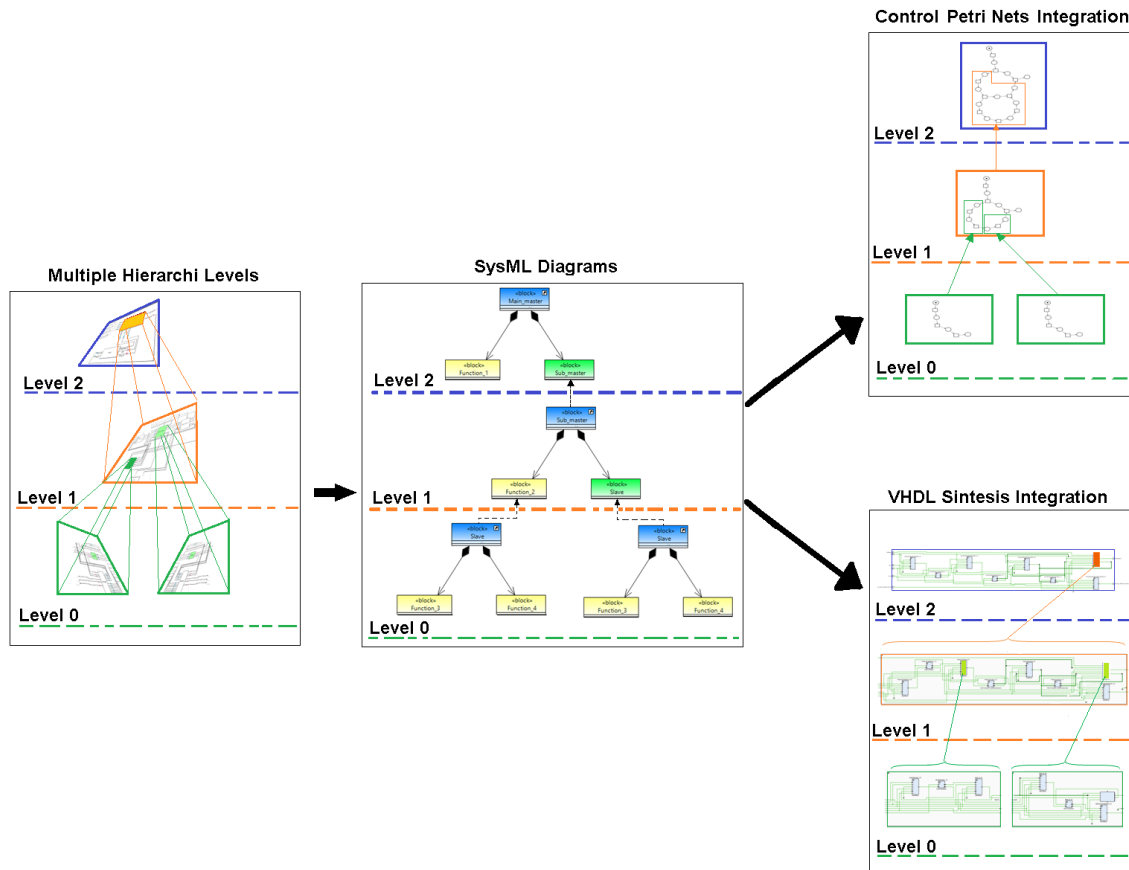


Fig. 16 HiLeS outil pour concevoir des systèmes embarqués à plusieurs niveaux hiérarchiques

Ce chapitre présente les briques fondamentales des modèles en temps réel basés sur FPGA en tant que contribution à d'autres études sur la base des microgrids sur les générateurs photovoltaïques. Dans ce contexte, on présente d'abord l'application de l'émulation en temps réel à l'étude des systèmes photovoltaïques en microgrides. Ensuite, le framework HiLeS est utilisé pour développer des systèmes d'émulation en temps réel basés sur le matériel intégré.

Dans ce chapitre a été introduit le framework HiLeS pour implémenter des modèles de composants du système photovoltaïque dans FPGA pour l'émulation en temps réel.

Le framework HiLeS permet de mettre en œuvre le modèle développé des systèmes photovoltaïques ombrés. En conséquence, ces tests sur la plateforme développée ont montré leur potentiel pour implémenter un modèle de microphères plus complexe en utilisant l'approche de niveau hiérarchique multiple à partir du modèle défini en utilisant l'approche base de composants. En outre, les performances des modèles mis en place confirment leurs caractéristiques pour l'émulation réelle.

0.6 Emulation en temps réel de l'onduleur Boost et conception de contrôle par mode de glissant

Le chapitre précédent a présenté la modélisation et l'émulation des systèmes d'alimentation en temps réel. Dans le *chapitre 0.5* a été étudié et modélisé en temps réel le générateur PV. Ce chapitre se concentrera sur l'émulation en temps réel des convertisseurs de puissance en utilisant un cas d'étude de l'onduleur Boost.

À ce stade, le chapitre actuel est destiné à récupérer les travaux précédents du *chapitre 0.4* pour générer des modèles d'émulation en temps réel. Le but de ces modèles d'émulation en temps réel est de fournir des outils utiles pour l'étude et le développement de systèmes d'alimentation complexes dans les microgrids. Ensuite, ces modèles en temps réel proposés cherchent à tirer parti de la précision et de l'adaptabilité des modèles développés.

Ce chapitre présente des modèles fondamentaux en temps réel des convertisseurs de puissance pour des études ultérieures sur les microgrids. Ces concepts fondamentaux sont utilisés pour modéliser l'onduleur Boost. En outre, les modèles développés dans une plate-forme en temps réel sont utilisés pour concevoir et mettre en œuvre des systèmes de contrôle. Le système de contrôle étudié dans ce chapitre est le contrôle en mode de glissant compte tenu de leurs propriétés de non-linéarité et de robustesse.

0.7 Conclusions et perspectives

Conclusions

Le *chapitre 0.2* a montré les aspects pertinents de la génération photovoltaïque et leur intégration dans les microgrids. Une réduction remarquable des prix des modules photovoltaïques suit la loi de Swanson pour une réduction progressive des prix. Cependant, les systèmes photovoltaïques sont également vulnérables aux conditions internes et externes et des mesures préventives devraient être prises afin de réduire leur impact sur la fiabilité du système et la production d'énergie. Dans le *chapitre 0.2*, nous avons également présenté les préoccupations actuelles concernant les architectures électroniques de puissance. Soulignant que la plupart des préoccupations concernant l'interaction des systèmes photovoltaïques et des microgrids reposent sur ces dispositifs électriques. Enfin, les méthodes de simulation et d'émulation ont été analysées pour identifier leur principal défi et contraignent à fournir une approche utile dans l'étude des préoccupations concernant les systèmes photovoltaïques dans les microgrids. FPGA a été identifié comme le dispositif de traitement le plus approprié pour traiter le degré complexe élevé d'émulation en temps réel du système photovoltaïque. Ensuite, une méthodologie appropriée est nécessaire pour développer les modèles de systèmes photovoltaïques en profitant de puissantes caractéristiques de traitement des FPGA.

Le *chapitre 0.3* a été consacré à l'étude du générateur photovoltaïque. Ce chapitre a présenté une méthodologie pour augmenter la précision et la portée des approches de modélisation conventionnelles des systèmes photovoltaïques. La principale contribution de cette approche est de définir une relation simplifiée appelée coefficient d'ombre apte à décrire le comportement complexe des modules photovoltaïques dans des conditions partiellement ombragées. En outre, l'analyse des résultats permet des interrelations identifiées entre les clients de l'ombre et les changements de tension de courant dans des conditions partiellement ombragées.

Discussion le *chapitre 0.4* a proposé une méthodologie basée sur les composants pour modéliser les convertisseurs de puissance. Cette approche a été utilisée pour modéliser les topologies du convertisseur Boost. Cette méthodologie a permis aux convertisseurs de puissance de modélisation indépendamment des changements dans le type de source ou de la charge en utilisant les modèles causaux et non causaux. Les modèles de ce perceptif peuvent être intégrés à d'autres modèles pour générer des systèmes plus complexes. Les résultats expérimentaux et théoriques ont validé les

modèles de convertisseurs Boost présentés. L'intégration de ces modèles développés avec des sources non linéaires et des charges non linéaires a montré des résultats appropriés et confirme la pertinence de la méthodologie proposée.

Au *chapitre 0.5* a été introduit le framework HiLeS pour mettre en œuvre des modèles de système photovoltaïque Composants dans FPGA pour l'émulation en temps réel. Le framework HiLeS permet de mettre en œuvre le modèle développé des systèmes photovoltaïques ombrés et l'onduleur Boost modélisé à l'aide de l'approche composante. En conséquence, ces tests sur la plateforme développée ont montré leur potentiel pour implémenter un modèle de microgrids plus complexe en utilisant l'approche de niveau hiérarchique multiple à partir du modèle défini en utilisant l'approche base de composants.

Le *chapitre 0.6* a présenté le modèle de mise en œuvre de convertisseurs de puissance pour les émulations en temps réel avec l'onduleur Boost comme un cas d'étude. Ces modèles ont été implémentés dans FPGA pour les émulations Hardware-in-the-Loop en temps réel. La comparaison des émulations en temps réel et des résultats expérimentaux a validé la méthodologie proposée. Une commande numérique en mode diapositive a été conçue pour l'onduleur Boost à l'aide des diagrammes SysML et du cadre HiLeS. Ce contrôleur développé a montré leur robustesse et une réponse rapide aux perturbations.

Perspectives

Cette dissertation a présenté l'intégration des différents outils d'émulation et de conception avec des systèmes électroniques et photovoltaïques qui ouvrent les portes aux futures applications industrielles. Cette intégration peut être étendue à l'étude d'autres systèmes énergétiques complexes ou intégrer d'autres ressources énergétiques alternatives et des charges non linéaires.

Les modèles proposés de systèmes photovoltaïques ombrés conviennent pour développer des modèles de propagation de l'ombre qui peuvent être intégrés aux modèles de convertisseurs de puissance pour concevoir des systèmes de contrôle innovants et des stratégies de suivi maximal du point de puissance avec une précision plus élevée. En outre, cette intégration peut être utile pour développer des modèles de production d'énergie plus précis. En outre, les résultats théoriques et expérimentaux des systèmes photovoltaïques partiellement ombrés fournissent des résultats utiles pour poursuivre

les études de diagnostic et de détection des défauts.

Les perspectives de ce travail intègrent les modèles développés à l'aide de l'approche basée sur les composants en une seule plate-forme en temps réel pour évaluer les interactions complexes dans les systèmes énergétiques basés sur les générateurs photovoltaïques, les convertisseurs de puissance, les charges non linéaires et le réseau électrique. La méthodologie de modélisation basée sur les composants peut également être étendue à d'autres topologies de convertisseurs de puissance, comme les convertisseurs multifonction ou les convertisseurs DC / DC entrelacés. En outre, la plate-forme d'émulation en temps réel développée peut être utilisée pour évaluer et développer de nouvelles méthodes de supervision et de détection de défauts.

Table of contents

Résumé	vii
0.1 Introduction	viii
0.2 Systèmes photovoltaïques en microgrids	ix
0.3 Modélisation du système photovoltaïque dans conditions d'ombre	xi
0.4 Développement du modèle Boost Inverter pour les applications photovoltaïques en microgrids	xvi
0.5 Développement d'un modèle de système photovoltaïque pour l'émulation en temps réel à l'aide de HiLeS	xxi
0.6 Emulation en temps réel de l'onduleur Boost et conception de contrôle par mode de glissant	xxiv
0.7 Conclusions et perspectives	xxv
List of figures	xxxiii
List of tables	xxxix
1 Introduction	1
2 Photovoltaic Systems in Microgrids	3
2.1 Introduction	3
2.2 Photovoltaic systems	5
2.2.1 PV generation and shadow impact	5
2.2.2 Architecture of PV systems	11
2.2.3 Reliability of PV systems	14
2.3 Integration of PV systems in Microgrids	16
2.3.1 PV grid integration	17
2.3.2 Power electronics in microgrids	19
2.3.3 Research challenges for integration of PV systems in microgrids	21
2.4 Real-time emulation of microgrids	22

2.4.1	Real-time simulation methods of power systems	23
2.5	Conclusion	24
3	PV System Modeling Under Shaded Conditions	27
3.1	Introduction	27
3.2	Modeling under shaded conditions and thermal impact	28
3.2.1	PV cell model for unshaded conditions	30
3.2.2	PV cell model for shaded conditions	31
3.3	Proposed partially shaded PV model	33
3.3.1	Partially shaded PV cell model	33
3.3.2	Shadow coefficient analysis	35
3.4	Experimental model validation	38
3.4.1	Photo-induced current test	38
3.4.2	Partially shading PV modules test	40
3.4.3	Comparison with other modeling approaches	46
3.5	Simulation of PV generation architectures	47
3.6	Conclusion	50
4	Development of Boost Inverter Model for PV Applications in Micro-	
	grids	51
4.1	Introduction	52
4.2	Component-based approach for modeling Boost converter topologies . .	54
4.2.1	State of the art Boost inverter modeling	54
4.2.2	Proposed approach for modeling Boost converter topologies . . .	58
4.2.3	Validation of modeling methodology	66
4.3	Boost inverter modeling	75
4.3.1	Mathematical framework for the Boost inverter	75
4.3.2	Component-based approach for Boost inverter modeling	78
4.3.3	Experimental setup to validate the modeling approach	81
4.4	Modeling of Boost inverter integration in Microgrids	86
4.4.1	The Boost inverter grid-connected model	86
4.4.2	Boost inverter for integration of PV systems in microgrids . . .	89
4.5	From component-based modeling to a multiple hierarchic level approach	91
4.6	Conclusion	92
5	PV System Modeling in Real-Time Using HiLeS	95
5.1	Introduction	95

5.2	Real-time emulation of PV systems in Microgrids	97
5.2.1	General context about real-time emulation of power systems . . .	97
5.2.2	FPGAs for real-time emulation of power systems	101
5.3	HiLeS for real-time emulations of PV systems	103
5.3.1	HiLeS framework for developing real-time emulations	104
5.3.2	Mathematical framework for the integration of HiLeS projects .	105
5.4	Modeling of shaded PV system using HiLeS	106
5.4.1	Shaded PV generator modeling using HiLeS	106
5.4.2	Numerical methods for implementation of PV models	109
5.5	Conclusion	112
6	Real-Time Emulation of Boost Inverter and Slide-mode Control De-	
	sign	113
6.1	Introduction	113
6.2	Modeling and emulation of Boost inverter using HiLeS	114
6.2.1	HiLeS framework to model and emulate the Boost inverter . . .	115
6.3	Design and emulation of control systems for the Boost inverter	118
6.3.1	Experimental test-bench to validate digital controllers	119
6.3.2	Slide-mode control for the Boost inverter	120
6.3.3	Slide-mode control implementation with HiLeS	125
6.4	Conclusion	132
7	Conclusions and Perspectives	133
7.1	Conclusions	133
7.2	Perspectives	134
8	Contributions and Publications	137
	References	139
	Appendix A Conventional Boost Converter Modeling	149
	Appendix B Boost Inverter Design and Fabrication	155
	Appendix C HiLeS Fundamentals	163
	C.1 HiLeS Formalism	163
	C.2 Automatic HDL code generators	167
	Appendix D Contribution to the HiLeS Framework	171

List of figures

1	La croissance des installations de systèmes photovoltaïques dans le monde entier	x
2	Micro-onduleur basé sur la topologie Boost Inverter	x
3	Feuille de route du prototypage virtuel dans ce document	xii
4	Test du module PV sous condition ombragée	xiii
5	Impact thermique de la cellule ombragée	xiii
6	Circuit équivalent électrique de cellule photovoltaïque modifié	xv
7	Montage expérimental	xv
8	I-V curves for test of monocrystalline PV module	xvi
9	Micro-onduleurs à deux étages et à un seul étage basés sur l'onduleur Boost pour l'intégration des systèmes photovoltaïques.	xvii
10	Principe de fonctionnement de l'ondulateur Boost.	xix
11	Méthode de modélisation basée sur les composants.	xix
12	Étapes pour la méthode de modélisation proposée.	xx
13	Onduleur Boost en tant que système basé sur les composants	xx
14	Modèle de l'onduleur Boost basé sur les composants	xxi
15	Chaîne de transformation modèle HiLeS	xxii
16	HiLeS outil pour concevoir des systèmes embarqués à plusieurs niveaux hiérarchiques	xxiii
2.1	Electrical energy from sunlight in a PV cell	5
2.2	PV cell as a fundamental unit in a PV system	6
2.3	Structure of a PV generator	6
2.4	Sectors of PV systems	6
2.5	Growth of PV systems installations worldwide	7
2.6	Annual growth in energy use by source	8
2.7	Improve of solar cell efficiency by technology	8
2.8	Histogram of reported degradation rates per year of PV modules	9

2.9	Dust and partial shadows on PV modules	10
2.10	Hot Spots on PV module	11
2.11	Elemental chain of a PV system	12
2.12	Basic architecture of a PV system	13
2.13	Example of typical PV system architectures	14
2.14	Micro-inverter based on Boost Inverter topology	14
2.15	Mean-Time-To-Failure (MTTF) of PV architectures	15
2.16	Microgrid structure	17
2.17	Top ten PV installed capacity by country, 2013	18
2.18	Contribution of PV production base on the installed capacity, 2013 . .	18
2.19	Crossing clouds above PV generator	19
2.20	Integration in microgrids of Distributed Energy Resources with power converters	20
2.21	Roadmap of virtual prototyping in this document	25
3.1	Test of PV module under shaded condition	29
3.2	Thermal impact of shaded cell	30
3.3	Single diode PV cell model	30
3.4	Shaded PV cell electrical equivalent circuit	32
3.5	PV module with bypass diodes	32
3.6	Partially shaded PV cell	33
3.7	Photo-induced currents in a partially shaded cell	34
3.8	Modified PV cell electrical equivalent circuit	35
3.9	Contribution of each group to the I-V curve	36
3.10	Contribution of shaded cells to the I-V curve	36
3.11	Influence of δ in a PV module with a single partially shaded cell	37
3.12	Activation of by-pass diode in a group with a shaded cell and power dissipation of shaded cell	38
3.13	Shaded PV cell test	39
3.14	Experimental setup	40
3.15	Experimental test for monocrystalline PV module	42
3.16	Experimental test for polycrystalline PV module	43
3.17	I-V curves for test of monocrystalline PV module	44
3.18	I-V curves for test of polycrystalline PV module	45
3.19	Comparison of PV models	46
3.20	Partial shading patron on centralized and decentralized architectures .	47
3.21	Total I-V curve in centralized architecture	48

3.22	Total P-V curve in centralized architecture	48
3.23	I-V curve of each panel in decentralized architecture	49
3.24	P-V curve of each panel in decentralized architecture	49
4.1	Two-stages and single-stage micro-inverters based on the Boost inverter for integration of PV systems.	53
4.2	Inverter based on DC/DC converters.	54
4.3	Operation principle of Boost inverter.	55
4.4	Potential application of Boost inverters in microgrids.	55
4.5	Boost converter basic circuit.	56
4.6	Boost inverter models reported in literature.	57
4.7	Component-based modeling method.	58
4.8	Steps for proposed modeling method.	60
4.9	Unidirectional Boost converter with source and load models.	62
4.10	Unidirectional Boost converter.	62
4.11	Bidirectional Boost converter.	64
4.12	Partial operation flow Boost converter model.	66
4.13	Boost converter model coupled load.	66
4.14	Boost converter model coupled V_{DC}	67
4.15	Unidirectional and bidirectional Boost converter simulated circuits . . .	67
4.16	Comparison proposed model with circuit simulation - Case 1.	68
4.17	Comparison proposed model with circuit simulation - Case 2.	69
4.18	Comparison proposed model with circuit simulation - Case 3.	69
4.19	Proposed model and average model of Boost converter	70
4.20	Schematic circuit for PV module - Boost converter test	71
4.21	Experimental Boost converter test	71
4.22	Coupling PV module - Boost	72
4.23	Component-based model for PV module and Boost converter integration	72
4.24	Irradiance patron during test	73
4.25	PV module and Boost converter voltage measurements. Boost output voltage (V_o), PV voltage (V_{pv}). <i>Vertical scale = 10 Volt/div. Horizontal scale = 10ms/Div.</i>	74
4.26	Simulation results of integration PV module - Boost converter. Boost output voltage (V_o), PV voltage (V_{pv})	74
4.27	Voltage (V_c) and current (I_L) of Boost converter (Left side) - Voltage (V_{pv}) and current (I_{pv}) of PV module (Right side)	75
4.28	Boost inverter circuit with conductive losses	77

4.29	Boost inverter gain	78
4.30	Boost inverter efficiency	79
4.31	Boost inverter as a system based on components	79
4.32	Boost inverter model based on components	80
4.33	Sinusoidal Pulse Width Modulation (SPWM)	81
4.34	Simulation results of Boost inverter	81
4.35	Results of Boost inverter gain with changes of load	82
4.36	Schematic circuit for PV module - Boost converter test	82
4.37	Component-based model of Boost inverter with PV module	83
4.38	Experimental I-V curve PV module	84
4.39	Experimental results for Boost inverter and PV module integration. I_o (1A/div). V_o (250Volt/div). V_{pv} (10Volt/div). I_{pv} (1A/div). Horizontal scale = 10ms/div.	85
4.40	Simulation results of Boost inverter output voltage	85
4.41	Simulation results of current and voltage for the PV module under test	86
4.42	Boost inverter integrated to the grid	87
4.43	Equivalent circuit grid connection	87
4.44	Component-based model of Boost inverter grid-connected	88
4.45	Current injection of Boost inverter into the grid. Grid voltage V_g Injected current I_o	89
4.46	Simplify PV system grid-connected.	90
4.47	Component-based model of simplify microgrid based on PV-Boost inverters.	90
4.48	Current injection of Boost inverters into microgrid in open loop operation.	91
4.49	From component-based modeling to multiple hierarchic approach.	92
5.1	HiLeS tool to design embedded systems with multiple hierarchic level	97
5.2	Computing capability (a) and time-step requirements (b) for different types of simulation in power systems.	99
5.3	Emulation methods and relevant time steps for real-time applications.	102
5.4	Comparative diagram frequency range and emulation complexity for electric power systems.	103
5.5	HiLeS model transformation chain	105
5.6	Partial Block Definition Diagram for PV model emulation	107
5.7	Partial Internal Block Diagram for PV model emulation	108
5.8	Partial Activity Diagram for PV model emulation	108
5.9	Generated signals in FPGA to emulate a partially shaded PV module	109

5.10	IBD modified Newton-Raphson method.	110
5.11	Activity Diagram for modified Newton-Raphson.	110
5.12	Calculated I-V curve for a PV module with a single shaded cell and several partial shaded areas.	111
5.13	Generated signals in FPGA to emulate a partially shaded PV module with fault in a by-pass diode	111
6.1	Boost inverter based on functional components	115
6.2	Partial Block Definition Diagram	115
6.3	Partial Internal Block Diagram	116
6.4	Partial Activity Diagram	116
6.5	Partial synthesis of Boost inverter model in FPGA	117
6.6	Simulation of Boost inverter inrush currents	117
6.7	Time step of 500nS for Boost inverter model	117
6.8	Test of Boost inverter emulation in FPGA and physical prototype . . .	118
6.9	Synchronization of Boost inverter prototype and model in FPGA . . .	118
6.10	Setup experimental for control design and validation	119
6.11	Final prototype controlled by an FPGA XC7A35T	119
6.12	Experimental results of Boost inverter in DC-AC operation	119
6.13	Structure of digital slide controller	123
6.14	Capacitor voltages with digital slide-mode control	124
6.15	Inductor currents with digital slide-mode control	125
6.16	Output voltage with digital slide-mode control	125
6.17	Block Definition Diagram for the digital PI controller	126
6.18	Internal Block Diagram for the digital PI controller	126
6.19	Activity Diagram for the digital PI controller	126
6.20	Associated Petri net for the digital PI controller	127
6.21	Block Definition Diagram for the slide-mode controller	127
6.22	Internal Block Diagram for the slide-mode controller	127
6.23	Activity Diagram for the slide-mode controller	128
6.24	Associated Petri net for the slide-mode controller	128
6.25	Activity Diagram for the slide-mode controller with reference signal . .	129
6.26	Associated Petri net for the total controller and reference signal generator	129
6.27	Integration of slide-mode controller and the Boost inverter model . . .	129
6.28	Digital signals for slide-mode controller implemented in FPGA	130
6.29	Emulation of Boost inverter output with sinusoidal reference	130
6.30	Boost inverter output for input voltage variation	131

6.31	Boost inverter output for load variation	131
A.1	Ideal Boost converter.	150
A.2	Waveforms of PWM signal and inductor current for ideal Boost converter. 150	
A.3	Boost converter with losses.	153
B.1	Boost inverter implemented	155
B.2	Drain-Source current SiC-MOSFET C3M0065090D	156
B.3	L-Current; L-Frequency Inductor AGP4233	157
B.4	Impedance-Frequency Capacitor MKP1848	157
B.5	Ciss, Coss characterization of SiC-MOSFET	157
B.6	Crss, $V_{GS_{th}}$ characterization SiC-MOSFET	158
B.7	Switching time Vs $R_{g_{ext}}$ from SiC-MOSFET datasheet	158
B.8	Selection driver SiC-MOSFET	159
B.9	PCB Boost inverter	159
B.10	Final prototype	159
B.11	Inductor current (I_L) and driver signal (<i>pwm</i>) on one Boost inverter leg 160	
B.12	DC regulated voltage ($V_{o_{DC}}$) and driver signal (<i>pwm</i>)	160
B.13	Experimental results of Boost inverter in DC-AC operation	161
B.14	Thermal image of power stage	161
C.1	Elements of HiLeS Language	164
C.2	Channel types defined by HiLeS	164
C.3	HiLeS model base services and ports	165
C.4	Control net and blocks integration on HiLeS architecture	166
C.5	Evolution of a block model into a functional, hierarchic and temporized structure	167
C.6	Example of multiple architecture for one interf	168
D.1	Multiple hierarchic level approach with HiLeS	172
D.2	Multiple hierarchic level approach with HiLeS	172

List of tables

2.1	Examples of successful microgrid projects	18
3.1	Test for photo-induced currents in shaded conditions	39
3.2	PV modules under test	41
3.3	Shading factor PV module monocrystalline	41
3.4	Shading factor PV module polycrystalline	42
3.5	Shading area and shadow coefficient for PV module TE 2200	43
3.6	Shading area and shadow coefficient for PV module YL290p-35b	44
3.7	Mean Squared Error (MSE) for proposed model	45
3.8	Comparison of power in centralized and decentralized architectures	50
4.1	Comparison of modeling methodologies.	59
4.2	Simulation parameters	68
4.3	Simulation cases	68
4.4	Mean Squared Error (MSE) - Simulated models	69
4.5	Experimental parameters	71
4.6	Simulation parameters for Boost inverter	80
4.7	Experimental parameters	84
4.8	Mean Squared Error (MSE) of V_o Boost inverter model	86
4.9	Simulation parameters	88
5.1	Hardware used for emulating the shaded PV systems	111
6.1	Total Harmonic Distortion output voltage Boost inverter	124
B.1	Design Parameters	156
B.2	List of main components	160
C.1	Comparison of Tools for Automatic Code Generation in Power Electronics Systems	169

Chapter 1

Introduction

In the new context of the electric industry, one of the most important global challenges is the modernization of the electrical grid to maximize the power quality, to predict and to manage the use of the electric energy performance, to avoid the grid instability. Photovoltaic (PV) systems integrated to microgrids are an attractive solution to respond at these concerns using specific power electronics converters and energy management systems.

The extensive use of power electronics converters and PV generators in microgrids has increased the power system complexity [1][2]. New modeling strategies are necessary to represent and to understand the better possible the behavior of PV systems connected to a microgrid in normal operation and failure conditions. Real-time simulations and control systems design in power electronics deal with high switching frequency devices increasing the processing speed requirements [3][4]. High performance devices are required to accomplish these processing features.

Additionally, photovoltaic technologies are growing continuously around the global electricity demand. The increasing interest in PV systems with large number of PV panels developed an important need of platforms for designing and testing these systems [5]. PV panel emulator is one of these possibilities to represent the association PV systems with devices associated with them [6]. However, several parameters must be considered to develop these PV emulators such as the environmental conditions and nonlinear loads [7][8]. These reasons encourage the growth of research works in the modeling of PV cells to PV arrays, power electronic converters and their hardware implementation in real-time emulations [9].

In this context, this dissertation aims to contribute to the research question about how to develop a suitable real-time emulation method able to be adapted to the evolutionary nature of current PV systems integrated to microgrids and at the same time able to follow their complex dynamic. In order to achieve this goal, first is studied the PV generators under working conditions. Then, power converters are modeled with an innovative methodology. Finally, the integration of PV systems is studied using a real-time approach by means of a modeling methodology based on the System Modeling Language and the High Level Specification of Embedded Systems.

This study focuses on PV systems under partially shaded conditions because of their negative impact in PV installations. In addition, a novel modeling strategy is applied to power electronics architectures to facilitate the model adaptability. For instance, in this work is analyzed a decentralized architecture based on the Boost inverter topology which is able to integrate PV systems with a high degree of efficiency and reliability. Results from partially shaded PV models and power electronics structures are analyzed and integrated to evaluate innovative control strategies taking advantage of the real-time processing devices.

Chapter II presents the general concepts about PV systems and their integration in microgrids. Chapter III explains the modeling approach of shaded PV systems. Chapter IV shows the modeling of a versatile power converter known as Boost inverter. Chapter V describes the HiLeS framework and the Systems Modeling Language for implementation of PV system models in embedded hardware. Chapter VI presents the modeling of the Boost inverter for real-time emulations and the design of a nonlinear controller. Finally, conclusions and perspectives are discussed.

The main contribution of this work in Chapter III is to define a simplify relation denominated shadow coefficient to describe the behavior of PV modules under working conditions. In Chapter IV is proposed a component-based methodology to model power converters independently of changes in the type of source or the load. In Chapter V is used the HiLeS tool to implement models of PV systems in FPGA to further development of real-time emulations. Finally, Chapter VI contributes with a real-time modeling methodology of power converters and the design of a digital nonlinear controller.

Chapter 2

Photovoltaic Systems in Microgrids

Contents

2.1	Introduction	3
2.2	Photovoltaic systems	5
2.2.1	PV generation and shadow impact	5
2.2.2	Architecture of PV systems	11
2.2.3	Reliability of PV systems	14
2.3	Integration of PV systems in Microgrids	16
2.3.1	PV grid integration	17
2.3.2	Power electronics in microgrids	19
2.3.3	Research challenges for integration of PV systems in microgrids	21
2.4	Real-time emulation of microgrids	22
2.4.1	Real-time simulation methods of power systems	23
2.5	Conclusion	24

2.1 Introduction

Currently, there is a growing interest in alternative and renewable energy resources because of the climate change people around the world have more conscience about environmental issues and energy supply constraints. The most common type of alternative energy in this context is the photovoltaic (PV) energy. This energy source has received many attention in recent years and it is commonly present on buildings throughout

the World. Power generation systems based on PV energy have several advantages such as easy implementation, scalability, and relative low cost. Indeed, the recent growth of microgrids, which integrate alternative energy resources into conventional grids, has taken advantages of these PV generation characteristics. A microgrid is a group of interconnected loads and distributed energy resources within clearly defined electrical boundaries that acts as a single controllable entity with respect to the grid. However, energy production from PV generation systems is influenced by several internal and external factors such as weather, cell temperature, solar position, aging, shadows, and other conditions. PV system design integrated to a microgrid must receive many attentions taking into account these factors that influence the final energy production and the structural health [38].

The integration of these PV generation systems into the microgrid requires suitable power electronics equipments to adapt the system features. These equipments known as power converters allow the control of power supply by PV generation stages. These converters are able to set the operating point close to the maximum power point in order to get efficiently the maximum power available. These power electronics equipments enable the reliable interconnection of direct current PV systems with alternative current power systems.

Performance evaluation of these PV systems and their integration with power systems in microgrids can be done through conventional simulation tools [16]. Some evaluations before implementation are more complex because of meteorological conditions, cost, space, and other features. PV system design requires controllable and repeatable conditions before actual field tests. The power generation performance analysis of PV systems integrated to electrical grids involve a stable, repeatable and controllable conditions. PV system emulations can arise as a suitable and safety stage between computational simulations and final field tests.

This chapter presents the fundamental concepts about PV systems and their integration in microgrids. The main concepts of PV systems connected in a microgrid is presented such as the power generation, the PV system architecture description, the interconnection with power converters, and the common faults in a PV system. The necessity of a real-time emulation is described with the employed methods of PV systems. Finally, this chapter highlights the current modeling and emulation research challenges to study the integration of PV system in microgrids.

2.2 Photovoltaic systems

2.2.1 PV generation and shadow impact

The PV generation systems are power systems able to supply electrical energy from solar energy. These power systems take advantage of sunlight by providing free and clean energy. As shown in Fig. 2.1, the energy of a photon arrives to the semiconductor material and produces electrical energy by means of the photoelectric effect [22]. PV cells are the fundamental unit in PV generation systems. A set of PV cells connected in series forms a structure denominated PV module, as shown in Fig. 2.2. Interconnection of PV modules allows increasing the output voltage to further coupling with power electronics converters. This interconnection of PV modules in series is called PV string. In order to increase the power, PV strings are connected in parallel to build PV arrays. Finally, a set of PV arrays can provide electrical power to large scale in power stations known as solar farms. Fig. 2.3 depicts the general structure of a PV generator.

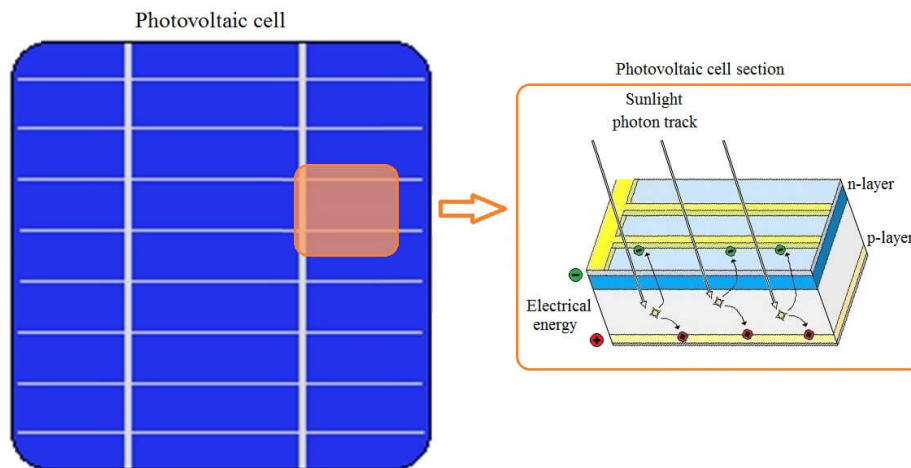


Fig. 2.1 Electrical energy from sunlight in a PV cell

The use of power systems based on PV generators are mainly deployed in three sectors as shown in [22]. The primary sector includes the residential PV installations in homes and small PV systems. The second sector covers commercial systems which may be between 10 kWp DC and multi-kilowatts and are most often installed on flat or low-slope roofs. The third sector includes the large scale PV power installations able to supply power to the utility sector level. Examples of this large scale PV installation or solar farm can provide energy until the megawatts range as reported in literature [39] [40]. Hundreds of thousands of PV modules can be installed in these large scale PV farms. From this perspective, power systems based on PV generators can cover

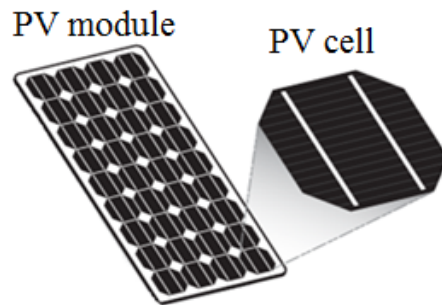


Fig. 2.2 PV cell as a fundamental unit in a PV system

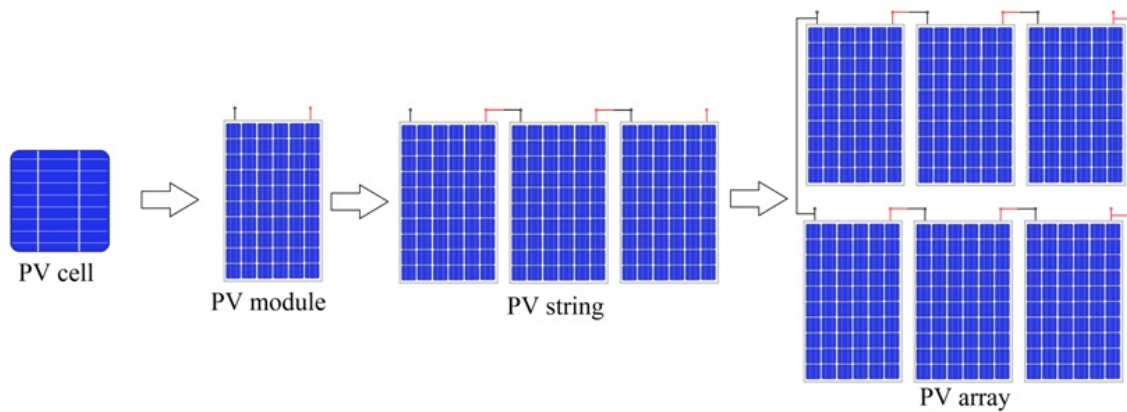


Fig. 2.3 Structure of a PV generator

installations from few PV modules to thousands or large quantity of them. As a consequence, innovative modeling and simulation approaches in real-time are required to deal with this high degree of complexity and scalability.



Fig. 2.4 Sectors of PV systems

The decreasing tendency toward lower market price encourages the installation of PV systems in all these sectors around the world. Fig. 2.5, from [41], shows the PV installation growth and the drastically price decreasing with historical values below 1US/W. This remarkable trend toward decreases market price is explained by the

Swanson's law [42]. The Swanson's law or learning curve for PV cell production is based on observations where the price of PV modules tends to drop 20 percent for every doubling of cumulative shipped volume. In others words, price can decrease to half every 10 years. As a consequence, the tendency of lower prices of PV systems leads toward more and more widespread use of PV systems as a suitable and environmental friendly solution for the current increasing energy consumption requirements. Additionally, according to L. Brown et al.[41], the annual growth of solar energy use in comparison with other energy sources has shown an important increase with a tendency to take the place of other energy sources not friendly with the environment such as carbon, oil or nuclear as shown in Fig. 2.6.

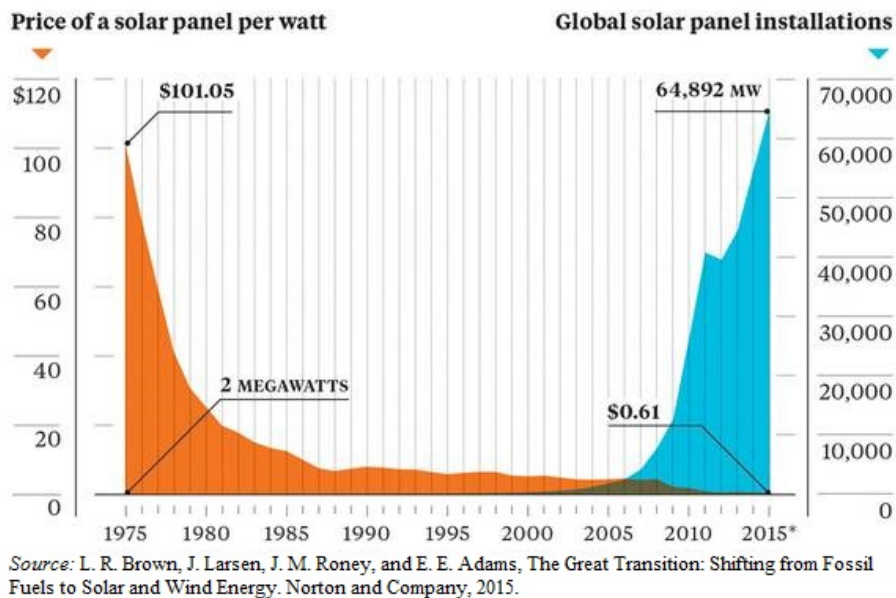


Fig. 2.5 Growth of PV systems installations worldwide

PV cell efficiency is another important aspect of current development of PV systems. Fig. 2.7, from [43], depicts the improvements in efficiency by PV cell technologies. Fig. 2.7 shows that the efficiency of PV cell technologies with high worldwide market section (mono-crystalline aprox. 24% and poly-crystalline aprox. 19% [43]) has not reported important improvements. This situation represents a challenge to both improve the manufacturing process of these technologies and decrease the losses in current and future PV installations based on these common technologies.

Taking into account the presented characteristics of PV generators and their promising perspectives of growth. The next subsection shows the several internal and

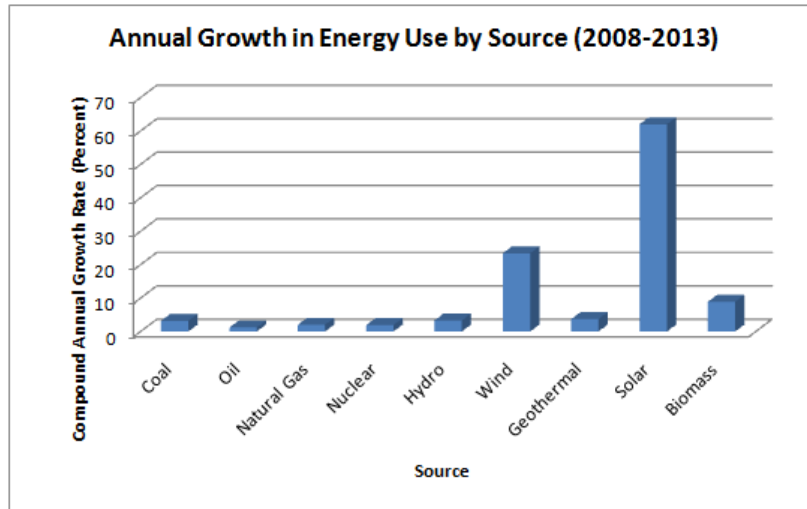


Fig. 2.6 Annual growth in energy use by source

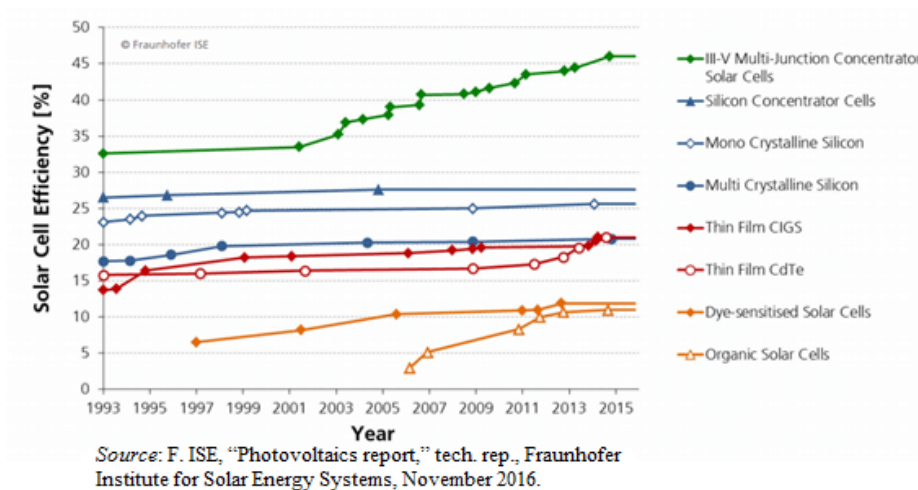


Fig. 2.7 Improve of solar cell efficiency by technology

external defects and issues associated with PV generators which represent an important concern for their development.

Defects in PV generators and shadow impact

Nowadays, most of manufactures guarantee a PV module life cycle around 25 years, but there are not test protocols to validate this lifetime [44]. Fig. 2.8, from [45], shows a histogram of degradation rate per year and the frequency of that level being reported in the literature (1920 literature sources [45]). Authors in [45] argue that the average annual degradation rate is 0.8% per year, whereas the most frequently reported value is

0.5% per year. As a consequence, the evaluation of different defects arises an important concern at the level of PV cells and PV modules.

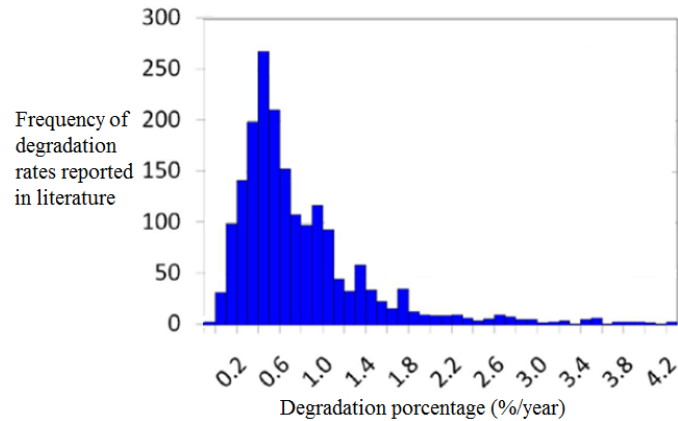


Fig. 2.8 Histogram of reported degradation rates per year of PV modules

According to [44], at level of PV cells the decrease of PV cell performance may be caused by:

- An increase of the series resistance value. The increase of the series resistance reduces the output voltage of the PV module and the fill factor of the characteristic of current-voltage (I-V) of the PV [46].
- A decrease of the shunt resistance value. The metal migration in the P-N junction causes a decrease of the open circuit voltage and by the same occasion a decrease of the maximal power [47].
- A deterioration of treatment surface (anti-reflective coating).
- Short circuits at level of interconnectors. This defect is more frequent in Thin-film cells because the upper and lower electrodes are closer.
- Open circuit of broken connectors for diverse reasons such as thermal constraints, large hail or microscopic cracks during assembly.

At level of PV modules, [44] argues that problems related to PV modules cause a gradual decrease of output power over time because of one or several failures in PV cells. Problems of open-circuit may appear at level of PV modules either in the junction box or in internal connectors. Short-circuits problems can appear related to the manufacturing process. These find their origin in the degradation of the electrical isolation due to the climatic effect exposition which induce delamination, cracks or

oxidation. In addition, PV generators are usually affected by shadows or dust as shown in Fig. 2.9 which decrease the power production and increase the risk of failures. Cracked or shaded cells give rise to a phenomenon which locally overheats the PV module leading to its perdition as shown in Fig. 2.10. This phenomenon is named *Hot spot*. The other cells of the string impose it a very high current in comparison to its short-circuit current. As a result, the shaded cells work in reverse bias (negative voltage) and dissipate an important power which can cause a heating leading to its destruction. To avoid this problem, manufactures integrate bypass diodes in the PV modules.

The study performed by [48] examines the behavior of the I-V curve of PV cell in reverse operation when cells are partially hidden. This study shows that this phenomenon of heating has direct consequences on the decrease of the output power of the PV modules. In the study made by [49], a PV module has been studied in order to measure the I-V curve of each cell. The behavior of PV cells on this curve is established when those are partially shaded. The deformation of this characteristic increases according to the number of shaded PV cells and generates two potential points of maximal power with the use of bypass diode. It can appear problems of overheating or under sizing at level of bypass diodes used in shading condition.

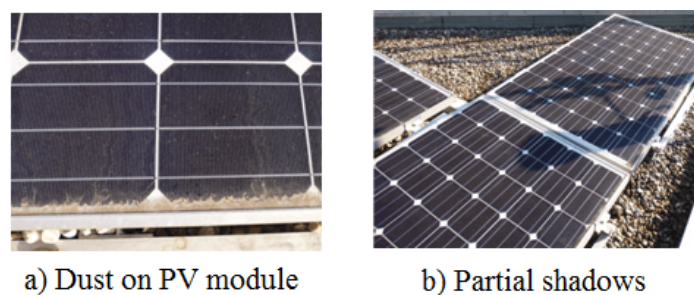


Fig. 2.9 Dust and partial shadows on PV modules

According to [44], Other defects may be present at level of PV generator such as:

- Physical defects of wiring and PV system connectors with the corrosion of the electrical contacts.
- Defects of non-return diodes connected in series on each string which function is to avoid the return of reverse current when strings are connected in parallel.

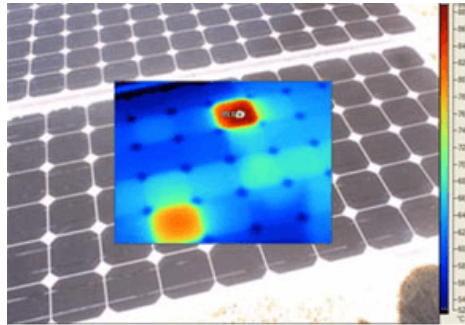


Fig. 2.10 Hot Spots on PV module

- Defects of encapsulation. The UV absorbers and others stabilizers applied in the material of encapsulation ensure a longer lifetime of this material. This leads to a progressive decrease of the output power of the PV module until its total failure.
- Defects of leakage current. This current may be created as a result of capacitive characteristic of the PV module and becomes dangerous in case of contact with the ground wire.

After description of defects and faults in PV generators, next subsection introduces to fundamental concepts of PV systems architectures.

2.2.2 Architecture of PV systems

A photovoltaic system is a power system designed to supply electrical power from solar energy. It consists of an arrangement of several components including PV generators and power converters. Fig. 2.11 shows an elementary PV chain which represents a simplify structure of a PV system.

As shown in Fig. 2.12, essential components in a PV systems are PV modules, power converters, maximum power point tracking (MPPT) systems, and batteries in some installations. PV modules are the first component in the energy transformation process. The function of PV modules is to transform the energy which comes from incident sunlight into DC electrical useful energy. Unfortunately, the DC electrical energy provided by the PV modules is unregulated and requires a suitable treatment before feeding loads. Power converters overcomes this issue of unregulated power by means of power electronics devices and control systems. The most common configurations of power converters in PV systems are the DC/DC and the DC/AC structures. A DC/DC power converter takes the unregulated DC power at the input and provides a

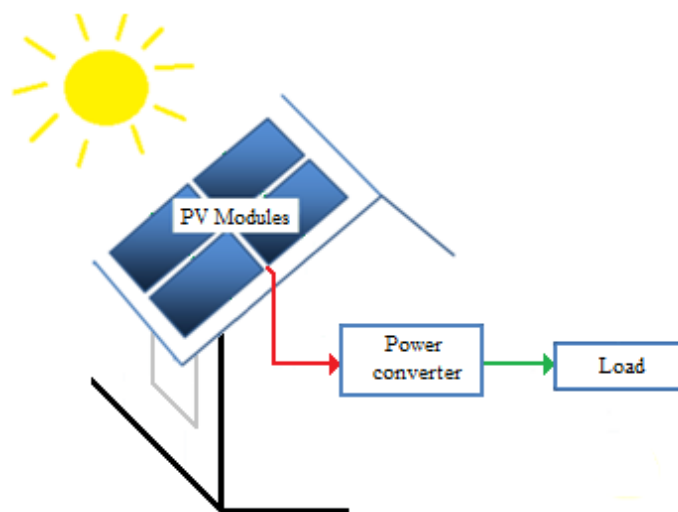


Fig. 2.11 Elemental chain of a PV system

regulate DC power to the output. In contrast, a DC/AC power converter completes a more complex process because transforms a Direct Current (DC) power input in an Alternative Current (AC) regulated power output.

Currently, PV installations consist of architectures built from arrays of several DC/DC and DC/AC interconnected power converters. In addition to power converts, PV systems require maximum power point tracking systems to keep the output power close to the maximum power available from the sun irradiance. Finally, the energy provided by PV systems depends on weather conditions; then, storage systems such as batteries could be used to compensate the constant weather changes. On the other hand, current advance in power converter technologies allows directly integrating PV systems into electrical power systems avoiding the use of store systems.

As described by [50], different types of architectures can be configured from fundamental components of PV systems. Fig. 2.13 depicts some basic typical architectures. Fig. 2.13a is a conventional architecture where the PV generator is connected to a centralized structure DC/DC - DC/AC. The main advantage of this centralization is the reduction of power electronics and control algorithm complexity; however, this structure is more vulnerable to PV generation faults and partial shadows. Architecture in Fig. 2.13b represents a mixed architecture. As shown in Fig. 2.13b, the PV modules are interconnected in a decentralized topology. In contrast, DC/DC converters are configured in a centralized topology in relation with the DC/AC power converter. This

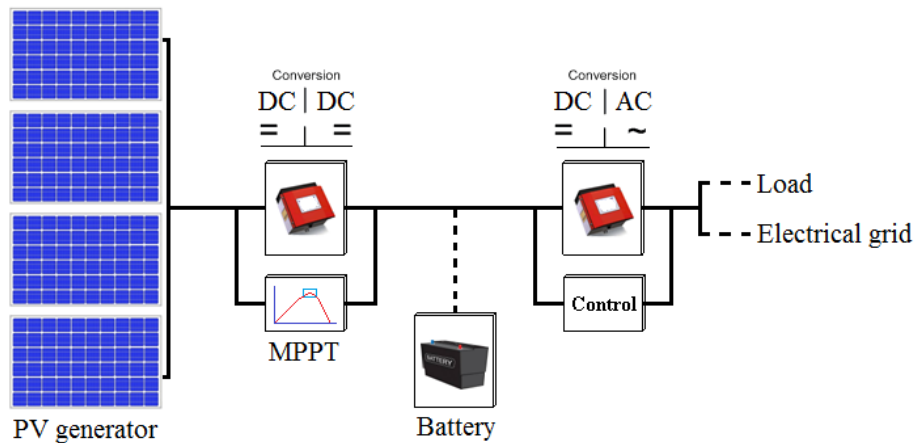


Fig. 2.12 Basic architecture of a PV system

mixed architecture allows to DC-DC power converters to follow the Maximum Power Point for each PV module. In addition, this architecture requires only a centralized DC/AC converter. This architecture allow better adaptation of non-uniform irradiance conditions and shadows increasing the suitable energy provided by the power systems. However, more quantity of DC/DC converters increase the complexity and the system price.

Finally, the architecture of Fig. 2.13c is totally decentralized improving the system reliability and the power production even under partial shaded conditions. However, this architecture requires more power converters and more complex control systems for system coordination. In addition, the power electronics stage in decentralized PV systems could decrease the global PV system efficiency. This impact on global efficiency is given by the high voltage elevation ratios and the increasing number of power converters according to the comprehensive study addressed by Picault in [22]. In this study presented by Picault, the author also highlight that despite these disadvantages many advantages of this decentralized architecture should be taking into account. First, the maximum power can be extracted from each PV module. Second, PV modules are independent each other; therefore, the impact of either shadows or faults in a PV module does not disturb the rest of the PV installation. Third, in case of PV module power converter failure only the affected converter is lost without shut down the whole power plant production. Finally, the system is easily upgradeable by simply adding additional modules to the PV installation.

Advantages of decentralized architectures have also been highlighted by authors such as Lopez [24] who presents the design and fabrication of a micro-inverter suitable to PV grid-tie applications. Results from [24] show that architecture of Fig. 2.13c presents interesting features to take advantage in microgrid applications. In this context, this document will describe in further sections the study and design of an innovative micro-inverter topology (See Fig.2.14) known as *Boost Inverter* able to interact with this decentralized and modular PV system architectures.

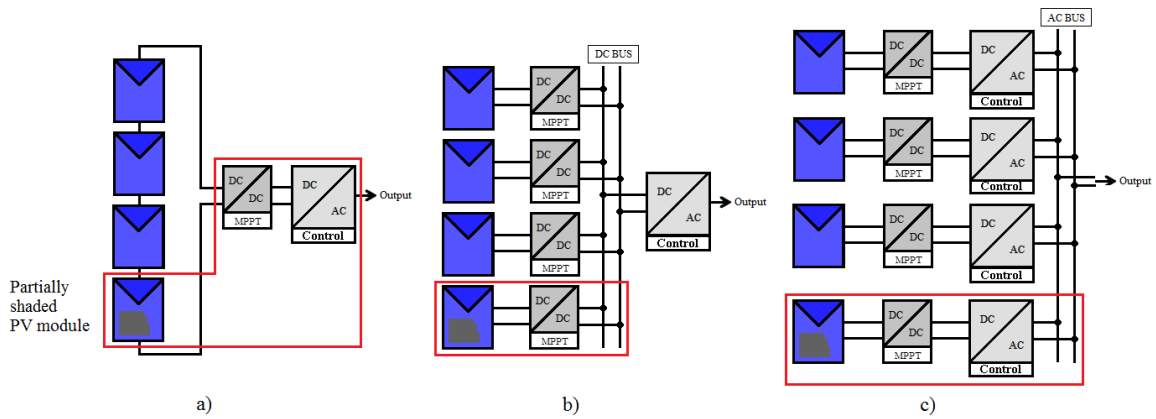


Fig. 2.13 Example of typical PV system architectures

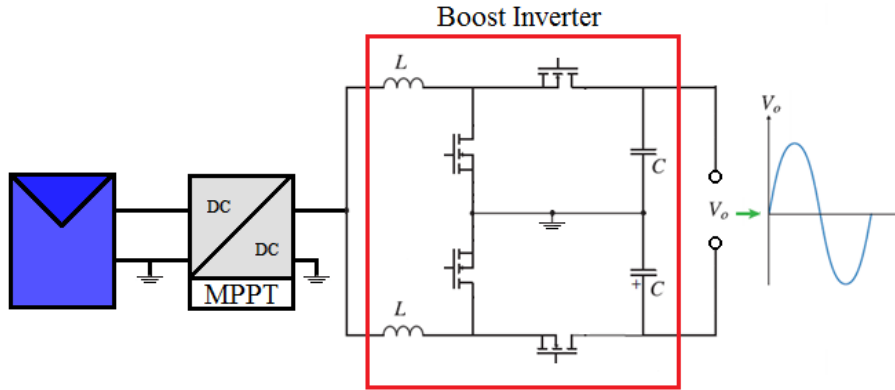


Fig. 2.14 Micro-inverter based on Boost Inverter topology

2.2.3 Reliability of PV systems

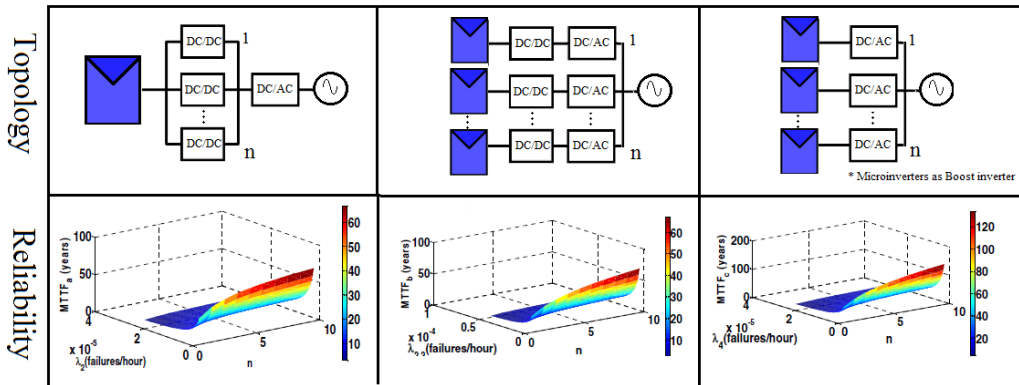
Given the previous advantages and disadvantages of decentralized PV architectures, current research challenges arise to explore innovative power converter topologies in

order to mitigate the drawbacks of this topology and take advantages of their characteristics. As mention before, some authors have proposed micro-inverter topologies based on a versatile power converter known as *Boost inverter*, Fig.2.14 [26]. This power converter is able to be reliably adapted to decentralized PV generation systems in electrical grids [30]. Indeed, reliability studies presented by Hofreiter et al. in [28] using Markov reliability models have shown that the Mean-Time-To-Failure (MTTF eq.(2.1)) from the reliability $R(t)$ of power systems based on Boost inverters is higher in comparison with conventional Boost-Buck DC-DC / DC-AC systems.

$$MTTF = \int_0^{\infty} R(t) \quad (2.1)$$

In addition, the reliability modeling proposed in [23] allows concluding that the Mean-Time-To-Failure (MTTF as defined in eq.(2.2)) in power systems with n parallel interconnected micro-inverters based on Boost inverters with failure rates λ is higher than in centralized architectures, as shown in Fig. 2.15. This conclusion arises because adding PV modules in a power systems has less impact in reliability in decentralized architectures based of Boost inverters that in conventional centralized topologies. Then, this feature is an important advantage to take into account for the scalability and reliability of PV systems integrated to microgrids.

$$MTTF = \frac{1}{\lambda} \sum_{x=1}^n \binom{n}{x} \frac{(-1)^{x+1}}{x} \quad (2.2)$$



Source: X. Shi and A. M. Bazzi, "Solar photovoltaic power electronic systems: Design for reliability approach," in 2015 17th European Conference on Power Electronics and Applications (EPE'15 ECCE-Europe), pp. 1–8, Sept 2015.

Fig. 2.15 Mean-Time-To-Failure (MTTF) of PV architectures

At this point, a general description about PV generation, PV defects, reliability, and PV system architectures have been presented. From these perspectives, next

section presents the integration of PV systems in microgrids and their essential role in the continuous worldwide growth of microgrids.

2.3 Integration of PV systems in Microgrids

Modern society depends critically on a stable supply of energy. According to [2], the growing concerns for electrical energy accessibility and the stationary infrastructure of current electrical networks have encouraged the integration of alternative energy resources motivating the development of microgrids. PV generation, probably the most distributed means of electricity production, is in this sense a suitable option to be incorporated in conventional electrical networks. However, the intermittent and complex nature of PV generation systems suggests many aspects to investigate in the fields of modeling, emulation, and energy management to make this association a more powerful option. This section describes the basic concepts of microgrids; additionally, integration aspects of PV systems are analyzed.

Microgrid definition

According to [1], microgrids comprise Low Voltage distribution systems with distributed energy resources (microturbines, fuel cells, PV generators, etc.) together with storage devices (flywheels, super-capacitors and batteries) and flexible loads. Microgrids can operate either in a non-autonomous way interconnected to the grid or in an autonomous way disconnected from the main grid. Efficient coordination of resources by an *Energy Management System* in a microgrid can provide several benefits to the overall power system performance. Fig 2.16 depicts a general example of microgrid structure.

Authors in [5] explain that microgrids currently use Information Communication Technologies to evaluate the power flows and balance production and consumption using local *Energy Management Systems*. These management systems include hardware and software capable of monitoring and controlling power generation units, such as PV generators, for safe and efficient system operation. As a result, the management of microgrids involve several layers including *Energy Management Systems*, distributed control devices, power electronic converters, power generation units, loads, and interactions with other neighbor microgrids.

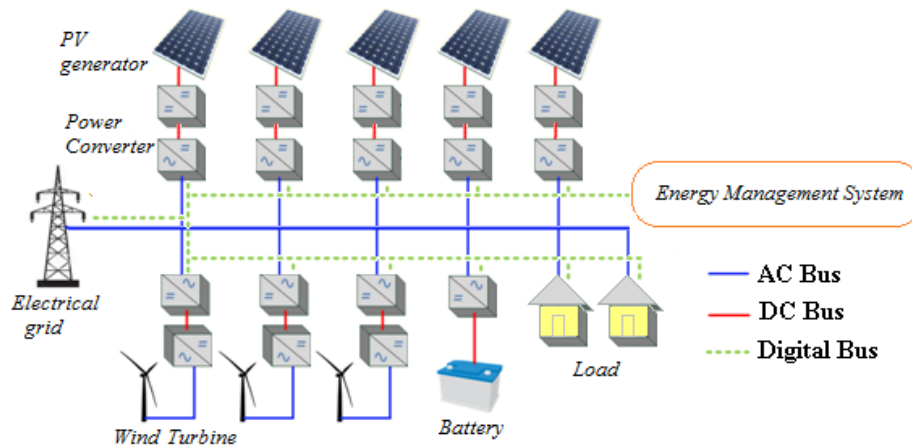


Fig. 2.16 Microgrid structure

2.3.1 PV grid integration

Power generation systems considered in microgrids concern renewable sources. Recently, the substantial increase of PV installations has represented an important function in the development of microgrids. The constant and decreasing tendency to lower prices and the generalized approval of costumers and energy policymakers have allowed the accelerated growth of PV grid integration. A global panorama shows that many countries have dedicated efforts to integrate PV systems as an alternative energy source. Fig. 2.17, from [5], presents the countries with higher installed PV generation capacity in 2013 according to the annual report of the *International Agency of Energy*. This installed PV capacity compared with the total generation capacity by country represents the impact on PV integration on power generation as shown in Fig. 2.18 (Source [5]). Fig. 2.18 depicts the progressive relevance of PV integrated systems in the global electric market.

Authors in [2] presents a survey of successful microgrid projects as shown in Table 2.1. The nature of distributed resource listed in Table 2.1 allows emphasizing the relevant contribution of PV systems to current expansion of microgrids.

However, the authors in [5] identify some research challenges caused by this integration. The main concern presented in [5] is the stochastic nature of the PV resource and the cloud dependency which can affect the grid voltage profile (Fig. 2.19, image source: <http://www.solaripedia.com/images/large/3427.jpg>). Report in [5] explains that this identified challenge is to mitigate the inherent PV stochastic nature by means

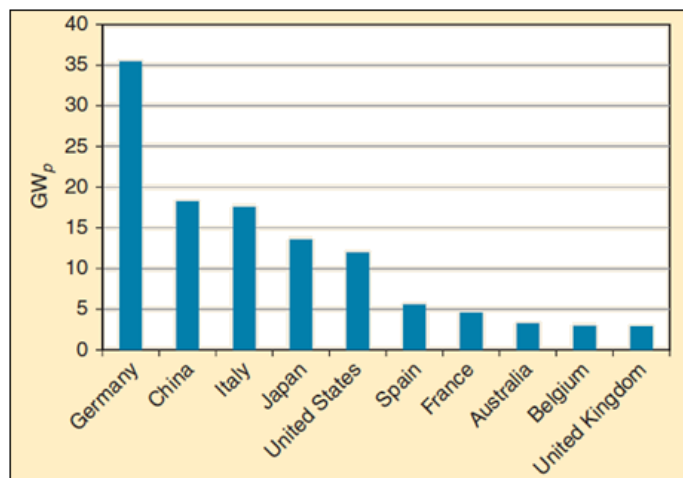


Fig. 2.17 Top ten PV installed capacity by country, 2013

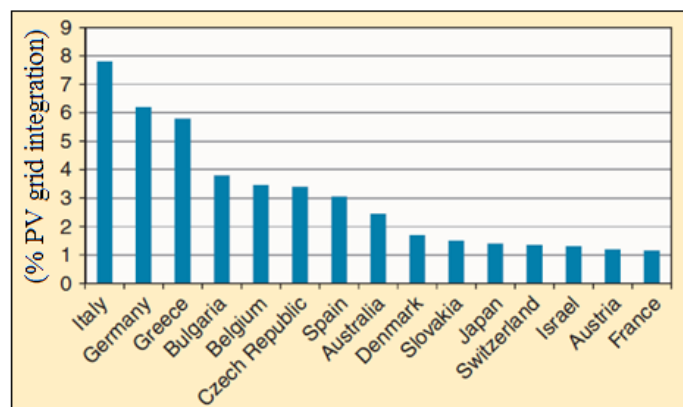


Fig. 2.18 Contribution of PV production base on the installed capacity, 2013

Table 2.1 Examples of successful microgrid projects

Country	Site	Distributed Energy and Storage Resources
Greece	Kythnos Island	10kW _p of PV, 53 kW battery bank, and 5kW diesel genset.
Singapore	Sino-Singapore	30kW _p of PV, 6kW of wind power, and four 15kW battery bank
USA	Morgantown	40kW _p of PV, 160kW of natural gas generators
China	Nanjing	50kW _p of PV, 15 kW wind power, and 300 Ah battery bank
China	Dongfushan	100 kW _p of PV, seven 30kW wind turbines
Japan	Hachinohe	100kW _p of PV, three 170kW gas generators.
Netherlands	Bronsbergen	315kW _p of PV distributed in approx. 100 homes
USA	San Diego	1.2MW _p of PV, and two 13.5MW gas turbines

of advanced control and management systems to allow supplying electrical power depending on the grid conditions. Another important concern identified by authors in

[5] is the coordination of PV generation systems with surrounding system components. Finally, the coordination of protections in case of fault is another important concern in current integration of PV generator in microgrids [51].



Fig. 2.19 Crossing clouds above PV generator

Most of these concerns rely on power electronics converters in charge of the regulated connection of PV generators with the microgrids. Consequently, the following subsection will be devoted to describe the main aspects about power electronics in microgrids.

2.3.2 Power electronics in microgrids

Power electronics equipment is the core component to make the interface of distributed energy and storage resources with the electrical grid. Power electronics converters allow efficiently integrating in microgrids several energy sources as shown in Fig. 2.20. Fig. 2.20 outlines the interaction of power converters with alternative energy sources, critical and non-critical loads in order to supply power according to the system requirements. At level of PV systems, power converters should be able to follow the maximum power point tracking methods from side PV and to generate the alternative current signals from side grid-tied. Topologies of PV Inverters can be classified as micro-inverters, string and mini-central converters, and central inverters [5].

Micro-inverters are small PV inverters with usually power range of 250–300 W and input voltage of 30–40 V. Each micro-inverter is directly coupled to a single PV module. At the AC grid side takes place the parallel connection of micro-inverters. Since the power level of micro-inverters are relatively small, mainly single-phase inverters

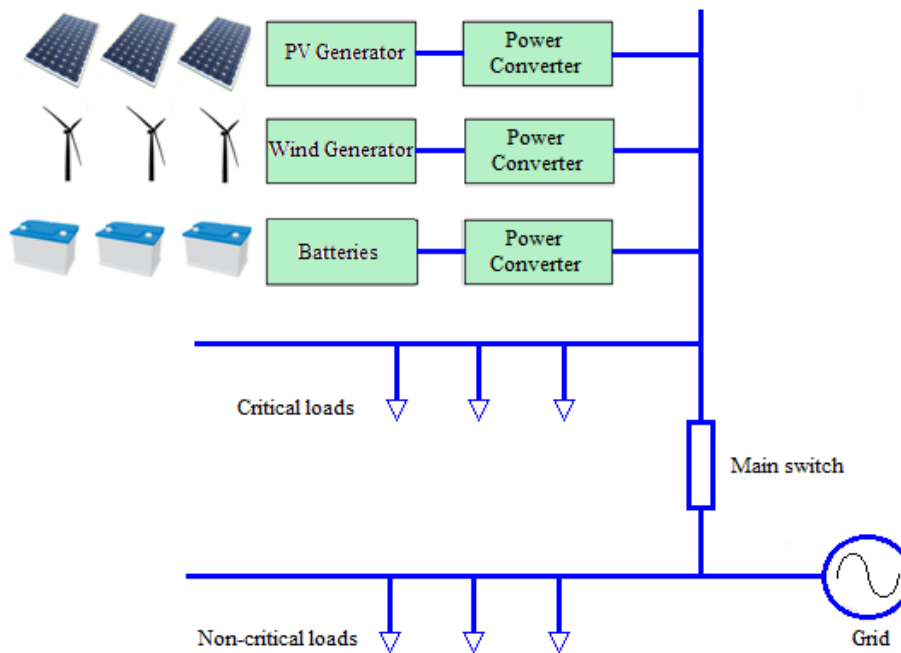


Fig. 2.20 Integration in microgrids of Distributed Energy Resources with power converters

are used. According to [5], new bi-directional micro-inverters able to operate in all four-quadrant will be a promising alternative to meet the power flow requirements of microgrids as well as the new requirements of public grids.

String and mini-central inverters are designed for systems in the power range approximately of 3–30 kW and a connection to the low-voltage grid [5]. Usually, these inverters are able to provide reactive power are well suitable to accomplish the microgrids requirements. Central inverters are designed for powers from 100 kW to megawatt range. They are typically connected to the medium- voltage grid and use medium-voltage transformers. Central inverters are also able to deliver reactive power and limit their power according to the requests of the grid operator. Therefore, they are well suited to the needs of microgrids [5].

As illustrated previously, power electronics converters in microgrids allow the integration of PV generators to microgrids in several scales. However, the rigorous work conditions and the influence of external factor such as shadows lead to the design process of power converters with a high degree of reliability and versatility. As a result, innovative modeling and development methodologies are needed to accomplish the

quality standards for these converters to PV microgrid applications.

To summarize the presented perspectives about PV systems and microgrids, next subsection will outline the general research challenges for the integration of PV systems in electrical grids.

2.3.3 Research challenges for integration of PV systems in microgrids

Fundamental topics about PV systems and integration in microgrids have been addressed through this chapter. From these aspects, following research challenges are identified:

- Maximize the energy production of a PV system influenced by several internal and external factors.
- Evaluation of PV systems performances integrated in power system performed by conventional simulation tools.
- Innovative modeling and simulation approaches to deal with this high degree of modularity and scalability.
- Decrease losses of current and future PV installations improving the manufacturing process and the efficiency of PV cells with technological improvements.
- Increase the system reliability identifying defects of PV cells and PV modules.
- PV generators are usually affected by shadows decreasing the power production and increasing the risk of failures. Then, preventive actions are necessary to mitigate their negative effects.
- Intermittence of solar energy on PV systems can affect the grid stability. As a result, innovative power electronics architectures and Energy Management Systems are required to decrease the vulnerability of PV power systems to environmental changes.
- Advanced Energy Management Systems in microgrids should be able to coordinate the distributed energy resources according to the electrical grid variations.
- Coordination of protections is still an important issue to explore in current integration of PV systems in microgrids.

- Power converters in microgrids allow the integration of PV generators in several scales. However, the work conditions and the influence of external factors such as shadows lead toward design processes with high degree of reliability and versatility. As a result, innovative modeling and design methodologies are needed to accomplish the performance requirements for these converters in microgrid applications.
- PV generation is a suitable option to be incorporated in distributed electrical networks. However, the intermittent and stochastic nature of PV systems require more investigation to increase the knowledge about the PV system behavior in microgrids.
- Model and design methodologies to accomplish great performance in shadows conditions leading toward design processes with high degree of reliability and versatility.

Complexity and high degree of scalability characterize the current growth of PV installations. The necessity to have a real time energy management of a PV systems in a microgrid requires a methodology of conception using adequate tools in order to respond at the problematic of a decentralized PV control. As a consequence, suitable methodologies are required to deal with the research challenges addressed by the continuous evolution of microgrids and PV systems. In this context, the following section presents a description of methodologies based on real-time emulation of PV systems intended to evaluate these power systems in a safety and reliable stage before final field tests.

2.4 Real-time emulation of microgrids

Since general use of PV systems in application such as power sources to aerospace satellites or integration to electrical grids, many authors have shown interest in concerns about PV system emulation [8]. This interest has been inspired by the need of assuring the reliability of the power systems before final employment. Several methods have been proposed to emulate the power supplied by PV sources. These methods are based on controlled voltage sources where control signals simulate the PV panel behavior. Additionally, literature review reports different types of controlled sources. Usually, these sources are based on either voltage amplification of cellular cells under controlled light or DC/DC converters controlled by analogical circuits [52], microcontrollers [53]

or FPGAs [54][55]. In digital devices, the PV signal is often simulated by means of mathematical models[8], lineal approaches [53], Lockup Tables [56] or artificial intelligence methods [57].

Power PV emulation method or also called Power Hardware-in-the-Loop (PHIL) is suitable to assess power electronics equipment [58]. However, the control system analysis of a PV system can be less appropriated in PV emulators due to higher costs and implementation concerns. Furthermore, control system evaluation of PV arrays requires more powerful simulation tools due to time step constrains [59].

In contrast, development of processing devices has allowed increasing the computer performance. Therefore, more complex models can be computed in real-time [60]. Indeed, PV real-time simulations can include power electronics models [61]. These types or emulation methods are classified as controller Hardware-in-the-Loop (CHIL) [58]. This controller HIL emulation is intended to assess in real-time the performance of control systems from current and voltage signals equivalent to sensor signals in the actual PV system [62].

2.4.1 Real-time simulation methods of power systems

There are several approaches to simulate the overall behavior of PV systems [21]. First approach is based on conventional simulation tools such as Matlab [63] or PSIM; however, this approach can be inadequate to model large PV arrays because the amount of components involved. Second method employs specialized PV software such as PVSyst [44], or PVCad; however, this method is restricted to predefined models and users are limited to evaluated innovative architectures. Finally, customer simulation tools are employed. This last approach uses specific tools developed to evaluated PV system behavior.

Two lines are defined in customer simulation tools. First line is based on system of equations for voltage and current of all the implicated interconnections [22]. However, this method is unsuitable to analysis large PV systems or changes in particular elements of the system. The other line consists in adding characteristics associated to cells, modules, strings and field [21]. The last approach is the most suitable to study large PV systems because it allows to model complex systems from less complicated component models. In addition, this perspective based of components allows evaluating the impact of changes in a part of the system on the overall system. As consequences, the influence of either external or internal features such as partially shadows, component

fails, mismatching, and aging can be analyzed.

Finally, there is a growth interest to research on PV system optimization [64], new PV architectures [22][63], PV system fault detection [44], and PV arrays integration with others energy sources [3]. Taking into account these research interests, to develop an environment to evaluate different topologies and conditions is appropriated for the novel challenges for the grid integration of PV systems.

Virtual prototyping of Power Systems

Fig. 2.21 shows the roadmap to design the virtual prototyping of PV systems integrated to microgrids. Through this work the roadmap presented in Fig. 2.21 will be followed. In the first step models of PV generators and power converters are developed. Then, these models are validated. Next, interaction between models is analyzed. Finally, real-time emulation of this model is implemented in FPGA.

2.5 Conclusion

This chapter has shown relevant aspects about PV generation and their integration in microgrids. Information resources allow predicting the continuous trend to growth of installed PV system around the world. In addition, a remarkable price decreasing of PV modules confirms the Swanson's law for progressive price reduction motivating even more the insertion of PV generators in the electrical market. However, PV systems also are vulnerable to internal and external conditions and preventive actions should be taken in order to reduce their impact in the system reliability and energy production.

Power converters have been presented as fundamental interface elements between energy provide by PV generators and electrical grid requirements. Power electronics architectures have shown suitable features according to safety integration conditions. In addition, most of concerns about interaction of PV systems and microgrid rely on these power devices. As a result, suitable modeling and design methods should be studied in order to ensure their reliability and normal operation.

Finally, simulation and emulation methods have been analyzed to identify their main challenge and constraints to provide a useful approach in the study of concerns about PV systems in microgrids. FPGA was identified as the most suitable processing

Roadmap of Virtual Prototyping

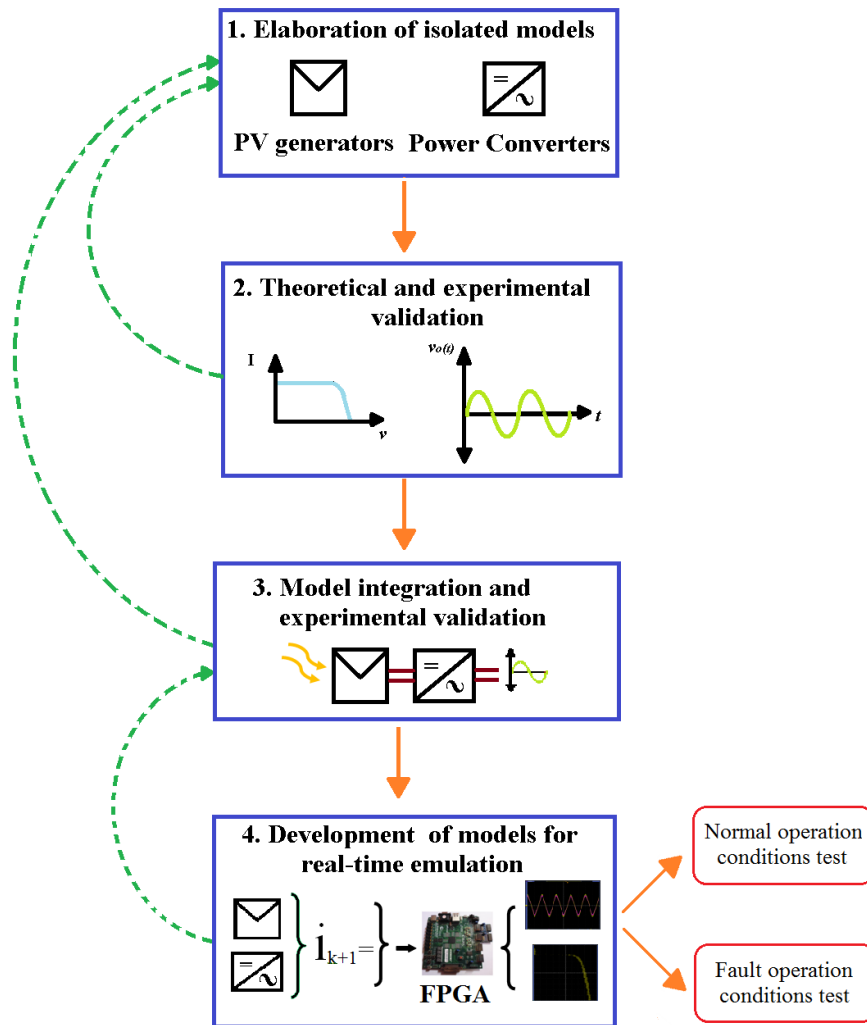


Fig. 2.21 Roadmap of virtual prototyping in this document

device to deal with the high complex degree of PV system real-time emulation. Then, a proper methodology is required to develop the PV system models taking advantage of powerful processing characteristics of FPGAs.

Chapter 3

PV System Modeling Under Shaded Conditions

Contents

3.1	Introduction	27
3.2	Modeling under shaded conditions and thermal impact	28
3.2.1	PV cell model for unshaded conditions	30
3.2.2	PV cell model for shaded conditions	31
3.3	Proposed partially shaded PV model	33
3.3.1	Partially shaded PV cell model	33
3.3.2	Shadow coefficient analysis	35
3.4	Experimental model validation	38
3.4.1	Photo-induced current test	38
3.4.2	Partially shading PV modules test	40
3.4.3	Comparison with other modeling approaches	46
3.5	Simulation of PV generation architectures	47
3.6	Conclusion	50

3.1 Introduction

The previous chapter has shown the importance to model accurately the electrical behaviour of PV array in normal and shading conditions. The current integration of

PV systems in electrical grids can be affected by internal and external factors. However, external factors such as shadows have more reported incidence. Shadows decrease the supplied energy [10] by the PV system and increase the risk of structural failures [11] [12]. Well known modeling methods to describe the PV system behavior under unshaded conditions are widely accepted in literature[13]. Others authors argue that modeling partially shaded PV systems is an important concern in current research of grid integrated PV systems [14]. For instance, there are few real-time methodologies for the test of diagnostic system taking into account different types of shadows characteristics and their impact on the electrical behavior of the PV system.

PV systems also interact with high switching frequency power converters [15], control systems [16], and fault detection methods[17]. The study of interactions among partially shaded PV systems and high speed processing systems [6][18] arises a novel research challenge. According to authors in [19], real-time approaches are fundamental for designing and verifying control algorithms, supervision strategies, and power electronic interfaces in PV systems. However, accurate models of partially shaded PV systems are difficult to develop for these applications because of the significant computational load and model complexity [20]. To respond at this problematic, the proposed study contributes with a suitable methodology which involve geometric and optical characteristics of shadows and their relation with PV electrical parameters. This approach provides a shadow coefficient which allows to increase the model accuracy without increasing the computational complexity for real-time emulations. The proposed model is evaluated and validated in actual shaded PV systems.

This chapter presents the PV models for unshaded and shaded conditions. First, the proposed model is described for partially shaded conditions. The experimental procedure is explained to validate the proposed model. Model validation and experimental results are discussed. This study is extended to centralized and decentralized PV generation structures in order to compare the performance of both topologies.

3.2 Modeling under shaded conditions and thermal impact

In shading conditions, PV systems have a high risk of structural failures and lost of power production. Some authors have studied this behavior of shaded PV cells in PV modules. In [65], Bishop presents a model for the reverse characteristics of shaded

solar cells based on works about the avalanche breakdown theory. Authors in [66] propose a numerical simulation for the description of partially shaded solar generators. In [67] shadow transmittance is investigated from the I-V characteristic behavior. Authors in [68] present a review of models and propose a model and procedure to evaluate the behavior of reverse bias shaded cells. In [38], Silvestre and Al. study the PV modules performance working in partial shaded conditions and simulate the influence of the shadow rate in the PV module parameters. In [69] is investigated the influence of shadow movement on the power characteristics. Thermal aspects are studied in [70]. A discrete I-V model presented in [71] a method to model and simulate the electrical behavior of shaded PV installations considering the shadow geometry. However, despite these important contributions, Fig. 3.1b shows experimental results where these proposed models can still be complemented to increase the model accuracy.

A typical partially shaded situation has been tested experimentally as shown in Fig. 3.1 and Fig. 3.1b. As shown in the experimental results of Fig. 3.1b, a reduced portion of shaded cell on PV module of Fig.3.1a has an important impact on the current-voltage characteristics. Additionally, the study of Bressan [11] shows that non-uniform shading has an important impact on PV performances despite the activation of by-pass diodes as shown in Fig. 3.2. In Fig. 3.2, from [11], an I-R thermography allows identifying the presence of a hot-spot area on a shaded PV cell increasing the cell temperature.

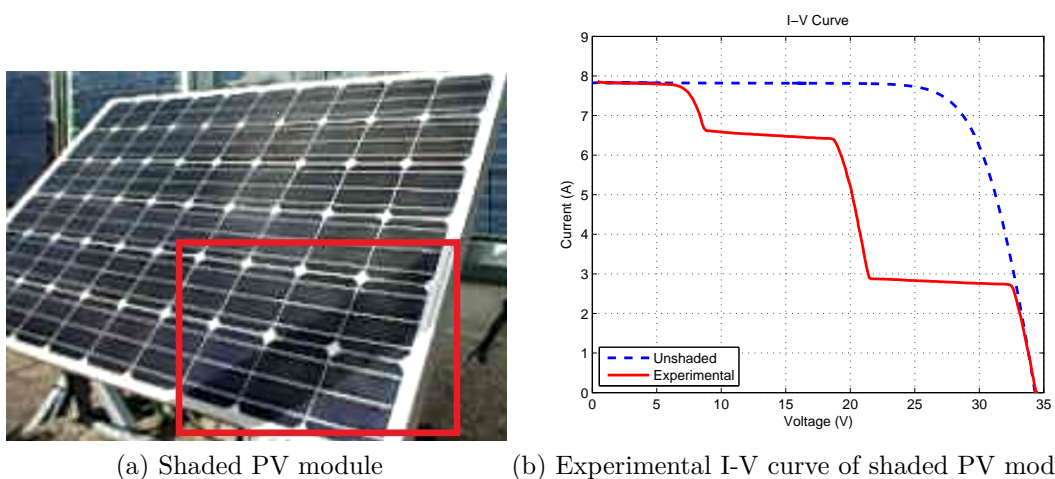


Fig. 3.1 Test of PV module under shaded condition

Most of PV models in the literature can represent all the I-V curve in normal condition or with the activation of the bypass diode. But to represent this pronounced slope characterizing the non-uniform shading condition is a real challenge for the

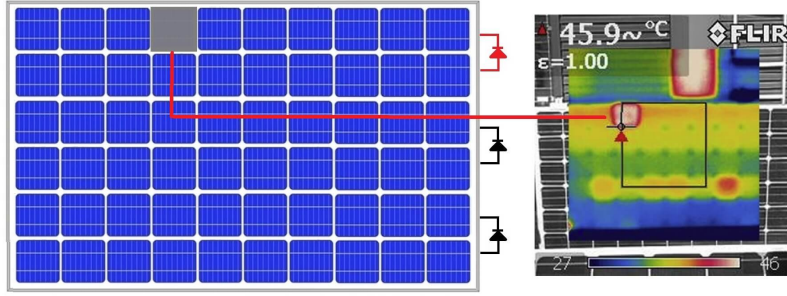


Fig. 3.2 Thermal impact of shaded cell

community. The first approach for the PV system modeling, the following subsection presents the conventional approaches consists in describing the behavior of PV modules under unshaded and shaded conditions. The second step deals with a new PV model taking into account geometric properties and optical properties of uniform and non-uniform shadows.

3.2.1 PV cell model for unshaded conditions

The PV cell behavior under unshaded conditions is described by eq.(3.1) using the single diode model [72], as shown in Fig. 3.3.

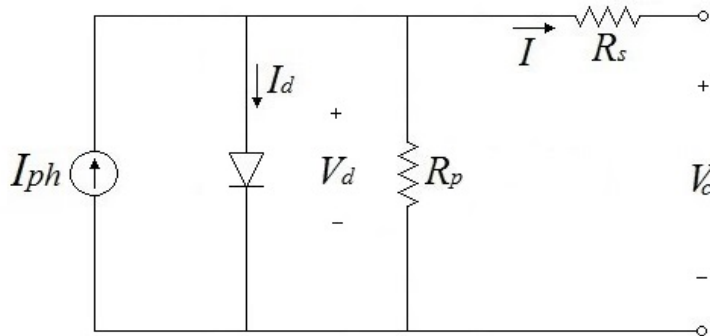


Fig. 3.3 Single diode PV cell model

$$I = I_{ph} - I_0 \left[e^{\left(\frac{V_c + IR_s}{V_t} \right)} - 1 \right] - \frac{V_c + IR_s}{R_p} \quad (3.1)$$

Where R_s is the series resistance associated to conductive losses, and R_p is the shunt resistance associated to distributed losses inside of the p-n material. I_0 is defined as the inverse saturation current, and V_t is the thermal voltage. I_{ph} is the photo-induced current given by eq.(3.2),

$$I_{ph} = I_{ph_{T_i}} = [I_{sc_STC} + (C_{T_i}(T_c - T_{STC}))] \frac{G_i}{G_{STC}} \quad (3.2)$$

Eq.(3.2) provides the expression for the totally illuminated photo-induced current $I_{ph_{T_i}}$ where G_i is the incident irradiance, C_{T_i} is the thermal current coefficient, and T_c is the cell temperature. I_{sc_STC} , T_{STC} , G_{STC} are the short circuit current, the cell temperature, and the incident irradiance for Standard Test Conditions (25°C, 1000W/m²).

3.2.2 PV cell model for shaded conditions

The PV model for unshaded conditions is well known accepted in PV system studies. However, a more detail analysis is also required due to shadows. This subsection presents the operation principles to describe the PV cell behavior for shaded operation conditions.

Totally shaded PV cells can be forced to carry current in reverse bias according to [65]. Consequently, a negative voltage can be produced in PV cell terminals and dangerous reverse current can increase. In reverse bias conditions, free electrons inside of the p-n material are able to gain enough energy to collide with atoms and separate other electrons [73]. After the collision, each new free electron can cause similar collisions, which lead to a sudden current multiplication or avalanching breakdown condition. Bishop in [65] describes this phenomena as a current multiplication effect modeled by eq.(3.3) in shaded PV cells using a nonlinear multiplier factor $M(V_d)$ associated with the shunt resistor current as shown in Fig. 3.4.

$$I = I_{ph} - I_0 \left[e^{\left(\frac{V_c + IR_s}{V_t} \right)} - 1 \right] - \frac{V_c + IR_s}{R_p} \left[1 + k \left(1 - \frac{V_c + IR_s}{V_b} \right)^{-n} \right] \quad (3.3)$$

Defining k as the fraction of current involved in avalanche breakdown, V_b as the breakdown voltage, and n as the avalanche breakdown exponent.

Shaded PV module and bypass diodes

PV cells connected in series build PV modules. Under shaded conditions, shaded cells can operate in reverse bias increasing the risk of structural failures [70]. Therefore, manufactures connect bypass diodes to groups of cells in order to avoid cell damages as shown in Fig. 3.5. However, despite by-pass diodes reverse bias cells can carry current

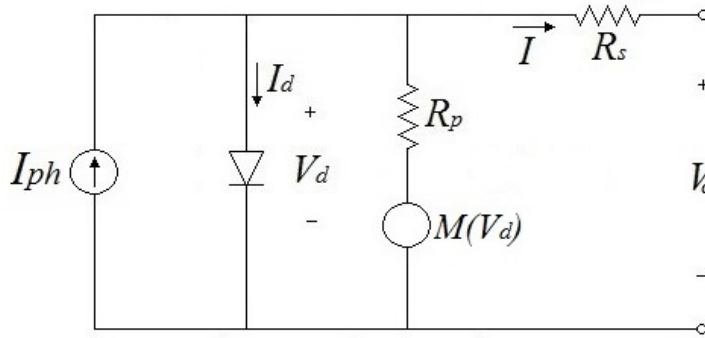


Fig. 3.4 Shaded PV cell electrical equivalent circuit

and the risk of structural failures can still arise [73], as shown in Fig. 3.2.

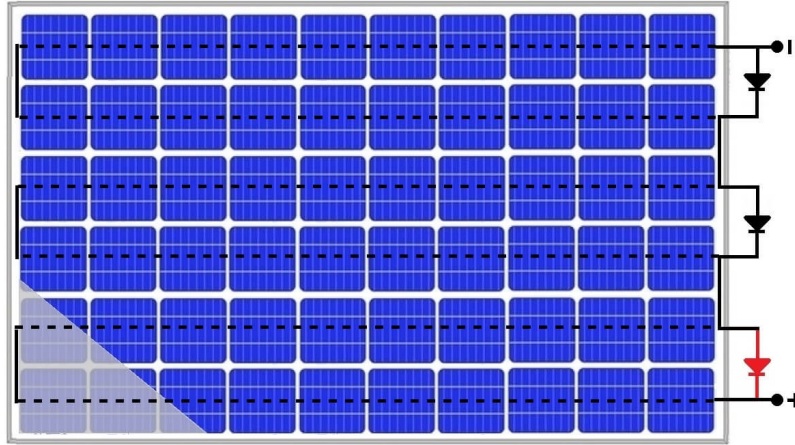


Fig. 3.5 PV module with bypass diodes

The group voltage V_G of PV cells connected to by-pass diodes is given by eq.(3.4),

$$V_{G_j} = \begin{cases} \sum_{i=1}^n V_{c_i} & \text{when } \sum_{i=1}^n V_{c_i} \geq 0 \\ V_{Bypass} & \text{when } \sum_{i=1}^n V_{c_i} < 0 \end{cases} \quad (3.4)$$

Then, Eq.(3.5) allows to evaluate the voltage of a PV module with m groups.

$$V_p = \sum_{j=1}^m V_{G_j} \quad (3.5)$$

The previous models describe the PV cell behavior under totally illuminated condition or totally shaded conditions. However, either geometric properties or optical properties of partial shadows have not been included. Models without these characteristics can lead to inaccurate results under actual partial shading conditions. Additionally, modeling methods that disregard the partial shadow characteristics are limited to describe other associated phenomena such as by-pass diode activation issues or hot spots due to localized partial shadows. The next subsection describes the proposed model of PV systems under partially shaded conditions.

3.3 Proposed partially shaded PV model

This section presents a more general model including shadow properties to increase the conventional model scope and to study other important phenomena in PV systems.

3.3.1 Partially shaded PV cell model

Partially shading cells have two main shadow features as shown in Fig. 3.6. The first feature is the shadow geometry represented by $a_s + a_i = 1$, where a_s is the percentage of shaded area, and a_i is the percentage of illuminated area. The second shadow feature is the optical property represented by the shadow transmittance τ and the shading factor S_f . The shadow transmittance is defined by the relation between the irradiance in the shaded area and the incident irradiance $\tau = G_s/G_i$ [69]. The shading factor S_f is defined by the shadow opacity where $0 \leq S_f \leq 1$ [74]. $S_f = 0$ means that the available irradiance shines on the PV cell. In contrast, $S_f = 1$ means that all available irradiance is blocked by the shadow. As a result, $S_f + \tau = 1$.



Fig. 3.6 Partially shaded PV cell

Diagram in Fig. 3.7a represents a schematic unshaded and shaded section of the partially shaded PV cell shown in Fig. 3.6. As shown in Fig. 3.7a, pairs electron-hole are generated when photons arrive to the p-n junction in the illuminated area. As a result, a photo-induced current I_{phi_i} is produced in the illuminated area. In contrast, less photons can arrive to the p-n junction in the shaded area ;then, less photo-induced current I_{phi_s} is produced. The total photo-induced current I_{phi_T} is given by eq.(3.6). The schematic circuit in Fig. 3.7b shows the proposed model for the photo-induced current.

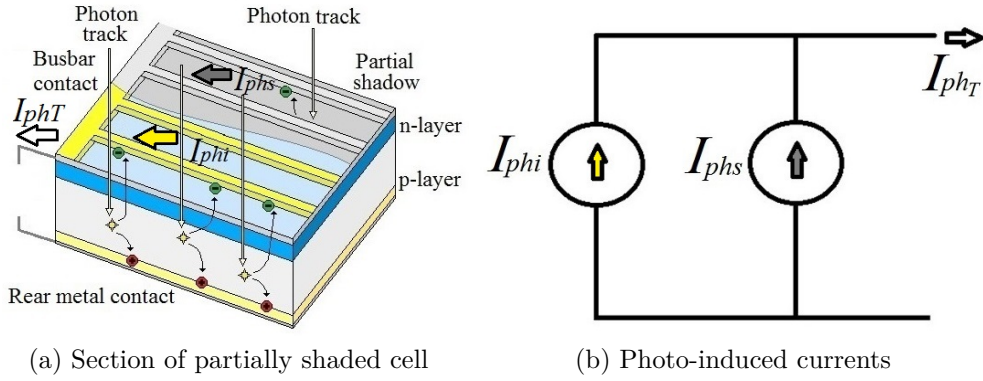


Fig. 3.7 Photo-induced currents in a partially shaded cell

$$I_{phi_T} = I_{phi_i} + I_{phi_s} \quad (3.6)$$

The current density definition $J = I/A$ allows the integration of shadow characteristics with PV cell electrical parameters. From definition of shadow transmittance τ , the relation between photo-induced current is given by $I_{phi_s} = \tau I_{phi_i}$ so, $J_{phi_s} = \tau J_{phi_i}$. Considering A_c as the total cell area,

$$J_{phi_T} A_c = J_{phi_i} A_i + J_{phi_s} A_s \quad (3.7)$$

thus,

$$J_{phi_T} = J_{phi_i} a_i + J_{phi_s} a_s \quad (3.8)$$

given that $I_{phi_T} = J_{phi_T} A_c$,

$$J_{phi_T} = J_{phi_i} a_i + \tau J_{phi_i} a_s \quad (3.9)$$

$$J_{phi_T} = J_{phi_i} (a_i + \tau a_s) \quad (3.10)$$

and solving to I_{ph_T} ,

$$I_{ph_T} = J_{ph_i} A_c (a_i + \tau a_s) \quad (3.11)$$

using the relations $S_f + \tau = 1$ and $a_s + a_i = 1$,

$$I_{ph_T} = I_{ph_{T_i}} (1 - a_s S_f) \quad (3.12)$$

Finally, it is necessary to define the shadow coefficient δ as $\delta = (1 - a_s S_f)$ where a_s is the shaded area and S_f is the shading factor. The photo-induced current is given by,

$$I_{ph_T} = I_{ph_{T_i}} \delta \quad (3.13)$$

where $I_{ph_{T_i}}$ is the photo-induced current for a totally illuminated PV cell given by eq.(3.2).

According to Bishop [65] and including I_{ph_T} , the eq.(3.3) is reformulated in eq.(3.14) and the equivalent circuit of Fig. 3.4 is depicted in Fig. 3.8.

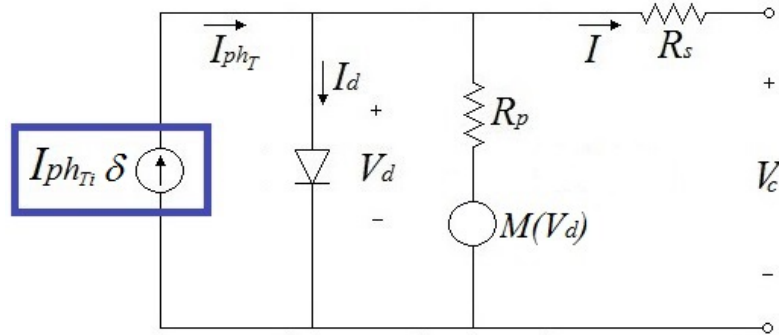


Fig. 3.8 Modified PV cell electrical equivalent circuit

$$I = I_{ph_{T_i}} \delta - I_0 \left[e^{\left(\frac{V_c + IR_s}{V_t} \right)} - 1 \right] - \frac{V_c + IR_s}{R_p} \left[1 + k \left(1 - \frac{V_c + IR_s}{V_b} \right)^{-n} \right] \quad (3.14)$$

Eq.(3.14) allows describing the influence of the shadow coefficient δ in the I-V curve and the power production.

3.3.2 Shadow coefficient analysis

As described previously, the shadow coefficient δ is expressed from relation between a_s and S_f . Given that $0 \leq a_s \leq 1$ and $0 \leq S_f \leq 1$. Thus; $0 \leq \delta \leq 1$. The following results

consider the behavior of δ between zero and one.

Fig. 3.9 shows the contribution of unshaded and shaded groups to the total I-V characteristic in a PV module. As shown in example of Fig. 3.9, the group with the shaded cell with the highest δ imposes the lowest contribution in the I-V curve.

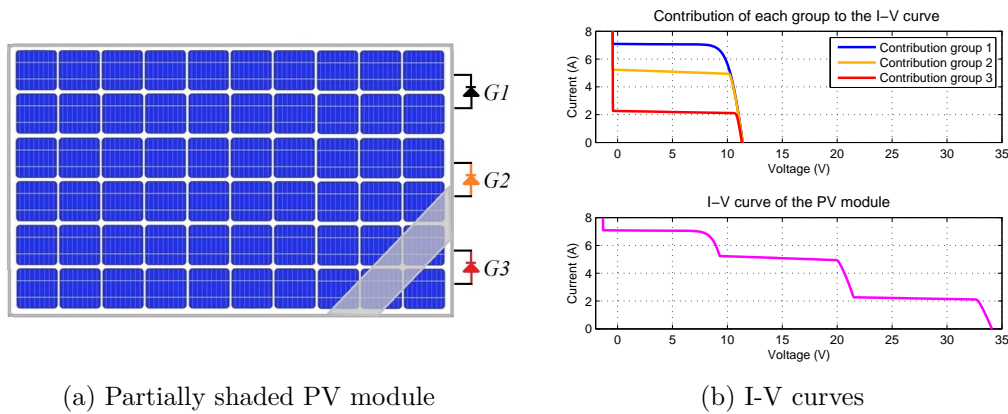


Fig. 3.9 Contribution of each group to the I-V curve

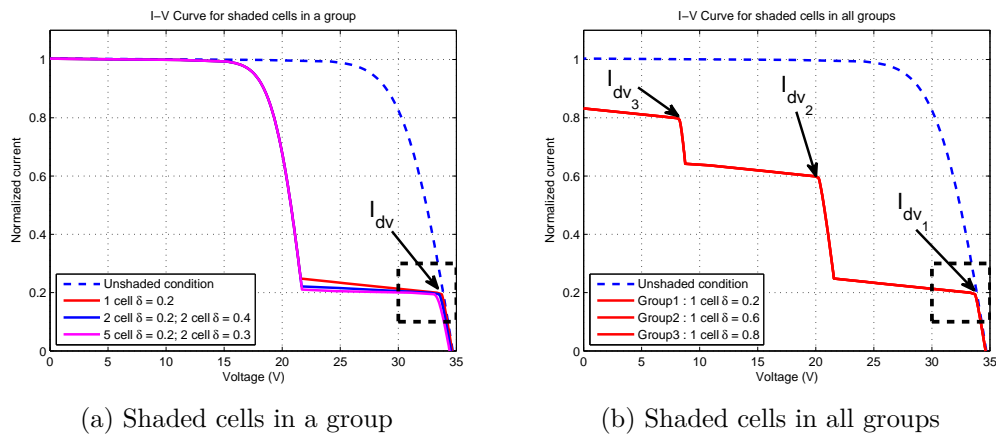


Fig. 3.10 Contribution of shaded cells to the I-V curve

Fig. 3.10 depicts the contribution of shaded cells to the changes in I-V curves. In Fig. 3.10, the PV module current is normalized in relation to the short circuit current in total illuminated condition I_{scT_i} . Fig. 3.10a represents a PV module with shaded cells in a single group.

Three cases are simulated in Fig. 3.10a. The first case simulates a single shaded cell with $\delta = 0.20$. The second case simulates two shaded cells with $\delta = 0.20$ and others two shaded cells with $\delta = 0.40$. In the third case, there are five shaded cells with $\delta = 0.20$ and two shaded cells with $\delta = 0.30$.

Results in Fig. 3.10a show that in a group with several shaded cells the shaded cell with the lowest δ causes the first divergence of current I_{dv} from the unshaded operation condition. Fig. 3.10a allows concluding that more shaded cells, with approximately the same lower value of δ , decrease the slope of the I-V curve. Results of Fig. 3.10b describe the PV module behavior when all groups have shaded cells. In this case, each divergence current I_{dv} in each group is associated to shaded cells with the lower δ . As an example, in Fig. 3.10b the first diverge of current I_{dv_1} is due to the group with $\delta = 0.20$. The second diverge of current I_{dv_2} depends on the group with $\delta = 0.60$, and the third diverge of current I_{dv_3} is produced by the group with $\delta = 0.80$. As a result, it is possible to conclude that each diverge current point I_{dv_m} is close to $I_{dv_m} = \delta_m I_{scTi}$ where δ_m is determined by the shaded cell with lowest shadow coefficient in the group.

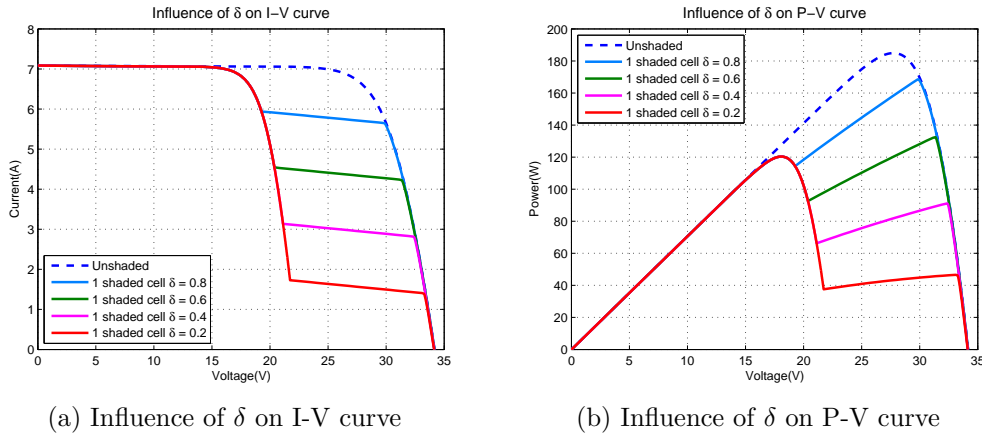


Fig. 3.11 Influence of δ in a PV module with a single partially shaded cell

Simulation results in Fig. 3.11a and Fig. 3.11b show that changes of δ in a single shaded cell produce important changes in current-voltage and power production features. Additionally, The partial shading phenomenon can produce power losses and cell overheating in spite of by-pass diode activation as shown in Fig. 3.12. This figure depicts the I-V characteristics of a group with one partially shaded cell and nineteen illuminated cells. In this case, the partially shaded cell has a shadow coefficient $\delta = 0.20$ and the by-pass diode is active. However, the shaded cell is forced to carry current in re-

verse bias and a power dissipation occurs as represented by the red rectangle in Fig. 3.12.

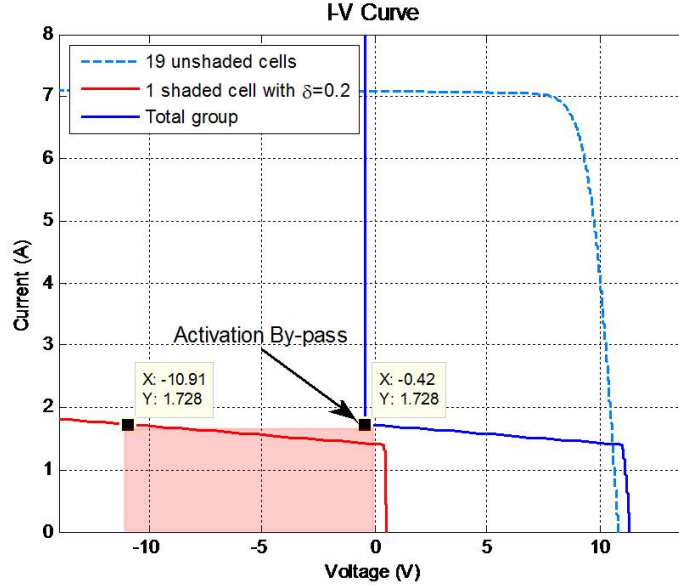


Fig. 3.12 Activation of by-pass diode in a group with a shaded cell and power dissipation of shaded cell

3.4 Experimental model validation

This subsection applies the analysis of the shadow coefficient to describe the behavior of PV modules with actual partial shadows and describes the setup experimental to validate the proposed model.

3.4.1 Photo-induced current test

Eq.(3.13) introduces the concept of shadow coefficient δ for linking the photo-induced current in partially shading conditions I_{phT} with the photo-induced current in total illuminated conditions I_{phT_i} . The following experimental procedure using a halogen lamp to light an isolated PV cell validates the proposed expression in eq.(3.13).

In this test a PV cell is covered by a material semi-transparent which emulates the shadow behavior with different orientations and proportions as shown in Fig. 3.13. The first step consists in measuring the short circuit currents in total illuminated condition I_{scT_i} and total shaded condition I_{scTS} . Next, eq.(3.13) in total shaded condition allows

to calculate the shading factor S_f considering $a_s = 1$ and $I_{ph} \approx I_{sc}$ according to eq.(3.15).

$$S_f \approx 1 - \frac{I_{scTS}}{I_{scTi}} \quad (3.15)$$

After, the short circuit currents are measured to partially shading condition for known shaded areas a_s and different orientations. Finally, the average of these measured currents is compared with photo-induced currents calculated by $I_{phT} \approx I_{scTi}(1 - a_s S_f)$. Table 3.1 summarizes these results showing that calculated photo-induced currents agree with measured short circuit currents for tested cases.

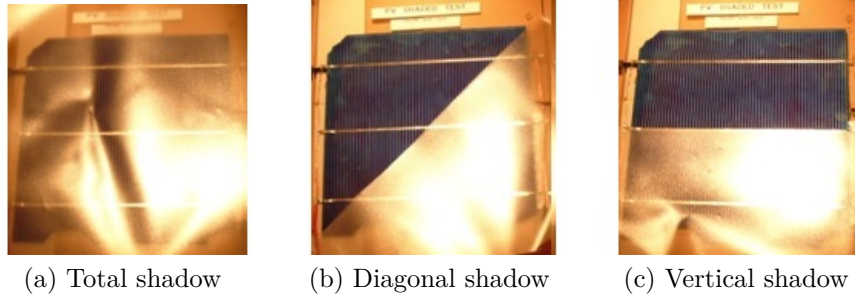


Fig. 3.13 Shaded PV cell test

Table 3.1 Test for photo-induced currents in shaded conditions

I_{scTS}	I_{scTi}	S_f	a_s	$I_{phT} calc.$	Average I_{scT}
0.285	0.380	0.25	0.75	0.309	0.310
			0.5	0.333	0.332
			0.25	0.356	0.355
1.891	2.525	0.251	0.75	2.050	2.051
			0.5	2.208	2.207
			0.25	2.367	2.368

These experimental results allow to validate the proposed model for photo-induced currents in partially shading conditions. Additionally, results show that the proposed expression $I_{phT} = I_{phTi} \delta$ is independent of shadow shape or orientation. The following experimental procedure takes into account these results to describe the behavior of partially shaded PV modules

3.4.2 Partially shading PV modules test

The following test aims to validate the proposed model on PV modules affected by partial shadows. In this experiment, two PV modules with intentional shadows on them are used to validate the proposed model. Characteristics of these PV modules are listed in Table 3.2. Fig. 3.14 describes the experimental setup. In this setup, an I-V curve tracer model MP-160 measures the current-voltage signals. A digital camera simultaneously records the shadow patron for further image processing. Additionally, a pyrometer model SP LITE detects the solar irradiance, and a thermographic camera is used to periodically monitor the PV module temperature.

The experimental test is explained as follows. First, the experimental setup stores measurements of I-V curves, solar irradiance, PV module temperature, and shadow patrons. Next registered information in first step is compared, and a specific shadow patron is selected to analysis. In this step, image processing methods are employed to measure the shaded cell areas for the selected shadow patron. After, the shadow coefficient δ_L is calculated for the PV cell with the largest shaded area a_{sL} using eq.(3.16). $I_{ph_{T_i}}$ in eq.(3.16) is calculated using eq.(3.2), and I_{dv} is measured from the first divergence current point in the I-V curve as shown in Fig. 3.17a.

$$\delta_L = \frac{I_{dv}}{I_{ph_{T_i}}} \quad (3.16)$$

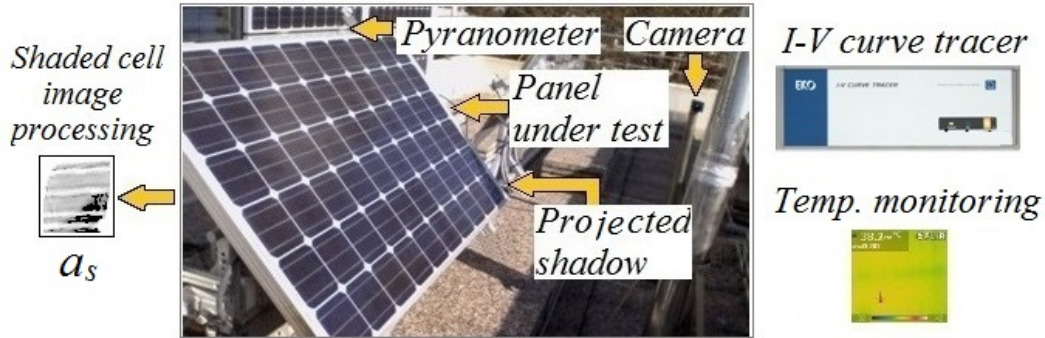


Fig. 3.14 Experimental setup

Then, the shading factor S_f is calculated in the PV cell with the largest shaded area replacing δ_L and a_{sL} in eq.(3.17)

$$S_f = \frac{1 - \delta_L}{a_{sL}} \quad (3.17)$$

Table 3.2 PV modules under test

Type Reference	Monocrystalline Tenesol TE 2200	Polycrystalline Yingli solar YL290p-35b
<i>Electrical parameters at STC</i>		
Max. Power (Pmax)	250Wp	290Wp
Voltage at Pmax (Vmp)	30.3V	35.8V
Current at Pmax(Imp)	8.3A	8.1A
Open circuit voltage (Voc)	37.3V	45.3V
Short circuit current (Isc)	8.6A	8.62A
<i>Thermal characteristics</i>		
Temp. coefficient of voltage	-129mV/°C	-149mV/°C
Temp. coefficient of current	4.4mA/°C	5.1mA/°C
<i>PV cell parameters</i>		
R_s	0.005Ω	0.007Ω
R_p	35Ω	45Ω
<i>Bishop model parameters</i>		
V_b	-30V	-17V
n	3.4	3.4
k	0.001	0.01

Finally, the shadow coefficients δ_n are calculated for each shaded PV cell considering their shading area a_{sn} and the same shading factor S_f for all shaded cells. These shadow coefficients are used to evaluate the I-V characteristics for the PV cells, the PV groups, and the PV module using eq.(3.4), eq.(3.5), and eq.(3.14). A conventional computational platform was used for these calculations.

Table 3.3 Shading factor PV module monocrystalline

	Case 1	Case 2
G_i	820W/m ²	910W/m ²
T_c	31°C	31°C
I_{phT_i}	7.07A	7.85A
I_{dv}	2.16A	2.7A
δ_L	0.31	0.34
a_{sL}	0.98	0.91
S_f	0.70	0.72

Table 3.4 Shading factor PV module polycrystalline

	Case 1	Case 2
G_i	710W/m ²	540W/m ²
T_c	31°C	30°C
$I_{ph_{T_i}}$	6.14A	4.67A
I_{dv}	1.33A	1.66A
δ_L	0.22	0.36
a_{sL}	0.97	0.90
S_f	0.8	0.71

The described procedure uses two types of shadows projected on the PV modules. The first type of shadow covers cell in all groups as shown in Fig. 3.15a and Fig. 3.16a. The second type of shadow covers a cell in a group and partially one cell of another group as shown in Fig. 3.15b and Fig. 3.16b. Table 3.3 summarizes the parameters and values to calculate the shading factor for shadows on the PV module Tenesol 2200 monocrystalline. Table 3.4 shows the values to evaluate the shading factor on the PV module Yingli YL290p-35b polycrystalline. Table 3.5 and Table 3.6 record shaded areas a_s for each studied case after image processing. Cells in Table 3.5 and Table 3.6 are enumerated according with their relative position in the PV module. For instance, cell C2.8 corresponds to the cell in the second row and eighth column as shown in Fig. 3.15a. Calculated shadow coefficients δ are also written in Table 3.5 and Table 3.6. Experimental and calculated I-V curves are depicted in Fig. 3.17 and Fig. 3.18.

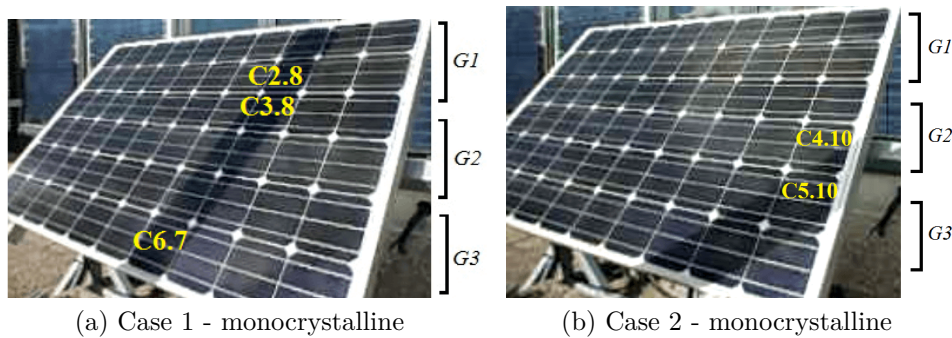


Fig. 3.15 Experimental test for monocrystalline PV module

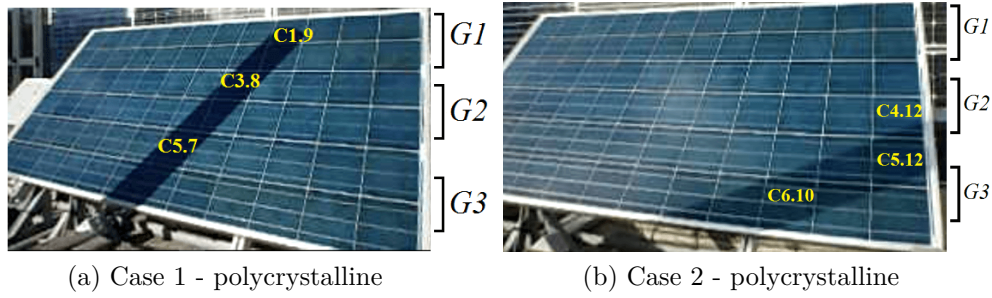


Fig. 3.16 Experimental test for polycrystalline PV module

Discussion of results

Results show that the shadow coefficient δ , which depends on shaded areas a_s and S_f , is directly associated with I-V curve changes. The PV cell with the lowest δ in the PV module causes the lowest divergence current point in the I-V curve. For instance, the cell 6.7 of group 3 for *case 1 - Monocrystalline* imposes the first divergence point in the I-V curve as shown in Table 3.5 and Fig. 3.17a. In *case 2 - Monocrystalline*, the lowest point is imposed by the C5.10 as shown in Table 3.5 and Fig. 3.17b.

Table 3.5 Shading area and shadow coefficient for PV module TE 2200

Group	Cell	<i>Case 1</i>		<i>Case 2</i>		
		a_s	δ	Cell	a_s	δ
1	C1.8	0.94	0.34			
	C2.8	0.96	0.33			
2	C3.7	0.17	0.88	C4.10	0.25	0.82
	C3.8	0.80	0.44			
	C4.7	0.40	0.72			
	C4.8	0.50	0.65			
3	C5.7	0.80	0.44	C5.9	0.35	0.75
	C5.8	0.20	0.86	C5.10	0.91	0.34
	C6.7	0.98	0.31	C6.8	0.40	0.72
				C6.9	0.89	0.37
				C6.10	0.15	0.89

Results also confirm that shaded cells with less shaded area in comparison with shaded cells with larger shaded area in the same group have a negligible contribution to the I-V curve. For instance, cells C3.9, C5.6, C5.8 in *case 1 - polycrystalline*, and cells C5.10, C6.8, C6.11 in *case 2 - polycrystalline* have a minimum impact on I-V results of

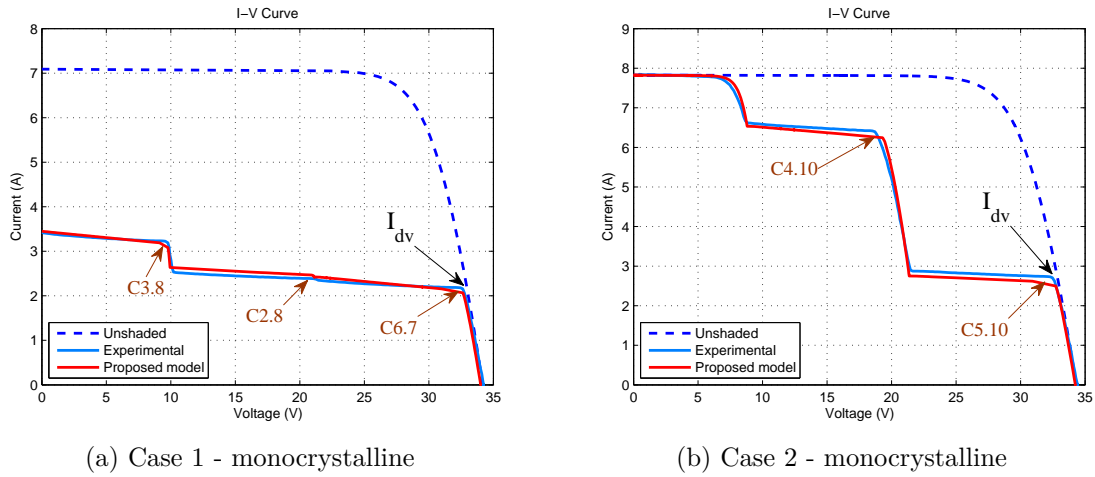


Fig. 3.17 I-V curves for test of monocrystalline PV module

Table 3.6 Shading area and shadow coefficient for PV module YL290p-35b

Group	Cell	<i>Case 1</i>		<i>Case 2</i>		
		a_s	δ	Cell	a_s	δ
1	C1.9	0.68	0.46			
	C2.8	0.64	0.49			
	C2.9	0.66	0.47			
2	C3.8	0.96	0.23	C4.12	0.19	0.86
	C3.9	0.11	0.91			
	C4.7	0.65	0.48			
	C4.8	0.65	0.48			
3	C5.6	0.10	0.92	C5.10	0.21	0.85
	C5.7	0.97	0.22	C5.11	0.80	0.43
	C5.8	0.11	0.91	C5.12	0.90	0.36
	C6.6	0.65	0.48	C6.8	0.22	0.84
	C6.7	0.65	0.48	C6.9	0.78	0.45
				C6.10	0.90	0.36
				C6.11	0.37	0.74

Fig. 3.18. In contrast, partially shaded cells with relative small shaded area are able to transform the I-V curve if they have the lowest shaded areas in the group. Examples of this behavior are shown in Fig. 3.17b and Fig. 3.18b where cells C4.10 in *case 2 - monocrystalline* and C4.12 in *case 2 - polycrystalline* are able to change the I-V curve.

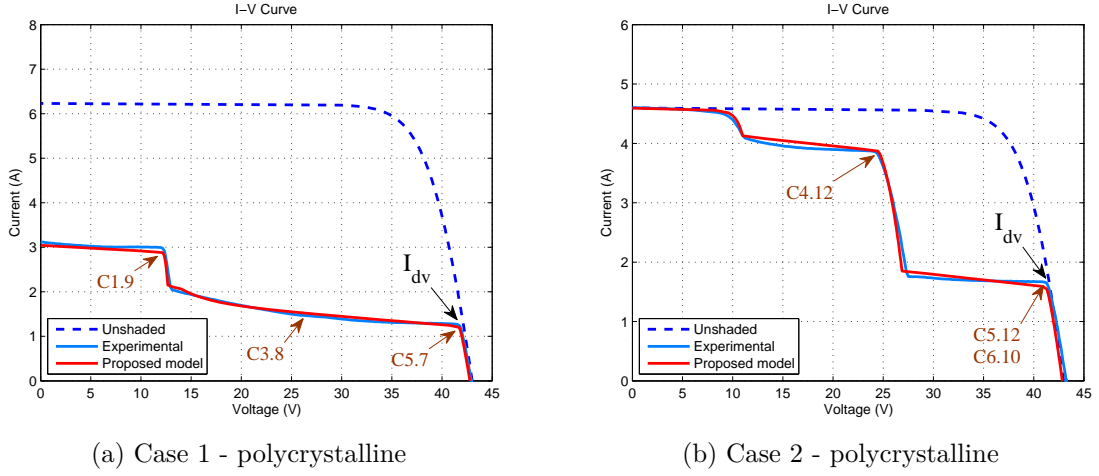


Fig. 3.18 I-V curves for test of polycrystalline PV module

Fig. 3.17a and Fig. 3.18a shows that groups of shaded cells with shadow coefficients close to the lowest shadow coefficient cause I-V curves with lower slope. As an example, cells C1.9, C2.8, and C2.9 of *case 1 - polycrystalline* produce less slope than the equivalent cell C3.8 in *case 1 - monocrystalline*. As a result, PV cells with partial shadows non-uniform distributed have more by-pass diode activation problems and generate higher temperatures.

Finally, the Mean Square Error (MSE) is used to compare the experimental results and the proposed model as shown in Table 3.7. MSE table shows that proposed model is suitable to explain the current-voltage behavior of PV modules under partially shading conditions. Results also demonstrate that the proposed partially shaded PV model is applicable to monocrystalline and polycrystalline technologies.

$$MSE = \frac{1}{n} \sum_{i=1}^n (e_i)^2 \quad (3.18)$$

Table 3.7 Mean Squared Error (MSE) for proposed model

	Monocrystalline		Polycrystalline	
	Case 1	Case 2	Case 1	Case 2
MSE	0.92%	1.07%	0.89%	1.01%

3.4.3 Comparison with other modeling approaches

Most of approach reported in literature disregard either the partial shaded area a_s or the shading factor S_f . However, disregard these shadow characteristics can lead to inaccurate results when the conventional models are compared with PV modules in actual partial shading conditions. Fig. 3.19 shows the experimental results of *case 1 - monocrystalline* compared with the proposed model and with other two approaches. The first approach disregards the shading area and assumes the cells totally shaded or unshaded [6]. The second approach takes into account the shaded area [71]. However; this approach overlooks the shading factor influence. Fig. 3.19 depicts the comparison with other methods to describe the current-voltage and power-voltages behavior. These figures show that disregard the shadow features can cause significant errors and lost of accuracy.

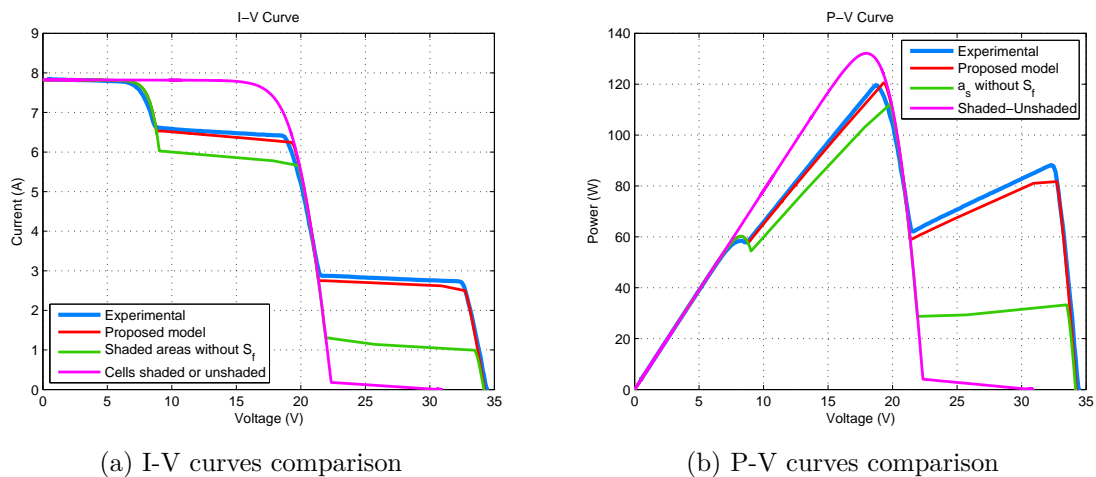


Fig. 3.19 Comparison of PV models

Additionally, methods reported in literature such as [75] and [38] suggest groups with cells under irradiance non-uniform. However, these methods do not specify a methodology to quantify this irradiance non-uniform. Finally, methods that disregard the partial shadow characteristics are limited to describe other associated phenomena such as by-pass diode activation issues or hot-spots due to localized partial shadows.

3.5 Simulation of PV generation architectures

Taking into account previous results, the proposed model is extended to PV generation systems connected in centralized and decentralized architectures according to description presented in *section 2.2.2*. Fig. 3.20 shows the PV modules simulate in centralized and decentralized PV generation architectures. PV modules in simulations have partially shaded PV cells as shown in Fig. 3.20.

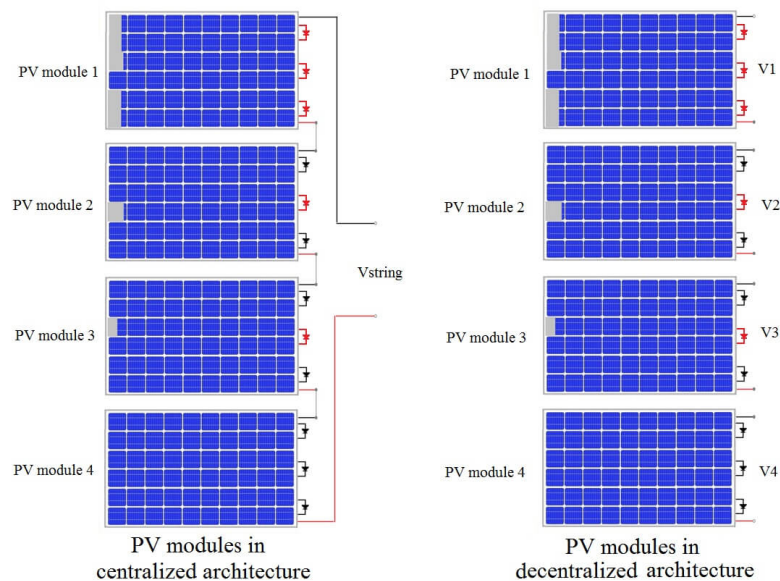


Fig. 3.20 Partial shading patron on centralized and decentralized architectures

Simulation results in Fig. 3.21 shows the total current-voltage behavior caused by the partial shadows and bypass diodes activation in a centralized architecture. In Fig. 3.21 also is compared the I-V curve for shaded and unshaded cases. In addition, Fig. 3.22 depicts the power production for this study case. In decentralized architecture PV modules have the same shadow patron of centralized case, but in this case each PV module is able to follow their own Maximum Power Point. Fig. 3.23 presents the I-V curve for each PV module with the same partial shadow patron, and power production is represented in Fig. 3.24.

Table 3.8 summarizes the total power production for decentralized and centralized structures. In centralized case, the maximum power production is given by the higher Maximum Power Point. In contrast, total power production P_{TD} for decentralized case with n PV modules is given by the contribution of the higher Maximum Power Point

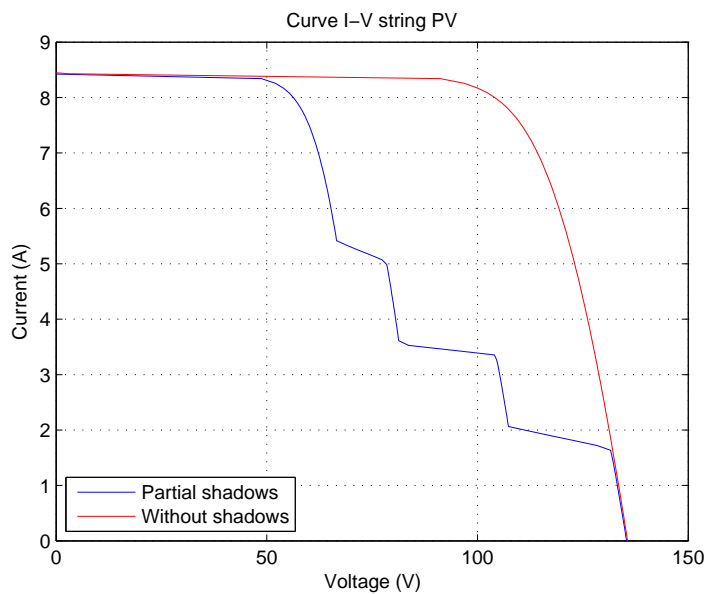


Fig. 3.21 Total I-V curve in centralized architecture

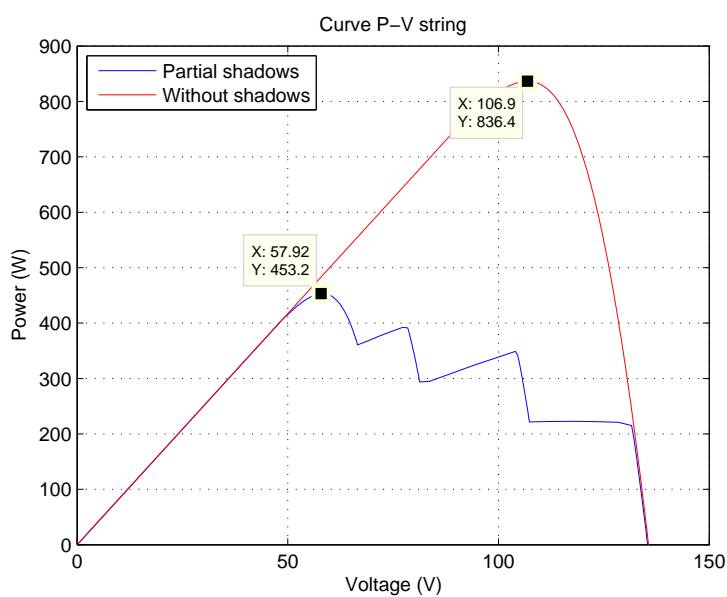


Fig. 3.22 Total P-V curve in centralized architecture

P_{Hi} of each i th PV module. Thus, total power production P_{TD} for decentralized case is defined by eq.(3.19).

$$P_{TD} = \sum_{i=1}^n P_{Hi} \quad (3.19)$$

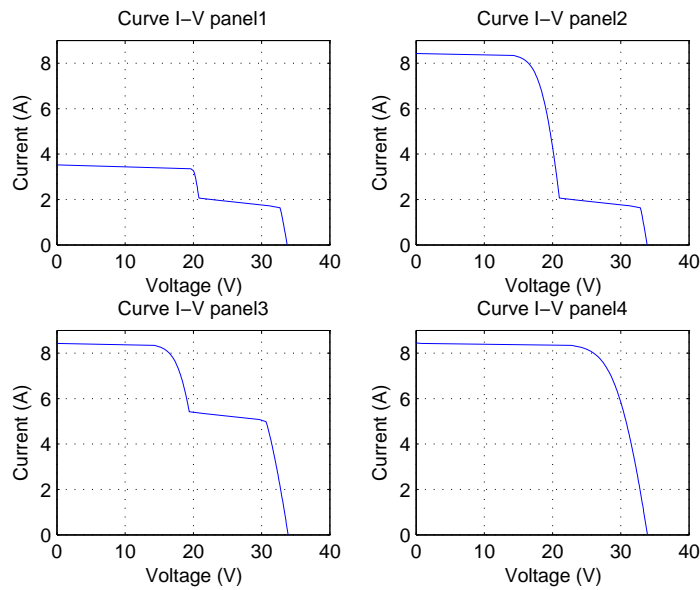


Fig. 3.23 I-V curve of each panel in decentralized architecture

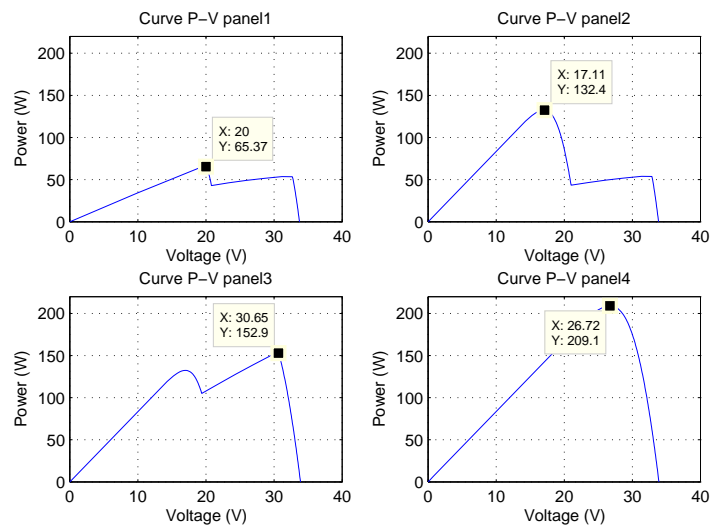


Fig. 3.24 P-V curve of each panel in decentralized architecture

Results show that the decentralized PV generation structure increase the power production in comparison with the centralized case. These results agree with other studies reported in literature such as the work presented in [22]. As consequence, decentralized PV generation structures show better performance in comparison with centralized structures.

Table 3.8 Comparison of power in centralized and decentralized architectures

Architecture	Maximum power (W)	(%) Max power unshaded case
Centralized	453.2	54.18
Decentralized	559.42	66.88
<i>Unshaded case</i>	<i>836.4</i>	-

However, in spite of improving the power production due to the decentralized PV generation, the power electronics stage in decentralized PV systems, *section 2.2.2*, could decrease the global PV system efficiency. This impact on global efficiency is given by the high voltage elevation ratios and the increasing number of power converters according to the comprehensive study addressed by Picault in [22]. In this study presented by Picault, the author also highlight that despite these disadvantages many advantages of this decentralized architecture should be taking into account. According to this line of reasoning, next chapter will be devoted to the study and modeling of this versatile power converter known as *Boost inverter* able to achieve the requirements of adaptability, performance, and reliability in current integration of decentralized PV systems in microgrids.

3.6 Conclusion

This chapter, presents a methodology to increase the accuracy and scope of conventional modeling approaches of PV systems. The main contribution of this approach is to define a simplify relation denominating shadow coefficient δ suitable to describe the complex behavior of PV modules under partially shading conditions. In addition, results analysis allows identified interrelations between shadow patrons and current-voltage changes in partially shaded conditions. Results have shown that conventional approaches which can disregard shadow characteristics such as shaded area or shading factor can lead to inaccurate results when models are compared with PV systems under actual partial shadows. This chapter described the PV generator behavior under shaded and unshaded conditions. Modeling methodology was extended to PV centralized and decentralized architectures. Results and studies about centralized and decentralized architectures showed that the better performance is achieved by the decentralized case. The following chapter will address the modeling and study of a power converter topology for decentralized architectures known as Boost inverter, and its integration to PV generation systems.

Chapter 4

Development of Boost Inverter Model for PV Applications in Microgrids

Contents

4.1	Introduction	52
4.2	Component-based approach for modeling Boost converter topologies	54
4.2.1	State of the art Boost inverter modeling	54
4.2.2	Proposed approach for modeling Boost converter topologies	58
4.2.3	Validation of modeling methodology	66
4.3	Boost inverter modeling	75
4.3.1	Mathematical framework for the Boost inverter	75
4.3.2	Component-based approach for Boost inverter modeling . .	78
4.3.3	Experimental setup to validate the modeling approach . .	81
4.4	Modeling of Boost inverter integration in Microgrids . . .	86
4.4.1	The Boost inverter grid-connected model	86
4.4.2	Boost inverter for integration of PV systems in microgrids .	89
4.5	From component-based modeling to a multiple hierar- chic level approach	91
4.6	Conclusion	92

4.1 Introduction

Discussion of *chapter 2* argued that PV generation is a promising alternative energy resource able to be integrated in current electrical grids. However, in *chapter 3* has been shown that PV systems can be drastically affected by external factors such as partial shadows. Results of *chapter 3* also remark that relative small shadows can affect the entire power production chain in centralized PV structures because PV modules are interconnected in series and faults are propagated through the power production chain [21].

Furthermore, comparison of centralized and decentralized PV generation topologies in *chapter 3* has shown that the performance of decentralized cases is higher than centralized configurations[22][23]. However, power electronics stage in decentralized architectures can increase the power system complexity and decrease the overall efficiency because the higher elevation ratio [22]. In this context, current research challenges arise to study and model innovative topologies able to overcome the disadvantages of decentralized topologies and take advantages of their characteristics. Therefore, conventional micro-inverter architectures based on two-stages topologies, Boost-Buck DC-DC / DC-AC converters, have been studied and widespread in the literature [24][25]. However, other micro-inverter architectures with higher efficiency and reliability based on the Boost inverter topologies are less reported in literature[26].

Micro-inverters based on the Boost inverter topology show more adaptable characteristics [27], higher reliability [28], scalability properties [23], and single-stage grid-connected features using less power electronics devices [29][30]. Therefore, taking into account the advantages of decentralized architectures and the promising perspectives of the Boost inverter in PV power systems [23], this chapter will present the study and modeling of this converter in order to contribute to the knowledge about its integration in PV systems (see Fig. 4.1).

This study develops a component-based methodology to model power converters applied to the Boost converter and Boost inverter topologies. The proposed component-based modeling methodology is intended to model the power converter as a building block which interacts with its environment through coupling stages. This approach allows modeling power converters with a high degree of detail disregarding the influence of changes in the power source and load models. As a consequence, these generated models of Boost inverter and Boost converter can be integrated with other models

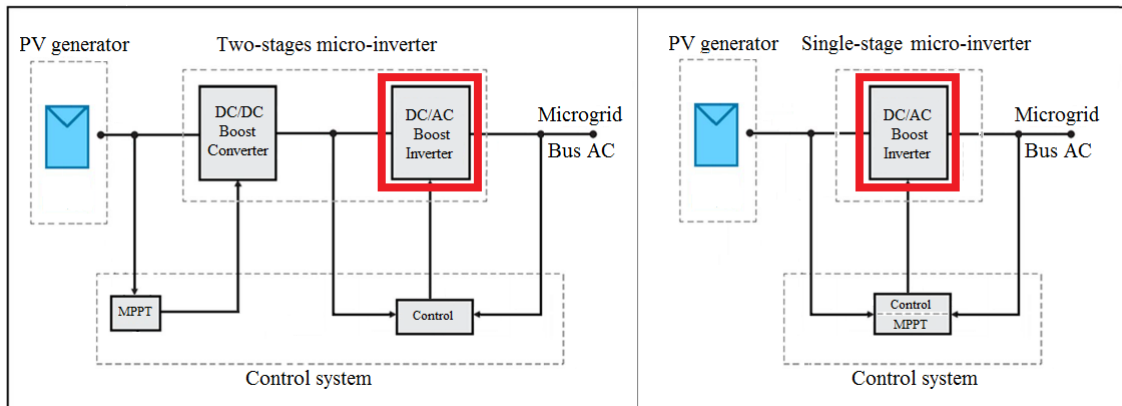


Fig. 4.1 Two-stages and single-stage micro-inverters based on the Boost inverter for integration of PV systems.

to generate more complex structures suitable for power system modeling in microgrids which are composed by several types of power sources, power converters, and loads.

This proposed modeling methodology is intended to real-time emulations in embedded hardware because the inherent advantages of current real-time emulation for the study of integration of power systems in microgrids [31][32]. Real-time emulations allow evaluating the power converter performance closer to actual operation conditions [3]. Indeed, real-time emulations of PV systems in microgrids are able to study the interaction of power converters and PV generators in normal and fault conditions [33]. These studies and tests can be developed in a secure environment without hazard damage on equipments and users [4]. In further chapters, this proposed modeling methodology will be employed for real-time emulations of Boost inverters in PV systems.

This chapter presents the modeling and study of micro-inverters based on the Boost inverter topology. The first part presents the fundamental concepts about micro-inverters topologies and introduces the proposed component-based modeling methodology. Then, the proposed methodology is applied to the unidirectional and bidirectional Boost converter modeling. Next, the boost inverter is modeled from the interaction of bidirectional Boost conventional model, and the experimental results are presented to validate the proposed modeling methodology. Finally, a study of Boost converter and Boost inverter association is presented. In the last section also the model of integration of the micro-inverter to the grid is developed.

4.2 Component-based approach for modeling Boost converter topologies

The Boost inverter is a power electronics converter which is part of a family of inverters formed by two DC/DC converters coupled in differential output voltage, as shown in Fig. 4.2. The Boost inverter is a transformerless power converter which provides a boosting AC output voltage from two individual bidirectional DC-DC Boost converters [34]. Fig. 4.3 shows the operation principle of this inverter. When the bidirectional Boost converters produce DC biased sinusoidal output signals 180° phase-shifted, the differential output is an AC output voltage.

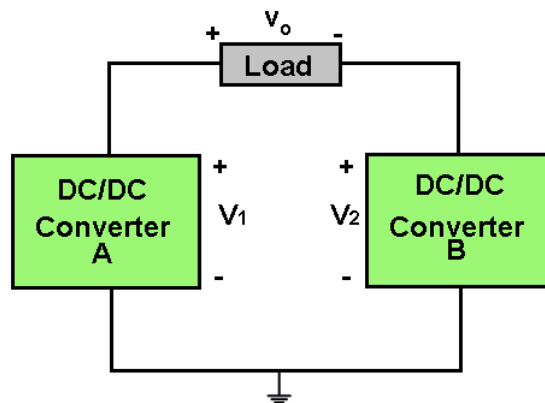


Fig. 4.2 Inverter based on DC/DC converters.

The great variety of potential applications of Boost inverters and Boost converters in microgrids (e.g. Fig. 4.4) and their interactions lead to develop modeling strategies to study the impact of these converters on the integration of PV systems in microgrids. These modeling research challenges are specially visible in application of real-time emulation where modeling of Boost inverters for real-time applications is less known in literature. Given the advantages of real-time emulation for the study of integrated systems in microgrids[31], the theoretical concepts of the proposed methodology are presented and validated in this section and implemented in embedded hardware in further chapters.

4.2.1 State of the art Boost inverter modeling

The state of the art about modeling of Boost inverter is focused on oriented-control approaches. Fig. 4.5 shows the basic circuit topology of a Boost inverter studied

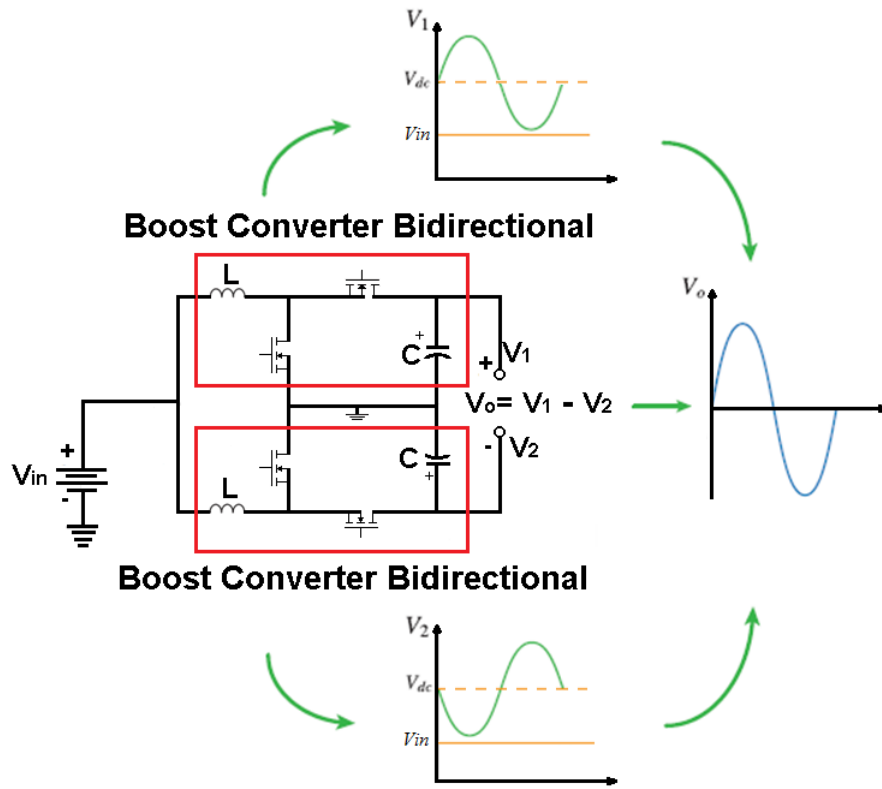


Fig. 4.3 Operation principle of Boost inverter.

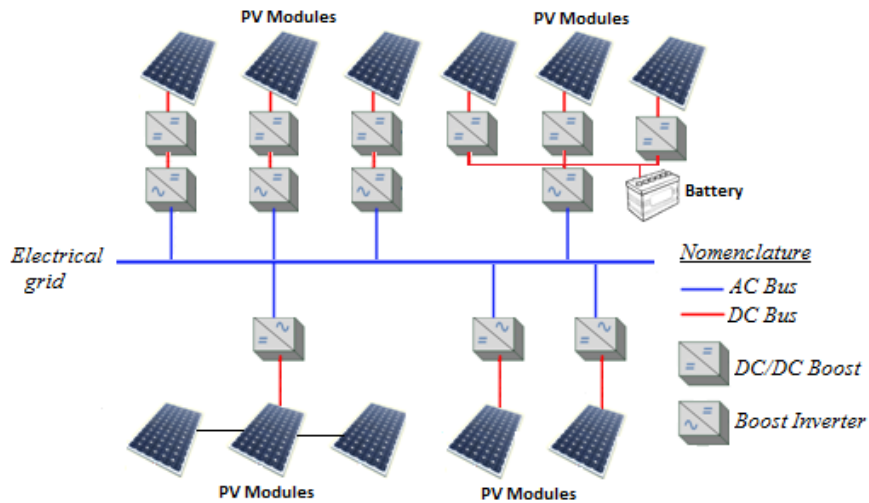


Fig. 4.4 Potential application of Boost inverters in microgrids.

in literature. Fig. 4.6 summaries relevant Boost converter models reported in literature.

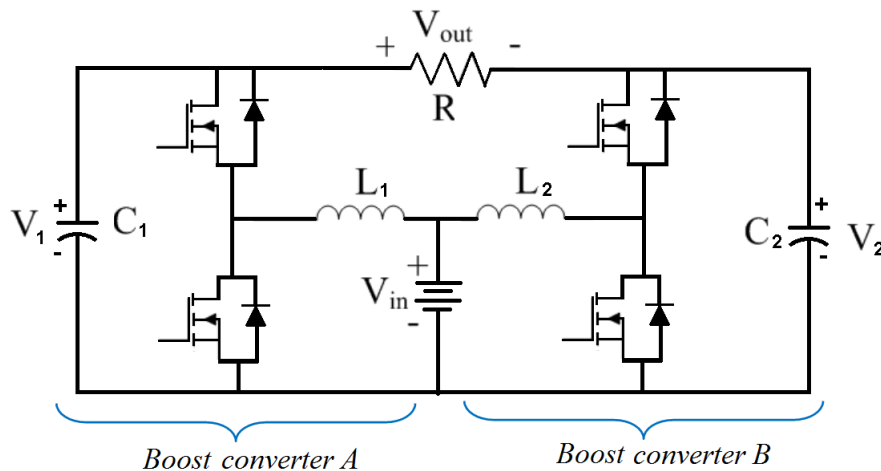


Fig. 4.5 Boost converter basic circuit.

Model I presented in [26] considers for analysis half Boost inverter coupled with a fixed source which represents the other Boost inverter half. This approach simplifies the analysis; however, dynamic of half inverter is disregarded. Caceres et al. introduce *Model I* to design a slide-mode control on each Boost inverter leg. *Model II* is proposed in [34] to study the control to output transfer function for frequency domain analysis in order to evaluate the Boost inverter stability. Authors of *Model III* in [76] assume the Boost inverter operating with two complementary control signals; then, two circuit configurations are obtained. In *Model III* the corresponding state equations in compact form are given, and the second method of Lyapunov is used as a stability criterion.

Model I to *Model III* represent the Boost inverter without grid connection. In contrast, *Model IV* and *Model V* are formulated to grid-connected applications. According to [77], *Model IV* can express the Boost inverter dynamic behavior using a simplified average model. AC operation of *Model IV* is simplified by means of a generic equivalent circuit of a grid-connected inverter linked to the AC grid through a lossless inductor. This model is intended to study the harmonic input current impact on the Boost inverter. Finally, *Model V* in [29] introduces a converter bilinear model obtained from the state-space model considering the grid connection and the switch action which enable or disable a given circuit topology. *Model V* is formulated to design a slide-mode current control for a Boost inverter grid-connected.

Table 4.1 summarizes a comparison of proposed models in literature. Information in Table 4.1 shows that proposed models are intended to control design. Most of them

<i>Model</i>	<i>Equivalent circuit</i>	<i>Partial model equations</i>
I		$\begin{bmatrix} \frac{di_{L_1}}{dt} \\ \frac{dV_1}{dt} \end{bmatrix} = \begin{bmatrix} \frac{-R_1}{L_1} & \frac{-1}{L_1} \\ \frac{1}{C_1} & \frac{-1}{C_1 R_1} \end{bmatrix} \begin{bmatrix} i_{L_1} \\ V_1 \end{bmatrix} + \begin{bmatrix} \frac{V_1}{L_1} \\ -\frac{i_{L_1}}{C_1} \end{bmatrix} \gamma + \begin{bmatrix} \frac{V_{in}}{L_1} \\ \frac{V_2}{C_1 R_1} \end{bmatrix}$
II		$\begin{cases} Z_a(s) = \frac{I_a S L - V_a (1-D)}{(1-D)^2 + S^2 C L} \\ Z_b(s) = \frac{S L}{R(1-D)^2 + S^2 C L} \end{cases}$
III		$\begin{cases} \frac{di_{L_1}(t)}{dt} = \frac{V_g}{L} - \frac{(1-u(t))}{L} v_1(t) \\ \frac{di_{L_2}(t)}{dt} = \frac{V_g}{L} - \frac{u(t)}{L} v_2(t) \\ \frac{dv_1(t)}{dt} = \frac{(1-u(t))}{C} i_{L_2}(t) - \frac{v_1(t) - v_2(t)}{r_o C} \\ \frac{dv_2(t)}{dt} = \frac{v_1(t) - v_2(t)}{r_o C} + \frac{u(t)}{C} i_{L_2}(t) \end{cases}$
IV		$\begin{cases} v_{in} - v_{L1} = (1-d) v_{o1} \\ i_{c1} + i_{o1} = (1-d) i_{L1} \\ i_{c1} = C_1 \omega \frac{V_g}{2} \cos(\omega t + \delta) \\ i_o = I_o \sin(\omega t + \alpha) \end{cases}$
V		$A_U = \begin{bmatrix} 0 & 0 & \frac{u-1}{L_1} & 0 & 0 \\ 0 & 0 & 0 & \frac{-u}{L_2} & 0 \\ \frac{1-u}{C_1} & 0 & 0 & 0 & \frac{-1}{C_1} \\ \frac{u}{C_2} & 0 & 0 & 0 & \frac{1}{C_2} \\ 0 & 0 & \frac{1}{L_3} & \frac{-1}{L_3} & \frac{-r}{L_3} \end{bmatrix} B = \begin{bmatrix} \frac{V_{in}}{L_1} \\ \frac{V_{in}}{L_2} \\ 0 \\ 0 \\ \frac{-V_{ac}}{L_3} \end{bmatrix}$

Fig. 4.6 Boost inverter models reported in literature.

simplified the Boost inverter behavior and use linear approaches. In contrast, the Boost inverter behavior is not linear and switched. Additionally, proposed models disregard the influence of conductive losses on inductors and switching devices. However, these characteristics have an important effect on efficiency and gain of actual power

converters [78]. Another drawback of most of proposed models in literature is the lack of scalability because these models are formulated for specific cases and applications. Then, these models should be updated when operation condition changes. For instant, change in either the type of load or the power source requires significant changes in the model increasing the analysis complexity. These features represent a significant disadvantage in real-time emulations of microgrids which requires the study of several scenarios with constant changes in the converter environment.

In this context, next section presents a component-based approach to model the Boost inverter and the Boost converter as a building blocks intended to further real-time emulations in embedded hardware. This methodology explores characteristics of adaptability, scalability, and model integration suitable for power system modeling in microgrids which are composed by several types of power sources, power converters, and loads.

4.2.2 Proposed approach for modeling Boost converter topologies

This section develops a component-based methodology to model power converters applied to the unidirectional and bidirectional Boost converter topologies. The proposed component-based modeling methodology is intended to model the Boost converters as building blocks which interact with their environment through coupling stages as shown in Fig. 4.7.

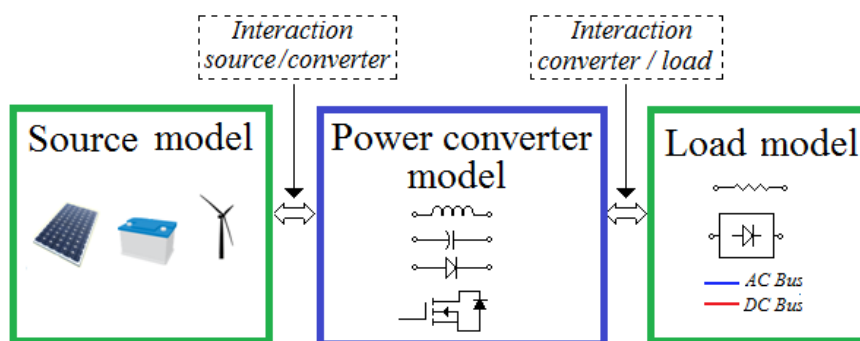


Fig. 4.7 Component-based modeling method.

Model- Ref.	Modeling method	Application given by authors	Grid Con.	Advantages	Disadvantages
<i>I-</i> [26]	Simplified half Boost inverter	Independent slide-mode control design of each Boost inverter leg.	Non	Simplify analysis	Dynamic of half inverter is disregarded. Model without losses.
<i>II-</i> [34]	Control to output transfer function	Frequency domain analysis. Control design.	Non	Simplify analysis. Sta- bility studies. Design in the Laplace domain.	Synchronization of switches is required. Model without losses. The model only considers per- turbation in the duty cycle.
<i>III-</i> [76]	State-space representation from two operation states	Sliding-mode control design for entire Boost inverter. Lyapunov method applied for stability analysis.	Non	Design of control sys- tem taking into account the dynamic behavior of whole inverter. Stability studies.	Synchronization of switches is required. Model with- out losses. Changes in the type of load increase the model complexity.
<i>IV-</i> [77]	Simplified average circuit model for half Boost inverter. AC operation modeled by a generic AC source grid- connected.	Study and mitigation of harmonics in the input current.	Yes	Simplify analysis. Inverter grid- connection studies. Harmonic analysis.	Model analysis is oriented to- ward harmonic analysis; how- ever, other dy- namics are not considered.
<i>V-</i> [29]	State-space considering the grid connection.	Slide-mode current control for a Boost inverter grid- connected.	Yes	Complete model. inverter grid- connection.	Model com- plexity in- creases con- siderably if conductive losses are included.

Table 4.1 Comparison of modeling methodologies.

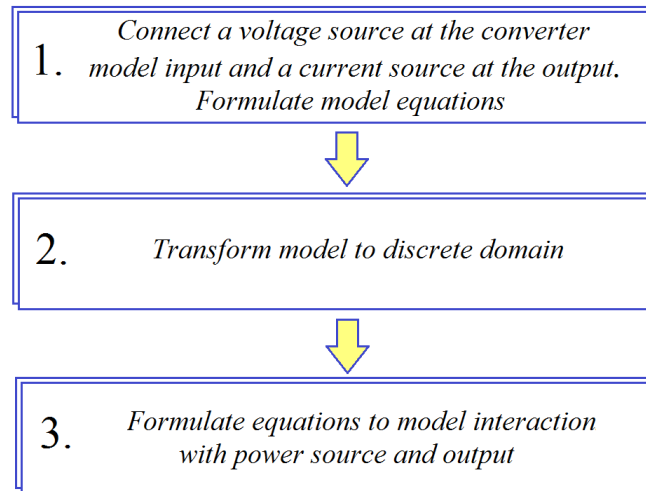


Fig. 4.8 Steps for proposed modeling method.

Fig. 4.8 summarizes the steps for the modeling methodology. In the first step, the source power model is replaced by a virtual voltage source and the load model is replaced by a virtual current source. This replacement is intended to respect the definition given in Bond Graph representation for the electrical field [79]. The aim of these changes is to formulate the power converter equations in terms of input and output voltages and currents independently of its electrical neighborhood. Second, the system of equations is converted in discrete form given that this method is intended to digital real-time emulations. Finally, the equations for interaction with output and power source should be formulated.

Some approaches have been reported in literature close to this proposed methodology [80][79]. Modeling methodology reported in [80] is focus on Simulink® blocks and presents several converter topologies as case of study. However, presented models in [80] only consider the ideal converter cases. Authors in [79] formalize a modeling methodology implemented in the non causal modeling language Modelica®. Authors in [79] argue that their non causal approach allows achieving the model generation of power electronics converters by not being constrained by the causality. Additionally, these authors remarks that this aspect is very important and allows to deals with small power electronics structures as well as with large power electronics structures [79].

Concerning to causality in the proposed component-based approach, a causal model definition is introduced. A causal model is defined as an abstract model that describes

the causal mechanisms of a system. A causal model is formally defined by Pearl in [81] as an ordered triple $\langle U, V, E \rangle$, where U is a set of exogenous variables whose values are determined by factors outside the model; V is a set of endogenous variables whose values are determined by factors within the model; and E is a set of structural equations that express the value of each endogenous variable as a function of the values of the other variables in U and V . According to this definition, the resulting models using our proposed approach are non casual models because changes in external factors do not modify the model structure. Nevertheless, the union of these non causal models provides an entire causal model due to the relationships between external and internal variables to each model. In other words, the proposed methodology is non causal when converters are isolated modeled, but it is became causal when resulting converter models are integrated into a power system model.

This modeling approach is applied to the Boost converter topologies as a case of study; nevertheless, this approach can also be extended to other types of power converters. The main advantages of this methodology is to model power converters with a high degree of detail disregarding subsequent changes in the power source and load models. Furthermore, these models are proposed to be integrated with other models to generate more complex structures suitable for power system modeling in microgrids [25][82].

Unidirectional Boost converter model

The Boost converter is a power converter used in a wide range of application. In PV systems, Boost converters are widely used because their features of boosting and power processing. In typical operation of Boost converter the output voltage is higher than the input voltage. Appendix A describes the operation principle of a unidirectional Boost converter and conventional modeling methodologies.

In this section, an example of Boost converter is modeled with battery and load models as shown in Fig. 4.9. Additionally, this case of study includes the power converter losses [78]. This circuit has unidirectional characteristics because in normal operation $i_L \geq 0$ due to the reverse bias of the diode. Fig. 4.10 depicts the first step after replaces the input voltage v_{in} and the output current i_o . Fig. 4.10 shows the operation states of the Boost converter as function of the PWM control signal $\{u = 0, 1\}$. From Fig. 4.10, the inductor current i_L and the capacitor voltage v_c are given by eq.(4.1) and eq.(4.2).

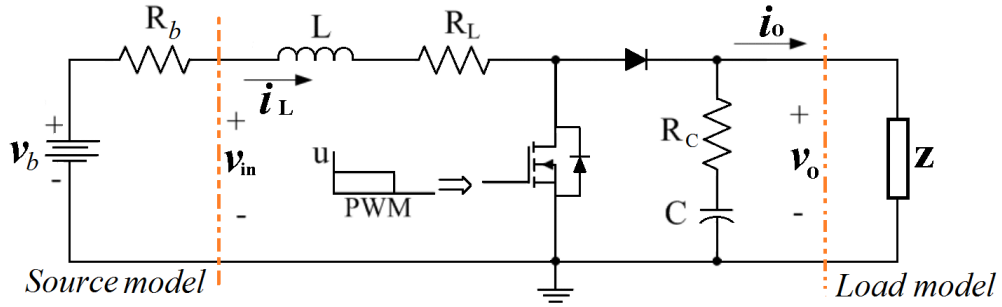


Fig. 4.9 Unidirectional Boost converter with source and load models.

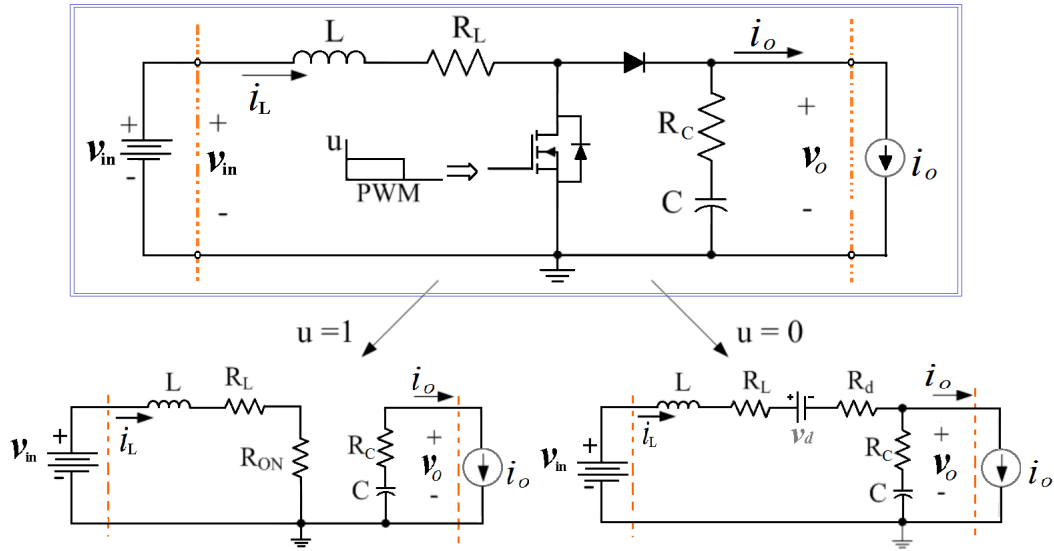


Fig. 4.10 Unidirectional Boost converter.

$$\frac{di_L}{dt} = \frac{1}{L} [v_{in} - i_L R_L - (i_L R_{on})u - (v_d + i_L R_d + i_L R_c - i_o R_c + v_c)(1-u)] \quad (4.1)$$

$$\frac{dv_c}{dt} = \frac{1}{C} [-i_o + i_L(1-u)] \quad (4.2)$$

Second step transforms the continuous model to the discrete form with sample time h as given by eq.(4.1) and eq.(4.2),

$$i_{L_{k+1}} = \frac{h}{L} [v_{in_k} - i_{L_k} R_L - (i_{L_k} R_{on}) u_k - (v_d + i_{L_k} R_d + i_{L_k} R_c - i_{o_k} R_c + v_{c_k})(1 - u_k)] + i_{L_k} \quad (4.3)$$

$$v_{c_{k+1}} = \frac{h}{C} [-i_{o_k} + i_{L_k}(1 - u_k)] + v_{c_k} \quad (4.4)$$

In the third step are defined the input and output interactions. In example of Fig. 4.9, the converter input interacts with a simplified battery model as a power source; thus,

$$v_{in_k} = v_{b_k} - i_L R_b \quad (4.5)$$

At the output connection, the converter interaction is given by,

$$v_{o_k} = v_{c_k} + R_c [i_{L_k}(1 - u_k) - i_{o_k}] \quad (4.6)$$

From example of Fig. 4.9, the load model with impedance Z can be calculated by,

$$i_{o_k} = \frac{v_{o_k}}{Z} \quad (4.7)$$

On the other hand, Boost converters can be connected to either a load Z or a DC reference voltage such a battery or DC regulated bus. Then, model with a DC reference voltage at the converter output $v_{o_k} = v_{DC}$ is given by,

$$v_{DC} = v_{c_k} + R_c [i_{L_k}(1 - u_k) - i_{o_k}] \quad (4.8)$$

Thus,

$$i_{o_k} = i_{L_k}(1 - u_k) + \frac{v_{c_k} - v_{DC}}{R_c} \quad (4.9)$$

To summarize, eq.(4.3) and eq.(4.4) represent the Boost converter model independent of source and load models. Eq.(4.6) represents the output voltage interaction. Finally, special application was formulated with a battery as power source eq.(4.5), impedance Z as load eq.(4.7), and DC reference voltage at the output eq.(4.9). In the next stage, the bidirectional Boost converter model is developed.

Bidirectional Boost converter model

Bidirectional Boost converters are used in applications where bidirectional power flow may be required. Bidirectional operation mode allows the current flow either toward the load or toward the input such as in battery charge systems [83]. Fig. 4.11 shows the case of study of Fig. 4.9 with a bidirectional Boost converter and after replace the input voltage and the output current. In bidirectional case, the diode of unidirectional topology is replaced by a power electronics switching device. Let us assume that both switching devices have similar conduction resistance R_{on} , the following model is proposed.

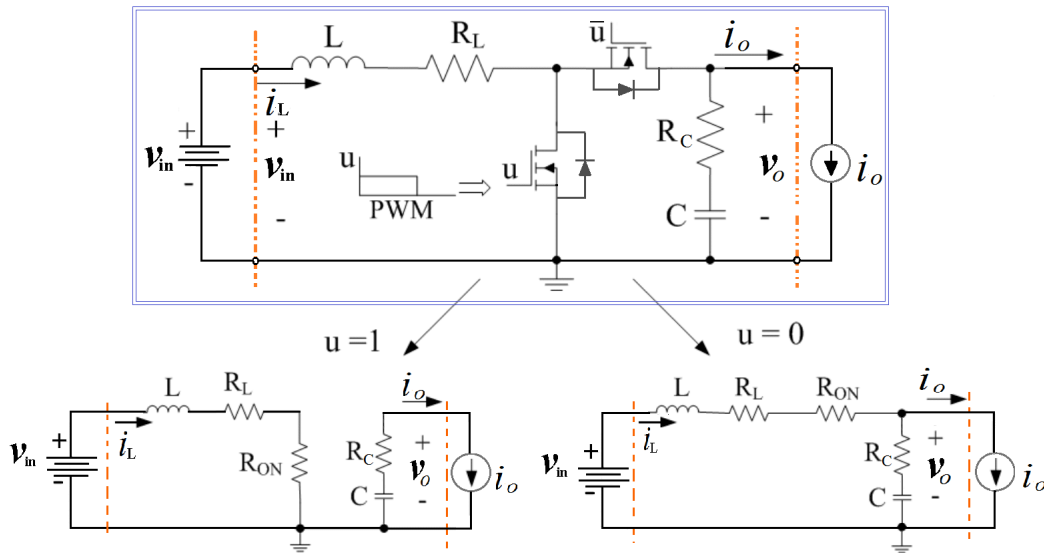


Fig. 4.11 Bidirectional Boost converter.

First, the circuit equations are formulated. Thus, the inductor current i_L and the capacitor voltage v_c in both operation states of control signal $\{u = 0, 1\}$ are given by (4.10) and (4.11),

$$\frac{di_L}{dt} = \frac{1}{L} [v_{in} - i_L(R_L + R_{on}) - (i_L R_C - i_o R_C + v_c)(1 - u)] \quad (4.10)$$

$$\frac{dv_c}{dt} = \frac{1}{C} [-i_o + i_L(1 - u)] \quad (4.11)$$

In the second step, the discrete form is given with a sample time h ,

$$i_{L_{k+1}} = \frac{h}{L} [v_{in_k} - i_{L_k}(R_L + R_{on}) - (i_{L_k}R_c - i_{o_k}R_c + v_{c_k})(1 - u_k)] + i_{L_k} \quad (4.12)$$

$$V_{c_{k+1}} = \frac{h}{C} [-i_{o_k} + i_{L_k}(1 - u_k)] + v_{c_k} \quad (4.13)$$

Finally, the input and output interactions are defined. The output voltage interaction is then,

$$v_{o_k} = v_{c_k} + R_c [i_{L_k}(1 - u_k) - i_{o_k}] \quad (4.14)$$

For example in Fig. 4.9, unidirectional and bidirectional converters have the same models to the power source and the load. Then, as a deduced with unidirectional case, the model with impedance Z as load can be calculated by eq.(4.7). The model with DC reference voltage at the converter output $v_{o_k} = v_{DC}$ is given by eq.(4.9), and model with the battery as power source is given by eq.(4.5).

General model for Boost converter topologies

Comparison of unidirectional and bidirectional Boost converter topologies allows to conclude a general model for the Boost converter. Eq.(4.3) and eq.(4.12) shows that the main difference between the unidirectional and bidirectional converter models is the inductor current i_L . Therefore, eq.(4.3) is selected as a base expression for i_L . In unidirectional case, eq.(4.3) represents the inductor current i_L ; additionally, in this operation mode i_L is constraint to $i_L \geq 0$. In bidirectional operation mode, $v_d = 0$ and $R_d = R_{on}$. Expressions for v_c are equal in both operation modes. As a result, the general Boost converter model is proposed using expressions eq.(4.3) and eq.(4.4). Fig. 4.12 depicts a partial the flow of operations to evaluate the general Boost converter model from eq.(4.3) and eq.(4.4). Flow of operations of Fig. 4.12 is intended to embedded hardware implementation which will be describe in next chapters.

Diagrams of Fig. 4.13 and Fig. 4.14 represent the final component-based model for the Boost inverter topologies. Fig. 4.13 depicts the interaction of Boost converter with a load. In Fig. 4.14, the Boost converter interacts with a DC voltage at the output; then, the Boost converter in this case regulates the current flow toward either a DC bus or a battery at the output. As shown in this application of the component-based approach, a general and detail converter model can be developed and model of inputs

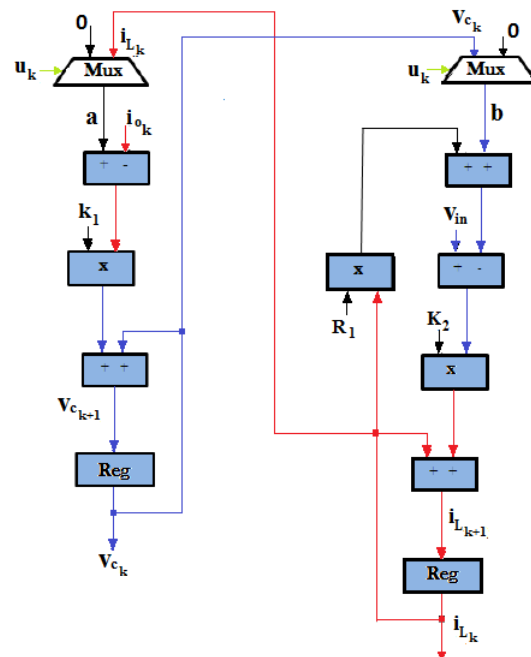


Fig. 4.12 Partial operation flow Boost converter model.

and outputs can be replaced without formulate again all the model. Finally, these proposed models are able to be implemented in either a programming language or in a building block oriented environment such as Simulink® or Modelica®.

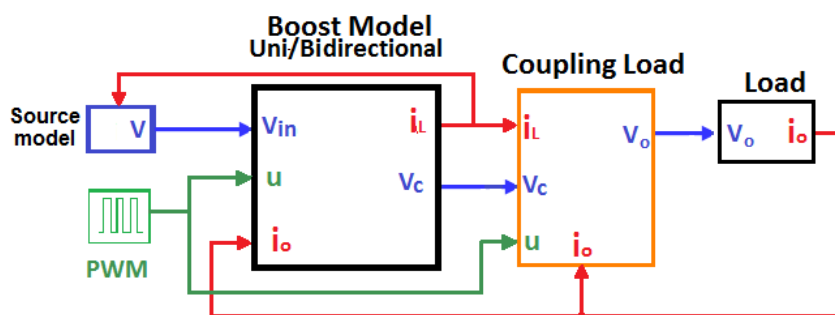


Fig. 4.13 Boost converter model coupled load.

4.2.3 Validation of modeling methodology

Validation of the proposed modeling approach is developed using open loop simulations and experimental results. In the first stage, simulation results of the proposed model are compared with the circuit simulations in a power electronics circuit simulator.

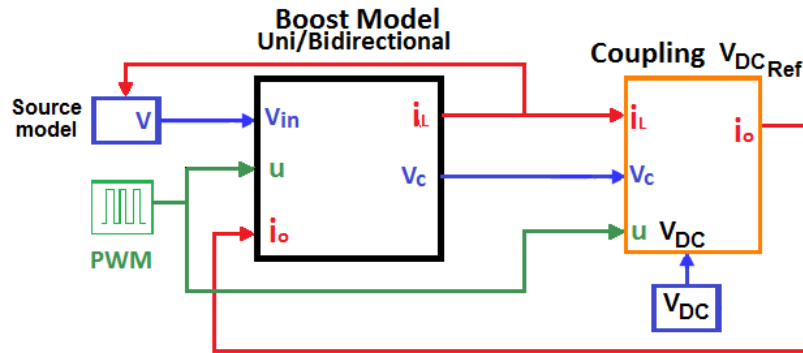


Fig. 4.14 Boost converter model coupled V_{DC} .

Then, results are compared with conventional modeling methodologies presented in Appendix A. Finally, experimental results are compared in an integrated system PV module - Boost converter.

Open loop simulations

Fig. 4.15 shows the circuits under test. As shown in Fig. 4.15, both topologies was tested. The tested circuits was simulated using the power electronics circuit simulator *PSIM*® and the component-based model of Boost converter was simulated in *Simulink*®. Circuit parameters are listed in Table 4.2 and case of study in Table 4.3. As shown in Table 4.3, in case 1 and 2 the load is a resistor and in case 3 a battery is connected at the converter output.

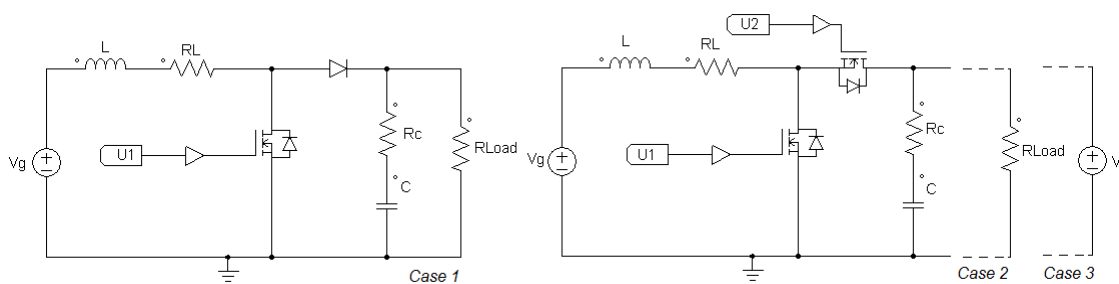


Fig. 4.15 Unidirectional and bidirectional Boost converter simulated circuits

Simulation results depicted in Fig. 4.16, Fig. 4.17, and Fig. 4.18 show that proposed modeling methodology agrees with expected results of simulated circuits in a power electronics simulator. Furthermore, Mean squared error (MSE) of results in Table 4.4 validate the accuracy of proposed methodology. As shown, in Table 4.4

Table 4.2 Simulation parameters

Model parameter	Value
L	$47 \mu H$
C	$47 \mu F$
R_L	0.01Ω
R_c	0.01Ω
R_d	0.18Ω
R_{on}	0.18Ω
V_d	$0.7 V$
V_g	$90 V$
F_{sw}	$100 KHz$
h	$0.1 \mu S$

Table 4.3 Simulation cases

	Mode	Duty cycle	Load
Case 1	Unidirect.	0.6	$R = 10 \Omega$
Case 2	Bidirect.	0.4	$R = 100 \Omega$
Case 3	Bidirect.	0.5	Batt = 120 V

capacitor voltage have less error in comparison with inductor current. Cause of this error difference could be associated to the switching dynamic of system because it has more impact in the inductor current than in the capacitor voltage.

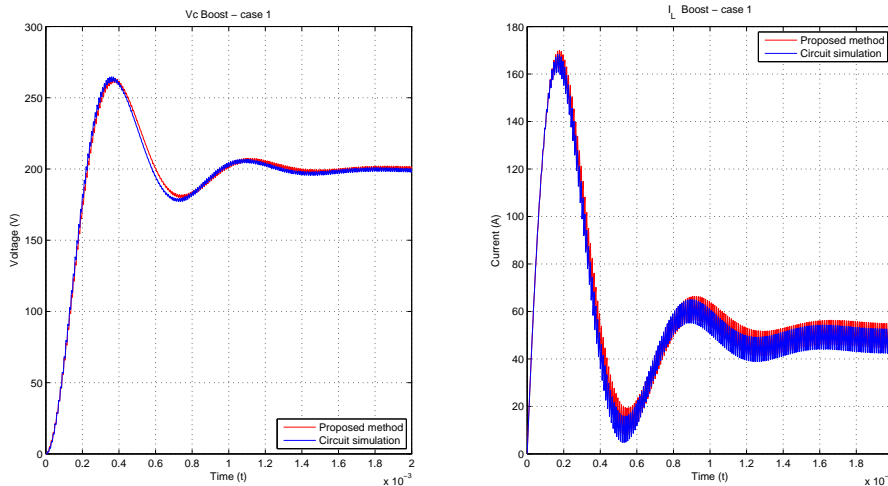


Fig. 4.16 Comparison proposed model with circuit simulation - Case 1.

$$MSE = \frac{1}{n} \sum_{i=1}^n (e_i)^2 \quad (4.15)$$

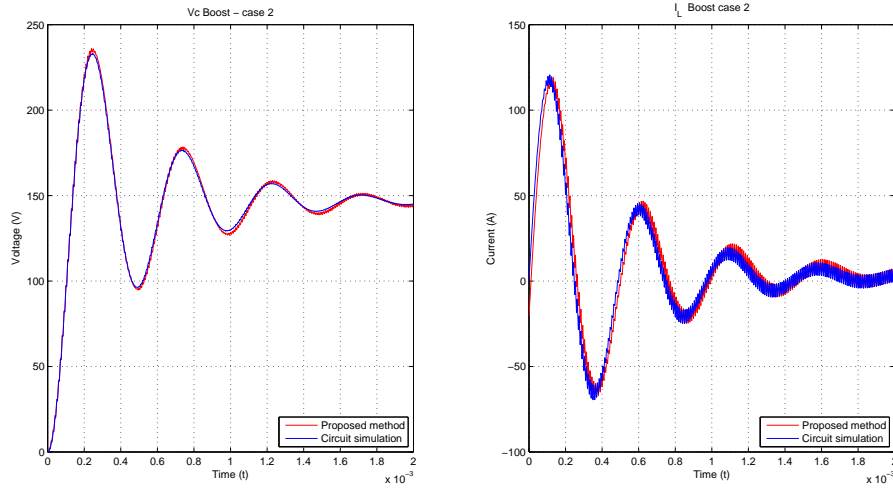


Fig. 4.17 Comparison proposed model with circuit simulation - Case 2.

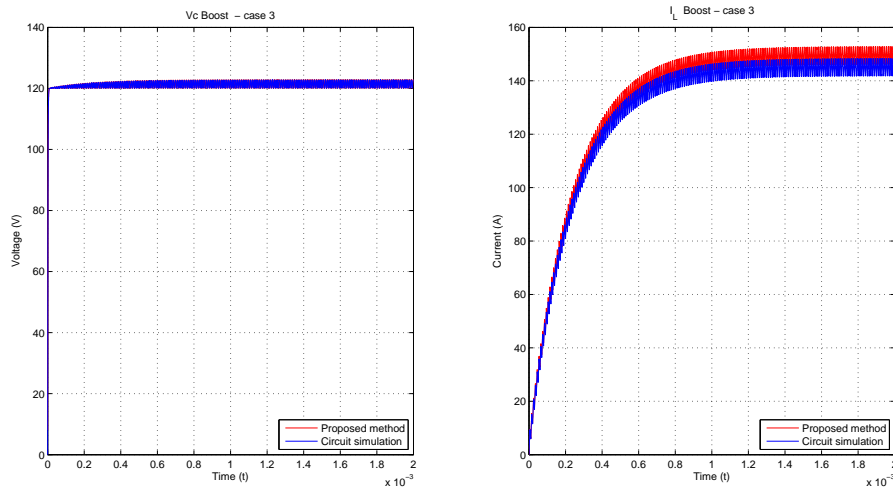


Fig. 4.18 Comparison proposed model with circuit simulation - Case 3.

Table 4.4 Mean Squared Error (MSE) - Simulated models

	V_c	I_L
Case 1	0.0042	0.0561
Case 2	0.0035	0.0375
Case 3	0.0041	0.0730

After simulation model and circuit, a comparison with conventional modeling methodology is presented. For comparison purpose, case 1 of Table 4.3 are compared with the average Boost converter model (A.29) presented in Appendix A. As shown in Fig. 4.19, component-based modeling results are consistent with average model results.

However, the average model requires a high degree of theoretical development when converter losses are included, as shown in Appendix A. Furthermore, this conventional modeling methodology requires a model reformulation for changes in the type of load or power source.

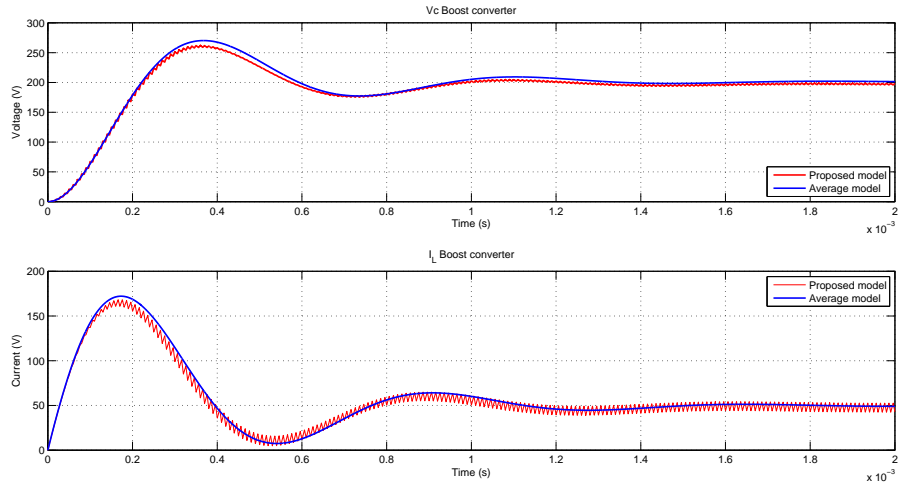


Fig. 4.19 Proposed model and average model of Boost converter

Next step to validate the proposed methodology is accomplished by means of experimental results with a Boost converter interconnected with a PV module as a source power.

Experimental validation of modeling methodology

In order to validate the proposed methodology applied in PV systems, a Boost converter is interconnected with a PV module. In this study case, the whole system is modeled using a component-based approach. The experimental setup is described in Fig. 4.20, and physical implementation is shown in Fig. 4.21. Table Fig. 4.7 lists the experimental parameters.

As shown in Fig. 4.20, the coupling between the PV module and the Boost converter requires an intermediate stage given by a capacitor to compensate the high non linearity of the PV module. Then, this interaction is analyzed from diagram Fig. 4.22. After numerical analysis, equations eq.(4.16) to eq.(4.18) provides the model for the coupling stage. Diagram of Fig. 4.23 describes the component-based model for PV module and Boost converter integration according with the proposed methodology. In this

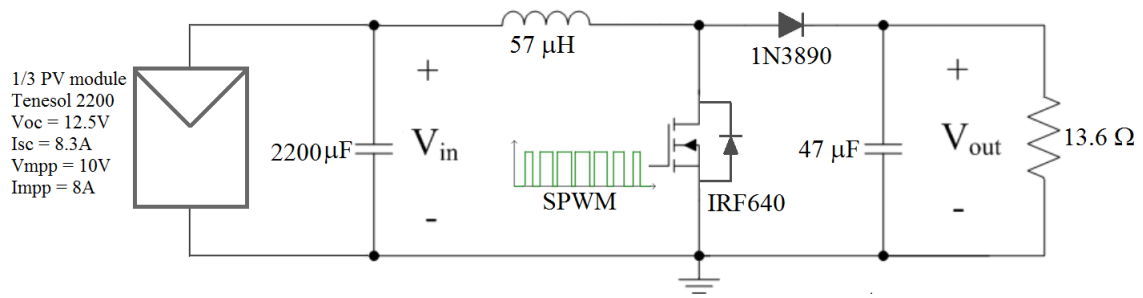


Fig. 4.20 Schematic circuit for PV module - Boost converter test

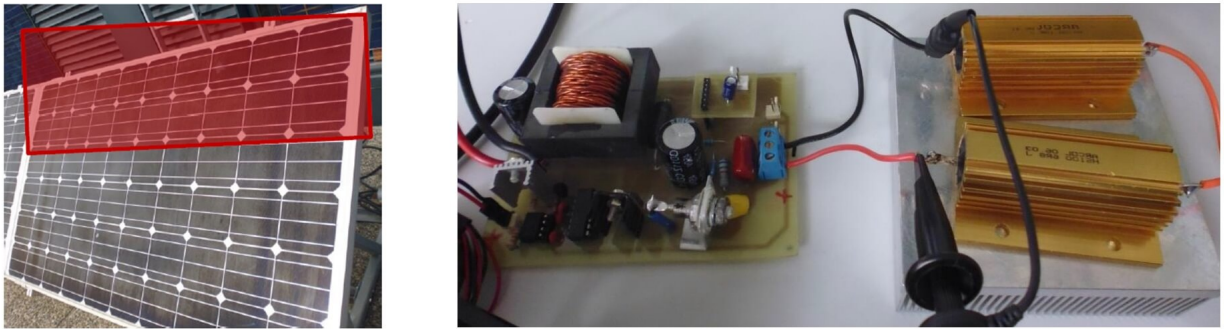


Fig. 4.21 Experimental Boost converter test

Table 4.5 Experimental parameters

Parameter	Value
L	$57 \mu H$
C	$47 \mu F$
R_L	0.1Ω
R_c	0.05Ω
R_d	0.1Ω
R_{on}	0.18Ω
V_d	$0.7 V$
C_f	$2200 \mu F$
R_{c_f}	0.04Ω
F_{sw}	$100 KHz$
h	$0.1 \mu S$

diagram, the PV module is modeled as described in section 3.2.1. Model of Fig. 4.23 is implemented in Simulink®, and results are compared with experimental measurements.

Experimental setup uses the third part of a PV module Tenesol 2200 as a power source, and other third part to monitor the current-voltage behavior of this PV module.

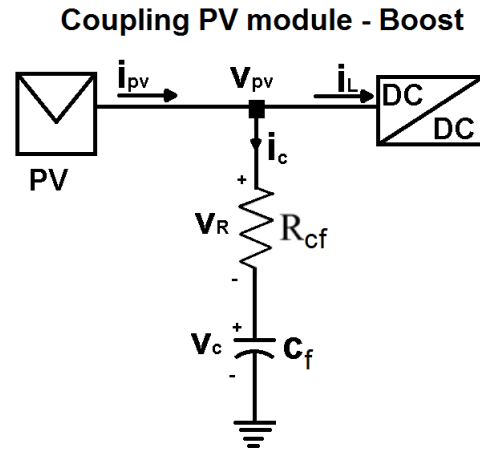


Fig. 4.22 Coupling PV module - Boost

$$i_{pvK} = \frac{(v_{pvK} - v_{cK})}{R_{cf}} + i_{LK} \quad (4.16)$$

$$v_{cK+1} = \frac{h}{R_{cf}C_f} (v_{pv} - v_{cK}) + v_{cK} \quad (4.17)$$

$$V_{opk} = v_{pv} \quad (4.18)$$

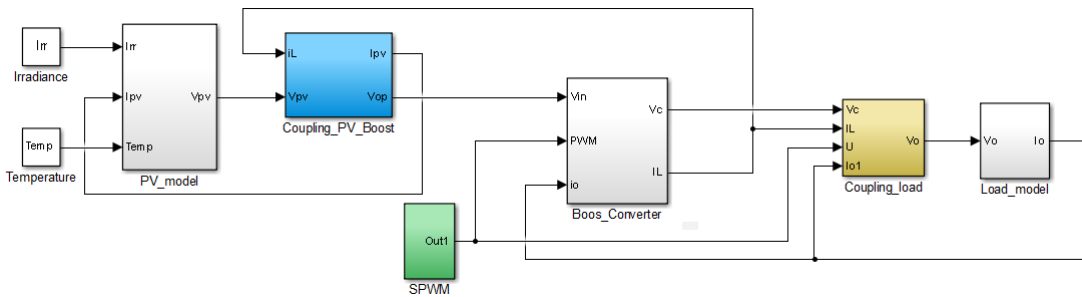


Fig. 4.23 Component-based model for PV module and Boost converter integration

This experiment was performed the Mars 4th 2016 in a sunny day in Toulouse-France (43°33'44.3"N 1°28'38.3"E). The ambient temperature was 17°C. The irradiance patron during the experiment is depicted in Fig. 4.24. This figure also shows the I-V curve of the PV module while electrical variables were measured.

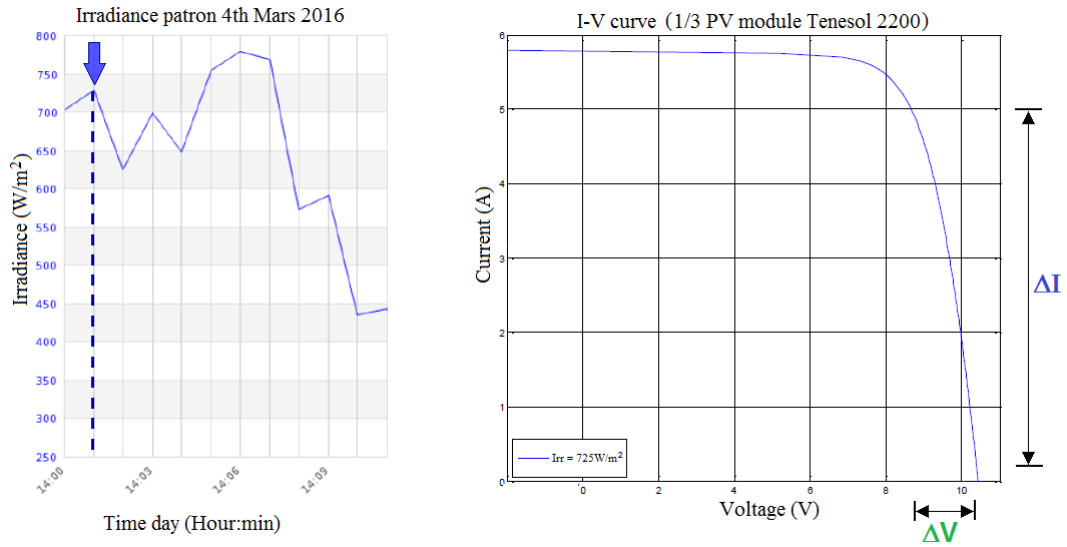


Fig. 4.24 Irradiance patron during test

Fig. 4.25 depicts the measurements of PV module voltage and Boost converter output voltage when a Sinusoidal Pulse Width Modulation (SPWM) signal drives the switching power electronics device. When a SPMW drives the switching device, this modulation causes a voltage variation quasi-sinusoidal on the load. Indeed, this is the principle of the Boost inverter. Fig. 4.25 shows the variation quasi-sinusoidal on the load and its effect on the PV module voltage. As shown in this figure, when the sinusoidal output is maximum the PV voltage trends to drop. In contrast, when sinusoidal output decreases, the PV module voltage increases until to reach a quasi-stable maximum value. This cycle continue indefinitely while the sinusoidal variation remains on the load.

According to experimental parameters (Table 4.5), component-based model is executed (Fig. 4.23). Model simulation results in Fig. 4.26 shows the coherence between expected results and simulations. As shown in Fig. 4.26, this proposed model is able to follow the high non linearity of coupling the PV module and the Boost converter. The dynamic of interaction between the sinusoidal output and the PV voltage variation harmonize as much in measurements as in simulations.

Simulation results in Fig. 4.27 shows in detail the interaction PV module - Boost converter. First, a sinusoidal voltage variation on the load causes a variation in the input current of the converter as shown in left side of Fig. 4.27. Next, this changes in the consumption of current requires changes in the current provided by the PV module

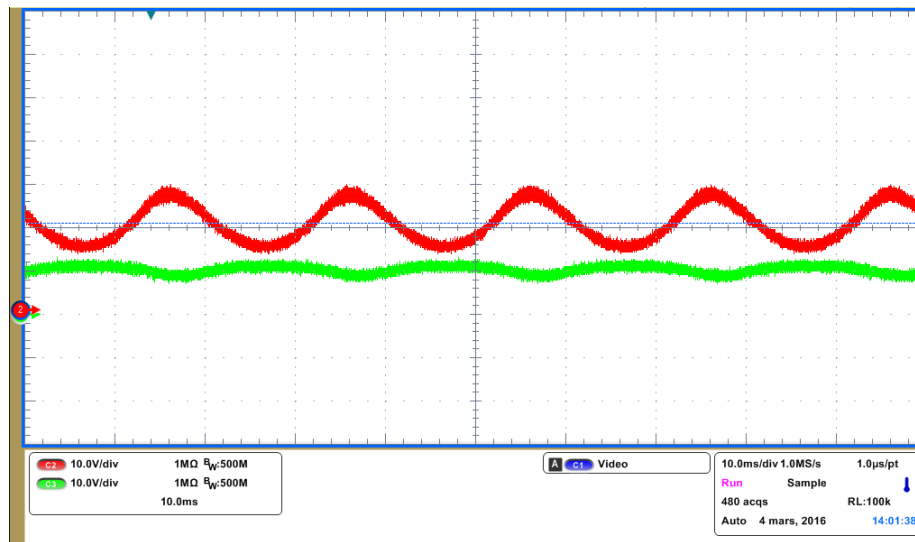


Fig. 4.25 PV module and Boost converter voltage measurements. Boost output voltage (V_o), PV voltage (V_{pv}). Vertical scale = 10 Volt/div. Horizontal scale = 10ms/Div.

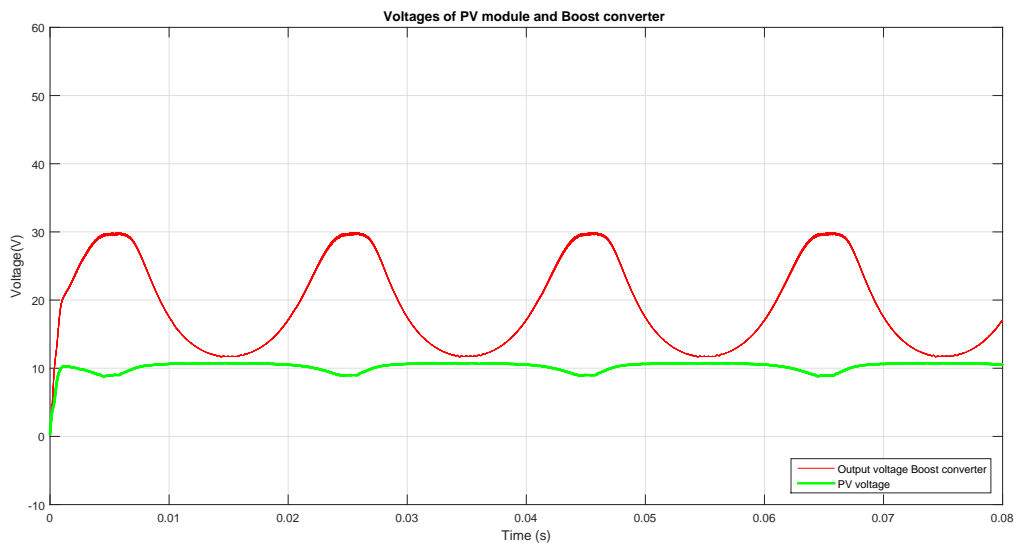


Fig. 4.26 Simulation results of integration PV module - Boost converter. Boost output voltage (V_o), PV voltage (V_{pv})

(Right side Fig. 4.27). This variation has a non linear behavior as shown in the I-V curve of Fig. 4.24 where these variations are represented by ΔV and ΔI . After, this variation of the PV current has an impact on the PV voltage which also affect the voltage at the input of the Boost converter. Finally, this distortion on the input Boost converter voltage conduces to a higher non linearity of the quasi-sinusoidal output

signal. This effect is more evident in the semi-cycle positive when the PV module voltage is more non linear.

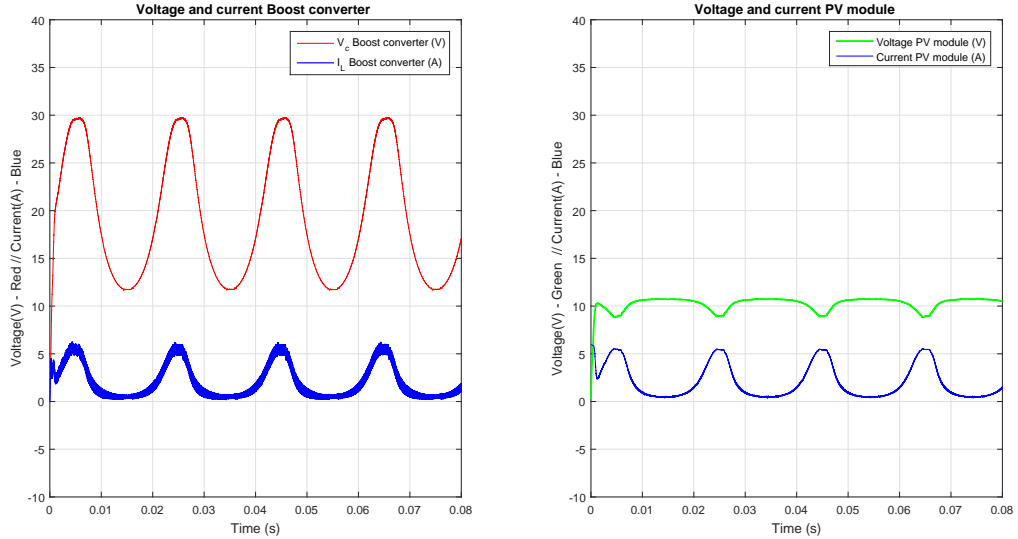


Fig. 4.27 Voltage (V_c) and current (I_L) of Boost converter (Left side) - Voltage (V_{pv}) and current (I_{pv}) of PV module (Right side)

To summarize, this section described the proposed component-based methodology. The Boost converter topologies was taken as case of study. Simulations and experimental result validate the proposed approach. Finally, this methodology allowed studying the interaction PV module - Boost converter when a quasi-sinusoidal signal is produced. Next section introduces the analysis of the Boost inverter, and component-based approach is used to model this versatile structure.

4.3 Boost inverter modeling

The Boost inverter is a transformerless power converter which provides an AC output voltage from two individual bidirectional DC-DC Boost converters. This section presents its operation principle and model using the component-based approach.

4.3.1 Mathematical framework for the Boost inverter

Two current bidirectional Boost converters constitute a single stage Boost inverter [34], as shown previously in Fig. 4.5. The output voltage v_o of a Boost inverter is a differential signal which becomes an AC voltage when both bidirectional Boost converters produce

dc-biased sinusoidal signals 180° phase-shifted, eq.(4.20) and eq.(4.21). Fig. 4.3 depicts this operation principle.

$$v_o = v_1 - v_2 \quad (4.19)$$

$$v_1 = V_{dc} + \frac{1}{2}A_o \text{Sin}(\omega t) \quad (4.20)$$

$$v_2 = V_{dc} + \frac{1}{2}A_o \text{Sin}(\omega t - \pi) \quad (4.21)$$

$$v_o = A_o \text{Sin}(\omega t) \quad (4.22)$$

The relationship between the output voltage and the input voltage for ideal components as a function of the duty cycle D is given by [34],

$$\frac{V_o}{V_{in}} = \frac{2D - 1}{D(1 - D)} \quad (4.23)$$

Usually, the relationship described by eq.(4.23) is reported in the literature [29]. However, this expression disregards the conductive losses and the load influence on the gain and efficiency. Taking into account the conductive losses, the boost inverter circuit is drawn in Fig. 4.28. Where $S1$ to $S4$ are ideal switches, R_{on} represents the conductive losses of switching devices, and R_L are the conductive losses associated to the inductors.

In the first operation state $S1$ - $S4$ are active and $S2$ - $S3$ are inactive. Let $R_s = R_L + R_{on}$ be the resistive losses, and let $D = 1 - D_1$ be the duty cycle. Solving the system of equations of the circuit in Fig. 4.28 in both operation states and applying the principle of inductor volt-second balance and the capacitor charge balance [78]. Then,

$$\langle V_{L1} \rangle = D(V_{in} - I_1(R_s)) + D'(V_{in} - I_1(R_s) - V_1) = 0 \quad (4.24)$$

$$\langle V_{L2} \rangle = D(V_{in} - I_2(R_s) - V_2) + D'(V_{in} - I_2(R_s)) = 0 \quad (4.25)$$

$$\langle I_{c2} \rangle = D\left(\frac{V_2 - V_1}{R}\right) + D'\left(I_1 + \frac{V_2 - V_1}{R}\right) = 0 \quad (4.26)$$

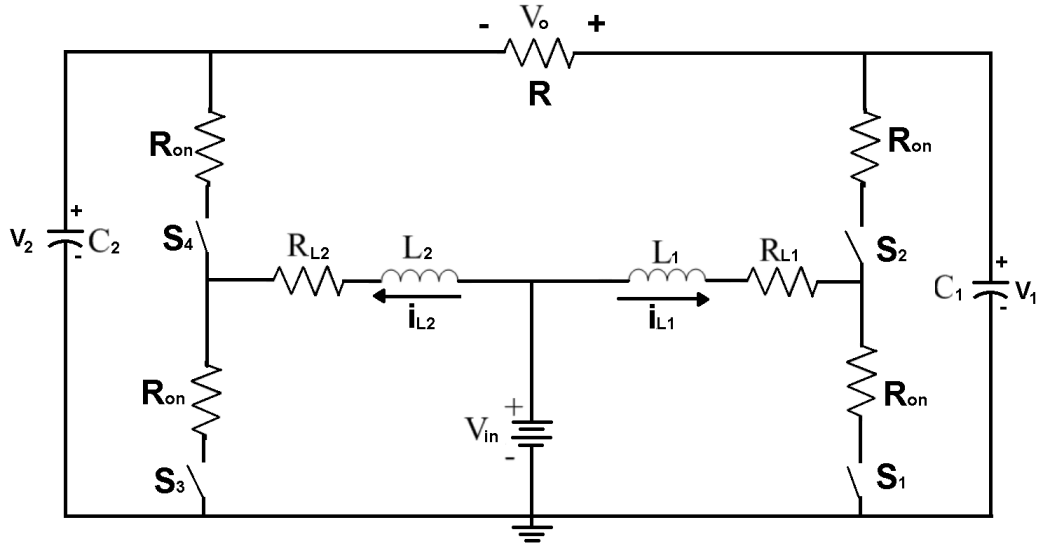


Fig. 4.28 Boost inverter circuit with conductive losses

$$\langle I_{c2} \rangle = D \left(I_2 + \frac{V_1 - V_2}{R} \right) + D' \left(I_1 + \frac{V_1 - V_2}{R} \right) = 0 \quad (4.27)$$

Solving the system of equations for the gain V_o/V_{in} ,

$$\frac{V_o}{V_{in}} = \frac{2D - 1}{\frac{R_s}{R} \left(\frac{1}{D'} + \frac{D'}{D} - 1 \right) + DD'} \quad (4.28)$$

Formulating the equation for the efficiency η ,

$$\eta = \frac{P_{out}}{P_{in}} = \frac{V_{out} I_{out}}{V_{in} I_{in}} = \left(\frac{V_{out}}{V_{in}} \right) \left(\frac{I_{out}}{I_{in}} \right) \quad (4.29)$$

$$I_{in} = I_1 + I_2 = I_o \left(\frac{2D - 1}{DD'} \right) \quad (4.30)$$

$$\eta = \left(\frac{2D - 1}{\frac{R_s}{R} \left(\frac{1}{D'} + \frac{D'}{D} - 1 \right) + DD'} \right) \left[\frac{1}{\frac{2D - 1}{DD'}} \right] \quad (4.31)$$

Fig. 4.29 and Fig. 4.30 depict the gain V_o/V_{in} and the converter efficiency η according to eq.(4.28) and eq.(4.31). Fig. 4.29 shows the relation between the duty cycle and the gain in a Boost inverter. This figure shows that relation gain - duty cycle is linear around $D = 0.5$, but this relation loses linearity for values of $D \geq 0.8$ and

$D \leq 0.2$. Indeed, Fig. 4.29 shows that Boost inverter presents an important instability around $D = 0.95$ and $D = 0.05$.

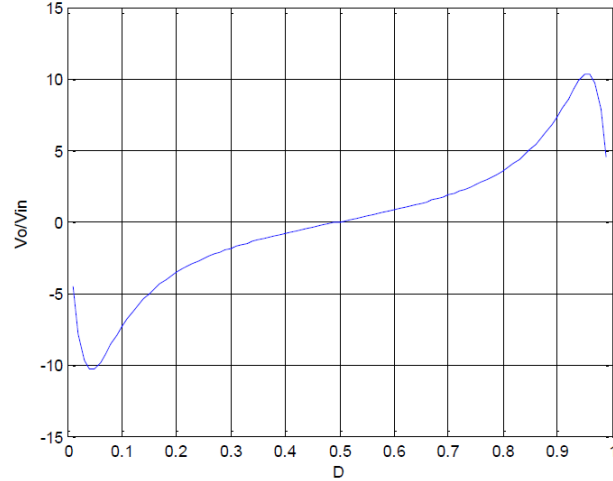


Fig. 4.29 Boost inverter gain

Fig. 4.30 shows the influence of the duty cycle on the efficiency. As shown in Fig. 4.30, variations of $D \geq 0.8$ and $D \leq 0.2$ impact drastically in converter efficiency. Then, Fig. 4.29 and Fig. 4.30 shows that the better operation range for operation of Boost inverter is between $D \geq 0.8$ and $D \leq 0.2$ where variation is more linear and efficiency is higher. Taking into account previous result, it is clear that a well developed model is necessary to describe the behavior of a Boost inverter. Therefore, the component-based approach will be applied to model the Boost inverter in the next section.

4.3.2 Component-based approach for Boost inverter modeling

The Boost inverter can be considered as a system where four components interact as shown in Fig. 4.31. The four components are the power source, the load, and the two bidirectional Boost inverters.

The following component-based model for the Boost inverter is formulated from analysis developed in section 4.2.2. Proposed model is shown in Fig. 4.32. In addition, the model load component in this diagram is given by eq. (4.32).

$$i_{01} = \frac{v_1 - v_2}{R_{Load}} \quad (4.32)$$

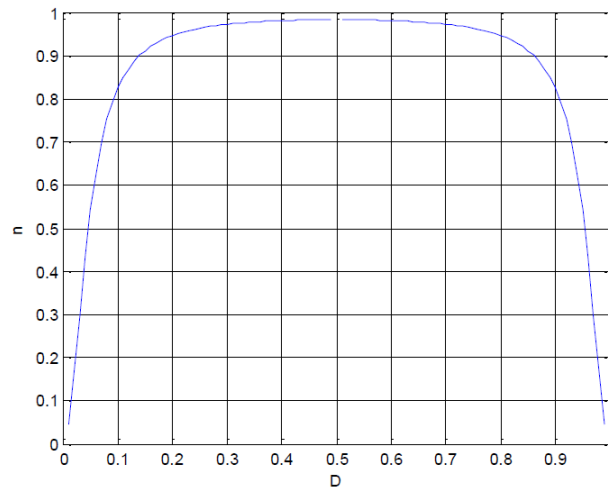


Fig. 4.30 Boost inverter efficiency

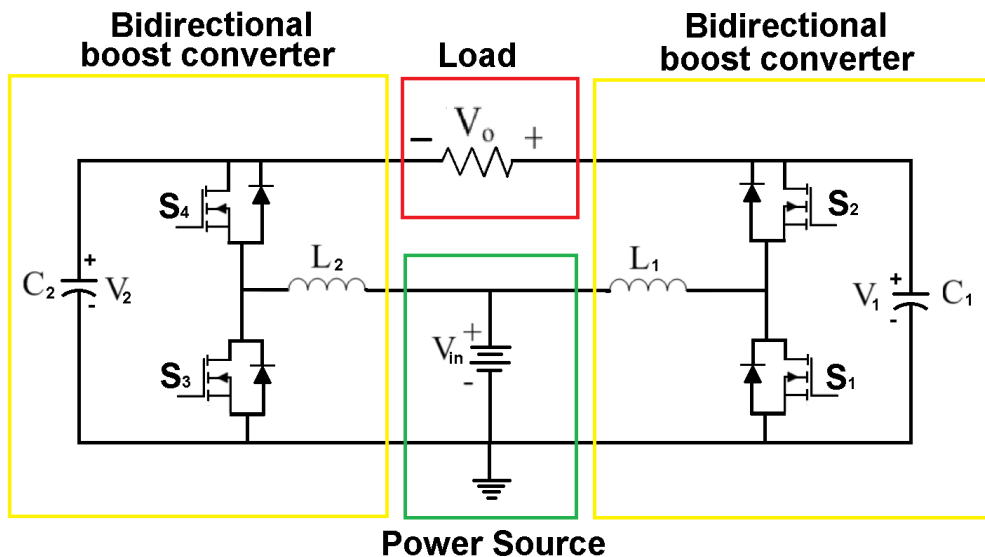


Fig. 4.31 Boost inverter as a system based on components

Model simulation is executed with parameters listed in Table 4.6. The Modulation SPWM used to drive the switching devices is shown in Fig. 4.33. In this figure the duty cycle is modulated around $D = 0.5$; then, parameter Δ determines the maximum variation of the SPWM signal. Simulation results are depicted in Fig. 4.34. In the first case, $\Delta D = 0.1$ and the output signal is closer to a sinusoidal signal because variations close to $D = 0.5$ are more linear. Then, results of Fig. 4.34a agree with expected variation depicted in Fig. 4.29. In the second case, $\Delta D = 0.35$ the signal lost linearity in relation with the SPWM control signal as shown in Fig. 4.34b. These simulation results agree with the theoretical framework presented in section 4.3.1 considering the

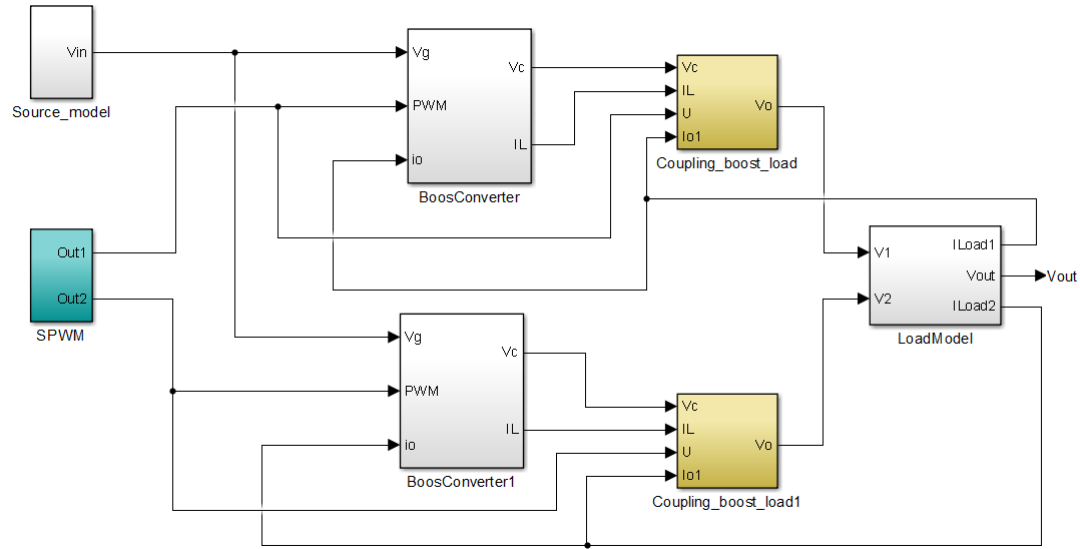


Fig. 4.32 Boost inverter model based on components

variation around of the duty cycle D around 0.5. Finally, changes of load are simulated. The gain for each case are presented in Fig. 4.35. This figure shows that results are coherent with expected behavior modeled in section 4.3.1.

Table 4.6 Simulation parameters for Boost inverter

Model parameter	Value
L_1, L_2	$47 \mu H$
C_1, C_2	$10 \mu F$
R_{L1}, R_{L2}	0.02Ω
R_{c1}, R_{c1}	0.06Ω
R_{on}	$65 m\Omega$
V_{in}	$30 V$
$F_{carrier}$	$100 KHz$
F_{modul}	$50 Hz$
h	$0.1 \mu S$

To sum up, the component-based methodology was employed to model the Boost converter. Simulation results were consistent with the expected behavior. In the next step, the Boost inverter model will be experimentally validated.

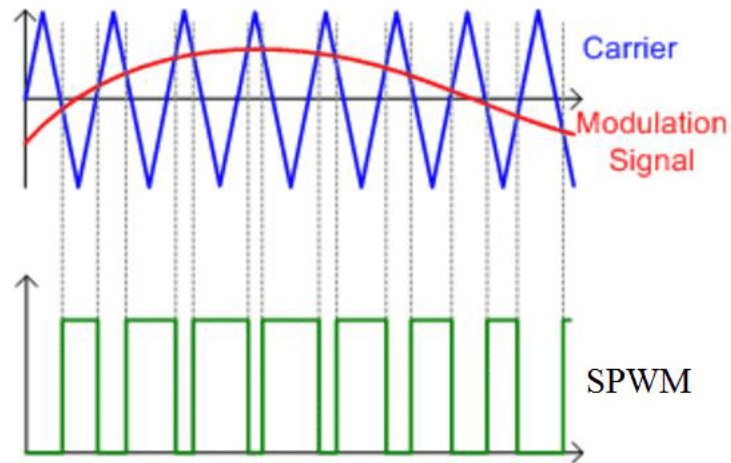


Fig. 4.33 Sinusoidal Pulse Width Modulation (SPWM)

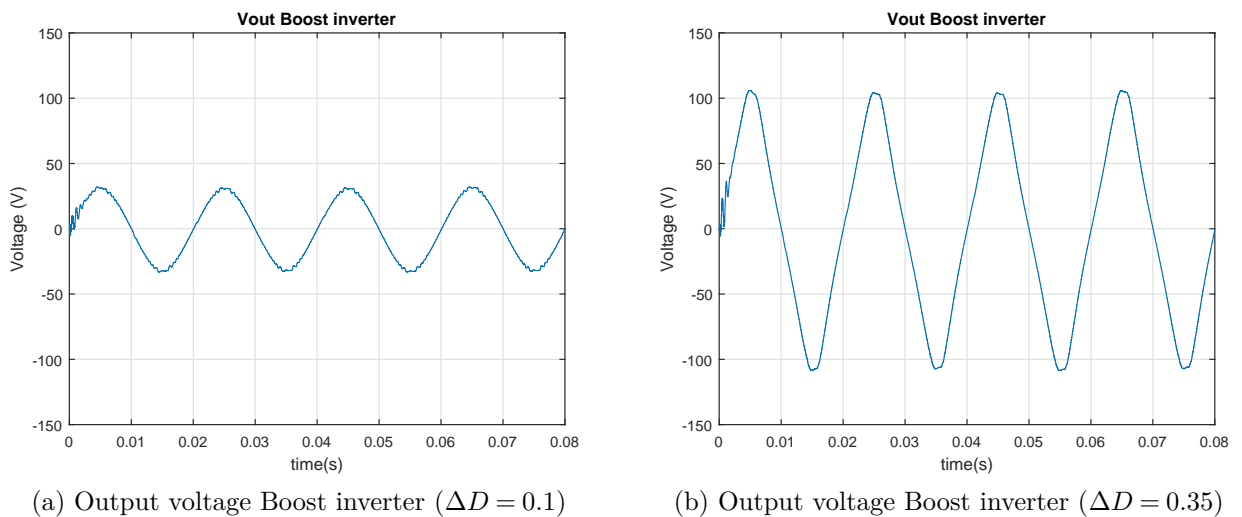


Fig. 4.34 Simulation results of Boost inverter

4.3.3 Experimental setup to validate the modeling approach

Experimental validation of proposed component-based approach is applied to a Boost inverter connected with a PV module. The purpose of these tests is to evaluate the permanence of the proposed methodology to describe the dynamic interaction between the power converter and a nonlinear source such as a PV module. Furthermore, the interest of these tests is to identify the main characteristics of Boost inverter integration in PV applications in order to increase the knowledge about this interaction. The implemented Boost inverter circuit is depicted in Fig. 4.36. Detail description of

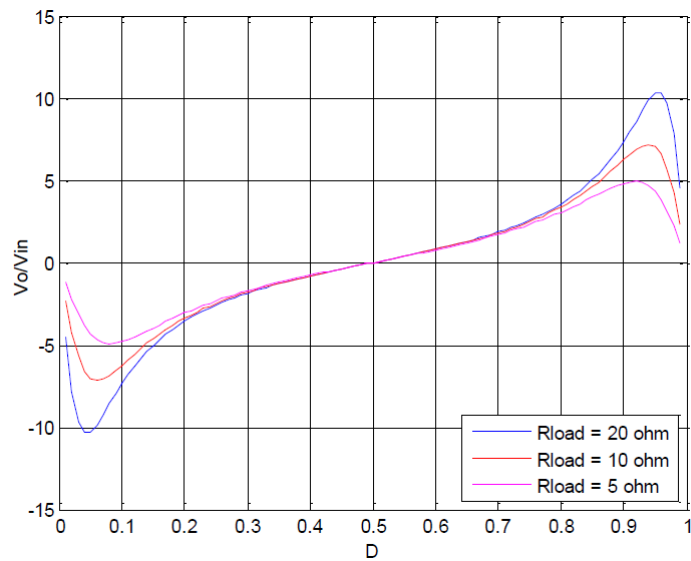


Fig. 4.35 Results of Boost inverter gain with changes of load

designed Boost inverter is presented in Appendix B.

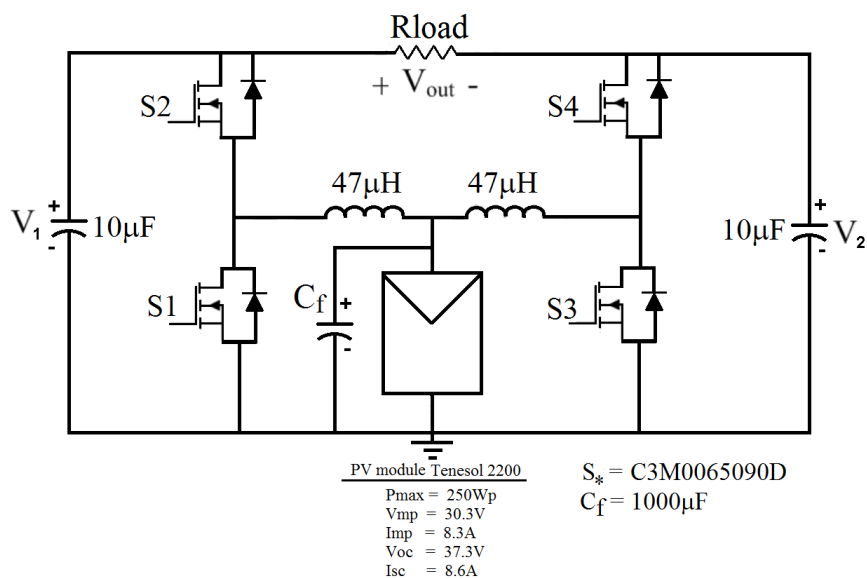


Fig. 4.36 Schematic circuit for PV module - Boost converter test

In this test, two PV modules were employed. One of this PV modules is employed to supply power to the Boost inverter, and the other one is employed as a reference to know the I-V curve of the equivalent PV module. In this setup, an I-V curve tracer model MP-160 measures the current-voltage signals. Additionally, a pyronometer

model SP LITE detects the solar irradiance.

In this study case, the whole PV system is modeled using a component-based approach. The PV module is modeled as described in section 3.2.1 and the Boost inverter as described in previous section. Model of Fig. 4.23 is implemented in Simulink®, and results are compared with experimental measurements.

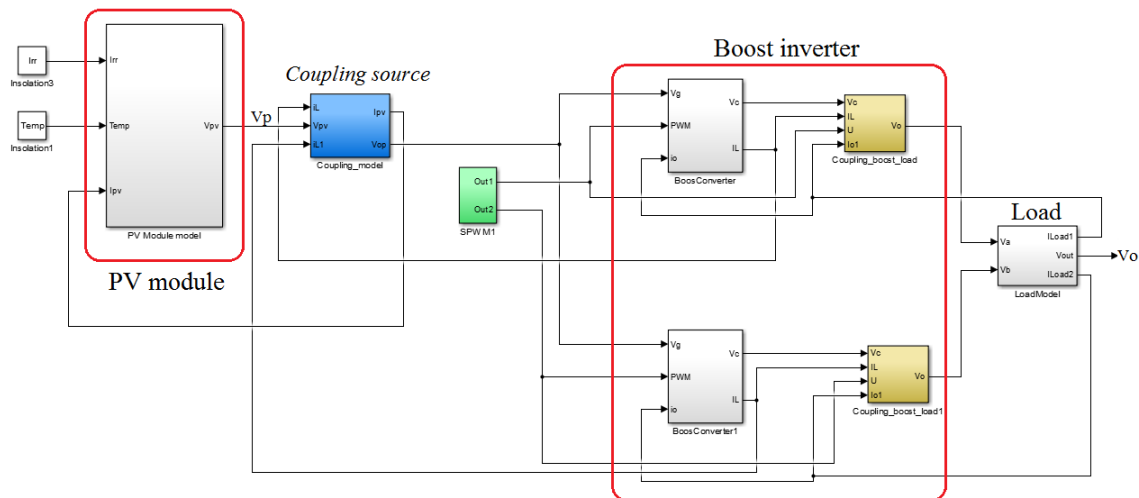


Fig. 4.37 Component-based model of Boost inverter with PV module

Experimental parameters for these tests are listed in Table 4.7. A set of power loads is employed to evaluate the Boost converter behavior. In addition, operation signals of power converter and PV module operation are compared in order to identify patrons of behavior. Fig. 4.38 shows the IV curve associated to the experimental result of Fig. 4.39.

Fig. 4.41 shows the simulation results according to experimental parameters. As shown in Fig. 4.41, the proposed model showed suitable results in relation with experimental tests. The proposed model is able to reproduce the dynamic interaction between these two nonlinear systems. Table 4.8 summaries the Mean Square Error (MSE) between experimental results of a series of test and simulations. This table allows concluding that proposed methodology is suitable to emulate the physical interaction between the PV source and the power converter.

Additionally, Fig. 4.38 shows the operation region in this case. This figure allows concluding that in this region the voltage has less fluctuation in comparison with the

Table 4.7 Experimental parameters

<i>Converter Parameter</i>	<i>Value</i>
L	$47 \mu H$
C	$10 \mu F$
R_L	0.1Ω
R_c	0.05Ω
R_{on}	$65m \Omega$
<i>Panel Parameter</i>	<i>Value</i>
P_{max}	$250 W$
V_{mp}	$30.3 V$
I_{mp}	$8.3 A$
V_{oc}	$37.3 V$
I_{sc}	$8.6 A$
<i>Capacitor coupling Parameter</i>	<i>Value</i>
C_f	$1000 \mu F$
R_{c_f}	0.05Ω
<i>SPWM parameter</i>	<i>Value</i>
$F_{carrier}$	$100 KHz$
F_{modul}	$50 Hz$

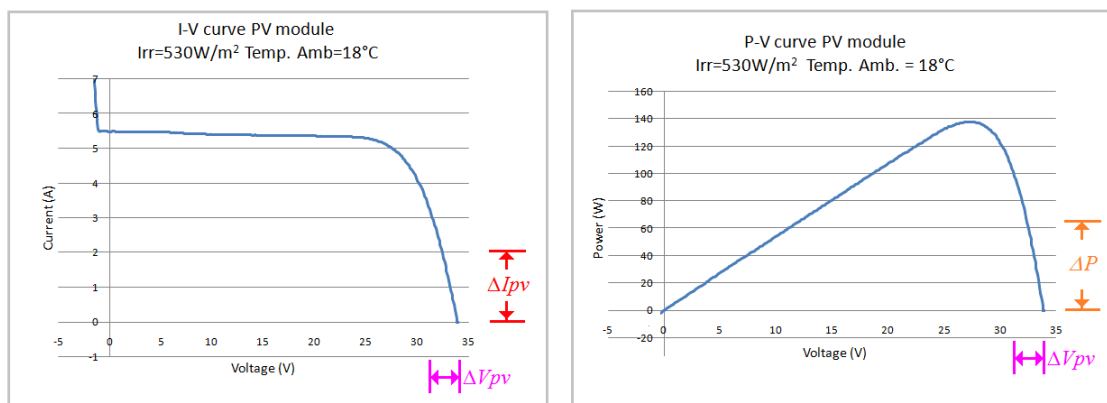


Fig. 4.38 Experimental I-V curve PV module

strong variations on the PV module current. Then, in this region the operation of the Boost inverter has more stability of voltage, but it operates far from the Maximum Power Point. On the other hand, the interrelation Fig. 4.38 and Fig. 4.39 considering the PV system at the Maximum Power Point lead to estimate that the output voltage will present less stability because the strong variation of the PV module voltage. Then, more robust control strategies will be needed to operate at this Maximum Power Point.

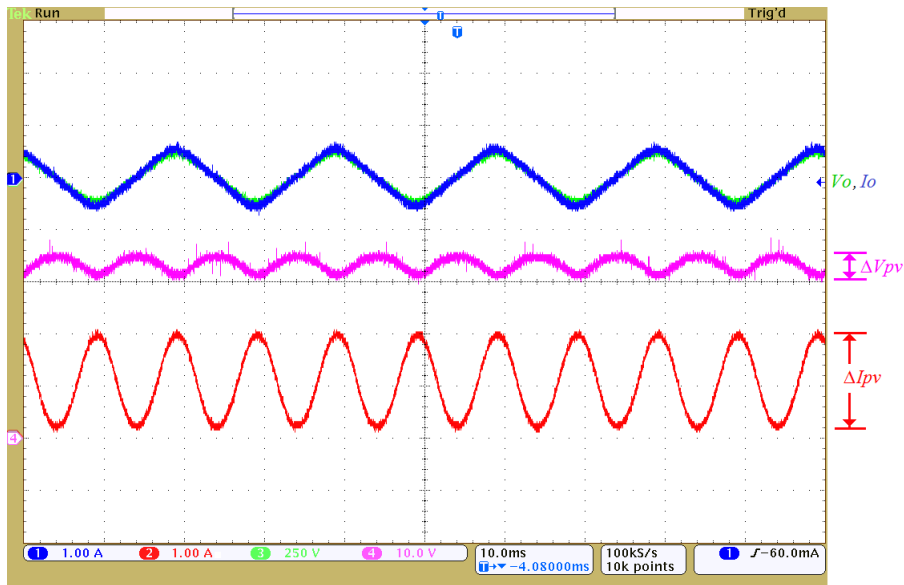


Fig. 4.39 Experimental results for Boost inverter and PV module integration. I_o (1A/div). V_o (250Volt/div). V_{pv} (10Volt/div). I_{pv} (1A/div). Horizontal scale = 10ms/div.

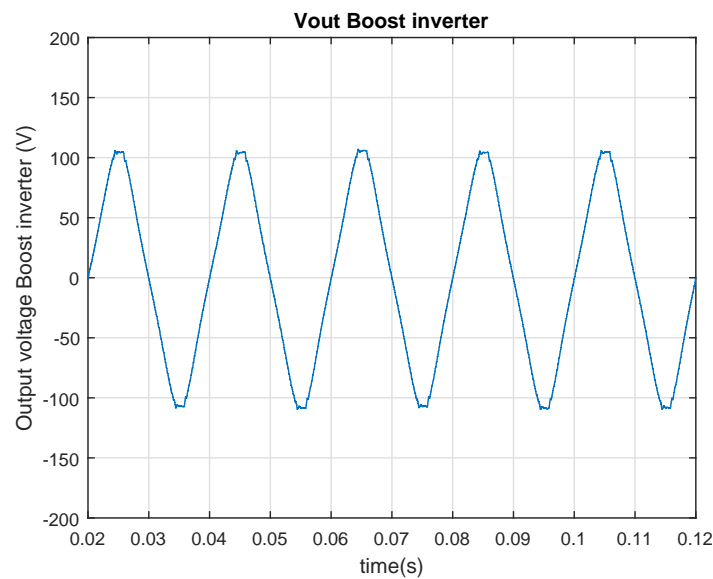


Fig. 4.40 Simulation results of Boost inverter output voltage

Finally, output voltage is slightly different of a quasi-sinusoidal signal because the relatively large variation of ΔD in order to achieve the appropriate gain to Boost the PV voltage. Then, according to these findings in stand-alone applications is advisable either to increase the number of PV modules connected in series or to include an

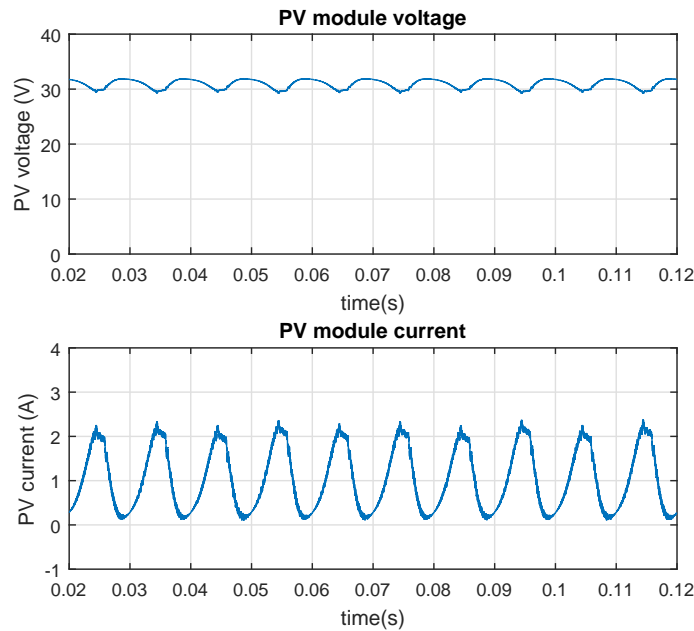


Fig. 4.41 Simulation results of current and voltage for the PV module under test

intermediate power converter stage to increase the input voltage avoiding the Boost inverter saturation.

Table 4.8 Mean Squared Error (MSE) of V_o Boost inverter model

	ΔD	$P_{Load}(W)$	$Irra.(W/m^2)$	MSE
Case 1	0.3	50	530	0.105
Case 2	0.3	50	602	0.237
Case 3	0.3	100	554	0.284

In the next section a model for the integration of the Boost inverter to the electrical grid will be presented.

4.4 Modeling of Boost inverter integration in Microgrids

4.4.1 The Boost inverter grid-connected model

The Boost inverter is suitable for integration of PV systems into microgrids. This integration requires the analysis of Boost inverter coupled to the grid. From this perspective, the following analysis using the component-based approach is employed to

model the integration of the Boost inverter into the electrical grids.

A Boost inverter is known as a micro-inverter when it is used to integrate a PV module with the electrical grid. Grid-connected micro-inverters require coupling inductors to limit the current toward the power system and to avoid short circuits. Fig. 4.42 shows a conventional equivalent RL circuit and an ideal AC source to represent the electrical grid [29]. Fig. 4.43 shows the equivalent circuit for grid-connection.

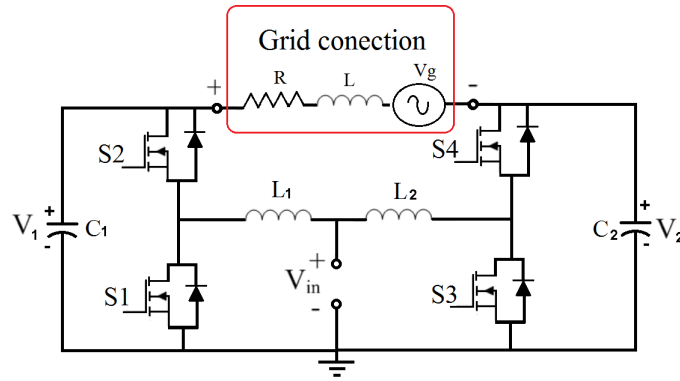


Fig. 4.42 Boost inverter integrated to the grid

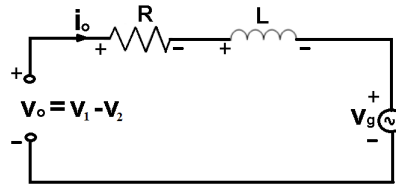


Fig. 4.43 Equivalent circuit grid connection

From Fig. 4.43, the coupling grid model is given by,

$$v_o = v_1 - v_2 \quad (4.33)$$

$$\frac{di_o}{dt} = \frac{1}{L} (v_o - v_g - i_o R) \quad (4.34)$$

$$i_{o_{K+1}} = \frac{h}{L} (v_{o_K} - v_{g_K} - i_{o_K} R) + i_{o_K} \quad (4.35)$$

Fig.4.44 shows the power system model of the Boost inverter grid-connected using the component-based methodology. In this diagram, eq.(4.35) is used to model the

grid-coupling stage. Additionally, a synchronized SPWM signal drives the power converter in order to ensure the synchronism between the electrical grid and the Boost inverter. Fig. 4.45 shows simulation results of Boost-inverter grid-connected model implemented in Simulink®. In Table 4.9 are listed the simulation parameters.

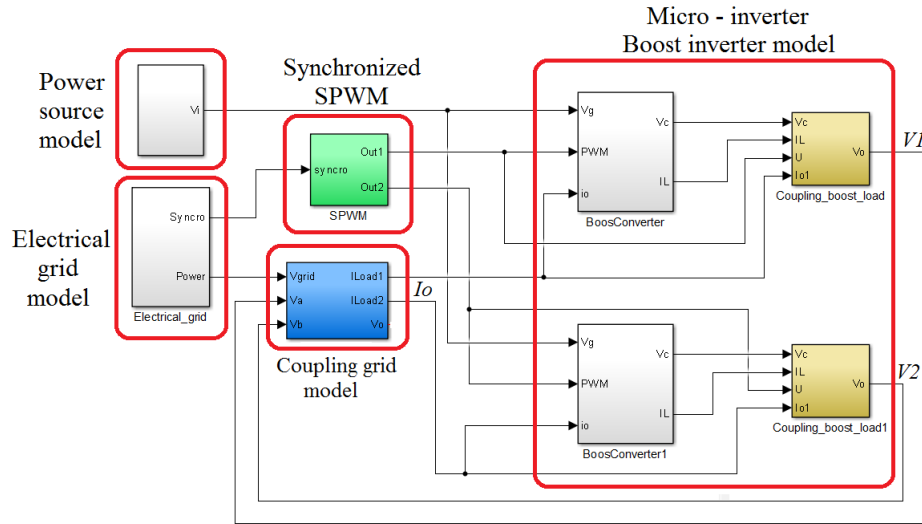


Fig. 4.44 Component-based model of Boost inverter grid-connected

Table 4.9 Simulation parameters

<i>Converter Parameter</i>	<i>Value</i>
L	$47 \mu H$
C	$10 \mu F$
R_L	0.1Ω
R_c	0.05Ω
R_{on}	0.18Ω
<i>Power source Parameter</i>	<i>Value</i>
V_{DC}	$80 V$
R_i	0.0Ω
<i>Grid-connected Parameter</i>	<i>Value</i>
V_{gmax}	$170 V$
L_g	$100 \mu H$
R_g	0.1Ω
<i>SPWM parameter</i>	<i>Value</i>
$F_{carrier}$	$100 KHz$
F_{modul}	$60 Hz$
ΔD	0.3

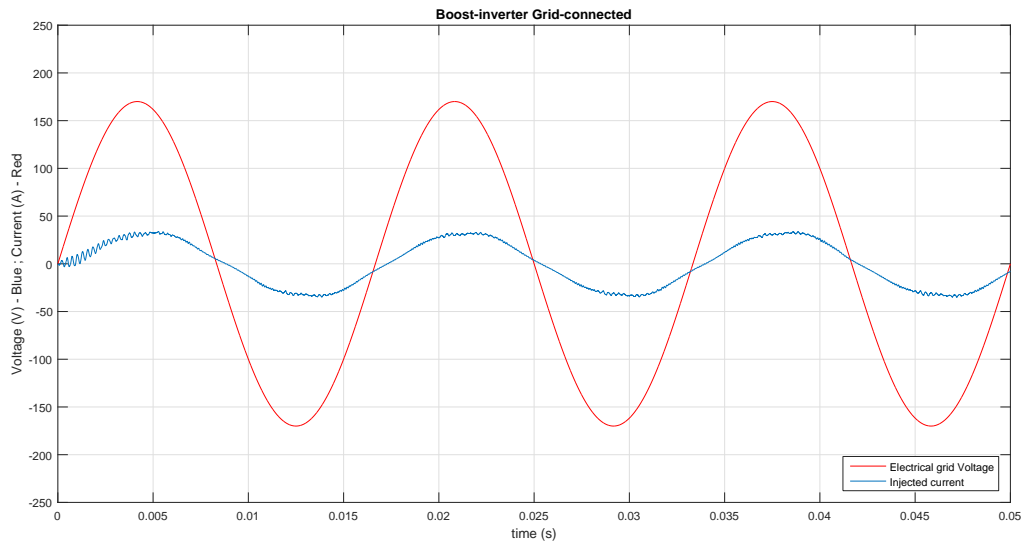


Fig. 4.45 Current injection of Boost inverter into the grid. Grid voltage V_g Injected current I_o .

Simulation results in Fig. 4.45 show that the Boost-inverter topology is suitable for integration into the electrical grid. Additionally, results reinforce the argument about the application of the component-based methodology to model power converters integrated to microgrids. In the next section the proposed approach will be extended to microgrid applications using a *multiple hierarchic approach*.

4.4.2 Boost inverter for integration of PV systems in microgrids

Presented models for integration *PV module - Boost inverter* and *Boost inverter - Grid* can be considered to form a complete PV chain grid-connected. Integration of these PV chains to the electrical grid allow accomplishing the first step to model a microgrid based on power PV systems. An illustrative simplify example of PV system grid-connected is shown in Fig 4.46. This system is analyzed and modeled in the diagram of Fig 4.47 using the component-base approach.

Simulation of this simplify microgrid model keeps parameters of Table 4.9 for the Boost inverters and Table 4.7 for the PV modules; however, V_{gmax} is set to 100V for avoiding inverter saturation. Additionally, Irradiance in this study case is different for each PV module where $Irr_1 = 950W/m^2$ and $Irr_2 = 810W/m^2$.

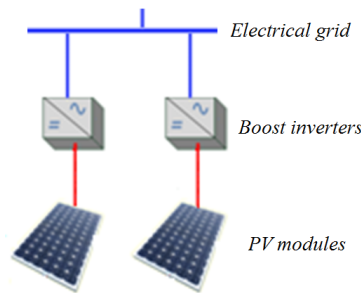


Fig. 4.46 Simplify PV system grid-connected.

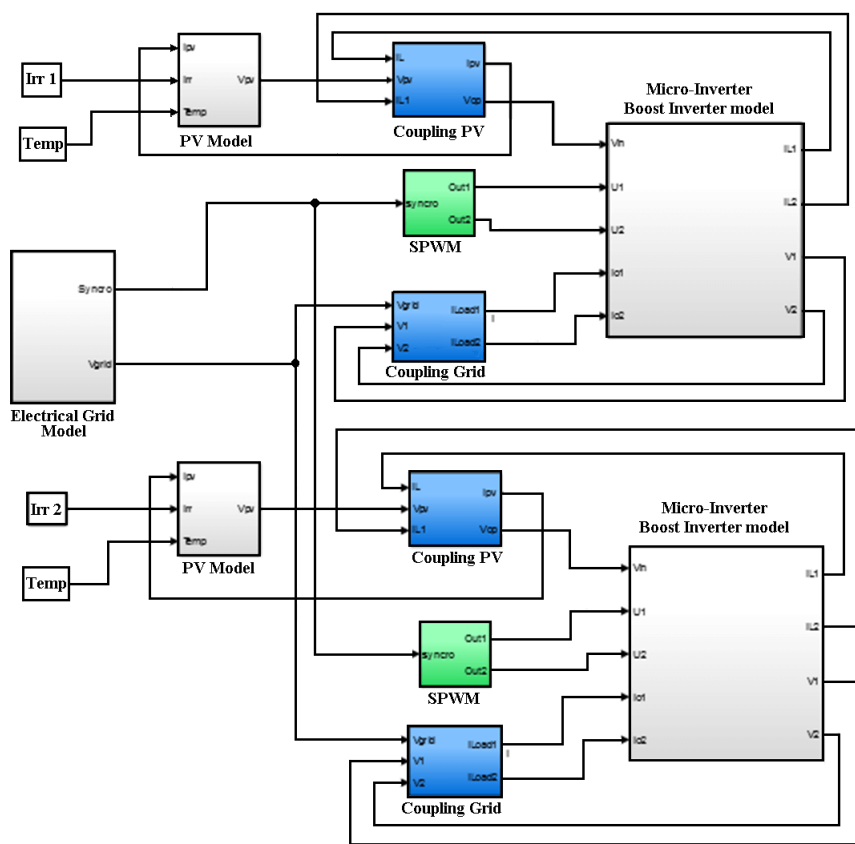


Fig. 4.47 Component-based model of simplify microgrid based on PV-Boost inverters.

Simulation results in Fig. 4.48 depicts the contribution of each micro-inverter to the injected current. In this case, the contribution is not uniform because irradiance is different for each PV module, and their relation $I-V$ is not linear. In addition, current waveforms are distorted because the system operates in open loop without a close loop control. Then, integration of Boost inverters in PV systems grid-connected requires robust and nonlinear control strategies which represent a research challenge as reported

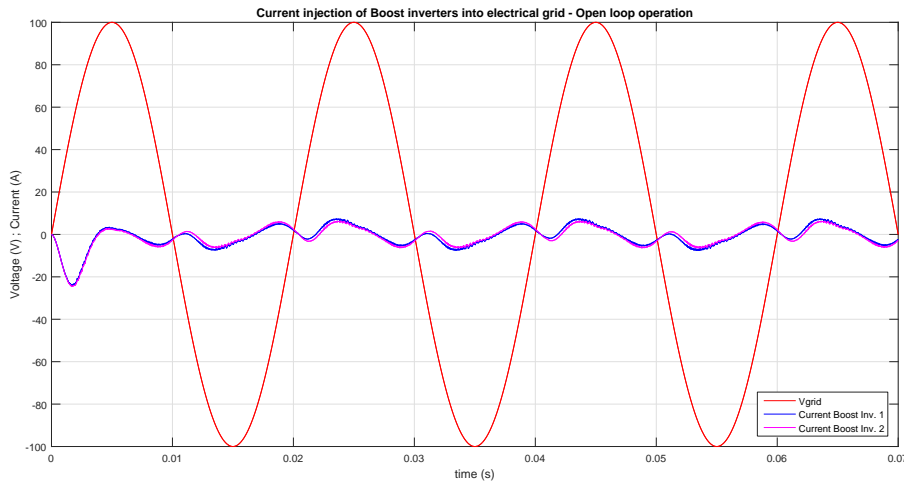


Fig. 4.48 Current injection of Boost inverters into microgrid in open loop operation.

in literature. Indeed, reported works in [84], [30], and [85] formulate advanced control techniques to regulate these systems.

Next section will introduce the concept of multiple hierarchic level modeling as an approach to integrated structural the model of components in a microgrid.

4.5 From component-based modeling to a multiple hierarchic level approach

As shown through this chapter, PV power systems integrated to microgrids are built by the interrelation of several components. These components include PV generators, power converters, and other associated elements. Therefore, a whole study of these power systems requires structural modeling strategies to deal with their complexity.

In order to contribute to this concern, in this work is presented a multiple hierarchic level approach intended to integrate structurally the microgrid component models. Fig. 4.49 represents this modeling approach which is totally complementary to the component-based methodology presented in this chapter. In Fig. 4.49, each modeled component is associated with components at the same level of hierarchic to generate models with higher complexity without lost of generality. Then, components at the same level either can be analyzed as whole or can be analyzed with higher detail in the lower level. In addition, this multiple hierarchic approach from component-based

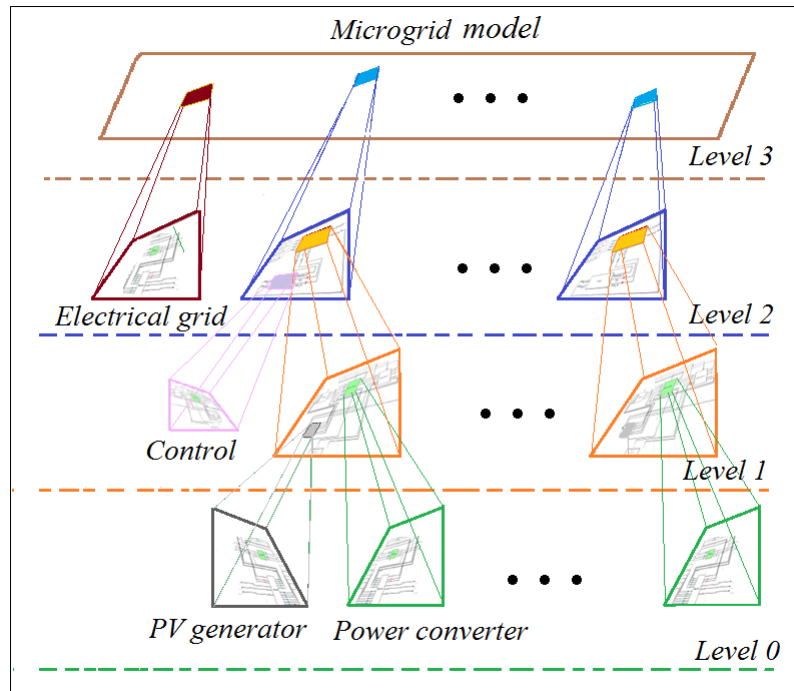


Fig. 4.49 From component-based modeling to multiple hierarchic approach.

models is suitable to be implemented in embedded hardware such as FPGA with a structural methodology which will be present in the next chapter.

4.6 Conclusion

Discussion of this chapter proposed a component-based methodology to model PV systems. This approach was employed to model Boost converter topologies. This methodology allowed modeling power converters independently of changes in the type of source or the load. Resulting models can be integrated with other models to generate more complex systems. This characteristic is relevant in the current evolution of power converters where continuous changes on their electrical borders should be evaluated.

Experimental and theoretical results validated the presented Boost converter models. Integration of these developed models with nonlinear sources and nonlinear loads showed suitable results. These results were able to reproduce in simulations the dynamic behavior of modeled components in comparison with the behavior of physical elements. As a consequence, successful results allowed to verify the accuracy, adaptability and

scalability of the proposed approach. Furthermore, results confirm the potential of proposed approach to emulate complex systems such as power PV systems integrated to microgrids. This chapter also introduces a multiple hierarchic level approach intended to integrate the developed models of microgrid components.

However, given the high degree of accuracy of the proposed models and the required computational load, a research challenge arises to implement these models for its use in the virtual prototyping of PV systems. This implementation requires a suitable trade-off between accuracy and execution time. In this context, the next section will introduce the free license tool HiLeS for developing embedded systems suitable to accomplish this purpose. Additionally, developed models will be implemented in FPGA given their powerful features of processing, adaptability, and scalability. These powerful features match with the component-based modeling approach presented through this chapter.

Chapter 5

PV System Modeling in Real-Time Using HiLeS

Contents

5.1	Introduction	95
5.2	Real-time emulation of PV systems in Microgrids	97
5.2.1	General context about real-time emulation of power systems	97
5.2.2	FPGAs for real-time emulation of power systems	101
5.3	HiLeS for real-time emulations of PV systems	103
5.3.1	HiLeS framework for developing real-time emulations	104
5.3.2	Mathematical framework for the integration of HiLeS projects	105
5.4	Modeling of shaded PV system using HiLeS	106
5.4.1	Shaded PV generator modeling using HiLeS	106
5.4.2	Numerical methods for implementation of PV models	109
5.5	Conclusion	112

5.1 Introduction

Previous chapters presented the modeling and integration of components in PV systems. *Chapter 2* discussed the aspect positives and negatives of these PV systems. *Chapter 2* remarked that the main drawbacks of PV systems are the inevitable shadows and the low reliability of centralized PV systems. Then, in *chapter 3* was studied the shadow phenomenon to better understand their nature and to provide more suitable

and accurate models. Following this line of thought, *chapter 4* was focused on the modeling and study of a promising decentralized power converter known as Boost inverter.

At this point, the present chapter is intended to recover the previous work of *chapters 3* to generate real-time emulation models. The purpose of these real-time emulation models is to bring useful tools for the study and development of complex systems such as PV power systems in microgrids. Then, these proposed models search to take advantages of real-time emulations [35][36]. However, the development of a platform for real-time emulation requires a well-structured design methodology which represents a research challenge because of the trade-off between adaptability and accuracy [37].

In this context, this chapter presents the free license tool HiLeS to develop embedded systems for real-time emulation of PV systems. HiLes framework is based on a top-down methodology able to aid in the design process of real-time emulation systems. Relevant feature of HiLeS is the automatic code generation from SysML specifications. In addition, HiLeS brings support to designers from the description of requirements stage until the final verification processes. These advantages arise because of the HiLeS framework is supported by two well-structured fundamentals, the SysML and the Petri nets background.

Processing devices are required to accomplish the high performance constrains in real-time emulation. Therefore, for this demanding task, FPGAs are selected as a processing device given their relevant features [33]. These features are suitable for real-time emulations and match perfectly with the component-based modeling approach. In addition, the HiLeS framework allows taking advantage of both FPGAs features and component-based modeling. Indeed, this framework can be extended to the multiple hierarchic level approach presented in *section 4.5* to develop complex embedded systems from well-defined structural components as shown in Fig. 5.1.

In the framework of this dissertation, the fundamental bricks to model the PV systems integrated to microgrids are the PV generator, the Boost inverter, and the control systems. This chapter presents the study and real-time emulation of shaded PV generators through the HiLeS framework for real-time emulation. The HiLeS framework is used to develop model in embedded hardware to decrease the execution time. Next chapter will be focused on the power electronics and control system stages.

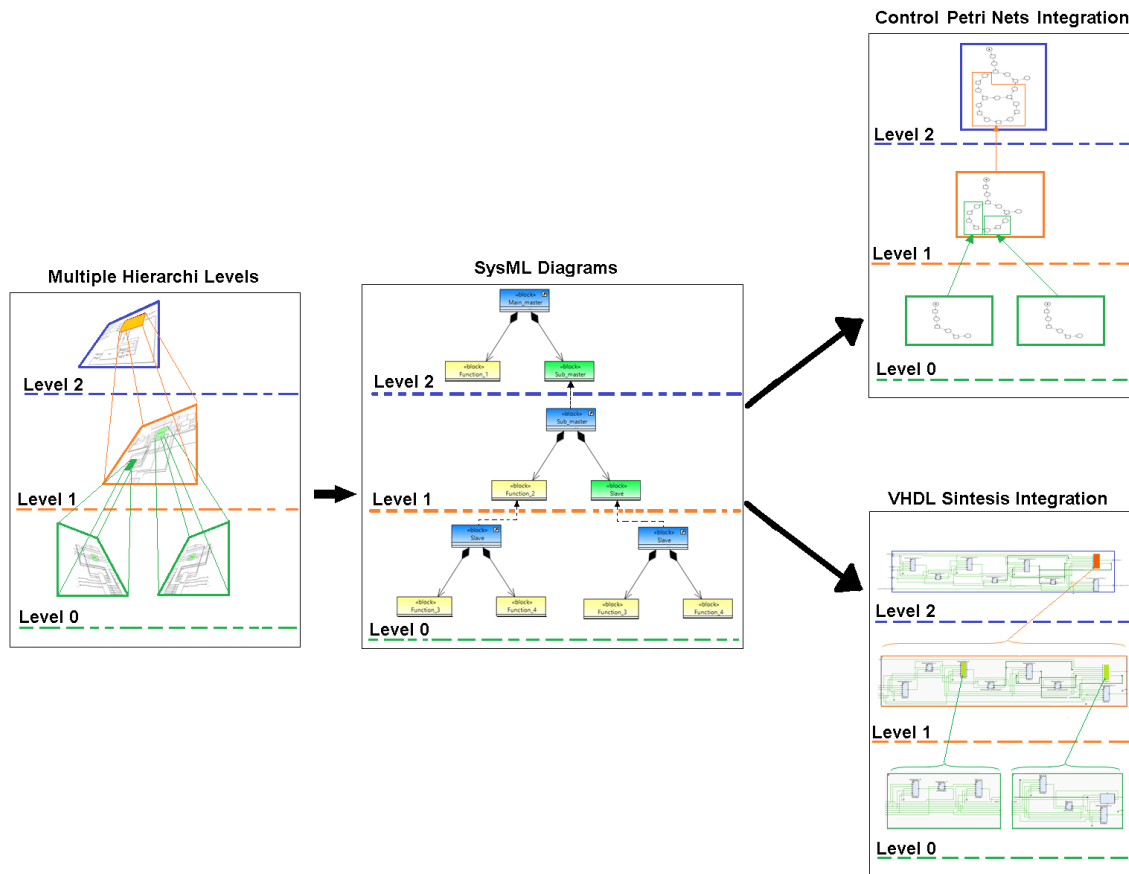


Fig. 5.1 HiLeS tool to design embedded systems with multiple hierarchic level

5.2 Real-time emulation of PV systems in Microgrids

5.2.1 General context about real-time emulation of power systems

A digital real-time emulation of the electric power system search to reproduce voltage and current waveforms with suitable accuracy. These signals are a representative behavior of the modeled power system being modeled. This aim requires a digital real-time emulator which is able to solve systems of equations in one time-step within the same time in real-world clock of sampling [82]. Therefore, it produces outputs at discrete time intervals, where the system states are computed at discrete interval times using a fixed time-step [86]. Two situations arise according to the time required by evaluate the model equations. If the execution time to calculate the model output

is shorter to the selected time step; then, the emulation is considered real-time. In contrast, if the emulation evaluates the model after the time-step an overrun occurs and the emulation is considered as non real-time or offline [86].

The real-time emulations are classified in two categories. The first category is full digital real-time emulation. In this category, all the emulation occurs inside of the processing device. The second category is the Hardware-in-the-Loop. For this category, an interchange of electrical signals occurs and digital-analog and analog-digital conversion are required. If the Hardware-in-the-Loop system involves real controller hardware that interacts with the rest of the simulated system, it is called controller hardware-in-the-loop (CHIL). On the other hand, any Hardware-in-the-Loop simulation involving power transfer the emulation is known as a power hardware-in-the-loop (PHIL).

According to Faruque et al. [86] a real-time emulator needs to solve a grid-scale model by roughly $50 \mu s$ or a smaller time-step to reproduce transients. Computing capability may be defined as the product of the number of nodes/buses in the simulated power network and the number of time steps. Additionally, smaller time-steps are required for power-electronic systems. In case of controlled digitally involve, high-frequency switching circuits may operate with a microcontroller having an internal clock speed with periods of $1 \mu s$ to $10 ns$. Then, an emulation of these system require more computing capability and the ability to emulate in the scale of nanoseconds.

Fig. 5.2, from [86], shows the relationship between computing nodes and time-step requirements for different systems. A real-time emulator is often configured to be scalable. The increment of computing power is possible by adding units where these individual computing units operate in parallel. However, communication between unit adds delays and communication bus become the system bottlenecks. Power processors or other hardware such as general-purpose central processing units (CPUs) work in parallel by sharing common memories or buses to minimize the communication latencies.

Recently, other trend in the real-time emulation field is the use field-programmable gate arrays (FPGAs) [87][60] that are gaining foundation as a computation hardware for real-time emulation. User-friendly block coding, automatic code generation capability, and interfacing capability allows to these hardware to be used as an auxiliary platform of large simulators that allow to model and then to simulate a system within a time-step

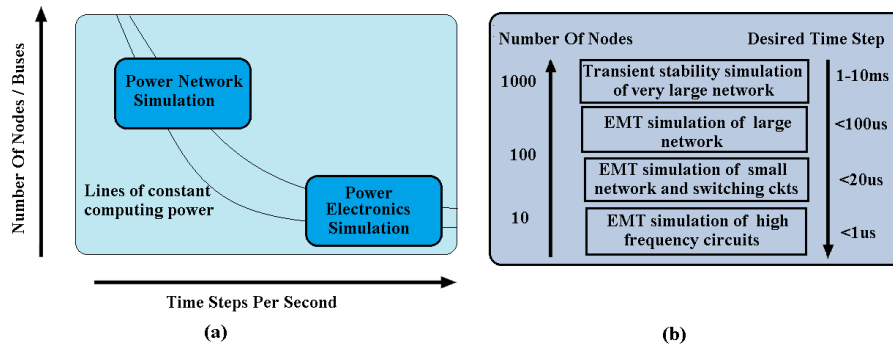


Fig. 5.2 Computing capability (a) and time-step requirements (b) for different types of simulation in power systems.

of nanoseconds [88]. Then, authors in [86] argue that these are other promising avenues for future exploration in the field of real-time emulation of the power system.

Virtual Prototyping Tools

The need for multidisciplinary virtual prototyping in power electronics has been well established; however, design tools capable of facilitating a rapid iterative virtual design process do not exist [89]. Rapid multi-domain physical simulation is the key enabling technology and the physical domains that are of interest in power electronic systems include electrical, EMI, thermal and mechanical. Then we conduct simulations to predict the effect that design choices (components, control algorithms) have on overall system performance. The requirements of this kind of tool is not ease to provide as it must:

1. ease the couple of the physical models with nonphysical models of linked components
2. support an efficient, automated process for generating these models from generally applicable and fundamental physics.
3. propose methods for description of the required multidisciplinary model
4. integrate design optimization techniques
5. provide user friendliness

The exiting solutions are both academic and commercial. In the academia the approach is to combine existing commercial physical simulation tools that are specialized

in one domain in a multidisciplinary design environment. These approaches present poor performance from speed and friendliness points of view.

An approach often used for multidomain physical simulation in power electronics is the circuit simulator plus imported equivalent circuit models of system properties expressed using relatively few simple ordinary differential equations. This manual process allows physical models in different domains to be combined in a common simulation platform with behavioral models of other system components.

One the most challenging problem is the integration or coupling of the various modeling tools and circuit simulators. The simulation tools available for this purpose are Modelica, MATLAB/SIMULINK, PSpice, PSIM, CASPOC, Synopsys SABER, ANSYS Simplorer, SIMSEN, MICROCAP, Scilab, Octave, KREAN, PSpice and GeckoCIRCUITS [90]. There is also the need to integrate simulators from domains as power systems, distributed generation systems, energy economics. We could mention tools as ETAP, SCADA, AnyLogic, PowerWorld, NREL PVWats, SimulationX [91].

Hardware-in-the-Loop Simulation Tools

Processes for engineering a system invariably include some degree of prototyping. Virtual prototyping can support initial system design work rapidly and efficiently, but as a system's design matures, the need for prototyping it physically increases. Hardware-in-the-loop (HIL) simulator could be defined as a setup that emulates a system by immersing faithful physical replicas of some of its subsystems within a closed-loop virtual simulation of the remaining subsystems. Hardware-in-the-loop (HIL) simulators are rapidly evolving from a control validation tools to a system modeling, simulation, and synthesis paradigm synergistic combining many advantages of both physical and virtual prototyping[92].

HIL simulators are taking more prevalence because its many advantages. In order to compare HiLeS IDE tool and better evaluate its contribution we must highlight the advantages below:

1. Cost effectiveness because it require less hardware than physical prototyping.
2. Rapid prototyping because the high capacity on chip, for example modern high complex FPGAs, controller prototypes, for instance, can be built rapidly and evaluated in the loop with virtual prototypes.

3. Fidelity and verisimilitude because by prototyping in hardware dynamics or other attributes that are not fully understood, HIL simulators often achieve fidelity levels unattainable through purely virtual simulation.
4. Simulation speed because hardware prototypes of complex physical phenomena run faster than purely virtual simulations of the same phenomena.
5. Repeatability because systems are tested in controlled lab settings through HIL simulation.
6. Safety because it is possible to simulate destructive events, to simulate a much broader range of operating conditions and to train humans.
7. Concurrent systems engineering because it allows different teams to develop different parts of a system in hardware without losing sight of integration issues.

Since the interactions between the physical and virtual components of a HIL simulator are bidirectional, it is crucial that the time steps match exactly between components. In consequence the virtual components must run in real time, which places hard time requirements on the HIL Real Time Digital Simulator (RTDS). Microprocessor based RTDS is ranging from 10^2 to 10^4 Hz time step, instead of FPGA based RTDS is ranging from 10^5 to 10^7 Hz time step. Hence fast microprocessors and even faster field-programmable gate arrays (FPGAs) are often used by HIL simulators to enable real-time virtual simulation. Commercial Power HIL simulators used in Power Electronics applications are OPAL RT, PLECS and Typhoon.

5.2.2 FPGAs for real-time emulation of power systems

The hardware for real-time emulation of power systems can be divided into the following categories [93], as shown in Fig. 5.3: (a) PC based, (b) custom processor based, (c) supercomputer based, and (d) field programmable gate array (FPGA) based. The PC-based uses general-purpose multicore processors that run on RT-Linux real-time operating system. Custom-processor-based real-time emulation are based on Power PC reduced instruction set computing (RISC) processors. Supercomputer-based real-time emulation are based on machines with large computational platform, such as Silicon Graphics International Corporation (SGI) supercomputers. The fourth type of emulator makes use of FPGAs as the main computational hardware that is used for both small-scale simulation activities [94] and large-scale systems [88].

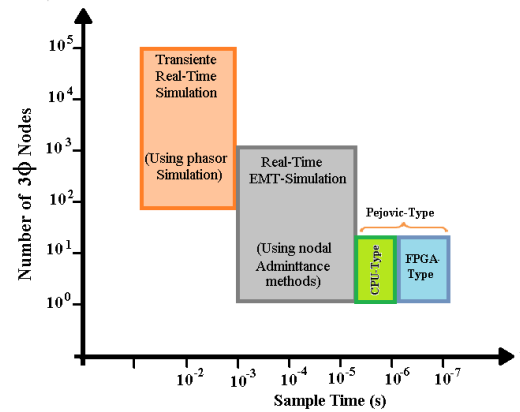


Fig. 5.3 Emulation methods and relevant time steps for real-time applications.

Three main solver approaches are applied in real-time emulation: the classic nodal admittance (CNA), the state-space nodal (SSN), and the Pejovic approach also commonly known as the associated discrete circuit (ADC) method [95]. The method Pejovicis extremely rapid because no matrix inversion is required. However, the method can be accurate only when using very small time steps, typically below $3 \mu s$. Simulation on FPGA is a good solution to achieve this particular performance. However, the coding of complex solvers for FPGAs is still very complex and often requires low-level FPGA programming expertise. Fig. 5.4, from [93], depicts the frequency range versus simulation complexity for electric power systems. In this figure high frequency emulation above 100 KHz are feasible for FPGA and represent a research challenge according to Lauss et al. [93].

To summarize this section, FPGAs are suitable devices to emulate electrical and electronics power systems in a wide range of frequencies and applications. However, main drawback of FPGAs is the complexity for developing code. Indeed, authors in [87] highlights the potential of FPGAs for application Hardware-in-the-Loop simulations; however, tools to take more advantages of these devices are still required. For these reasons, in next section will present the HiLeS framework as a tool to develop embedded systems in order to contribute with a structural methodology to take advantages of FPGAs and decrease the effort in the design process.

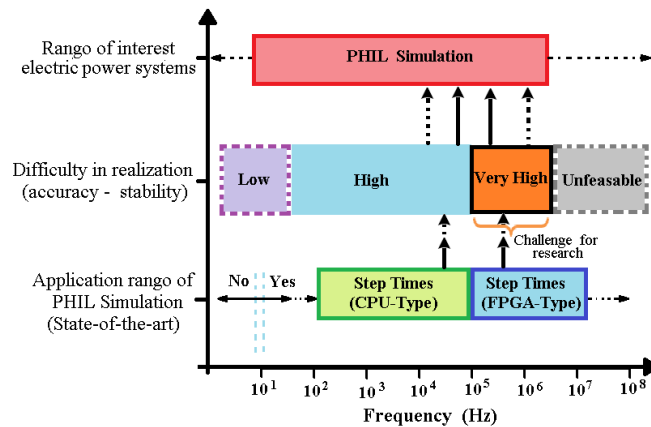


Fig. 5.4 Comparative diagram frequency range and emulation complexity for electric power systems.

5.3 HiLeS for real-time emulations of PV systems

The HiLeS framework was developed for aiding to embedded system designers during the design process. The HiLeS framework purpose is to serve as a platform to create Embedded System Product Lines. It incorporates both tools developed by the group and open source tools to provide an Integrated Development Environment (IDE) suitable for system specification, product line construction and virtual prototype generation [96] [97]. The HiLeS framework serves as a tool for:

- System-level design in SysML
- Visualization and validation of the system-level model in SysML (Papyrus Editor)
- Automatic Virtual Prototype (VP) generation in Hardware Description Language.
- Visualization of intermediate models
- Interface to TINA: formal Petri Net verification tool for HiLeS model validation

Figure 5.5 shows the HiLeS Model Transformation Chain, which includes support to Papyrus for SysML modeling. The transformation rules start from the formal representation of the requirements in SysML and go through to the creation of a virtual prototype described in a hardware description language (HDL) and in a Petri Net code. It is assumed that the HiLeS meta-model is the pivot calculi model. The automatic transformations included are described below [98]:

Tr_1 is responsible for transforming the structure information in the SysML model to HiLeS.

Tr_2 is responsible for transforming the behavior information in the SysML model to HiLeS. One of the advantages of using Activity Diagrams is that they are based on Petri Nets and since in the HiLeS formalism behavior representation is based on Petri Nets, the transformation is more straight forward than with sequence diagrams.

Tr_3 is responsible for transforming the HiLeS Model to a HDL (Hardware Description Language) model, designer could choose VHDL-AMS, VHDL or VERILOG-AMS, VERILOG.

Tr_4 is responsible for transforming a VHDL-AMS model to VHDL-AMS code (virtual prototype), which will be simulated and allow verifying design requirements

Tr_5 is responsible for extracting from the HiLeS Model the embedded Petri nets and transforming to TINA net code, which will be analyzed to test properties as boundedness, liveness, etc.

Tr_6 is responsible for generating the Verilog-AMS model, and

Tr_7 is responsible for generating the Verilog-AMS code.

A detail description of HiLeS formalism can be consulted in Appendix C.

5.3.1 HiLeS framework for developing real-time emulations

The HiLeS framework is a tool to develop embedded system of general use; however, in this work HiLeS is used to design embedded systems intended to real-time emulations of PV systems. The proposed design methodology is represented in Fig. 4.49 of section 4.5. This approach takes advantages of HiLeS framework to implement the multiple hierarchic level approach from developed models using the component-based approach.

In order to achieve this goal was implement the multiple hierarchic level method in HiLeS as shown in Fig. 5.1. Details of this contribution to the methodology are presented in Appendix D. This scalability of HiLeS project is also formalized by means of the Petri nets theory. Next section develops the mathematical framework to val-

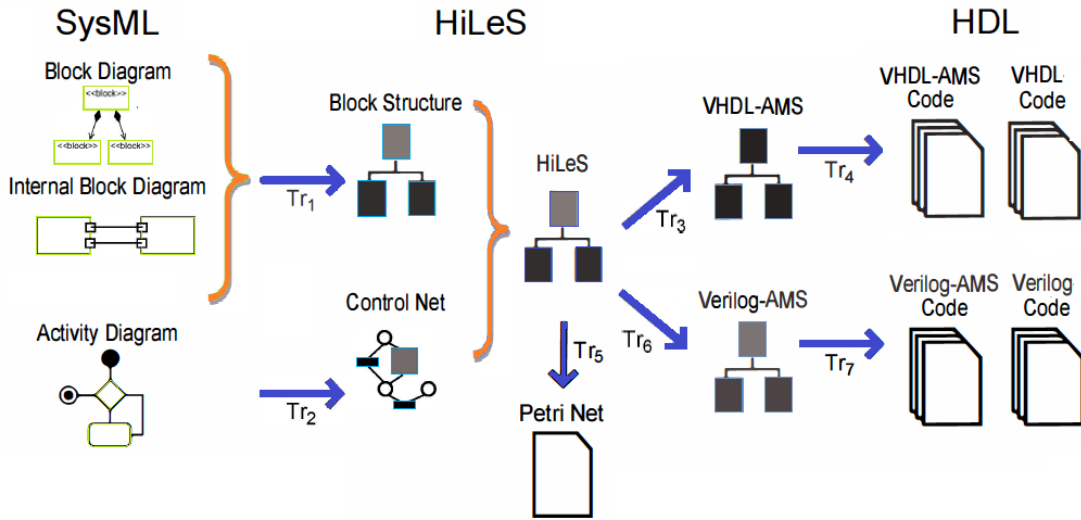


Fig. 5.5 HiLeS model transformation chain

idated the HiLeS projects integration, and further sections present the modeling of fundamental brick of PV systems using the HiLeS framework.

5.3.2 Mathematical framework for the integration of HiLeS projects

A HiLeS project is expressed as a hierarchy of Structural blocs arranged in any number of description levels. Each Structural bloc correspond to a behavioral action. A Structural block should be specified as a set of functional blocs and a HiLeS control net (*HCN*). The *HCN* is responsible of sequencing the operations or actions performed by the functional blocks. A *HCN* is a totally synchronized Petri Net, where every transition has an associated event corresponding to the completion of an operation or an action of a functional block [99].

Definition 1

A HiLeS Control Net *HCN* is a triple $\{R, E, S\}$ such that: R is an Ordinary Simple Petri Net, E is a set of events corresponding to the functional block completion signals and S is a complete function from the set T of the transitions of R to E . For validation purposes R is tested for correctness. Correctness is understood as *HLS* has the properties of Boundedness and Liveness.

Boundedness

Property 1

The condition that R be safe for an initial marking m_0 is sufficient for the HCN to be safe for the same initial marking. The HCN should be safe in order to exclude operations or actions (functional blocs) invoked twice or more at the same time. An functional block should be invoked always after its last completion but not before.

Liveness

Property 2

The condition that R be live for an initial marking m_0 is a necessary and sufficient condition for HLP to be live for the same initial marking.

Property 3

The condition that R be deadlock-free for an initial marking m_0 is sufficient condition for HCN to be deadlock-free for the same initial marking.

System Integration

In a HiLeS project a number of description levels can follow on from one another. From the HCN point of view, a transitions of the level $i + 1$ could represent complex operations of the level i , downwards in the hierarchy. The process of replacing a transition This process could be done top-down or bottom-up seamless assuring the system integration and the reuse of projects and blocks. The transformation rules from one level to the next are specified in a way that a transitions is always replaced by a "well formed" HCN . This rules are done in a way that the properties boundedness and liveness are preserved. The final model will exhibit the properties preserved by the well formed blocks.

5.4 Modeling of shaded PV system using HiLeS

5.4.1 Shaded PV generator modeling using HiLeS

Accurate partially shaded PV models are challenges to calculate in real-time because of their non-linearity and complexity. In this context, the HiLeS framework is employed to

develop computational units adapted to the shaded PV model characteristics presented in *chapter 3*. The following simplify example illustrates the design approach based on HiLeS to emulate a shaded PV system.

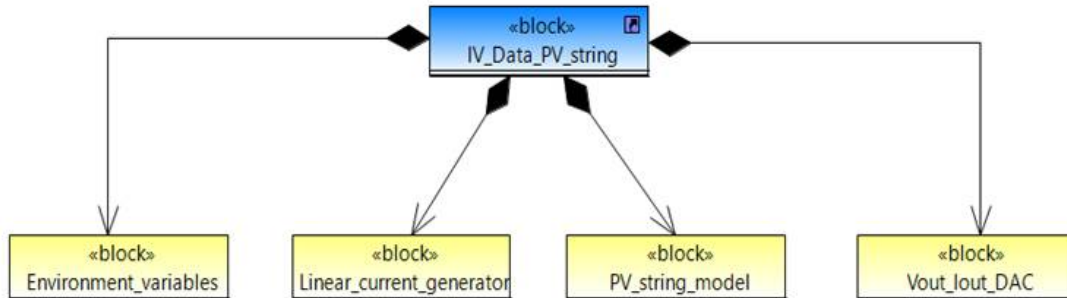


Fig. 5.6 Partial Block Definition Diagram for PV model emulation

The partial Block Definition Diagram of Fig.5.6 depicts the main components for shaded PV model emulation in FPGA. Fig.5.6 shows that the system has four components. The first component provides information about environmental variables. The second component models a linear current source as an input to the PV model. The third component represents the partial PV model. The last component in this diagram is intended to interact with Digital-to-Analogical converters to provide analogical signal from digital model information.

After defining components in the Block Definition Diagram, component interactions are described in the Internal Block Diagram. Fig.5.7 shows the information flow among the defined components. In this stage, the central component is the PV model which receives predefined information about external variables. The preset external variables to the model are the cell temperature, solar irradiance, shading patron considering the shadow coefficients δ_n more relevant for the operation state, and a current signal emulated by a linear current source. At this point, the PV model processes the input information and sends digital data results to the component in charge of establishing communication with Digital-to-Analogical converters.

Finally, Activity Diagrams represent the operation sequences and the model computational processes. Fig. 5.8 depicts the operation sequence for the Internal Block

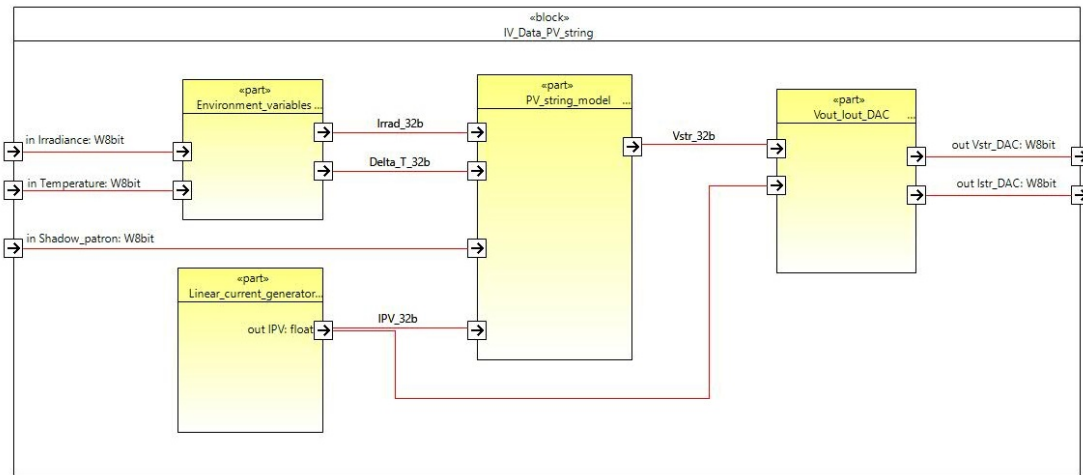


Fig. 5.7 Partial Internal Block Diagram for PV model emulation

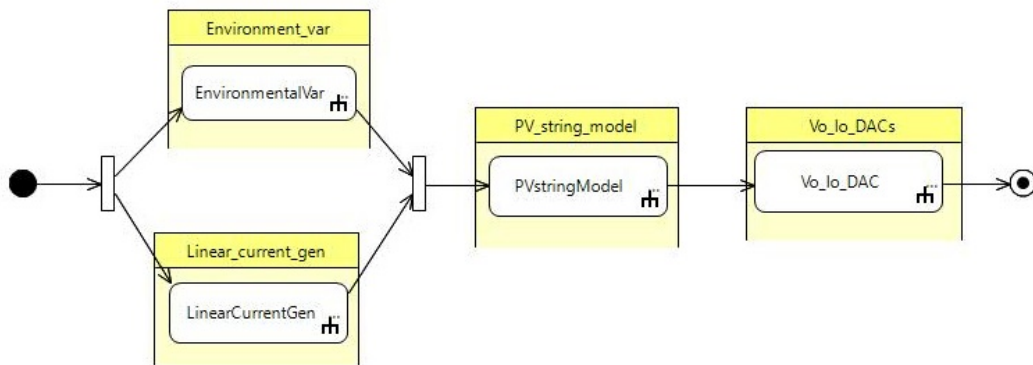


Fig. 5.8 Partial Activity Diagram for PV model emulation

Diagram of Fig. 5.7. In this stage, the equations from the PV model are solved using the powerful computing features of the FPGA.

Fig.5.9 shows the results of scaled signals to emulate in FPGA the unshaded and the partially shaded PV module behavior. The processing time to evaluate a point in the I-V curve is $10.5\mu\text{s}$ and approximately 4ms to generate an I-V curve suitable to real-time applications according to fast computing methods reported in literature. Related works of fast computing methods for PV modeling such as [19] presents a response time of 23ms to compute an unshaded I-V curve or authors in [20] argue a computing time around $10\mu\text{s}$ to evaluate a complex thermal and electrical PV model.

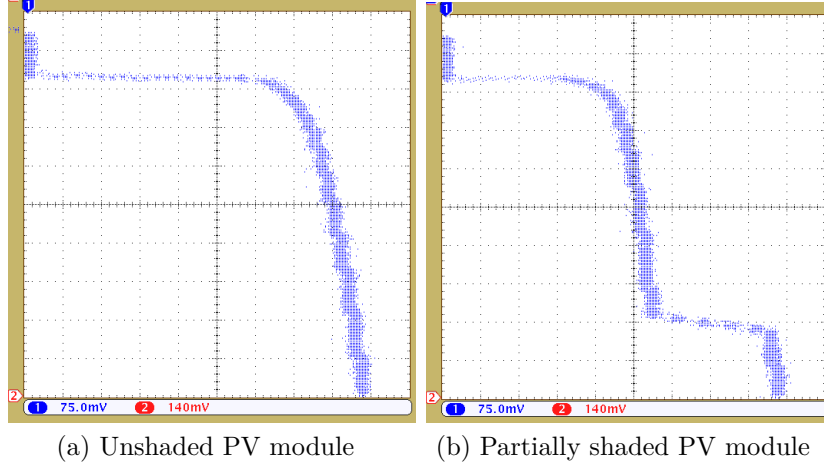


Fig. 5.9 Generated signals in FPGA to emulate a partially shaded PV module

5.4.2 Numerical methods for implementation of PV models

Solution of eq.(3.14) in *chapter 3* describes the behavior of shaded PV systems. The numerical method usually employs to solve this type of nonlinear equations is the Newton-Raphson method [100]. This iterative numerical method is given by,

$$V_{dn+1} = V_{dn} - \frac{f(V_{dn})}{f'(V_{dn})} \quad (5.1)$$

Eq.(5.1) shows that implement the Newton-Raphson method requires a high degree of computational effort due to the evaluation of $f'(V_{dn})$. As a result, we proposed employing a modified Newton-Raphson method. This proposed method evaluates the discrete derivative of $f(V_{dn})$ from,

$$f'(V_{dn}) = \lim_{h \rightarrow 0} \frac{f(V_{dn} + h) - f(V_{dn})}{h} \approx \frac{f(V_{dn} + \Delta V) - f(V_{dn})}{\Delta V} \quad (5.2)$$

where ΔV is selected to ensure the quadratic convergence for the proposed method. The modified Newton-Raphson method is then,

$$V_{dn+1} = V_{dn} - \frac{(\Delta V) f(V_{dn})}{f(V_{dn} + \Delta V) - f(V_{dn})} \quad (5.3)$$

Eq.(5.3) decrease the computational effort because the function $f(V_d)$ is only evaluated and not $f'(V_d)$.

FPGA-based real-time emulation of shaded PV systems

The FPGA-based computational unit developed in SysML to emulate in real-time the behavior of shaded PV systems from method presented in previous section is shown in Fig.5.10 and Fig.5.11.

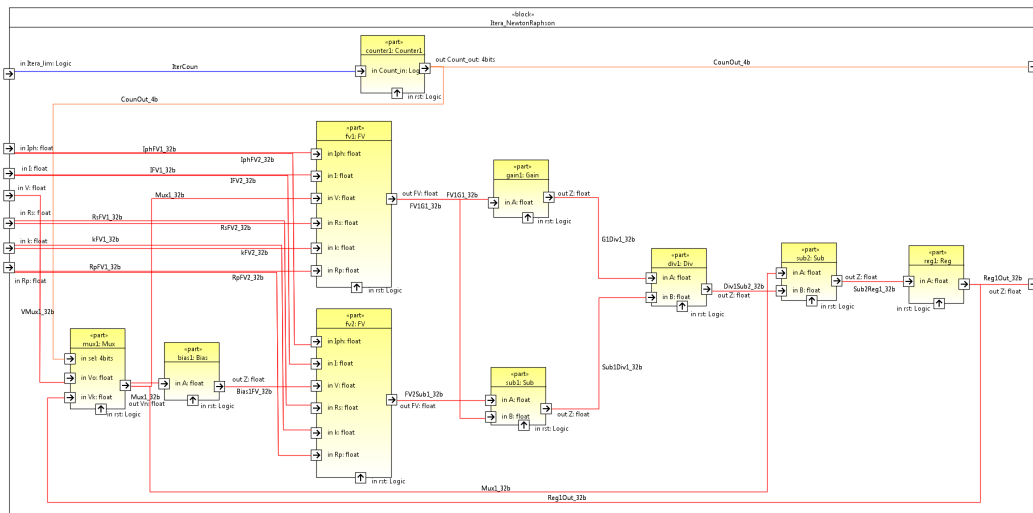


Fig. 5.10 IBD modified Newton-Raphson method.

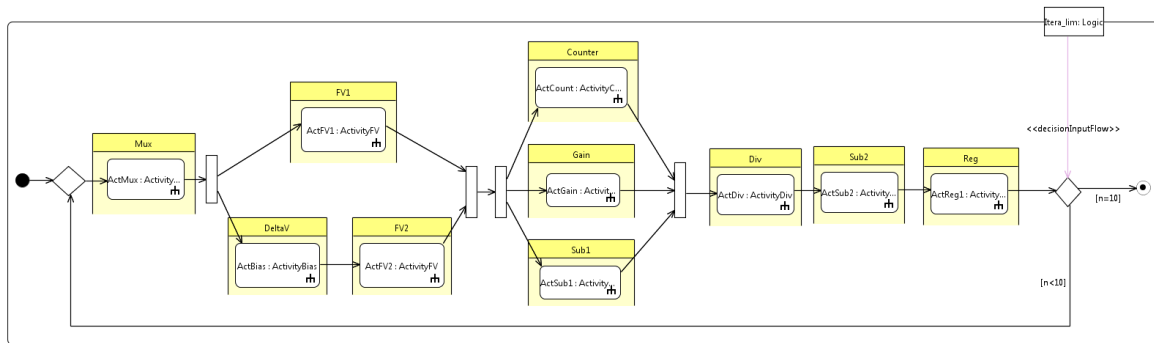


Fig. 5.11 Activity Diagram for modified Newton-Raphson.

Calculation results of implementation are compared with a conventional computational approach for a PV module with a single shaded cell as shown in Fig.5.12. The execution time for this shaded PV model is around $8.3\mu S$ which is a suitable time for real-time applications. Fig.5.13a and Fig.5.13b show the experimental emulation results for a PV module in normal operation and for a PV module with a single shaded cell. Table 5.1 summaries the used hardware.

Table 5.1 Hardware used for emulating the shaded PV systems

Device	Reference	Description
FPGA	XC7Z020-CLG484	Resource utilization: LUT 15%; Flip-flops 5%; DSP 10%
DAC	AD5541A	High-speed 16-bit DAC.

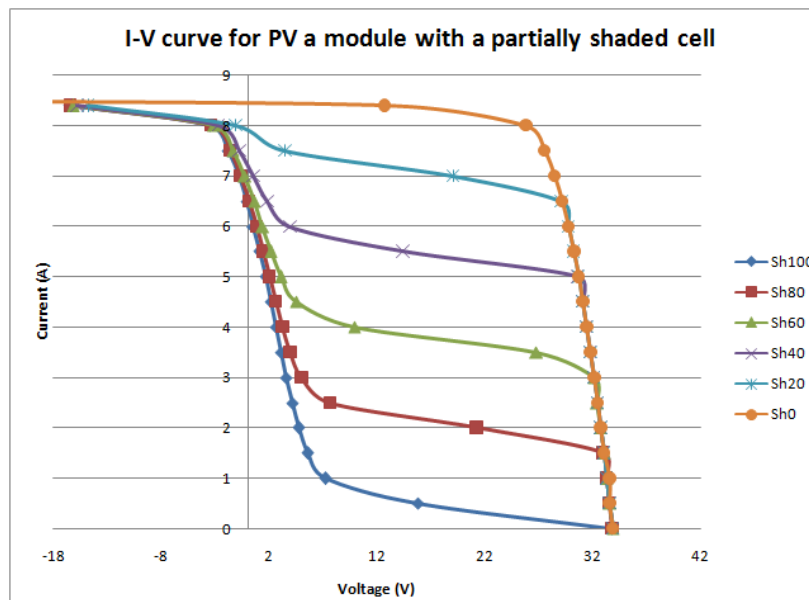
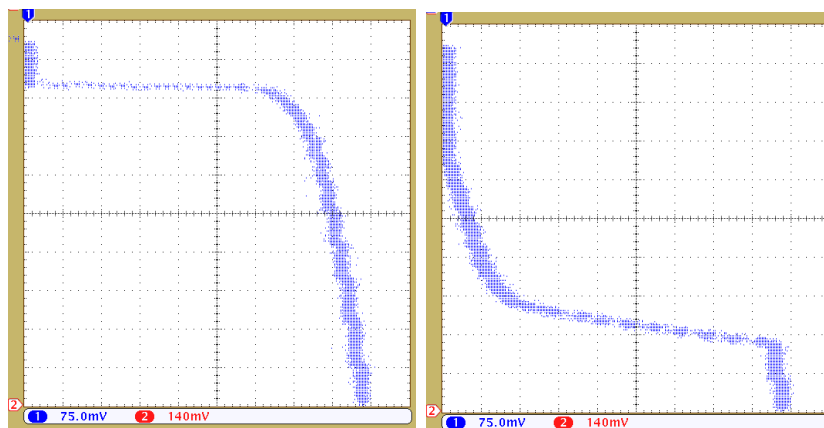


Fig. 5.12 Calculated I-V curve for a PV module with a single shaded cell and several partial shaded areas.



(a) Unshaded PV module

(b) I-V curve emulation of PV module with single shaded cell and fault in a by-pass diode.

Fig. 5.13 Generated signals in FPGA to emulate a partially shaded PV module with fault in a by-pass diode

5.5 Conclusion

In this chapter was introduced the HiLeS framework to implement models of PV system components in FPGA for real-time emulation. The HiLeS framework allows implementing the model developed using a component based approach. As a consequence, these tests on the developed platform shown their potential to implement more complex models of microgrids using the multiple hierarchic level approach from model defined using the component-base approach. In addition, performance of implemented models confirm their features for real-emulation.

In order to achieve the aim of integrating projects in HiLeS a transformation rule was formulated and features of Papyurus were considered as explain in the Appendix D. In this section, the mathematical framework to validated these integration also was presented using the Petri nets theory.

The proposed real-time PV models have correctly emulated the behavior of actual PV modules under several working conditions. It was validated the accuracy and versatility of proposed emulating approach. SysML made easier the development and verification of architectures before model implementation in FPGA. Next chapter will be focused on the power electronics and control system stages.

Chapter 6

Real-Time Emulation of Boost Inverter and Slide-mode Control Design

Contents

6.1	Introduction	113
6.2	Modeling and emulation of Boost inverter using HiLeS	114
6.2.1	HiLeS framework to model and emulate the Boost inverter	115
6.3	Design and emulation of control systems for the Boost inverter	118
6.3.1	Experimental test-bench to validate digital controllers	119
6.3.2	Slide-mode control for the Boost inverter	120
6.3.3	Slide-mode control implementation with HiLeS	125
6.4	Conclusion	132

6.1 Introduction

Previous chapter introduced the modeling and emulation of power systems in real-time. In *chapter 5* was studied and modeled in real-time the PV generator. In contrast, this chapter will be focused on the real-time emulation of the power converters using a case of study the Boost inverter.

At this point, the current chapter is intended to recover the previous works in *chapter 4* to generate real-time emulation models. The purpose of these real-time emulation models is to bring useful tools for the study and development of complex power systems in microgrids. Then, these proposed real-time models search to take advantages of accuracy and adaptability of developed models.

This chapter presents fundamental real-time models of power converters for further studies in microgrids. These fundamental concepts are used to model the Boost inverter. In addition, the developed models in a real-time platform are used to design and implement control systems. The control system studied in this chapter is the slide-mode control given their non-linearity and robustness properties.

First, this chapter presents the application of the real-time emulation method on the Boost inverter. Next, the slide-mode control is presented and a digital approach is developed. Finally, the HiLeS framework is used to design and implement in FPGA this digital slide-mode control.

6.2 Modeling and emulation of Boost inverter using HiLeS

Hardware-in-the-Loop (HIL) simulation is a cost-effective and safe method to test and emulate physical devices. HIL in power electronics allows designing and evaluating control systems, power converters, and power devices in a safety environment before actual interconnection of physical system. Usually the HIL methodology requires powerful processing devices and tools to develop the models for real-time simulations. As a consequence, FPGAs are suitable processing devices for these applications given their features of parallel processing, execution time, and hardware adaptability.

However, HIL emulations based on FPGA require tools to decrease the design complexity. In this context, the HiLeS framework provides a free license design tool to automatically generate VHDL code. This code is intended to implement in FPGA high level models described by SysML. This section will present the HIL model for the Boost inverter for further design and emulation of their control systems.

6.2.1 HiLeS framework to model and emulate the Boost inverter

The modeled Boost inverter (Fig.6.1) in *section 4* through the component-based approach is represented by SysML diagrams in this section. The Block Definition Diagram of Fig.6.2 shows the main components of this power electronics system.

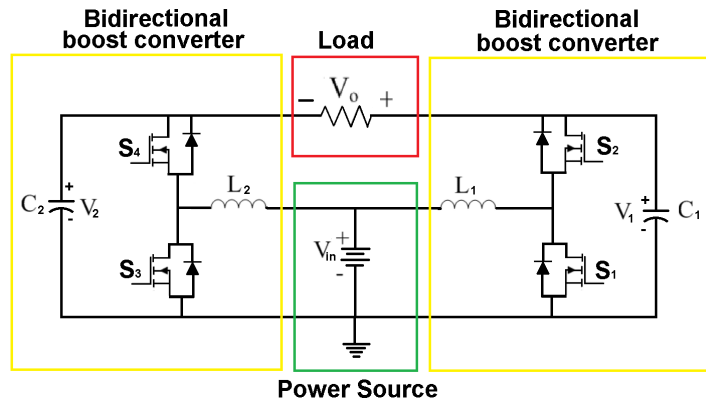


Fig. 6.1 Boost inverter based on functional components

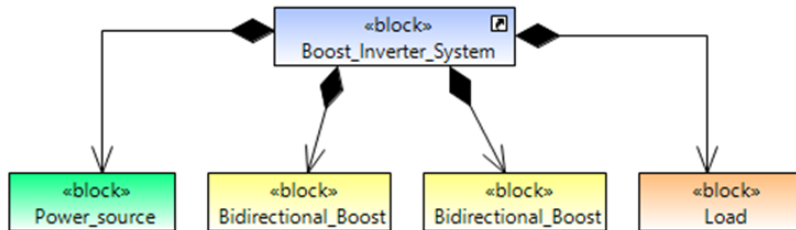


Fig. 6.2 Partial Block Definition Diagram

The activity diagram of Fig. 6.3 shows the components interconnections. Finally, Fig. 6.4 shows the partially Activity Diagram to describe the computational process to evaluate the bidirectional Boost converter behavior using equations of *section 4*.

The VHDL code generated from the SysML models is synthesized in the Artix-7 series FPGA using the Vivado Design Suite WebPACK Free Edition. Synthesis is shown in Fig.6.5. Fig.6.6 depicts the VHDL simulation results of the V_c and I_L signals for the bidirectional Boost converter model in an open-loop start-up. Fig.6.7 shows the single PWMs pulses $U1$ and $U2$ and the resulting I_L signals. As shown in Fig.6.7, the achieved time step is around 500nS which is suitable for real-time applications.

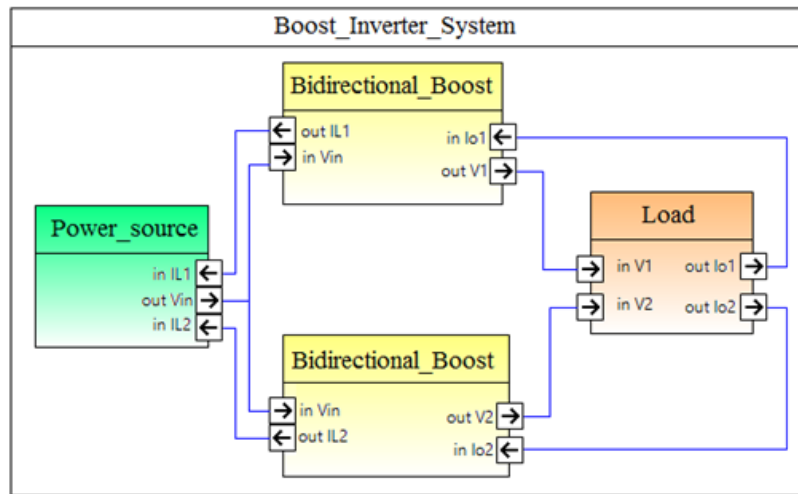


Fig. 6.3 Partial Internal Block Diagram

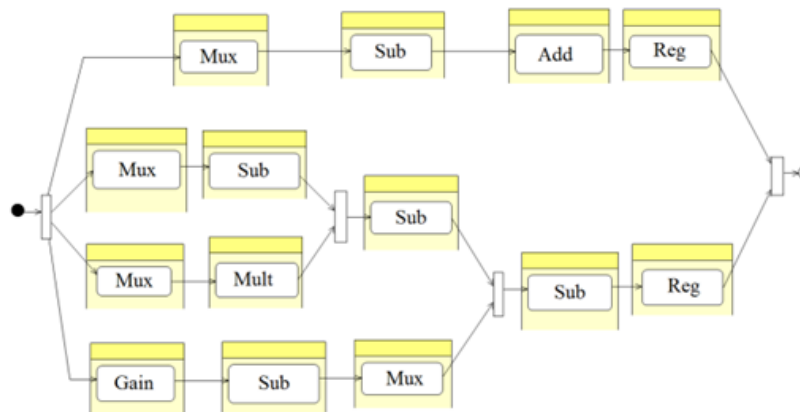


Fig. 6.4 Partial Activity Diagram

Fig.6.8 shows the setup experimental to compare the Boost inverter modeled in FPGA and the physical prototype. Comparison results are shown in Fig.6.9a and Fig.6.9b. Comparison results confirm that component-based methodology is able to be implemented in FPGA with suitable results in agreement with physical converters. In addition, next section will explain the design and verification of control systems for the Boost inverter using the developed virtual prototype.

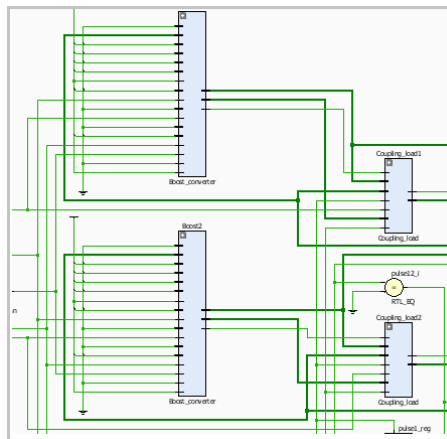


Fig. 6.5 Partial synthesis of Boost inverter model in FPGA

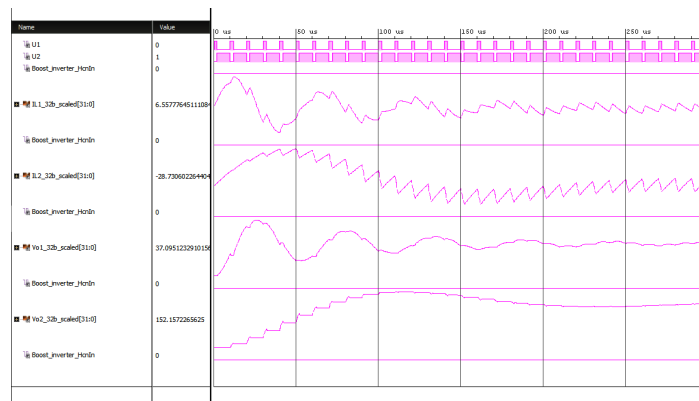


Fig. 6.6 Simulation of Boost inverter inrush currents

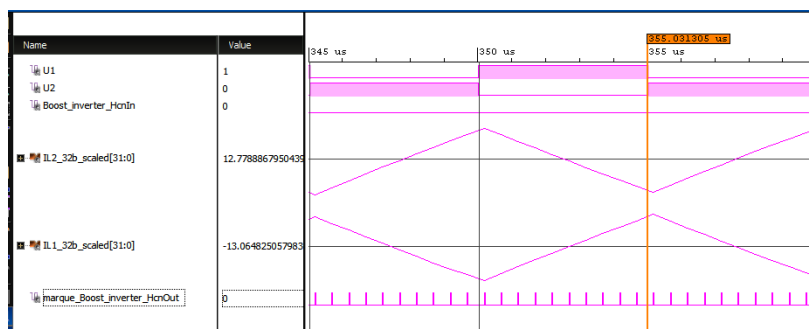


Fig. 6.7 Time step of 500ns for Boost inverter model

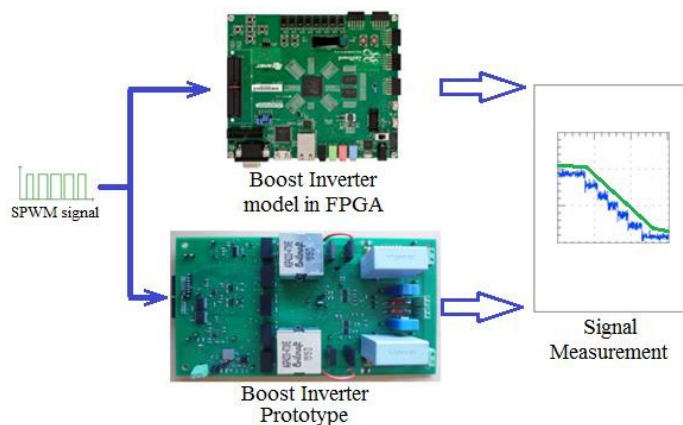


Fig. 6.8 Test of Boost inverter emulation in FPGA and physical prototype

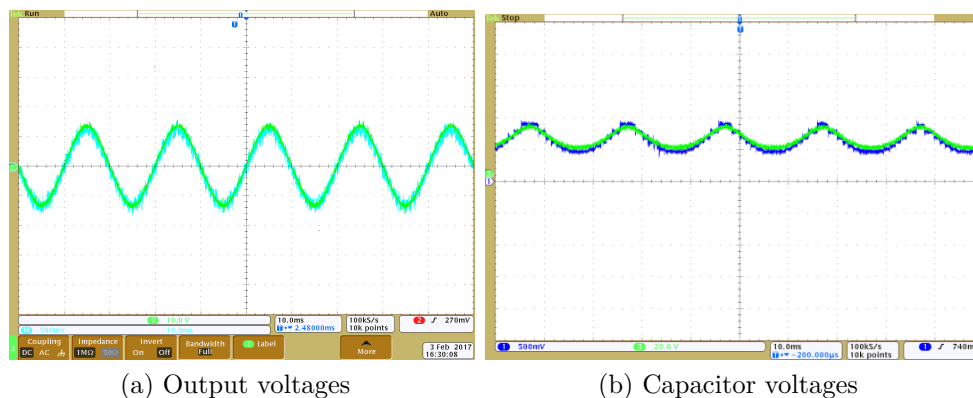


Fig. 6.9 Synchronization of Boost inverter prototype and model in FPGA

6.3 Design and emulation of control systems for the Boost inverter

The Boost inverter is a versatile architecture able to supply power according to the control strategy. In the current literature, analog control techniques have been designed and implemented to drive the behavior of the Boost inverter. As an alternative of design and implementation, a digital control is used in this section to take advantage of its design flexibility and operation adaptability. This section presents the slide-mode control design using SysML and HiLeS for an adequate implementation in FPGA. The slide-mode control is emulated in VHDL using a HIL approach and compared with expected results.



Fig. 6.10 Setup experimental for control design and validation

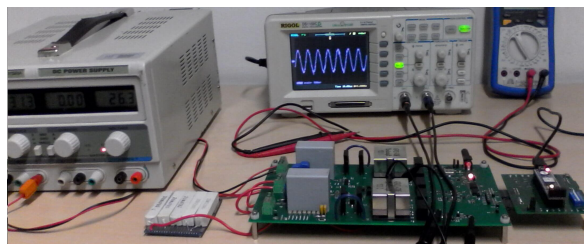


Fig. 6.11 Final prototype controlled by an FPGA XC7A35T

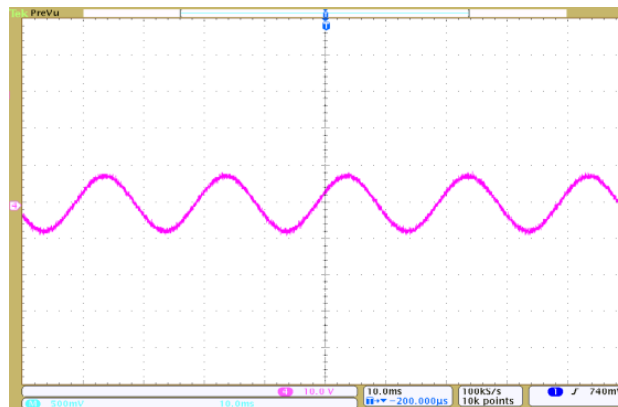


Fig. 6.12 Experimental results of Boost inverter in DC-AC operation

6.3.1 Experimental test-bench to validate digital controllers

This section shows the developed prototype to test the designed controllers for the Boost inverter. Fig.6.10 shows the designed Printed Circuit Board for the Boost inverter prototype using an FPGA as digital control unit with interface with the power stage using specific driver circuits. Fig.6.11 presents the final prototype working from a DC power input until a AC signal generated by the controller. Fig.6.11 shows the Boost inverter controlled by an FPGA XC7A35T of Xilinx and configured with Vivado™. Experimental result in Fig.6.12 shows the performance of Boost inverter working in

DC-AC configuration.

Next section presents the design and implementation of a nonlinear control able to drive this power converter to follow a sinusoidal reference.

6.3.2 Slide-mode control for the Boost inverter

Operation of Boost inverter requires a robust control method given the non-linearity of this power converter. The slide-mode control is the selected method for this task. The slide-mode control is a nonlinear technique with robust and fast response to disturbances. This control method depends on a sliding surface $S(x, t)$, which is defined for the Boost inverter in [76] by eq.6.1,

$$S(x, t) = i_{L2}(t) - i_{L1}(t) - k(t) \quad (6.1)$$

where $k(t)$ is the output of a PI controller,

$$k(t) = k_p (v_{ref} - v_o) + \int_{-\infty}^t k_i (v_{ref} - v_o) dt \quad (6.2)$$

According to [76], the existence of a sliding-mode requires stability of the state trajectory to the sliding surface $S(x, t) = 0$. The second method of Lyapunov is the criterion for stability of the state trajectory. The second method of Lyapunov requires selecting a positive definite function $V(x, t)$. Where,

$$V(x, t) = \frac{1}{2} S^2(x, t) \quad (6.3)$$

that has a negative time derivative in the region of attraction [101]. The necessary conditions to establish the switching behavior and the Boost inverter states are satisfied when,

$$u(t) = 1 \text{ for } S(x, t) > 0 \quad (6.4)$$

and

$$u(t) = 0 \text{ for } S(x, t) < 0 \quad (6.5)$$

Hence,

$$S(x, t) \cdot \dot{S}(x, t) < 0 \quad (6.6)$$

The control design presented in [76] establishes the switching operation in the sliding mode by the behavior of the capacitor voltages and the inductor currents around the equilibrium point $k(t) = 0$. Thus,

$$\frac{di_{L1}}{dt} = \frac{V_g}{L} - \frac{v_1 v_2}{L(v_1 + v_2)} + \frac{\dot{k} v_2}{(v_1 + v_2)} \quad (6.7)$$

$$\frac{di_{L2}}{dt} = \frac{V_g}{L} - \frac{v_1 v_2}{L(v_1 + v_2)} + \frac{\dot{k} v_2}{(v_1 + v_2)} \quad (6.8)$$

$$\frac{dv_1}{dt} = \frac{v_2 i_1}{C(v_1 + v_2)} + \frac{L \dot{k} i_1}{C(v_1 + v_2)} - \frac{v_1 - v_2}{RC} \quad (6.9)$$

$$\frac{dv_2}{dt} = \frac{v_1 - v_2}{RC} + \frac{v_1 i_2}{C(v_1 + v_2)} - \frac{L \dot{k} i_2}{C(v_1 + v_2)} \quad (6.10)$$

The input signal is the small amplitude; therefore, the effects on the inverter variables are predicted by a linear approach around the equilibrium point. The resulting model must be able to describe the interdependence among the respective increments of the state variables and the input signal where the superscript ($\hat{}$) stands the increments of the inverter variables [76]. Evaluating the partial derivatives of eq.(6.7) to eq.(6.10) for i_{L1} , v_1 , v_2 , k , \dot{k} , according to [76].

$$\frac{\partial \widehat{i_{L1}}}{dt} = \frac{\partial}{\partial i_{L1}} \left(\frac{\partial \widehat{i_{L1}}}{dt} \right) \widehat{i_{L1}} + \frac{\partial}{\partial v_1} \left(\frac{\partial \widehat{i_{L1}}}{dt} \right) \widehat{v_1} + \frac{\partial}{\partial v_2} \left(\frac{\partial \widehat{i_{L1}}}{dt} \right) \widehat{v_2} + \frac{\partial}{\partial k} \left(\frac{\partial \widehat{i_{L1}}}{dt} \right) \widehat{k} + \frac{\partial}{\partial \dot{k}} \left(\frac{\partial \widehat{i_{L1}}}{dt} \right) \widehat{\dot{k}} \quad (6.11)$$

$$\frac{\partial \widehat{i_{L2}}}{dt} = \frac{\partial}{\partial i_{L1}} \left(\frac{\partial \widehat{i_{L2}}}{dt} \right) \widehat{i_{L1}} + \frac{\partial}{\partial v_1} \left(\frac{\partial \widehat{i_{L2}}}{dt} \right) \widehat{v_1} + \frac{\partial}{\partial v_2} \left(\frac{\partial \widehat{i_{L2}}}{dt} \right) \widehat{v_2} + \frac{\partial}{\partial k} \left(\frac{\partial \widehat{i_{L2}}}{dt} \right) \widehat{k} + \frac{\partial}{\partial \dot{k}} \left(\frac{\partial \widehat{i_{L2}}}{dt} \right) \widehat{\dot{k}} \quad (6.12)$$

$$\frac{\partial \widehat{v_1}}{dt} = \frac{\partial}{\partial i_{L1}} \left(\frac{\partial \widehat{v_1}}{dt} \right) \widehat{i_{L1}} + \frac{\partial}{\partial v_1} \left(\frac{\partial \widehat{v_1}}{dt} \right) \widehat{v_1} + \frac{\partial}{\partial v_2} \left(\frac{\partial \widehat{v_1}}{dt} \right) \widehat{v_2} + \frac{\partial}{\partial k} \left(\frac{\partial \widehat{v_1}}{dt} \right) \widehat{k} + \frac{\partial}{\partial \dot{k}} \left(\frac{\partial \widehat{v_1}}{dt} \right) \widehat{\dot{k}} \quad (6.13)$$

$$\frac{\partial \widehat{v_2}}{dt} = \frac{\partial}{\partial i_{L1}} \left(\frac{\partial \widehat{v_2}}{dt} \right) \widehat{i_{L1}} + \frac{\partial}{\partial v_1} \left(\frac{\partial \widehat{v_2}}{dt} \right) \widehat{v_1} + \frac{\partial}{\partial v_2} \left(\frac{\partial \widehat{v_2}}{dt} \right) \widehat{v_2} + \frac{\partial}{\partial k} \left(\frac{\partial \widehat{v_2}}{dt} \right) \widehat{k} + \frac{\partial}{\partial \dot{k}} \left(\frac{\partial \widehat{v_2}}{dt} \right) \widehat{\dot{k}} \quad (6.14)$$

Given the optimal operation point,

$$x = [i_{L1}(t), i_{L2}(t), v_1(t), v_2(t)] = [0, 0, V_g, V_g] \quad (6.15)$$

Thus,

$$\frac{d\hat{i}_{L1}}{dt} = -\frac{1}{4L}\hat{v}_1 - \frac{1}{4L}\hat{v}_2 + \frac{1}{2}\hat{k} \quad (6.16)$$

$$\frac{d\hat{i}_{L2}}{dt} = -\frac{1}{4L}\hat{v}_1 - \frac{1}{4L}\hat{v}_2 + \frac{1}{2}\hat{k} \quad (6.17)$$

$$\frac{d\hat{v}_1}{dt} = \frac{1}{2C}\hat{i}_{L2} - \frac{1}{RC}\hat{v}_1 + \frac{1}{RC}\hat{v}_2 + \frac{1}{2C}\hat{k} \quad (6.18)$$

$$\frac{d\hat{v}_2}{dt} = \frac{1}{2C}\hat{i}_{L2} + \frac{1}{RC}\hat{v}_1 - \frac{1}{RC}\hat{v}_2 \quad (6.19)$$

In state-space representation,

$$\hat{x}(t) = \begin{bmatrix} 0 & -\frac{1}{4L} & -\frac{1}{4} \\ \frac{1}{2C} & -\frac{1}{RC} & \frac{1}{RC} \\ \frac{1}{2C} & \frac{1}{RC} & -\frac{1}{RC} \end{bmatrix} \hat{x}(t) + \begin{bmatrix} \frac{1}{2} \\ 0 \\ 0 \end{bmatrix} \hat{k}(t) + \begin{bmatrix} 0 \\ 0 \\ \frac{1}{2C} \end{bmatrix} \hat{k}(t) \quad (6.20)$$

$$\hat{y}(t) = [0 \ -1 \ 1] \hat{x}(t) \quad (6.21)$$

Using the Laplace transform to obtain the control to output transfer function of the inverter $G(s) = \hat{y}(s)/\hat{k}(s)$, as shown in [76],

$$\hat{G}(S) = \frac{\hat{Y}(S)}{\hat{k}(S)} = [0 \ -1 \ 1] \begin{bmatrix} S & \frac{1}{4L} & \frac{1}{4} \\ \frac{-1}{2C} & S + \frac{1}{RC} & \frac{-1}{RC} \\ \frac{-1}{2C} & \frac{-1}{RC} & S + \frac{1}{RC} \end{bmatrix}^{-1} \begin{bmatrix} \frac{S}{2} \\ 0 \\ \frac{1}{2C} \end{bmatrix} \quad (6.22)$$

Then,

$$G(s) = \frac{1}{\frac{2C}{s + \frac{1}{RC}}} \quad (6.23)$$

A PI controller is developed using a parallel configuration and parameters are set using direct synthesis [102].

$$T(s) = \frac{\left(s + \frac{k_i}{k_p}\right) \left(\frac{k_p}{2C}\right)}{s^2 + s \left(\frac{2}{RC} + \frac{k_p}{2C}\right) + \frac{k_i}{2C}} \quad (6.24)$$

Eq. 6.24 expressed in normalized form as,

$$T(s) = \frac{(s + a) \left(\frac{\omega_n^2}{a}\right)}{s^2 + s(2\zeta\omega_n) + \omega_n^2} \quad (6.25)$$

To determine the value of the natural frequency of the inverter, in this document is used a frequency range around 650Hz. To find the values of k_i and k_p , a natural frequency is determined for the 650 Hz controller equivalent to $\omega_n = 4.085[\text{rad/seg}]$ a damping factor of $\zeta = 0.7$ [102]. Taking into account the circuit parameters with capacitors of $10\mu\text{F}$. Thus, $k_i = 333$ and $k_p = 0.11$.

Digital slide-mode control

Using the slide-mode control defined by eq.(6.1), the Fig.6.13 shows in the discrete domain the proposed structure for the digital slide-mode control.

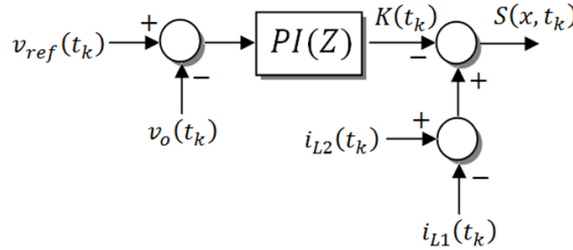


Fig. 6.13 Structure of digital slide controller

After obtaining the design parameters through the analogous architecture from eq.(6.25), the digital PI control is implemented using a Zero-Order Hold ZOH function with a sample time of $1\mu\text{s}$,

$$PI(z) = \frac{11z - 10.9}{z - 1} \quad (6.26)$$

The PI controller is designed and coupled according to the characteristics of the Boost inverter features. The Jury criterion is applied to verify the stability of the PI control in closed loop [102]. The transfer function to analyze is then,

$$T(z) = \frac{0.01621z - 0.0162}{z^2 - 1.9640z + 0.9646} \quad (6.27)$$

The Jury criterion applied in the close loop system indicates that the three sufficient and necessary conditions are accomplished on the characteristic polynomial $D(z) = z^2 - 1.9640z + 0.9646$ to verify the closed loop stability,

- $D(1) > 0$ where $D(1) = 0.0006$
- $(-1)^n D(-1) > 0$ where $D(-1) = 3.9286$
- $|a_0| < a_2$ where $|0.96446| < 1$

The designed digital slide-mode control is simulated and results are shown in Fig.6.14, Fig.6.15, and Fig.6.16. Capacitor voltages are represented in Fig.6.14. This figure shows that the designed digital control is able to follow the nonlinear behavior of the Boost inverter. Fig.6.15 depicts the inductor currents which operate as expected.

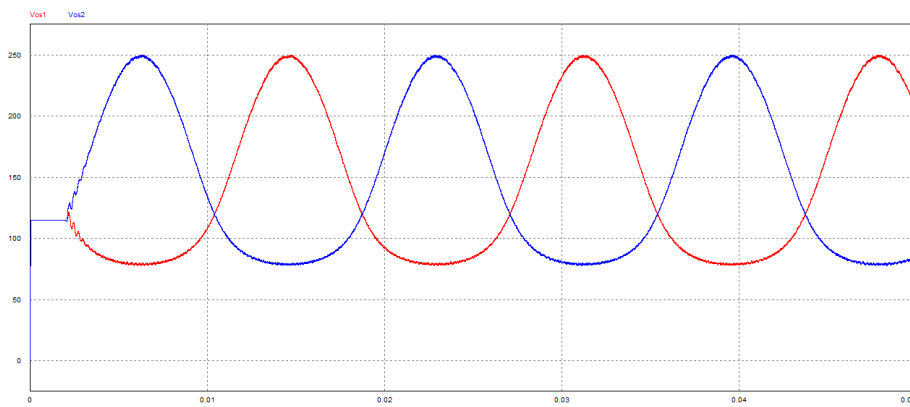


Fig. 6.14 Capacitor voltages with digital slide-mode control

Table 6.1 Total Harmonic Distortion output voltage Boost inverter

V_{in} (V)	V_{out} RMS (V)	Load (Ω)	THD (%)
60	119.8	200	0.54
60	120.1	500	0.55
60	120.2	1000	0.57
30	119.7	200	0.37
30	119.9	500	0.37
30	120.1	1000	0.36

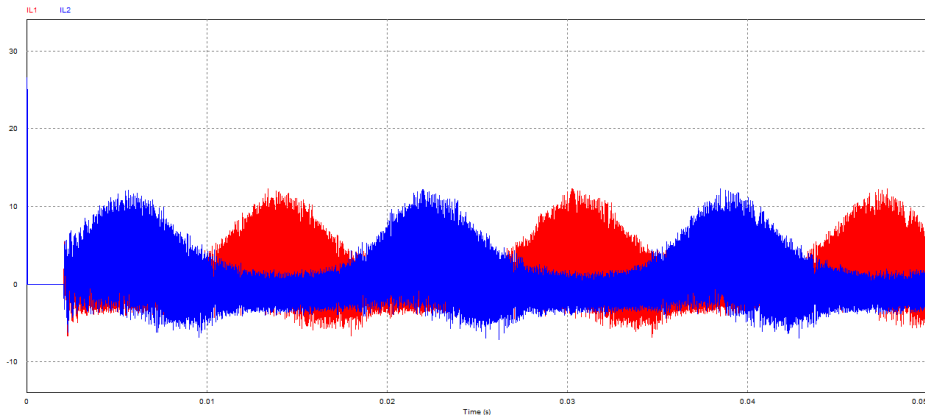


Fig. 6.15 Inductor currents with digital slide-mode control

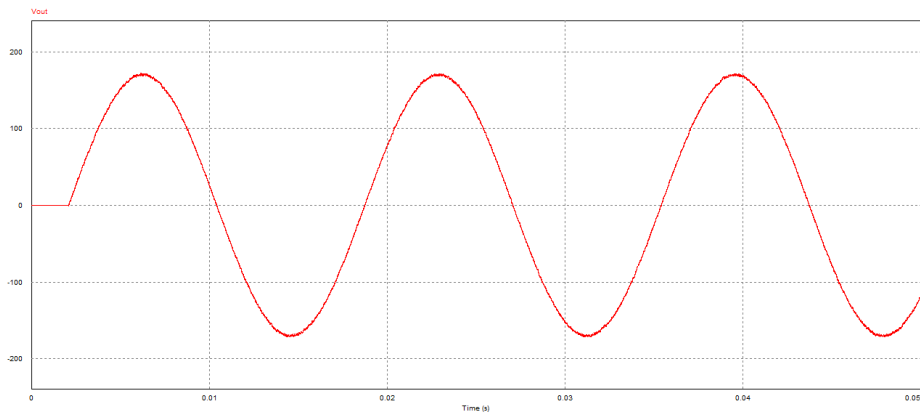


Fig. 6.16 Output voltage with digital slide-mode control

Output voltage in Fig.6.16 presents low distortion in relation with the sinusoidal reference signal. Tabla 6.1 summarizes the Total Harmonic Distortion THD in a set of tests with different input voltages and loads [102]. Results show the low harmonic distortion of this inverter which is a requirement for their integration in electrical grids and microgrids.

6.3.3 Slide-mode control implementation with HiLeS

After design of the digital slide-mode controller, this section presents its implementation using SysML and HiLeS. The control system is defined by the SysML diagrams in each stage and HiLeS is used to generate the code for implementation [102].

The first stage in the implementation is to define the PI control structure. For this purpose, eq.(6.26) is represented as an equation of differences in eq.(6.28) and describe

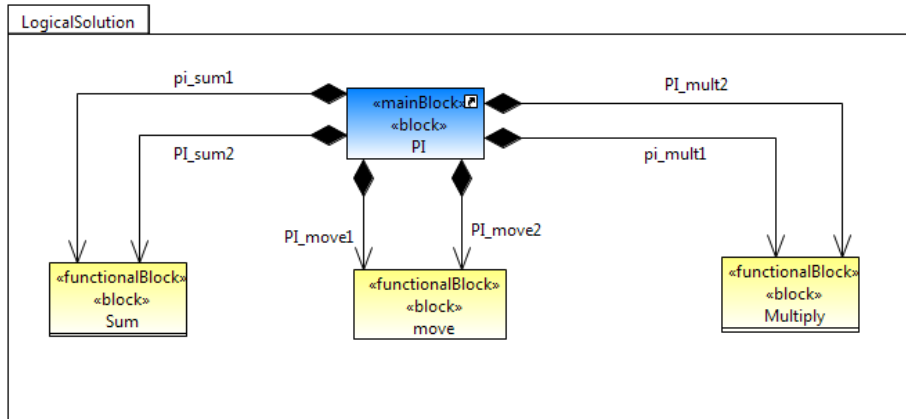


Fig. 6.17 Block Definition Diagram for the digital PI controller

using SysML diagrams. Fig.6.17, Fig.6.18, and Fig.6.19 show the SysML diagrams to represent the digital PI controller. Fig.6.20 depicts the equivalent Petri net generated by HiLeS to represent the operation sequence of the PI controller.

$$d_n = 11e_n + 10.9e_{(n-1)} + d_{(n-1)} \tag{6.28}$$

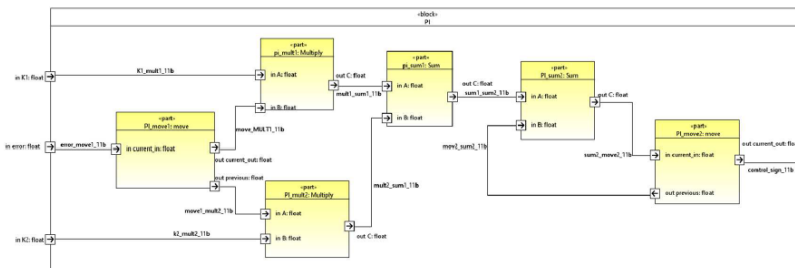


Fig. 6.18 Internal Block Diagram for the digital PI controller

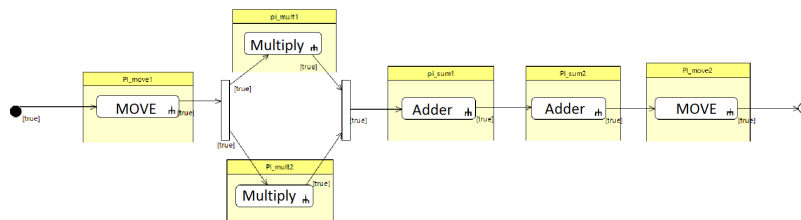


Fig. 6.19 Activity Diagram for the digital PI controller

In the second design stage, the slide-mode controller is implemented according to the structure presented in Fig.6.13. In this design step, the HiLeS tool is employed to

import the previous designed PI controller as a block functional.

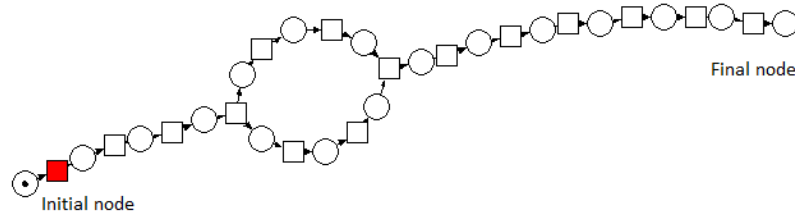


Fig. 6.20 Associated Petri net for the digital PI controller

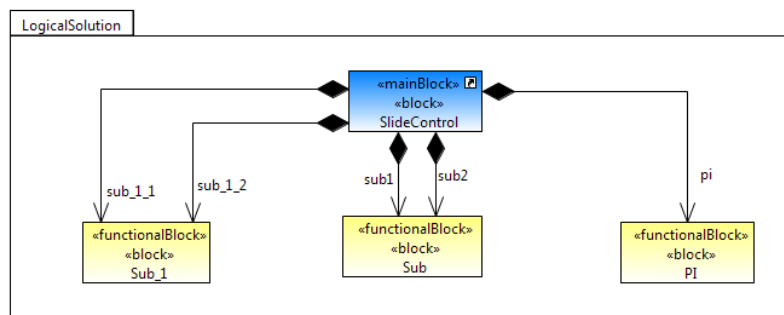


Fig. 6.21 Block Definition Diagram for the slide-mode controller

Fig.6.22 shows the Block Definition Diagram to describe the functional components that form the digital slide-mode controller. In Fig.6.22, the Internal Block Diagram represents the interaction between functional components of Fig.6.22 where the PI control block is imported from previous design.

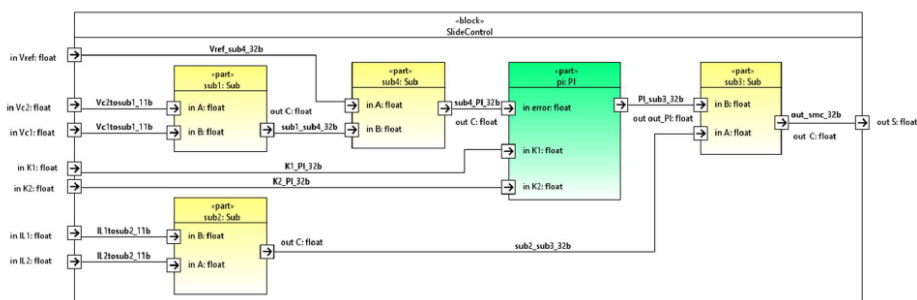


Fig. 6.22 Internal Block Diagram for the slide-mode controller

Finally, Fig.6.23 depicts the Activity Diagram to evaluate the designed slide-mode controller where the operation sequence calculates the PI controller results. Following

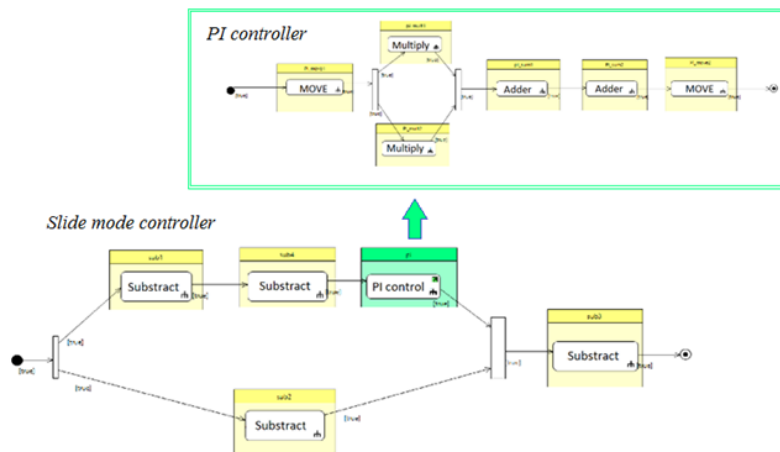


Fig. 6.23 Activity Diagram for the slide-mode controller

the design approach proposed in *Annex D*, Fig.6.24 shows the integration of Petri net from the the digital PI controller with the slide-mode controller to increase the design robustness and to allow the reuse of previous controllers.

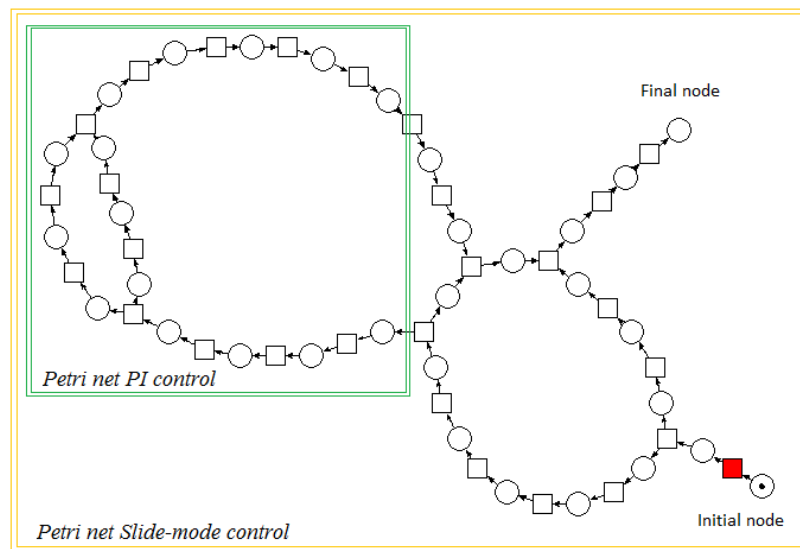


Fig. 6.24 Associated Petri net for the slide-mode controller

For the design of the third stage, it is necessary to import the stage of the slide-mode control and to generate the sinusoidal reference signal. At this stage, the generation block of the reference signal operates in parallel to the control block and the generation of the control signals, as shown in Fig.6.25.

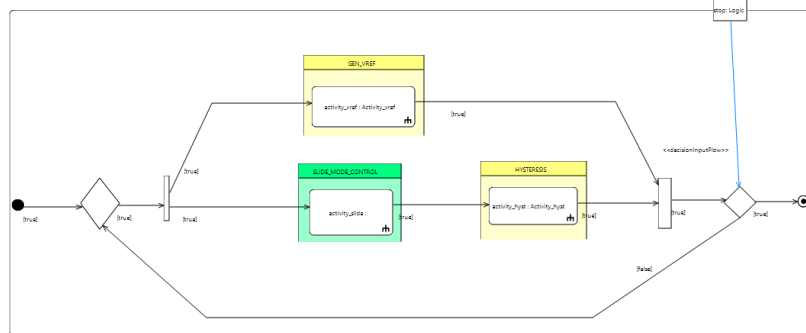


Fig. 6.25 Activity Diagram for the slide-mode controller with reference signal

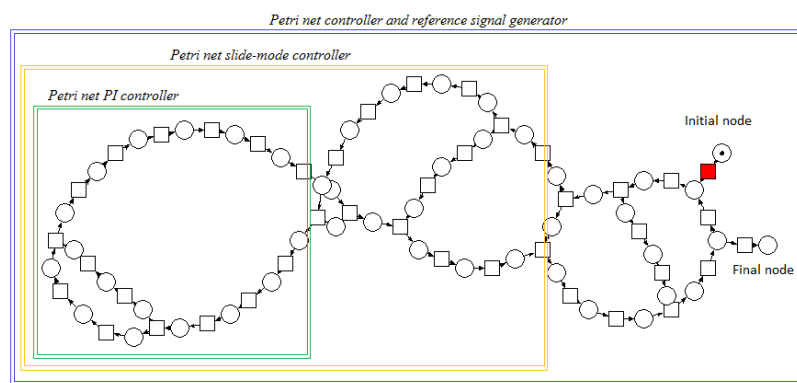


Fig. 6.26 Associated Petri net for the total controller and reference signal generator

Fig.6.26 depicts the generated Petri net which integrates the PI controller Petri net and the slide-mode controller Petri net in a multiple hierarchic approach.

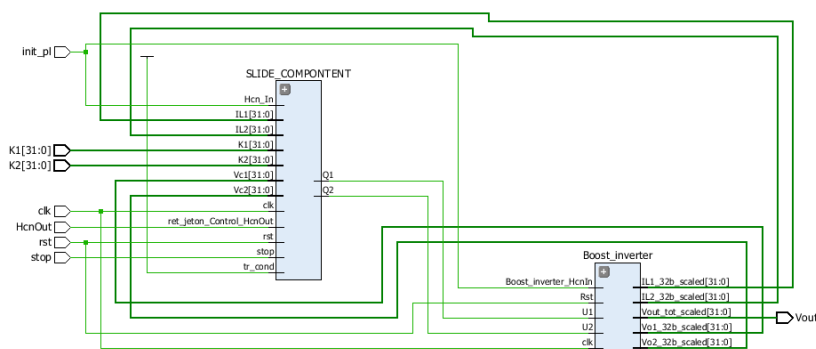


Fig. 6.27 Integration of slide-mode controller and the Boost inverter model

Real-time emulation of slide-mode control using a HIL approach

The controller is verified in Vivado WebPACK® of Xilinx using the Hardware-in-the-Loop (HIL) prototype of the Boost inverter developed in *section 6.2*. This virtual HIL prototype allows performing real-time tests avoiding safety problems and component damage in extreme operation conditions with equivalent results to the actual power converter. Fig.6.27 shows the integration between the slide-mode controller and the HIL Boost inverter model.

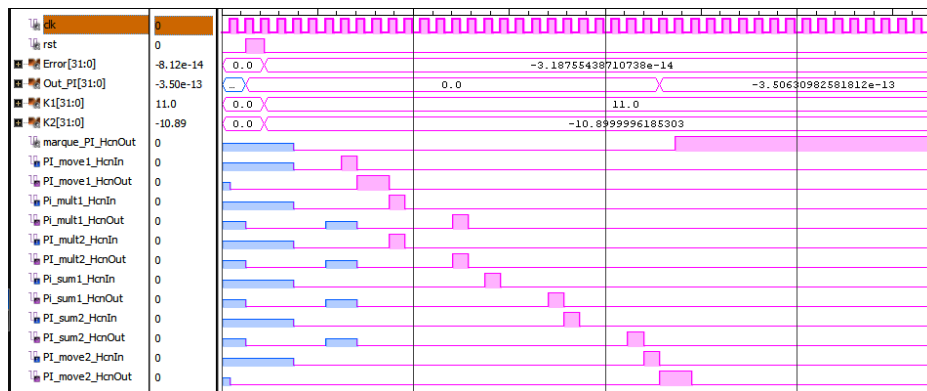


Fig. 6.28 Digital signals for slide-mode controller implemented in FPGA

Fig.6.28 outlines the sequence of digital signals associated to the Petri net of Fig.6.24 which allows evaluating and verifying the suitable sequence of operation for the digital slide-mode controller implemented in FPGA.

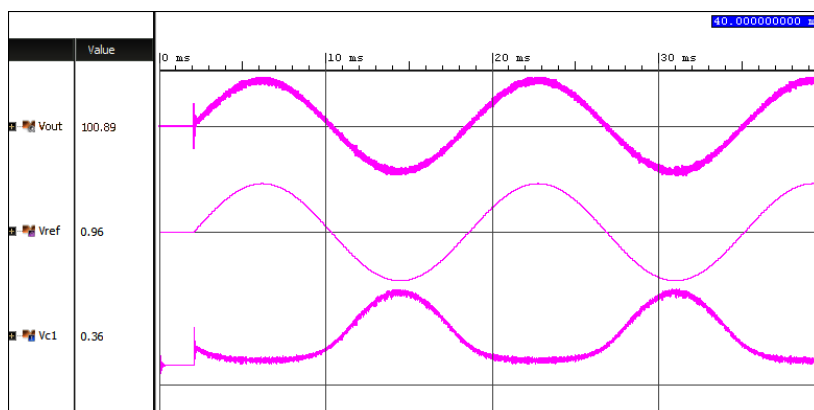


Fig. 6.29 Emulation of Boost inverter output with sinusoidal reference

Fig.6.29 presents the output voltage from the emulation of the power converter controller by the slide-mode controller with a sinusoidal reference signal. Fig.6.29 also shows the capacitor voltage behavior which agrees with the expected behavior from simulation results. Emulation results show that the implemented controller is able to drive the Boost inverter to provide a sinusoidal output with low distortion.

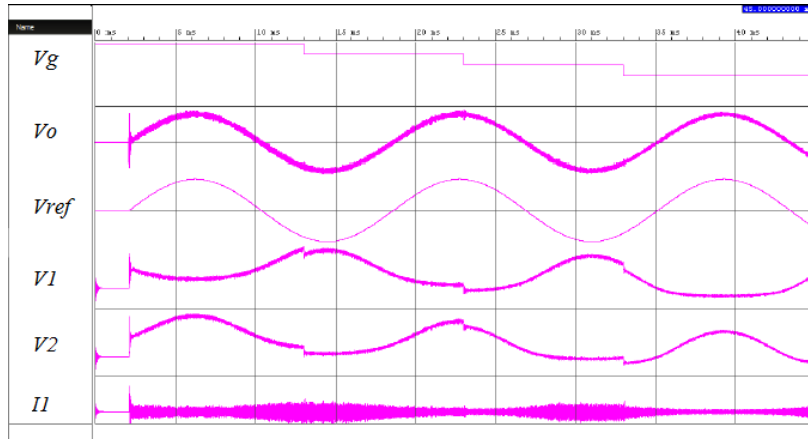


Fig. 6.30 Boost inverter output for input voltage variation

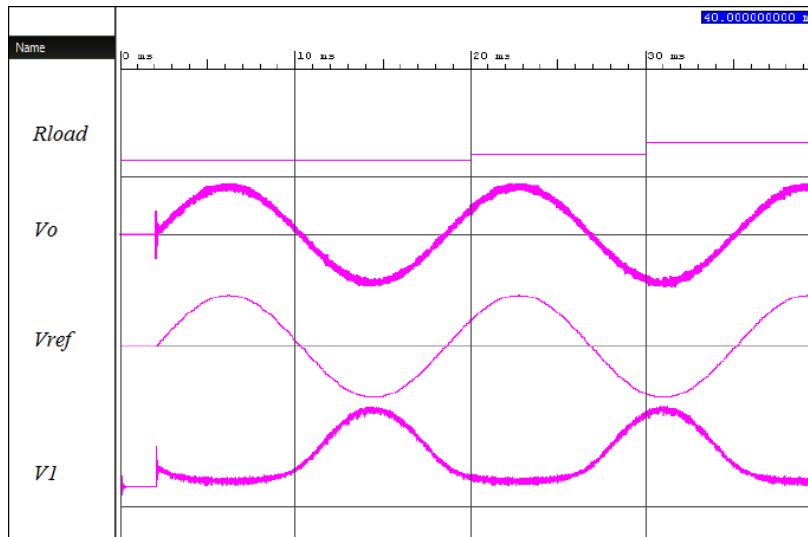


Fig. 6.31 Boost inverter output for load variation

Two operation conditions are carried out to determine the robustness of the slide-mode control. The first test is the input voltage variation. Fig.6.30 shows the results of input voltage variations of 10V from 60V to 30V. Theses results allow validating

the controller robustness and their fast response as expected for this nonlinear controller.

The second test is the controller response to the load variation. Fig.6.31 depicts a load variation from 200Ω to 50Ω with low output voltage variation. Comparing the error between the output voltage and the reference the MSE was 2.39%. Results show the control robustness in terms of the load and voltage variations.

6.4 Conclusion

In this chapter was presented the HiLeS framework to implement models of power converters with the Boost inverter as a case of study. These models was implemented in FPGA for real-time Hardware-in-the-Loop emulations. Results of real-time emulations were compared with experimental results of an actual Boost inverter to validate the proposed methodology.

A digital slide-mode control was designed for the Boost inverter. This controller has allowed to generate the standard AC voltage suitable for grid connections. It was be tested the robustness of the slide-mode control for variations of either the power supply or the load.

SysML made easier the control system architecture design before implementation in FPGA. The digital slide-mode control design in stages using HiLeS allowed implementing the control structure decreasing the development time. The framework to integrate the controller stages also was presented using the Petri nets theory.

Chapter 7

Conclusions and Perspectives

7.1 Conclusions

Chapter 2 showed the relevant aspects about PV generation and their integration in microgrids. A remarkable price decreasing of PV modules follows the Swanson's law for progressive price reduction. However, PV systems also are vulnerable to internal and external conditions and preventive actions should be taken in order to reduce their impact in the system reliability and energy production. In chapter 2 was also presented the current concerns about Power electronics architectures, highlighting that most of the concerns about the interaction of PV systems and microgrids rely on these power devices. Finally, simulation and emulation methods have been analyzed to identify their main challenge and constraints to provide a useful approach in the study of concerns about PV systems in microgrids. FPGA was identified as the most suitable processing device to deal with the high complex degree of PV system real-time emulation. Then, a proper methodology is required to develop the PV system models taking advantage of powerful processing characteristics of FPGAs.

Chapter 3 was devoted to studying the PV generator. This chapter presented a methodology to increase the accuracy and scope of conventional modeling approaches of PV systems. The main contribution of this approach is to define a simplify relation denominated shadow coefficient suitable to describe the complex behavior of PV modules under partially shading conditions. In addition, results analysis allows identified interrelations between shadow patrons and current-voltage changes in partially shaded conditions.

Discussion Chapter 4 proposed a component-based methodology to model power converters. This approach was employed to model Boost converter topologies. This methodology allowed modeling power converters independently of changes in the type of source or the load using the concept of causal and non causal models. Models from this perspective can be integrated with other models to generate more complex systems. Experimental and theoretical results validated the presented Boost converter models. Integration of this developed models with nonlinear sources and nonlinear loads showed suitable results and confirm the pertinence of the proposed methodology.

In chapter 5 was introduced the HiLeS framework to implement models of PV systems in FPGA for real-time emulation. The HiLeS framework allowed implementing the developed models with a suitable tradeoff between execution time and accuracy. As a consequence, these tests on the developed platform showed their potential to implement more complex models of PV systems integrated to microgrids using the multiple hierarchic level approach.

Chapter 6 presented the model implementation of power converters for real-time emulations with the Boost inverter as a case of study. These models was implemented in FPGA for real-time Hardware-in-the-Loop emulations. Comparison of real-time emulations and experimental results validated the proposed methodology. A digital slide-mode control was designed for the Boost inverter using the SysML diagrams and the HiLeS framework. This developed controller showed their robustness and fast response to disturbances.

7.2 Perspectives

This dissertation presented the integration of the different emulation and design tools with power electronics and photovoltaic systems which open the doors to future industrial applications. This integration can be extended to the study of other complex energy systems or integrate other alternative energy resources and nonlinear loads.

The proposed models of shaded PV systems are suitable to develop shadow propagation models which can be integrated with power converter models to design innovative control systems and Maximum Power Point Tracking strategies with higher accuracy. In addition, this integration can be useful to develop more accurate power production

models. Also, the theoretical and experimental results of partial shaded PV systems provide findings useful to further studies of diagnosis and fault detection.

Perspectives of this work integrate the developed models using the component-based approach in a single real-time platform to evaluate the complex interactions in energy systems based on PV generators, power converters, nonlinear loads, and the electrical grid. The component-based modeling methodology can also be extended to other power converter topologies such as multi-phase inverters or interleaved DC/DC converters. Furthermore, the developed real-time emulation platform can be used to evaluate and develop novel supervision and fault detection methods.

The proposed Hardware-in-the-Loop approach based on HiLeS and SysML provides a useful tool to develop and test innovative power converter architectures and advanced control strategies.

The presented component-based modeling methodology and the multiple hierarchic approach allow modeling in further research complex systems able to be implemented and emulated in powerful processing devices such as FPGAs.

Chapter 8

Contributions and Publications

The main contributions of this work was to define in Chapter III a simplify relation denominated shadow coefficient suitable to describe the behavior of PV modules under shading conditions. In Chapter IV was proposed a component-based methodology to model power converters independently of changes in the type of source or the load and applied to the Boost inverter. In chapter V and VI was introduced the HiLeS framework to implement models of PV systems in FPGA to developed a real-time emulation platform and nonlinear control systems.

This work has led to the following publications and related articles:

[P1] A. Gutierrez, M. Bressan, F. Jimenez, C. Alonso. Development of Real-time Supervision HIL Emulator of Shaded PV Systems. In *International Conference on Renewable Energy Research and Applications (ICRERA)*, San Diego–USA, 2017.

[P2] A. Gutierrez, M. Bressan, F. Jimenez, C. Alonso. Development of Boost Inverter SysML Model for Hardware-In-The-Loop Simulations. In *International Conference on Theory and Application of Modeling and Simulation in Electrical Power Engineering (ELECTRIMACS)*, Toulouse–France, 2017.

[P3] C. Dominguez, A. Gutierrez, H.R. Chamorro, J.F. Jimenez. SysML Methodology for FPGA-based Controller Design for Quadcopters. In *7th Annual Information Technology, Electronics and Mobile Communication Conference (IEMCON)*, Vancouver – Canada, 2016.

[P4] M. Bressan, Y. E. Basri, A. G. Galeano, and C. Alonso. A shadow fault detection method based on the standard error analysis of I-V curves. In *Renewable Energy Journal*,

ISSN: 0960-1481, vol. 99, pp. 1181-1190, 2016.

[P5] A. Gutierrez, H.R. Chamorro, J.F. Jimenez, J.F. Villa, C. Alonso. Hardware-in-the-loop simulation of PV systems in micro-grids using SysML models. In *IEEE 16th Workshop on Control and Modeling for Power Electronics (COMPEL)*, Vancouver – Canada, 2015.

[P6] A. Gutierrez, H.R. Chamorro, J.F. Jimenez, J.F. Villa, C. Alonso. SysML methodology for HIL implementation of PV models. In *17th European Conference on Power Electronics and Applications (EPE'15 ECCE-Europe)*, Geneva – Switzerland, 2015.

[P7] J. Mayorga, C. Dominguez, A. Gutierrez, H.R. Chamorro, J.F. Jimenez. Development of Real-Time Control Emulator in FPGA using HiLeS Methodology. In *41st Annual Conference of the IEEE Industrial Electronics Society*, Yokohama - Japan, 2015.

[P8] A. Gutierrez, H.R. Chamorro, and J.F. Jimenez. Hardware-in-the-Loop based SysML for Model and Control Design of Interleaved Boost Converters. In *15th Workshop on Control and Modeling for Power Electronics (COMPEL)*, Santander - Spain , 2014.

[P9] A. Gutierrez, H.R. Chamorro, and J.F. Jimenez. Supervisory Control for Interleaved Boost Converters using HiLeS-Designer. In *16th European Conference on Power Electronics and Applications (EPE'14-ECCE Europe)*, Lappeenranta - Finland, 2014.

[P10] A. Gutiérrez, J.F. Jiménez. Automatic Code Generation for Hardware-in-the-Loop Simulation of Differential Equations Using Model-Driven Engineering. In *Paradigma – Electronic Journal in Software Development*, ISSN: 2011-0065, vol.8, No. 1. Universidad de los Andes, Bogotá-Colombia, 2014.

[P11] A. Gutiérrez, H. Chamorro, F. Jiménez, S. Silva, G. Cote, M. Díaz, H. Hoyos. Book chapter: Hardware-in-the-Loop Simulations and Control Systems Based on FPGA for Power Electronics. In *Microgrids in Hydroelectricity and Power Electronics: Environmental Impacts, Emerging Technologies and Challenges*, ISBN: 978-1-63321-737-9, Nova Publishers, New York, 2014.

References

- [1] N. Hatziargyriou, “Microgrids - large scale integration of microgeneration to low voltage grids,” tech. rep., National technical university of Athens, 2006.
- [2] N. Hatziargyriou, *Microgrids architectures and control*. John Wiley and Sons, 2014.
- [3] D. Ocnasu, *Modélisation, Commande et Simulation Temps-Réel Hybride des Systèmes de Génération Non Conventionnels*. PhD thesis, Université Joseph Fourier, France, 2008.
- [4] S. Abourida, S. Cense, C. Dufour, and J. Bélanger, “Hardware-in-the-loop simulation of electric systems and power electronics on fpga using physical modeling,” in *Power Engineering, Energy and Electrical Drives (POWERENG), 2013 Fourth International Conference on*, pp. 775–780, May 2013.
- [5] S. Bacha, D. Picault, B. Burger, I. Etxeberria-Otadui, and J. Martins, “Photovoltaics in microgrids: An overview of grid integration and energy management aspects,” *IEEE Industrial Electronics Magazine*, vol. 9, pp. 33–46, March 2015.
- [6] R. Kadri, H. Andrei, J.-P. Gaubert, T. Ivanovici, G. Champenois, and P. Andrei, “Modeling of the photovoltaic cell circuit parameters for optimum connection model and real-time emulator with partial shadow conditions,” *Energy*, vol. 42, no. 1, pp. 57 – 67, 2012. 8th World Energy System Conference, {WESC} 2010.
- [7] J. Agrawal and M. Aware, “Photovoltaic system emulator,” in *2012 IEEE International Conference on Power Electronics, Drives and Energy Systems (PEDES)*, pp. 1–6, Dec 2012.
- [8] E. Koutroulis, K. Kalaitzakis, and V. Tzitzilonis, “Development of an fpga-based system for real-time simulation of photovoltaic modules,” *Microelectronics Journal*, vol. 40, no. 7, pp. 1094 – 1102, 2009.
- [9] J.-H. Jung and S. Ahmed, “Real-time simulation model development of single crystalline photovoltaic panels using fast computation methods,” *Solar Energy*, vol. 86, no. 6, pp. 1826 – 1837, 2012.
- [10] A. E. Brooks, D. Cormode, A. D. Cronin, and E. Kam-Lum, “Pv system power loss and module damage due to partial shade and bypass diode failure depend on cell behavior in reverse bias,” in *Photovoltaic Specialist Conference (PVSC), 2015 IEEE 42nd*, pp. 1–6, June 2015.

- [11] M. Bressan, Y. E. Basri, A. Galeano, and C. Alonso, "A shadow fault detection method based on the standard error analysis of i-v curves," *Renewable Energy*, vol. 99, pp. 1181 – 1190, 2016.
- [12] Y. E. Basri, M. Bressan, L. Seguier, H. Alawadhi, and C. Alonso, "A proposed graphical electrical signatures supervision method to study {PV} module failures," *Solar Energy*, vol. 116, pp. 247 – 256, 2015.
- [13] R. Rajesh and M. C. Mabel, "A comprehensive review of photovoltaic systems," *Renewable and Sustainable Energy Reviews*, vol. 51, pp. 231 – 248, 2015.
- [14] S. Malathy and R. Ramaprabha, "Comprehensive analysis on the role of array size and configuration on energy yield of photovoltaic systems under shaded conditions," *Renewable and Sustainable Energy Reviews*, vol. 49, pp. 672 – 679, 2015.
- [15] F. E. Lahouar, M. Hamouda, and J. B. H. Slama, "Design and control of a grid-tied three-phase three-level diode clamped single-stage photovoltaic converter," in *Ecological Vehicles and Renewable Energies (EVER), 2015 Tenth International Conference on*, pp. 1–7, March 2015.
- [16] M. F. Yaden, M. Melhaoui, E. Baghaz, and K. Hirech, "Energy management system produced by photovoltaic systems," in *Multimedia Computing and Systems (ICMCS), 2014 International Conference on*, pp. 1619–1624, April 2014.
- [17] M. Bressan, Y. El-Basri, and C. Alonso, "A new method for fault detection and identification of shadows based on electrical signature of defects," in *2015 17th European Conference on Power Electronics and Applications (EPE'15 ECCE-Europe)*, pp. 1–8, Sept 2015.
- [18] P. C. D. Goud, R. Gupta, A. K. Singh, and P. Samuel, "Gmppt of solar pv array under partial shading condition using labview fpga," in *Industrial Electronics Society, IECON 2015 - 41st Annual Conference of the IEEE*, pp. 003411–003416, Nov 2015.
- [19] A. C. Atoche, J. V. Castillo, J. Ortegon-Aguilar, R. Carrasco-Alvarez, J. Sandoval, and A. Colli-Menchi, "A high-accuracy photovoltaic emulator system using {ARM} processors," *Solar Energy*, vol. 120, pp. 389 – 398, 2015.
- [20] J.-H. Jung and S. Ahmed, "Real-time simulation model development of single crystalline photovoltaic panels using fast computation methods," *Solar Energy*, vol. 86, no. 6, pp. 1826 – 1837, 2012.
- [21] L. Bun, *Détection et Localisation de Défauts pour un Système PV*. PhD thesis, Université de Grenoble, France, 2011.
- [22] D. picault, *Reduction of mismatch losses in grid-connected Photovoltaic systems using alternative topologies*. PhD thesis, Université de Grenoble, France, 2010.
- [23] X. Shi and A. M. Bazzi, "Solar photovoltaic power electronic systems: Design for reliability approach," in *2015 17th European Conference on Power Electronics and Applications (EPE'15 ECCE-Europe)*, pp. 1–8, Sept 2015.

- [24] O. L. Santos, *Contribution to the DC-AC conversion in photovoltaic systems: Module oriented converters*. PhD thesis, Université de Toulouse, France, 2015.
- [25] S. M. Sharkh, M. A. Abusara, G. I. Orfanoudakis, and B. Hussain, *Power electronic converters for microgrids*. John Wiley and Sons, 2014.
- [26] R. O. Caceres and I. Barbi, "A boost dc-ac converter: analysis, design, and experimentation," *IEEE Transactions on Power Electronics*, vol. 14, pp. 134–141, Jan 1999.
- [27] S. Danyali, S. H. Hosseini, and G. B. Gharehpetian, "New extendable single-stage multi-input dc-dc/ac boost converter," *IEEE Transactions on Power Electronics*, vol. 29, pp. 775–788, Feb 2014.
- [28] E. Hofreiter and A. M. Bazzi, "Single-stage boost inverter reliability in solar photovoltaic applications," in *2012 IEEE Power and Energy Conference at Illinois*, pp. 1–4, Feb 2012.
- [29] F. Flores-Bahamonde, H. Valderrama-Blavi, J. M. Bosque, A. Leon-Masich, and L. Martinez-Salamero, "Grid-connected boost inverter for small-wind urban integration: Analysis and design," in *IECON 2012 - 38th Annual Conference on IEEE Industrial Electronics Society*, pp. 433–439, Oct 2012.
- [30] D. Lopez, F. Flores-Bahamonde, S. Kouro, M. A. Perez, A. Llor, and L. Martínez-Salamero, "Predictive control of a single-stage boost dc-ac photovoltaic microinverter," in *IECON 2016 - 42nd Annual Conference of the IEEE Industrial Electronics Society*, pp. 6746–6751, Oct 2016.
- [31] O. Nzimako and A. Rajapakse, "Real time simulation of a microgrid with multiple distributed energy resources," in *2016 International Conference on Cogeneration, Small Power Plants and District Energy (ICUE)*, pp. 1–6, Sept 2016.
- [32] S.-J. Oh, C.-H. Yoo, I.-Y. Chung, and D.-J. Won, "Hardware-in-the-loop simulation of distributed intelligent energy management system for microgrids," *Energies*, vol. 6, no. 7, pp. 3263–3283, 2013.
- [33] M. Matar, M. Saeedifard, A. Etemadi, and R. Iravani, "An fpga-based hardware-in-the-loop simulator for multilevel converter systems," in *International Conference on Power Systems Transients*, June 2011.
- [34] R. Caceres and I. Barbi, "A boost dc-ac converter: operation, analysis, control and experimentation," in *Industrial Electronics, Control, and Instrumentation, 1995., Proceedings of the 1995 IEEE IECON 21st International Conference on*, vol. 1, pp. 546–551 vol.1, Nov 1995.
- [35] L. A. Montoya, D. Montenegro, and G. Ramos, "Adaptive protection testbed using real time and hardware-in-the-loop simulation," in *2013 IEEE Grenoble Conference*, pp. 1–4, June 2013.
- [36] J. Wang, *Versatile Three-Phase Power Electronics Converter based Real-time Load Emulators*. PhD thesis, University of Tennessee, 2015.

- [37] M. D. O. Faruque, T. Strasser, G. Lauss, V. Jalili-Marandi, P. Forsyth, C. Dufour, V. Dinavahi, A. Monti, P. Kotsampopoulos, J. A. Martinez, K. Strunz, M. Saeedifard, X. Wang, D. Shearer, and M. Paolone, “Real-time simulation technologies for power systems design, testing, and analysis,” *IEEE Power and Energy Technology Systems Journal*, vol. 2, pp. 63–73, June 2015.
- [38] S. Silvestre and A. Chouder, “Effects of shadowing on photovoltaic module performance,” *Progress in Photovoltaics: Research and Applications*, vol. 16, no. 2, pp. 141–149, 2008.
- [39] R. K. Varma, S. A. Rahman, T. Vanderheide, and M. D. N. Dang, “Harmonic impact of a 20-mw pv solar farm on a utility distribution network,” *IEEE Power and Energy Technology Systems Journal*, vol. 3, pp. 89–98, Sept 2016.
- [40] A. Mohammadirad and K. Nagasaka, “Modelling a 20mw scale solar farm in an unused angled area near fukushima nuclear power plant,” in *2015 International Conference on Advanced Mechatronic Systems (ICAMechS)*, pp. 194–199, Aug 2015.
- [41] L. R. Brown, J. Larsen, J. M. Roney, and E. E. Adams, *The Great Transition: Shifting from Fossil Fuels to Solar and Wind Energy*. Norton and Company, 2015.
- [42] L. Partain, R. Hansen, S. Hansen, D. Bennett, A. Newlands, and L. Fraas, “Swanson’s law, plan to mitigate global climate change,” in *2016 IEEE 43rd Photovoltaic Specialists Conference (PVSC)*, pp. 3335–3340, June 2016.
- [43] F. ISE, “Photovoltaics report,” tech. rep., Fraunhofer Institute for Solar Energy Systems, November 2016.
- [44] M. Bressan, *Développement d’un outil de supervision et de contrôle pour une installation solaire PV*. PhD thesis, Université de Perpignan, France, 2014.
- [45] J. H. Wohlgemuth, S. Kurtz, and NREL, “Using accelerated testing to predict module reliability,” in *IEEE Photovoltaic Specialists Conference (PVSC)*, 2011.
- [46] E. van Dyk and E. Meyer, “Analysis of the effect of parasitic resistances on the performance of photovoltaic modules,” *Renewable Energy*, vol. 29, pp. 333–344, 2004.
- [47] E. L. Meyer and E. E. van Dyk, “The effect of reduced shunt resistance and shading on photovoltaic module performance,” in *IEEE Photovoltaic Specialists Conference (PVSC)*, 2005.
- [48] S. Guo, T. M. Walsh, A. G. Aberle, and M. Peters, “Analysing partial shading of pv modules by circuit modelling,” in *IEEE Photovoltaic Specialists Conference (PVSC)*, 2012.
- [49] M. Alonso-Garcia, J. Ruiz, and F. C. lo, “Experimental study of mismatch and shading effects in the i-v characteristic of a photovoltaic module,” *Solar Energy Materials and Solar Cells*, vol. 90, pp. 329–340, 2006.

- [50] Y. E. Basri, *Architecture de puissance distribuée reconfigurable dédiée à l'optimisation de l'énergie PV*. PhD thesis, Université de Toulouse, France, 2013.
- [51] R. A. Walling, R. Saint, R. C. Dugan, J. Burke, and L. A. Kojovic, "Summary of distributed resources impact on power delivery systems," *IEEE Transactions on Power Delivery*, vol. 23, pp. 1636–1644, July 2008.
- [52] D. M. K. Schofield, M. P. Foster, and D. A. Stone, "Low-cost solar emulator for evaluation of maximum power point tracking methods," *Electronics Letters*, vol. 47, pp. 208–209, February 2011.
- [53] D. D. Lu and Q. N. Nguyen, "A photovoltaic panel emulator using a buck-boost dc/dc converter and a low cost micro-controller," *Solar Energy*, vol. 86, no. 5, pp. 1477 – 1484, 2012.
- [54] D. Ickilli, H. Can, and K. S. Parlak, "Development of a fpga-based photovoltaic panel emulator based on a dc/dc converter," in *2012 38th IEEE Photovoltaic Specialists Conference*, pp. 001417–001421, June 2012.
- [55] P. Rajesh, S. Rajasekar, R. Gupta, and P. Samuel, "Solar array system simulation using fpga with hardware co-simulation," in *2014 IEEE 23rd International Symposium on Industrial Electronics (ISIE)*, pp. 2291–2296, June 2014.
- [56] J. Chavarría, D. Biel, F. Guinjoan, A. Poveda, F. Masana, and E. Alarcón, "Fpga-based design of a step-up photovoltaic array emulator for the test of pv grid-connected inverters," in *2014 IEEE 23rd International Symposium on Industrial Electronics (ISIE)*, pp. 485–490, June 2014.
- [57] A. Mellit, H. Mekki, A. Messai, and H. Salhi, "Fpga-based implementation of an intelligent simulator for stand-alone photovoltaic system," *Expert Systems with Applications*, vol. 37, pp. 6036 – 6051, August 2010.
- [58] W. Ren, M. Steurer, and T. Baldwin, "Improve the stability and the accuracy of power hardware-in-the-loop simulation by selecting appropriate interface algorithms," *IEEE Transactions on Industry Applications*, vol. 44, pp. 1286 – 1294, July 2008.
- [59] M. Matar and R. Iravani, "Fpga implementation of the power electronic converter model for real-time simulation of electromagnetic transients," *IEEE Transactions on Power Delivery*, vol. 25, pp. 852–860, April 2010.
- [60] A. Myaing and V. Dinavahi, "Fpga-based real-time emulation of power electronic systems with detailed representation of device characteristics," in *2011 IEEE Power and Energy Society General Meeting*, pp. 1–11, July 2011.
- [61] R. Selvamuthukumar and R. Gupta, "Rapid prototyping of power electronics converters for photovoltaic system application using xilinx system generator," *IET Power Electronics*, vol. 7, pp. 2269–2278, September 2014.

- [62] B. Lu, X. Wu, H. Figueroa, and A. Monti, "A low-cost real-time hardware-in-the-loop testing approach of power electronics controls," *IEEE Transactions on Industrial Electronics*, vol. 54, pp. 919 – 931, March 2007.
- [63] L. Lavado, *Architectures de Puissance et Commande associées pour la gestion des ombres dans des installations PV*. PhD thesis, Université de Grenoble, France, 2013.
- [64] R. Missaoui, *Gestion Énergétique optimisée pour un bâtiment intelligent multi-sources multi-charges: différents principes de validations*. PhD thesis, Université de Grenoble, France, 2012.
- [65] J. Bishop, "Computer simulation of the effects of electrical mismatches in photovoltaic cell interconnection circuits," *Solar Cells*, vol. 25, no. 1, pp. 73 – 89, 1988.
- [66] V. Quaschnig and R. Hanitsch, "Numerical simulation of current-voltage characteristics of photovoltaic systems with shaded solar cells," *Solar Energy*, vol. 56, no. 6, pp. 513 – 520, 1996.
- [67] H. Kawamura, K. Naka, N. Yonekura, S. Yamanaka, H. Kawamura, H. Ohno, and K. Naito, "Simulation of i-v characteristics of a {PV} module with shaded {PV} cells," *Solar Energy Materials and Solar Cells*, vol. 75, no. 3â€“4, pp. 613 – 621, 2003. {PVSEC} 12, {PART} {III}.
- [68] M. Alonso-Garcia and J. Ruiz, "Analysis and modelling the reverse characteristic of photovoltaic cells," *Solar Energy Materials and Solar Cells*, vol. 90, no. 7-8, pp. 1105 – 1120, 2006.
- [69] S. Guo, T. M. Walsh, A. G. Aberle, and M. Peters, "Analysing partial shading of pv modules by circuit modelling," in *2012 38th IEEE Photovoltaic Specialists Conference*, pp. 002957–002960, June 2012.
- [70] S. Wendlandt, A. Drobisch, D. Tornow, M. Friedrichs, S. Krauter, and P. Grunow, "Operating principle of shadowed c-si solar cell in pv-modules," in *Solar World Congress (SWC) 2011*, pp. 1–10, September 2011.
- [71] E. Diaz-Dorado, J. Cidras, and C. Carrillo, "Discrete i-v model for partially shaded pv-arrays," *Solar Energy*, vol. 103, pp. 96 – 107, 2014.
- [72] D. Jena and V. V. Ramana, "Modeling of photovoltaic system for uniform and non-uniform irradiance: A critical review," *Renewable and Sustainable Energy Reviews*, vol. 52, pp. 400 – 417, 2015.
- [73] W. Herrmann, W. Wiesner, and W. Vaassen, "Hot spot investigations on pv modules-new concepts for a test standard and consequences for module design with respect to bypass diodes," in *Conference Record of the Twenty Sixth IEEE Photovoltaic Specialists Conference - 1997*, pp. 1129–1132, Sep 1997.
- [74] L. F. L. Villa, T. P. Ho, J. C. Crebier, and B. Raison, "A power electronics equalizer application for partially shaded photovoltaic modules," *IEEE Transactions on Industrial Electronics*, vol. 60, pp. 1179–1190, March 2013.

- [75] M. Orozco-Gutierrez, J. Ramirez-Scarpetta, G. Spagnuolo, and C. Ramos-Paja, "A technique for mismatched {PV} array simulation," *Renewable Energy*, vol. 55, pp. 417 – 427, 2013.
- [76] F. Flores-Bahamonde, H. Valderrama-Blavi, J. M. Bosque-Moncusí, G. Garcia, and L. Martínez-Salamero, "Using the sliding-mode control approach for analysis and design of the boost inverter," *IET Power Electronics*, vol. 9, no. 8, pp. 1625–1634, 2016.
- [77] D. B. W. Abeywardana, B. Hredzak, and V. G. Agelidis, "A rule-based controller to mitigate dc-side second-order harmonic current in a single-phase boost inverter," *IEEE Transactions on Power Electronics*, vol. 31, pp. 1665–1679, Feb 2016.
- [78] R. W. Erickson, *Fundamentals of Power Electronics*. Chapman and Hall, second ed., 1997.
- [79] L. Allain, A. Merdassi, L. Gerbaud, and S. Bacha, "Automatic modelling of power electronic converter, average model construction and modelica model generation," in *Automatic modelling of Power Electronic Converter*, 2009.
- [80] C. M. Christophe Batard, Frederic Poitiers and N. Ginot, *MATLAB - A Fundamental Tool for Scientific Computing and Engineering Applications*. InTech, 2012. Chapter 3. Simulation of Power Converters Using Matlab-Simulink.
- [81] J. Pearl, *Causality: Models, Reasoning, and Inference*. Cambridge University Press, 2000.
- [82] D. Maksimovic, A. M. Stankovic, V. J. Thottuvelil, and G. C. Verghese, "Modeling and simulation of power electronic converters," *Proceedings of the IEEE*, vol. 89, pp. 898–912, Jun 2001.
- [83] N. Sakr, D. Sadarnac, and A. Gascher, "A new combined bidirectional boost converter and battery charger for electric vehicles," in *IECON 2015 - 41st Annual Conference of the IEEE Industrial Electronics Society*, pp. 001258–001263, Nov 2015.
- [84] M. Tampubolon, I. Purnama, P. C. Chi, J. Y. Lin, Y. C. Hsieh, and H. J. Chiu, "A dsp-based differential boost inverter with maximum power point tracking," in *2015 9th International Conference on Power Electronics and ECCE Asia (ICPE-ECCE Asia)*, pp. 309–314, June 2015.
- [85] M. Kaliamoorthy, R. M. Sekar, and I. G. C. Raj, "Solar powered single stage boost inverter with ann based mppt algorithm," in *2010 INTERNATIONAL CONFERENCE ON COMMUNICATION CONTROL AND COMPUTING TECHNOLOGIES*, pp. 165–170, Oct 2010.
- [86] M. D. O. Faruque, T. Strasser, G. Lauss, V. Jalili-Marandi, P. Forsyth, C. Dufour, V. Dinavahi, A. Monti, P. Kotsampopoulos, J. A. Martinez, K. Strunz, M. Saeedifard, X. Wang, D. Shearer, and M. Paolone, "Real-time simulation technologies for power systems design, testing, and analysis," *IEEE Power and Energy Technology Systems Journal*, vol. 2, pp. 63–73, June 2015.

- [87] J. J. Rodriguez-Andina, M. D. Valdes, and M. J. Moure, “Advanced features and industrial applications of fpgas a review,” *IEEE Transactions on Industrial Informatics*, vol. 11, pp. 853–864, Aug 2015.
- [88] G. Parma and V. Dinavahi, “Real-time digital hardware simulation of power electronics and drives,” in *2007 IEEE Power Engineering Society General Meeting*, pp. 1–1, June 2007.
- [89] P. L. Evans, A. Castellazzi, and C. M. Johnson, “Design tools for rapid multidomain virtual prototyping of power electronic systems,” *IEEE Transactions on Power Electronics*, vol. 31, pp. 101–110, March 2016.
- [90] N. Maithil, R. Agrawal, S. Bharadwaj, and D. P. Kothari, “Simulation tools for power electronics. an overview,” *International Journal on Emerging Technologies*, vol. 4, no. 1, pp. 104–107, 2013.
- [91] P. Bazan and R. German, “Hybrid simulation of renewable energy generation and storage grids,,,” in *Proceedings of the 2012 Winter Simulation Conference*, 2012.
- [92] H. K. Fathy, Z. S. Filipi, J. Hagen, and J. L. Stein, “Review of hardware-in-the-loop simulation and its prospects in the automotive area,” 2006.
- [93] G. F. Lauss, M. O. Faruque, K. Schoder, C. Dufour, A. Viehweider, and J. Langston, “Characteristics and design of power hardware-in-the-loop simulations for electrical power systems,” *IEEE Transactions on Industrial Electronics*, vol. 63, pp. 406–417, Jan 2016.
- [94] D. Majstorovic, I. Celanovic, N. D. Teslic, N. Celanovic, and V. A. Katic, “Ultralow-latency hardware-in-the-loop platform for rapid validation of power electronics designs,” *IEEE Transactions on Industrial Electronics*, vol. 58, pp. 4708–4716, Oct 2011.
- [95] S. Y. R. Hui and S. Morrall, “Generalised associated discrete circuit model for switching devices,” *IEE Proceedings - Science, Measurement and Technology*, vol. 141, pp. 57–64, Jan 1994.
- [96] F. Jimenez, *Specification et Conception de Micro-systemes Bases sur des Circuits Asynchrones*. PhD thesis, Institut National des Sciences Appliquees (Toulouse, Fra), LAAS-CNRS (Toulouse, Fra), Uniandes (Bogota, Col)., 2000.
- [97] “<https://hiles.uniandes.edu.co/>.”
- [98] H. Hoyos, R. Casallas, and F. Jimenez, “Model-based framework for embedded system product line,” in *IECON 2012 - 38th Annual Conference on IEEE Industrial Electronics Society*, pp. 3101–3106, Oct 2012.
- [99] D. Rene and H. Alla., *Discrete, Continuous, and Hybrid Petri Nets*. Springer, 2005.

-
- [100] E. Batzelis, P. Georgilakis, and S. Papathanassiou, “Energy models for photovoltaic systems under partial shading conditions: a comprehensive review,” *Renewable Power Generation, IET*, vol. 9, no. 4, pp. 340–349, 2015.
- [101] V. Utkin, J. Guldner, and J. Shi, *Sliding mode control in electromechanical systems*. CRC Press, second ed., 2009.
- [102] J. H. M. Vasquez, “Estudio de convertidores adaptativos dc-dc/ac para su uso en redes inteligentes y sistemas fotovoltaicos,” Master’s thesis, Universidad de los Andes, 2017.
- [103] H. Abdelgawad and V. K. Sood, “Performance analysis of boost converter by using different integration algorithms,” in *2016 IEEE Canadian Conference on Electrical and Computer Engineering (CCECE)*, pp. 1–5, May 2016.
- [104] M. R. Modabbernia, A. R. Sahab, M. T. Mirzaee, and K. Ghorbany, “The state space average model of boost switching regulator including all of the system uncertainties,” *Advanced Materials Research*, vol. 4, no. 1, pp. 3476–3483, 2011.

Appendix A

Conventional Boost Converter Modeling

In this appendix, conventional modeling methodologies of switched state-space and state-space averaged are applied to the Boost converter analysis [82]. The scope of these models is the ideal Boost converter and the Boost converter with associated losses.

Ideal Boost converter modeling

Switched state-space model

The Boost converter is a power converter used in a wide range of application. These applications go from low power to high power. In PV systems Boost converters are widely used because of their features. In typical operation of the boost converter the output voltage is higher than the input voltage. Fig. A.1 shows a conventional ideal Boost converter circuit [78].

As shown in Fig. A.1 and Fig. A.2, when control PWM signal u is high the switch is close. In contrast, when control PWM signal u is low the switch is open. The switch in Fig. A.1 controls the current flow through the inductor as shown in Fig. A.2. Waveforms in Fig. A.2 correspond to steady-state operation in continuous conduction mode. In this operation mode $I_L > 0$. The control PWM signal is high during dT_s and low during $(1-d)T_s$; then d is defined as a duty cycle.

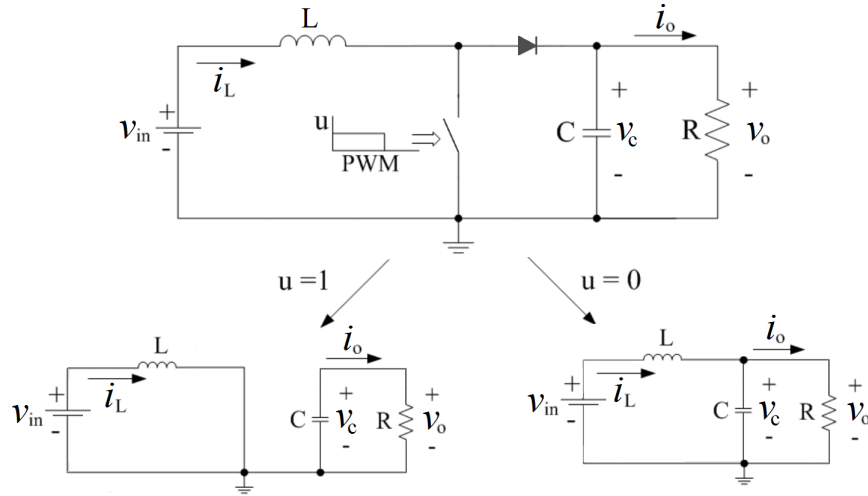


Fig. A.1 Ideal Boost converter.

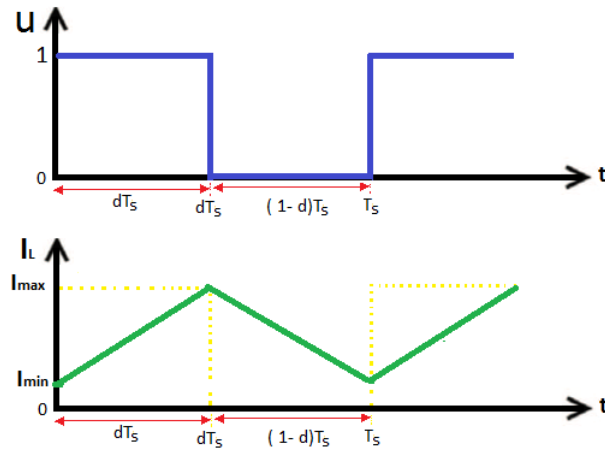


Fig. A.2 Waveforms of PWM signal and inductor current for ideal Boost converter.

The inductor current and capacitor voltage are the natural state variables of the Boost converter, the resistor voltage is the output, and using the notation in Fig. A.1. The following state-space model of eq.(A.2) to eq.(A.5) describes the switch in ON-state [103].

$$\begin{cases} \dot{x} = A_1 x + B_1 v_{in} \\ v_o = C_1 x \end{cases} \quad (\text{A.1})$$

$$x = \begin{bmatrix} i_L \\ v_c \end{bmatrix} \quad (\text{A.2})$$

$$A_1 = \begin{bmatrix} 0 & 0 \\ 0 & -\frac{1}{RC} \end{bmatrix} \quad (\text{A.3})$$

$$B_1 = \begin{bmatrix} \frac{1}{L} \\ 0 \end{bmatrix} \quad (\text{A.4})$$

$$C_1 = [0 \quad 1] \quad (\text{A.5})$$

Eq.(A.6) to eq.(A.9) describes the state-space model when switch is OFF.

$$\begin{cases} \dot{x} = A_2x + B_2v_{in} \\ v_0 = C_2x \end{cases} \quad (\text{A.6})$$

$$A_2 = \begin{bmatrix} 0 & -\frac{1}{L} \\ \frac{1}{C} & -\frac{1}{RC} \end{bmatrix} \quad (\text{A.7})$$

$$B_2 = \begin{bmatrix} \frac{1}{L} \\ 0 \end{bmatrix} \quad (\text{A.8})$$

$$C_2 = [0 \quad 1] \quad (\text{A.9})$$

State-space averaged model

To design an analog feedback control scheme, a tractable model that relates the modulating signal or the duty ratio to the output voltage is required. Since the ripple in the instantaneous output voltage is relative small, and since the details of this small output require less interest in the of design the feedback compensation, the small ripple can be neglected [103]. Then ,

$$\dot{\bar{x}} = [A_1d + A_2(1-d)] \bar{x} + [B_1d + B_2(1-d)] v_{in} \quad (\text{A.10})$$

$$\begin{bmatrix} \frac{di_L}{dt} \\ \frac{dv_c}{dt} \end{bmatrix} = \begin{bmatrix} 0 & \frac{-(1-d)}{L} \\ \frac{(1-d)}{C} & \frac{-1}{RC} \end{bmatrix} \begin{bmatrix} i_L \\ v_c \end{bmatrix} + \begin{bmatrix} \frac{1}{L} \\ 0 \end{bmatrix} v_{in} \quad (\text{A.11})$$

$$v_o = [0 \quad 1] \begin{bmatrix} i_L \\ v_c \end{bmatrix} \quad (\text{A.12})$$

Now, applying standard linearization techniques and small perturbations as follows:

$$i_L = I_L + \hat{i}_L; \quad v_c = V_c + \hat{v}_c; \quad v_{in} = V_{in} + \hat{v}_{in}; \quad d = D + \hat{d} \quad (\text{A.13})$$

Separating terms of \hat{i}_L , \hat{v}_c , \hat{v}_{in} , \hat{d} . Hence, the small signal model of the Boost converter is given as below [103].

$$\begin{cases} \dot{x} = A_p x + B_p v_{in} \\ v_o = C_p x \end{cases} \quad (\text{A.14})$$

where,

$$A_p = \begin{bmatrix} 0 & -\frac{(1-d)}{L} \\ \frac{(1-d)}{C} & -\frac{1}{RC} \end{bmatrix} \quad (\text{A.15})$$

$$B_p = \begin{bmatrix} \frac{1}{L} \\ 0 \end{bmatrix} \quad (\text{A.16})$$

$$C_p = [0 \quad 1] \quad (\text{A.17})$$

Boost converter modeling with losses

Fig. A.3 shows a conventional Boost converter circuit including losses associated to inductor R_L , switching device R_{on} , and diode R_s , V_d [78].

Switched state-space model

The following state-space model of eq.(A.18) to eq.(A.23) describes the switch in ON-state of Boost converter circuit including losses [104].

$$\begin{cases} \dot{x} = A_1 x + B_1 v \\ v_o = C_1 x \end{cases} \quad (\text{A.18})$$

$$x = \begin{bmatrix} i_L \\ v_c \end{bmatrix} \quad (\text{A.19})$$

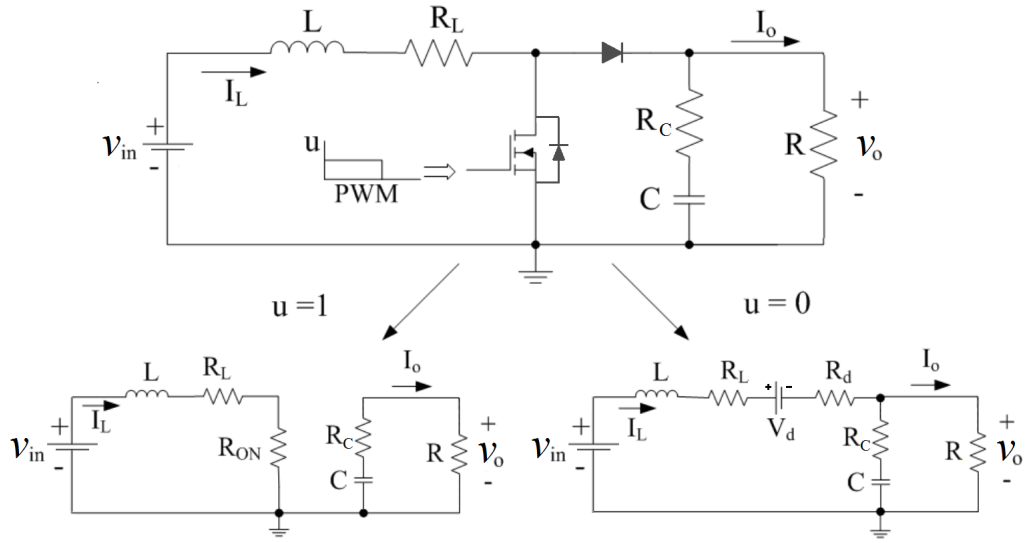


Fig. A.3 Boost converter with losses.

$$v = \begin{bmatrix} v_{in} \\ v_D \end{bmatrix} \quad (\text{A.20})$$

$$A_1 = \begin{bmatrix} \frac{-(R_L + R_{on})}{L} & 0 \\ 0 & \frac{-1}{C(R + R_c)} \end{bmatrix} \quad (\text{A.21})$$

$$B_1 = \begin{bmatrix} \frac{1}{L} & 0 \\ 0 & 0 \end{bmatrix} \quad (\text{A.22})$$

$$C_1 = \begin{bmatrix} 0 & \frac{R}{R + R_c} \end{bmatrix} \quad (\text{A.23})$$

Eq.(A.24) to eq.(A.28) describes the state-space model when switch is OFF.

$$\begin{cases} \dot{x} = A_2 x + B_2 v \\ v_o = C_1 x \end{cases} \quad (\text{A.24})$$

$$A_2 = \begin{bmatrix} \frac{-R_L}{L} - \frac{R_d}{L} - \frac{RR_c}{L(R + R_c)} & \frac{-R}{L(R + R_c)} \\ \frac{1}{C} - \frac{R_c}{C(R + R_c)} & \frac{-1}{C(R + R_c)} \end{bmatrix} \quad (\text{A.25})$$

$$A_2 = \begin{bmatrix} \frac{-(RR_L + RR_d + R_c R_L + R_c R_d + RR_c)}{L(R + R_c)} & \frac{-R}{L(R + R_c)} \\ \frac{R_c}{C(R + R_c)} & \frac{-1}{C(R + R_c)} \end{bmatrix} \quad (\text{A.26})$$

$$B_2 = \begin{bmatrix} \frac{1}{L} & \frac{-1}{L} \\ 0 & 0 \end{bmatrix} \quad (\text{A.27})$$

$$C_2 = \begin{bmatrix} \frac{RR_c}{R+R_c} & \frac{R}{R+R_c} \end{bmatrix} \quad (\text{A.28})$$

State-space averaged model

The average state-space model of Boost converter including losses is describe by eq.(A.29) to eq.(A.36) [104].

$$\begin{cases} \dot{\hat{x}} = A_p \hat{x} + B_p \hat{v} + E \hat{d} \\ \hat{v}_o = C_p \hat{x} + F \hat{d} \end{cases} \quad (\text{A.29})$$

where,

$$A_p = \begin{bmatrix} \frac{-R_{on}d - R_L - R_d(1-d)}{L} - \frac{RR_c(1-d)}{L(R+R_c)} & \frac{-R(1-d)}{L(R+R_c)} \\ \frac{R(1-d)}{C(R+R_c)} & \frac{-1}{C(R+R_c)} \end{bmatrix} \quad (\text{A.30})$$

$$B_p = \begin{bmatrix} \frac{1}{L} & -\frac{(1-d)}{L} \\ 0 & 0 \end{bmatrix} \quad (\text{A.31})$$

$$C_p = \begin{bmatrix} \frac{(1-d)RR_c}{R+R_c} & \frac{R}{R+R_c} \end{bmatrix} \quad (\text{A.32})$$

$$E = \begin{bmatrix} \frac{K + R^2(1-D)V_{in} - K(1-D) + R^2(1-D)^2}{L\Delta} \\ \frac{-RV_{in} - R(1-D)v_D}{C\Delta} \end{bmatrix} \quad (\text{A.33})$$

$$F = \frac{-RR_c V_{in} + RR_c(1-D)V_D}{\Delta} \quad (\text{A.34})$$

where Δ and K are given by,

$$\Delta = (R_L + R_{on})(R + R_c) + (RR_c + RR_d + R_cR_d - RR_{on} - R_cR_{on})(1-D) + R^2(1-D)^2 \quad (\text{A.35})$$

$$K = RR_c + RR_d + RdR_c - R_cR_{on} - RR_{on} \quad (\text{A.36})$$

Appendix B

Boost Inverter Design and Fabrication

The Boost inverter of Fig.B.1 is designed to increase a DC input voltage from 60V to 311V peak AC output voltage with a load of 500W. According to design parameters and comprehensive simulations, the criterion to choose the main components are summarized in Table B.1.

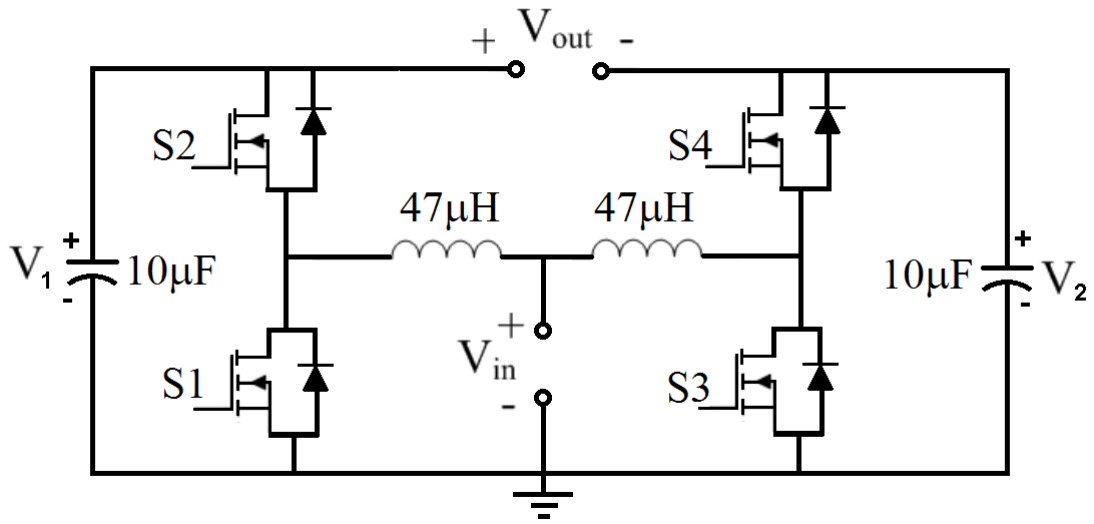


Fig. B.1 Boost inverter implemented

Fig. B.2, Fig. B.3, Fig. B.4 correspond to the selected commercial devices which accomplish the design requirements. Based on the advanced and innovative properties of wide band gap materials, silicon carbide SiC-MOSFETs feature very low R_{DSon} resistance combined with excellent switching performance, translating into more efficient

Table B.1 Design Parameters

Design constraint	Value
$I_{MOS_{max}}$	19.5 A
$V_{MOS_{max}}$	450 V
$I_{L_{max}}$	18.3 A
L	47 μF
C	10 μF
F_{sw}	100 KHz

and compact systems. Compared with silicon MOSFETs, SiC-MOSFETs exhibit low on-state resistance even at high temperatures and excellent switching performances versus the best-in-class IGBTs in all temperature ranges, simplifying the thermal design of power electronic systems. For these reasons, SiC-MOSFET was selected as switching device for this prototype. In order to choose the suitable driver for the SiC-MOSFETs, a series of test was developed at the characterization laboratory of LAAS-CNRS.

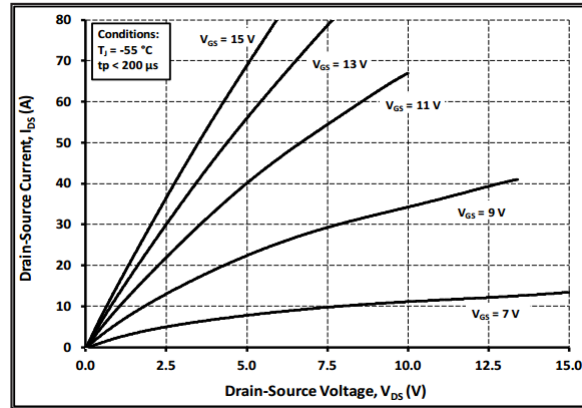


Fig. B.2 Drain-Source current SiC-MOSFET C3M0065090D

Fig. B.5b, Fig. B.5a, Fig. B.6a depict the experimental results of parasitic capacitance characterization. Taking into account the characterization results and Switching $V_S R_{g_{ext}}$ behavior from data sheet (Fig. B.7), the driver 1EDI20N12AF was selected as a suitable device to accomplish these design constraints. Fig. B.8 illustrates about definitions of C_{iss} , C_{oss} , C_{rss} , R_{gon} , R_{goff} , and their relation with the characteristics of selected driver. Additionally, Fig. B.6b shows the measured $V_{GS_{th}}$. This measured $V_{GS_{th}}$ and the data sheet specifications lead to choice a dual polarity source to drive the MOSFET. Therefore, in this design the MGJ2D121505SC isolated power source

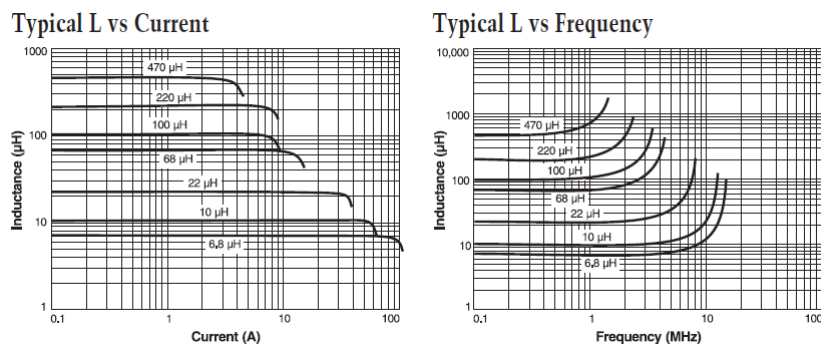


Fig. B.3 L-Current; L-Frequency Inductor AGP4233

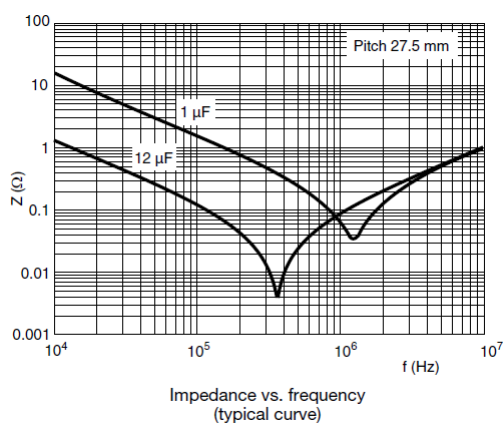
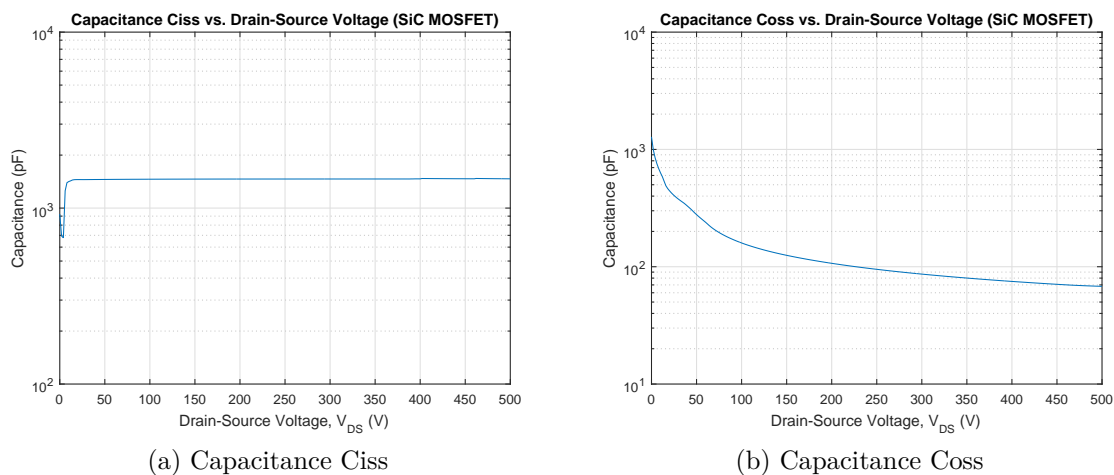


Fig. B.4 Impedance-Frequency Capacitor MKP1848

gate drive was selected to supply the voltages to the MOSFET Gate.



(a) Capacitance Ciss

(b) Capacitance Coss

Fig. B.5 Ciss, Coss characterization of SiC-MOSFET

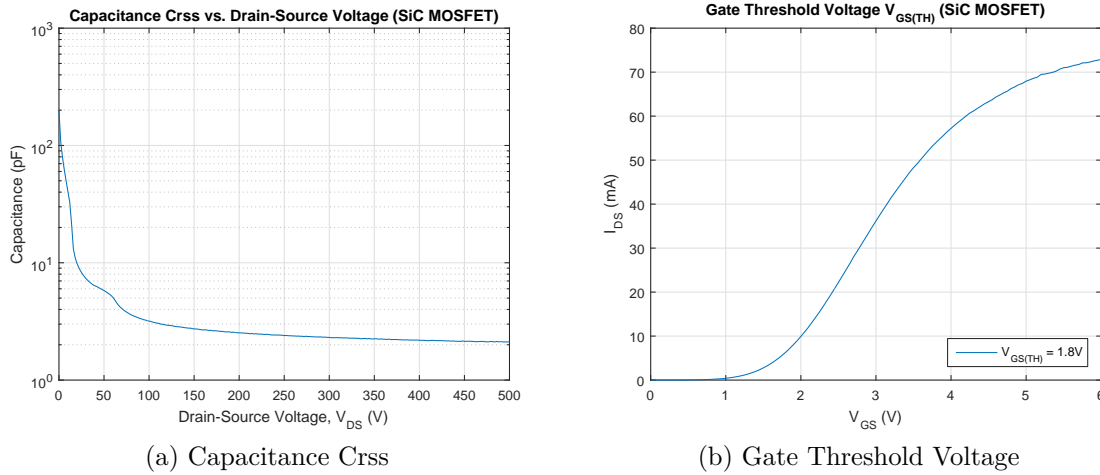


Fig. B.6 C_{rss} , $V_{GS_{th}}$ characterization SiC-MOSFET

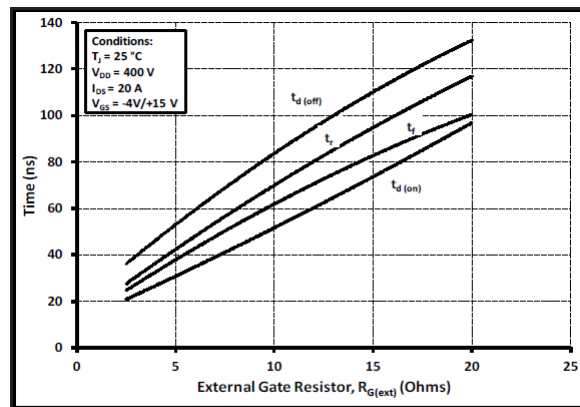


Figure 27. Switching Times vs. $R_{G(ext)}$

Fig. B.7 Switching time Vs $R_{G_{ext}}$ from SiC-MOSFET datasheet

Table B.2 lists the main components for the designed Boost inverter.

Experimental results for the prototype in DC/DC operation are shown in Fig.B.11 for inductor current and in Fig.B.12 for the output voltage. These results show the suitable operation of designed converter with low noise in inductor current and regulated output voltage when the PWM signal drives the SiC-MOSFET. Fig. B.13 illustrates the experimental results for DC/AC operation. Results of DC/AC operation allow verifying the normal sinusoidal operation when a SPWM signal drives the power stage.

Finally, the thermal behavior of the power stage is tested as shown in Fig. B.14. This figure allows confirming the thermal robustness of the SiC-MOSFET; however,

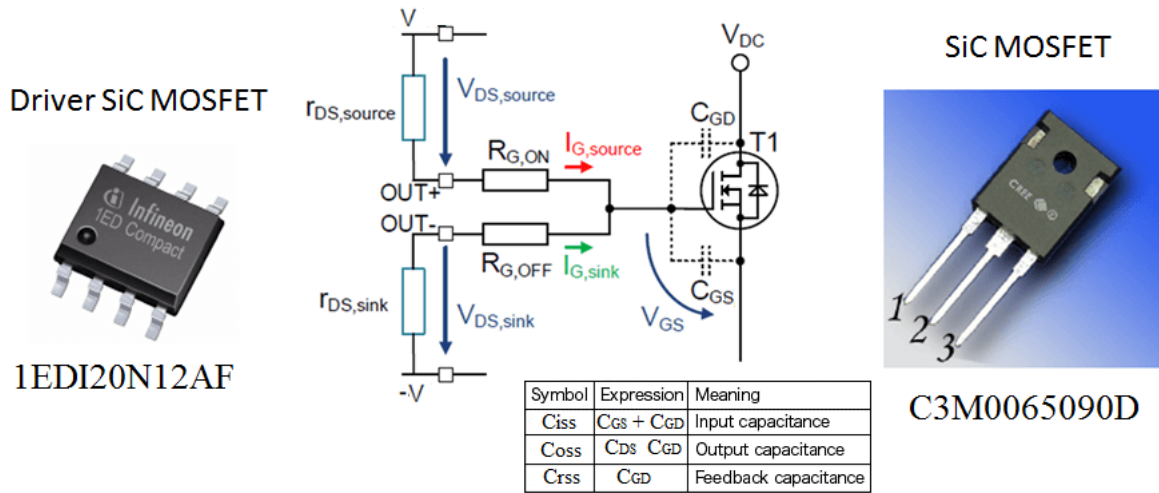


Fig. B.8 Selection driver SiC-MOSFET

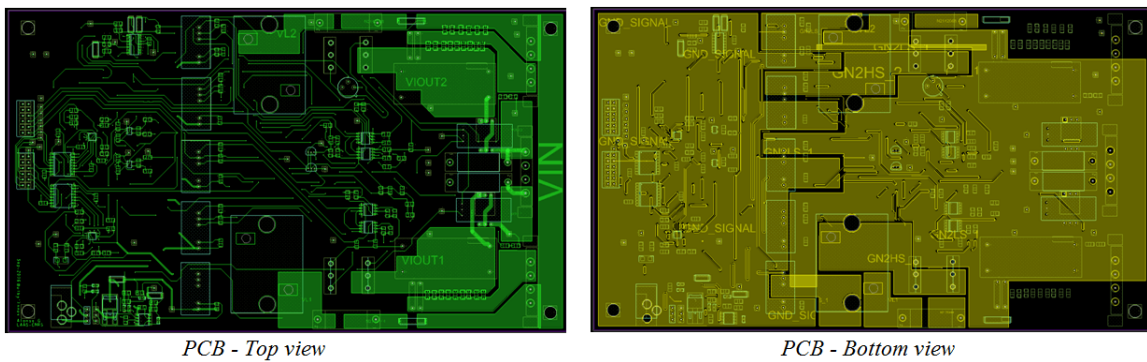


Fig. B.9 PCB Boost inverter

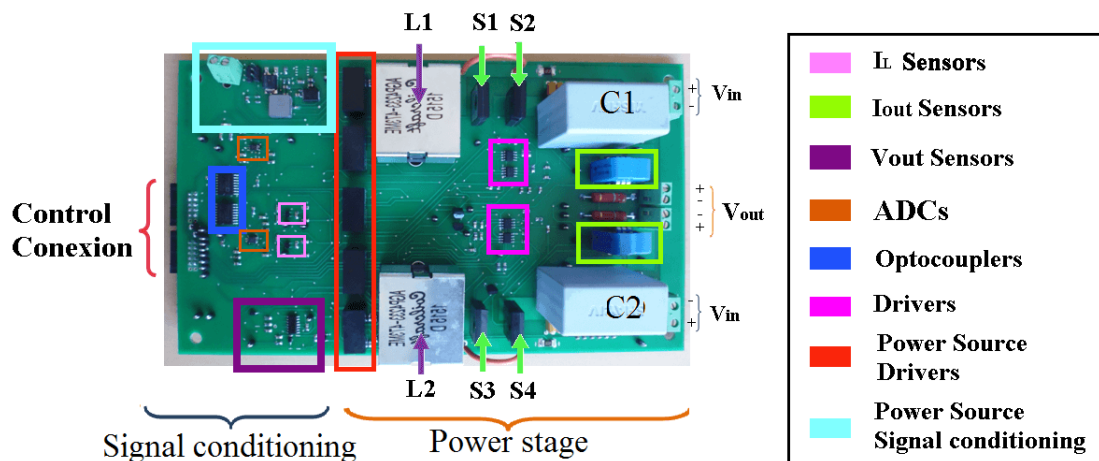
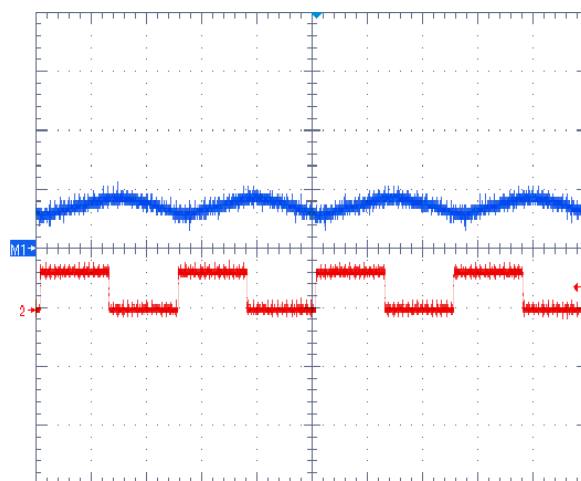
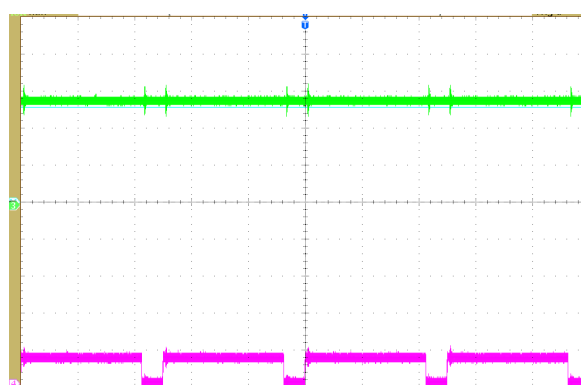


Fig. B.10 Final prototype

Table B.2 List of main components

Component	Reference
$C_1 - C_2$	$10 \mu F$
$L_1 - L_2$	$47 \mu H$
$S_1 - S_4$	C3M0065090D - SiC MOSFET
Driver MOSFET	1EDI20N12AF
Power Driver	MGJ2D121505SC
Ioutsensor	LTS-15-NP
ILsensor	INA197
Vsensor	Resistive divider
ADC	ADC124S101
Optocoupler	ADuM3401CRWZ

Fig. B.11 Inductor current (I_L) and driver signal (pwm) on one Boost inverter legFig. B.12 DC regulated voltage (V_{ODC}) and driver signal (pwm)

this thermal image also shows that the isolated power sources that supply energy to the MOSFET Gates represent a possible power loss. Then, further prototype designs

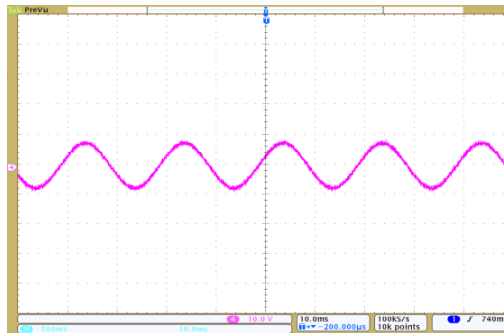


Fig. B.13 Experimental results of Boost inverter in DC-AC operation

should be considered this aspect in order to improve the converter efficiency.

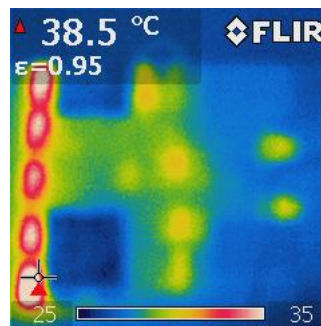


Fig. B.14 Thermal image of power stage

Appendix C

HiLeS Fundamentals

HiLeS proposal is based on a **formalism** based on Petri Nets and a global system design **methodology**. HiLeS tools integrated novel features as a high-level graphic semantic, a formal representation of functional states and an automatic generation of VHDL-AMS code. HiLeS provided design functionality validation by execution of the generated code on HDL's simulators (i.e. System Vision) and structural validation by the evaluation of control net using Time Petri net Analyzers (i. e. Tina) [96].

C.1 HiLeS Formalism

HiLeS formalism consists of a language and a methodology. The language is an extension to the Petri nets that incorporates continuous behavior and hierarchy. The methodology is intended to support embedded system design. Additionally, HiLeS defines the mapping rules to represent a HiLeS model in a hardware description languages. This enables designers to build virtual prototypes that allow technological independent analysis and operational verifications, with both formal and simulation verification of specifications and requirements.

The HiLeS formalism was created to support designing processes with a formal behavioral model and to integrate novel features as a high level graphic semantic, a formal representation of functional states and compatibility with multidisciplinary representation languages for digital, analog and mixed signal descriptions. With HiLeS it is possible to describe asynchronous and concurrent behaviors, and either time, event, or mixed driven dynamics.

The elements of HiLeS language are presented graphically in figure C.1 (Page 164).

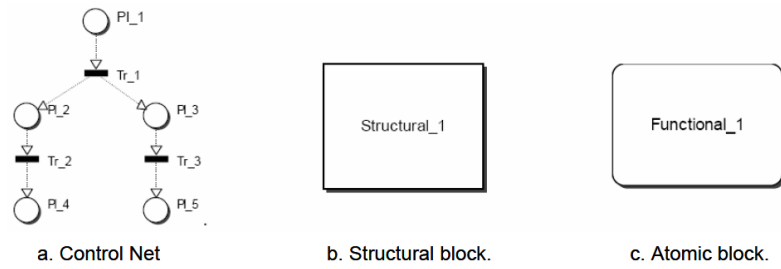


Fig. C.1 Elements of HiLeS Language

Control Model

The control model of a system described by HiLeS is based on ordinary Timed Petri Nets (figure C.1 a). The Petri net represents the execution of control commands and the blocks synchronization. The graph is constructed with two types of nodes: the places and transitions, two places can't be directly linked and two transitions neither. All the transitions got a triggering time of zero or superior. The Petri net arcs are represented by dashed arrows.

Structural and Atomic models

The structural blocks are represented by rectangles and allow the structural and hierarchical decomposition of the system (figure C.1 b). They admit all input/output channel types. Structural blocks can contain other structural or atomic blocks and a hierarchical control net. The Atomic blocks, or Functional blocks, are represented by round corner rectangles and describe the system continuous behavior in the form of differential, algebraic or logic equations (figure C.1 c). Atomic blocks don't have hierarchical properties.

The channels

The blocks or models and the control net are linked with channels (figure C.2, Page 164).

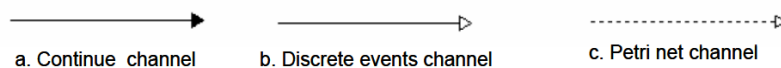


Fig. C.2 Channel types defined by HiLeS

The channels transport two signals types: continuous signals and discrete events signals. The nature of the signal depends on the in/out ports nature (electronic digital, electronic analog, electric, mechanic, thermal, chemical, etc.)

We consider the Petri net arcs as a particular type of discrete event channel that indicates: the flow of the token at the control net, an atomic block trigger signal, an atomic block activities acknowledgement, and a structural blocks control net signal exchanging.

Services and Ports



Fig. C.3 HiLeS model base services and ports

The services and ports are the input/output points of an environment and black box respectively (figure C.3, Page 165).

Depending on his class, they contain a nature or a type also, following the VHDL-AMS connection semantic.

The services are the environment exchange points of a functional description. The ports represent the exchanges of a black box on a given environment. A port of a black box is a equivalent to a service inside the box.

HiLeS Methodology

Time management and integration of the information and control

The blocks execution time is carried by the control Petri net as the trigger interval of an associated transition, knowing that it could be linked to several exit transitions. It's the time interval in which the transition could be crossed. At the figure C.4, (Page 166) an interval $[T1, T2]$ for the transition Tr_4 is equivalent to the block $Process_1$ execution time. This associated interval is important for a good control net design and to obtain a better performance of the verification process.

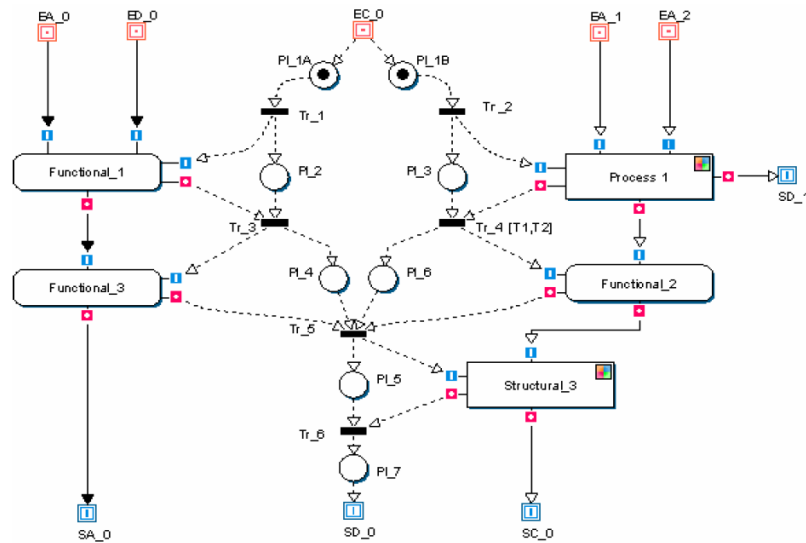


Fig. C.4 Control net and blocks integration on HiLeS architecture

Definition of Hierarchy

Starting from the HiLeS formalism elements, one can use HiLeS to make a high level description of a system. The structures specifications permit to detail the system mechanism (Figure C.3 a, Page 165). The Petri net – Blocks interaction describes the behavior of the system, the control instruction execution and the activities scaling on a hierarchic structure. HiLeS give a description that allows to:

1. Decompose a parent block in child blocks (C.3 b, Page 165)
2. Recompose a parent block from multiple child blocks

On identifying an elementary synthesis compound: the conjunction of block and a transition-place-transition.

Multiple Architecture Principle

This principle defines the structural construction of blocks by the way of using one or multiple architectures. The principle allows the designer to define different solutions for a given functionality without changing the interface. This principle is inherent to the classic VHDL entity-architecture construction and it has been already suggested by the “paradigm of reconfigurable models” for the systems conception. To better show the principle, the block Structural_1 (Figure C.6 a, Page 168) has 4 inputs (In_01, In_02, In_03, In_04) and an output (Out_01). The icon at the top-right corner of the

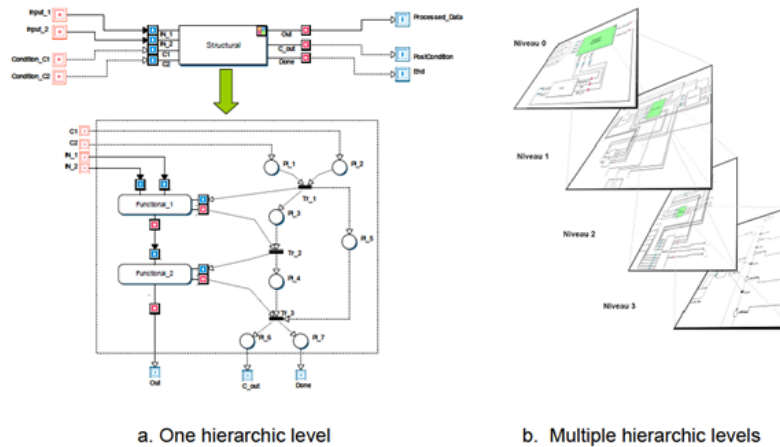


Fig. C.5 Evolution of a block model into a functional, hierarchic and temporized structure

block indicates the presence of at least one architecture. The block's Inputs/Outputs are kept, and we propose two possible solutions at figure C.6 a and c.

C.2 Automatic HDL code generators

In this section HiLeS is compared with other tools to automatic VHDL code generation. Because the IP core assets created by HiLeS IDE tool are FPGA oriented we must compare with existing tools for FPGA programming. The most used tools for FPGA programming are classified as:

1. C/C++/SystemC based: The hability oo tools for FPGA programing is brought about High Level Synthesis (Handel-C) is reality now with Spectra-Q form Altera and Vivado HLx from Xilinx. Output is Verilog and VHDL.
2. Phyton based: Phyton is a very popular across industry and academis even for embedded systema. The best example of this kind of tool is MyHDL. Output is VHDL and Verilog.
3. SCALA based: SCALA language for embedded systems was developped by EPFL at Laussana. CHISEL is new HDL tool developped at UC Berkley, same as SPICE. Outputs C++ and Verilog. Verification with C++ with software model. Other recent example is SPINAL HDL.
4. HASKEL based: Haskell is an functional programation language based on lambda-calculi and combinational logic. BSV (Bluespec SystemVerilog) is a HLS gen-

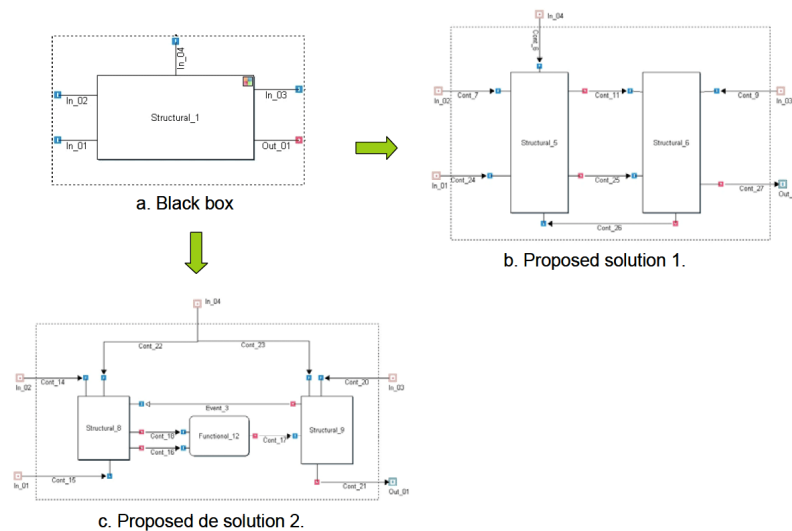


Fig. C.6 Example of multiple architecture for one interf

erating synthesisable Verilog and System C. System C are cycle accurate with Verilog and more fast to validate.

5. MATLAB/SIMULINK based: This popular languages supports a HDL coder producing synthesisable Verilog/VHDL. Complied with DO 254 requirements. HDL coder enables you also to perform hardware (FPGA) in the loop testing and co-simulation to see the difference between the original algorithm and the implemented hardware algorithm, which helps you explore the design space.
6. G language based: LabVIEW FPGA framework is a HLS tool for FPGA. Bit files produced is only for ZYNQ Xilinx FPGA for proprietary Compact RIO devices. Cloud based compilation for speediness. It could be used in C based environments which uses NI Real Time Systems. StateCAD9 by Xilinx
7. UML/SysML based (Lacks precise execution semantics – Not well suited for modeling plant and continuous control algorithms): (AMoDE-RT DERCS), SMU (MODCO), Enterprise Architect Engineering Edition from Iconix generation in VHDL, Verilog, and SystemC, simulation of sysml, simulation vhdl, Rational Rhapsody, Saturn (SystemC, IP-XACT, ARTiSAN Studio)

Table C.1 Comparison of Tools for Automatic Code Generation in Power Electronics Systems

Tool or Platform	Criteria					
	Abstract level	Output Code	System integration	Valid. & Verification	User friendliness	Simul. Complexity
Matlab/Simulink	Behavior	VHDL, Verilog, C	Low	Co-simul., State-Flow	Graph. Language	FPGA RTDS
Mades/Marte	System	VHDL	Low	Zot tool	SysML Diagrams	FPGA RTDS
Labview	Behavior	VHDL	Low	C code	Graph. language	FPGA RTDS
Enterprise Architect	System	VHDL, Verilog, System C	Low	Simul.	SysML	FPGA
HiLeS IDE	System	VHDL-AMS, Verilog-AMS	High	Time Petri nets, TINA simulation	SysML Diagrams	FPGA RTDS

Appendix D

Contribution to the HiLeS Framework

This Appendix presents the transformation chain proposed to integrate HiLeS projects in projects with higher hierarchic in order to apply the multiple hierarchic level approach.

Project integrator¹

Re-use of HiLeS Projects into other HiLeS projects allow creating models even more complex as shown in Fig. D.1. We added the possibility of support model imports in the transformation chain to take advantage of this re-use characteristics. The model import functionality uses the Papyrus import tool which allows to users import models that are included in the workspace.

To archive this goal we add to the SysML to HiLeS model to model transformation the possibility of support imported models in the transformation chain. One of the most important thing is to detect what is going to be the main entry entity of the model. As we know, the Block with the “*MainBlock*” profile assigned is the principal Block in our project, but when we import projects there are going to be more than one MainBlocks, the idea is to transform the MainBlock of the current project as the MainBlock of all projects. We did this by adding a guard that validates the condition: A MainBlock cannot be a MainBlock inside an imported package. The following part

¹This contribution was developed in collaboration with Kevin Sanchez (MSc) at the Universidad de los Andes

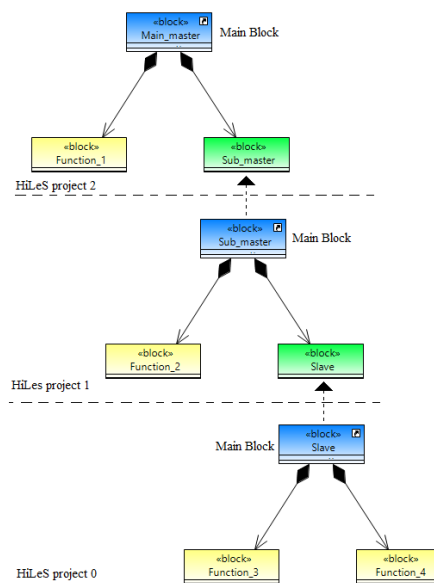


Fig. D.1 Multiple hierarchic level approach with HiLeS

of the rule MainBlock Structural shows the guard.

rule MainBlock2Structural

```
.
  transform mainBlock :SysML!HiLeS::MainBlock
.
  to blk :HiLeS!Structural
```

guard: not SysML!PackageImport.all().collect(pi | pi.importedPackage).collect(pe | pe.packagedElement). flatten().select(pak|pak.isTypeOf(SysML!Package)).collect(elem|elem.packagedElement).flatten().includes(mainBlock.base_Class)

To import a model form a workspace project we have to open the current model, then the “*Model explorer view*” and finally right click. A popup menu will be open, there we select Import–>Import Package From Workspace. In the window we have to find the project from we want to import the model and select just the .uml file. Finally we click on OK.

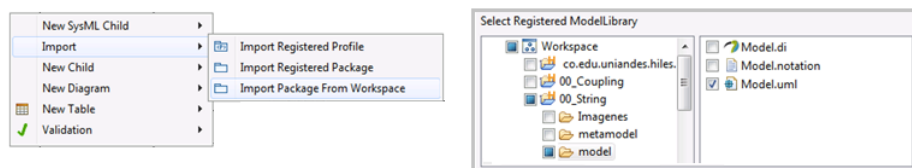


Fig. D.2 Multiple hierarchic level approach with HiLeS

The selected project will be imported in our project, so from here we can use the Blocks created in the imported package into our diagram. It is important to know that we have to add Blocks, Ports and other elements directly from the imported package in the model explorer view in order to recognize and transform in the Sysml to HiLeS transformation the whole structure and behavior of the used Block.